CZECH TECHNICAL UNIVERSITY IN PRAGUE
Faculty of Nuclear Sciences and Physical Engineering

Department of Physics

DISSERTATION

B physics studies at the ATLAS experiment

Prague, 2023

Ing. Lukáš Novotný

České vysoké učení technické v Praze
Fakulta jaderná a fyzikálně inženýrská

Katedra fyziky

Disertační práce

Studium B fyziky na experimentu ATLAS

Praha, 2023 Ing. Lukáš Novotný

Bibliographic Entry

Author	Ing. Lukáš Novotný Czech Technical University in Prague Faculty of Nuclear Sciences and Physical Engineering Department of Physics
Title	B physics studies at the ATLAS experiment
Degree Programme	Application of Natural Sciences
Field of study	Nuclear Engineering
Supervisor	Ing. Michal Marčišovský, Ph.D. Czech Technical University in Prague Faculty of Nuclear Sciences and Physical Engineering Department of Physics
Academic Year	2022/2023
Number of Pages	242
Key words	CP violation, lifetime measurement, B-Physics, ATLAS, LHC

Bibliografický záznam

Autor	Ing. Lukáš Novotný České vysoké učení technické v Praze Fakulta jaderná a fyzikálně inženýrská Katedra fyziky
Název práce	Studium B fyziky na experimentu ATLAS
Studijní program	Aplikace přírodních věd
Studijní obor	Jaderné inženýrství
Školitel	Ing. Michal Marčišovský, Ph.D. České vysoké učení technické v Praze Fakulta jaderná a fyzikálně inženýrská Katedra fyziky
Academic Year	2022/2023
Number of Pages	242
Key words	narušení CP symetrie, meření doby života, B-Fyzika, ATLAS, LHC

Abstract

This thesis focuses on the study of the CP violation and B meson lifetime properties. The Standard Model predicts the CP violating mixing phase ϕ_s to be very small and its theoretical value is very well constrained, while any measured deviations from the Standard Model value can indicate New Physics not described by the Standard Model. The first analysis described in this thesis is devoted to the CP violation in decays of $B_s^0 \to J/\psi\phi$. This measurement was performed using 80.5 fb^{-1} of the proton–proton collisions at a centre-of-mass energy of $\sqrt{s}$ = 13 TeV at the Large Hadron Collider recorded by the ATLAS detector. This analysis uses a precise determination of the initial flavour tagging probability using the decays of $B^\pm \to J/\psi K^\pm$. The results of the CP violation phase and B_s^0 lifetime properties were combined with the previous ATLAS measurements at a centre-of-mass energy of 7 and 8 TeV. The combined results agree with the Standard Model and they are:

$$\begin{aligned}
\phi_s &= -0.087 \;\pm\; 0.036 \;\text{(stat.)} \pm\; 0.021 \;\text{(syst.) rad},\\
\Delta\Gamma_s &= \;\; 0.0657 \pm 0.0043\,\text{(stat.)} \pm 0.0037\,\text{(syst.) ps}^{-1},\\
\Gamma_s &= \;\; 0.6703 \pm 0.0014\,\text{(stat.)} \pm 0.0018\,\text{(syst.) ps}^{-1}.
\end{aligned}$$

The second analysis presented in this thesis focuses on the measurement of the B^0 effective lifetime using $B^0 \to J/\psi(\mu^+\mu^-)K^{*0}(\pi^\pm K^\mp)$ decays in the 139 fb^{-1} data sample of pp collisions collected with the ATLAS detector during the 13 TeV LHC run between years 2015 and 2018. The extracted results are

$$\begin{aligned}
\tau_{B^0} &= 1.5174 \pm 0.0012\,\text{(stat.)} \pm 0.0016\,\text{(syst.) ps},\\
\Gamma &= 0.6586 \pm 0.0005\,\text{(stat.)} \pm 0.0006\,\text{(syst.)} \pm 0.0038\,\text{(ext.) ps}^{-1}.
\end{aligned}$$

Combining this value with the average decay width Γ_s, their ratio is

$$\frac{\Gamma}{\Gamma_s} = 0.9825 \pm 0.0022\,\text{(stat.)} \pm 0.0028\,\text{(syst.)} \pm 0.0057\,\text{(ext.)}.$$

The lifetime and Γ values show perfect agreement with the world average values and theoretical predictions. The 3σ tension of the Γ/Γ_s ratio is driven by the tension of the Γ_s.

Abstrakt

Tato disertační práce se věnuje studiu narušení CP symetrie a době života B mezonů. Fáze ϕ_s popisující CP narušení je ve Standardním modelu částic velice přesně určená. Jakékoliv odchylky od této teoretické hodnoty mohou naznačit existenci fyziky mimo popis Standardním modelem. První analýza v této práci studuje narušení CP symetrie v rozpadu $B_s^0 \to J/\psi\phi$. Toto měření využívá statistiku 80.5 fb^{-1} proton–protonových srážek při těžišťové energii $\sqrt{s} = 13$ TeV měřených detektorem ATLAS na LHC. Tato analýza využívá určení počátečního stavu B_s^0 mezonu pomocí tagovací pravděpodobnosti získané z analýzy rozpadu $B^\pm \to J/\psi K^\pm$. Měřené hodnoty fáze ϕ_s a vlastnosti doby života byly zkombinovány s předchozími měřeními detektorem ATLAS při těžišťových energiích 7 TeV a 8 TeV. Kombinované výsledky

$$
\begin{aligned}
\phi_s &= -0.087 \;\pm\; 0.036\ \text{(stat.)} \;\pm\; 0.021\ \text{(syst.) rad},\\
\Delta\Gamma_s &= \;\;0.0657 \;\pm\; 0.0043\ \text{(stat.)} \;\pm\; 0.0037\ \text{(syst.) ps}^{-1},\\
\Gamma_s &= \;\;0.6703 \;\pm\; 0.0014\ \text{(stat.)} \;\pm\; 0.0018\ \text{(syst.) ps}^{-1}
\end{aligned}
$$

souhlasí se Standardním modelem.

Další analýza prezentovaná v této práci se zaměřuje na měření efektivní doby života B^0 pomocí rozpadů $B^0 \to J/\psi(\mu^+\mu^-)K^{*0}(\pi^\pm K^\mp)$ ve 139 fb^{-1} pp srážek nasbíraných detektorem ATLAS při těžišťové energii 13 TeV v letech 2015 až 2018. Získané výsledky jsou

$$
\begin{aligned}
\tau_{B^0} &= 1.5174 \;\pm\; 0.0012\ \text{(stat.)} \;\pm\; 0.0016\ \text{(syst.) ps},\\
\Gamma &= 0.6586 \;\pm\; 0.0005\ \text{(stat.)} \;\pm\; 0.0006\ \text{(syst.)} \;\pm\; 0.0038\ \text{(ext.) ps}^{-1}.
\end{aligned}
$$

Spojíme-li tuto hodnotu s průměrnou šířkou rozpadu Γ_s, je jejich poměr následující

$$
\frac{\Gamma}{\Gamma_s} = 0.9825 \pm 0.0022\ \text{(stat.)} \pm 0.0028\ \text{(syst.)} \pm 0.0057\ \text{(ext.)}.
$$

Hodnoty životnosti a Γ vykazují dokonalou shodu s průměrnými světovými hodnotami a teoretickými předpověďmi. Odchylka 3σ poměru Γ/Γ_s se řídí danou odchylkou Γ_s.

ACKNOWLEDGEMENTS

I would like to express my deepest gratitude to my supervisor Michal Marčišovský for his invaluable advice, patience, helpfulness, and guidance during the realisation of this thesis. Furthermore, I would like to thank Václav Vrba for providing me the opportunity to participate in the ATLAS experiment at CERN and for his overall support during my work and studies. My profound gratitude goes to Mária Smižanská for the helpful discussions, advice and leadership of our analysis group. Many thanks also belong to James William Walder, Adam Edward Barton, Radek Novotný and Pavel Řezníček for always helping me with the problems I came across and for answering all my questions related to physics and coding. I am also especially grateful to Mária Marčišovská, Tomáš Jakoubek and Andrew Mark Wharton for helping with proofreading of this thesis.

I would also like to offer my thanks to my friends and colleagues at the Faculty of Nuclear Sciences and Physical Engineering of Czech Technical University in Prague for their academic support. Last but not least, I would like to thank my family, friends and above all Kristýna Šrámková for supporting me during my journey over the past few years.

Lukáš Novotný

Declaration

I hereby declare that this thesis is the result of my own work and all the sources I used are in the list of references. I have no objection to usage of this work in compliance with the act §60 Law No. 121/2000 Coll. (Copyright Act), and with the rights connected with the copyright act including the changes in the act.

Prohlášení

Prohlašuji, že jsem tuto práci vypracoval samostatně a použil jsem pouze podklady uvedené v přiloženém seznamu. Nemám závažný důvod proti použití tohoto díla ve smyslu §60 zákona č.121/2000 Sb., o právu autorském, o právech souvisejících s právem autorským a o změně některých zákonů (autorský zákon).

V Praze dne: ....

Ing. Lukáš Novotný

Table of Contents

Page

List of Tables

List of Figures

Introduction

The study of particle physics is critical to understanding our world's laws of physics. According to current knowledge, the universe is composed of tiny particles bound by several forces. The best mathematical and physical description is provided by the Standard Model, but it is not an entirely satisfactory theory. The Standard Model has parameters that cannot be predicted by theory. Furthermore, it cannot explain all known phenomena (for example, gravity is not included in the Standard Model, dark matter and energy are not described or predicted by the Standard Model, and it does not explain the matter-antimatter asymmetry). For these reasons, the Standard Model must still be verified by the experiments, and the theories beyond the Standard Model must be tested. Experimental particle physics provides great tools for the study of such theories. Moreover, it pushes forward the development of electrical engineering, accelerator and detector design and computing.

The study of the CP violation is a crucial test of the Standard Model. It provides the verification of the predictions via the study of the CKM matrix. The CP violation is well predicted by theories. Any deviations from the Standard Model predicted value can show imperfections and give higher importance to theories beyond the Standard Model.

This thesis focuses on studying the CP violation in the $B_s^0 \to J/\psi\phi$ decay together with the measurement of the B_s^0 lifetime properties. The analysis uses data from the Large Hadron Collider proton–proton collisions recorded in Run2 by the ATLAS experiment. The studied decay is sensitive to the initial flavour estimation of the B_s^0 meson due to the mixing of the B_s^0 and $\overline{B}_s^0$ mesons and their decay into the same final state that is detected. The supplementary analysis in this thesis is devoted to the measurement of the B^0 meson lifetime in the $B^0 \to J/\psi K^{*0}$ decay. This analysis provides the crosscheck of the correct approaches in measuring the B meson lifetime properties.

This thesis is organised into nine chapters. The first chapter provides an overall description of the particle world. Here, a brief overview of particle physics is included, followed by the description and categorisation of the elementary building blocks in the Standard Model: quarks, leptons and force carriers. Appropriate attention is paid to the discrete symmetries in the Standard Model, their violation and the incorporation of the CP violation into the Standard Model.

The second chapter is dedicated to the theoretical background of $B_s^0-\overline{B}_s^0$ mixing. The B meson properties are followed by the description of the $B_s^0-\overline{B}_s^0$ mixing via the difference between flavour and mass eigenstates using the effective Hamiltonian and the time-dependent B_s^0 wave functions. Furthermore, the B meson polarization and angular analysis are discussed. Lastly, the theoretical predictions and experimental observations of the CP violation by several experiments are presented.

The third chapter describes the Large Hadron Collider, its injection chain and layout. The past, present and future Large Hadron Collider performance is discussed. A brief overview of the seven main experiments at the Large Hadron Collider ring is provided.

The fourth chapter presents the details of each of the ATLAS detector subsystems: the Inner Detector, Electromagnetic Calorimeter, Hadronic Calorimeter and Muon Spectrometer. The sensors and modules are detailed in this chapter, together with the ATLAS operation modes and expected improvements in the future.

The following chapter introduces the ATLAS Trigger and Data Acquisition system levels: Level-1 Trigger and High Level Trigger. The physics object reconstruction is also detailed, and the format of the recorded data is discussed. The software used by ATLAS is also presented in this chapter.

The sixth chapter is devoted to the B physics program at ATLAS. It includes the description of the B meson production at the Large Hadron Collider, the ATLAS triggers dedicated to the B physics studies and the main research goals of the ATLAS B-Physics and Light States (BLS) working group. Finally, some recent results of the BLS working group are discussed.

The last three chapters present two analyses that are also the main focus of this thesis:

- Measurement of the CP-violating phase ϕ_s by ATLAS at 13 TeV [1],
- Precision measurement of the B^0 meson lifetime in $B^0 \to J/\psi K^{*0}$ decays [2].

The main contribution of the author to the first analysis is described in the seventh chapter. It includes an overview of the flavour tagging parameters and their extraction in the flavour tagging algorithms. The analysis [1] calibrates the flavour tagging using the self-tagged channel $B^{\pm} \to J/\psi K^{\pm}$. The event and candidate selection of this channel is described in the seventh chapter. The results of the $B^{\pm}$ mass fit and the ATLAS flavour tagging performance are presented. The propagation of the $B^{\pm}$ tagging information into the B_s^0 initial flavour tagging estimation is also included.

The eighth chapter provides details of the measurement of the CP-violating phase ϕ_s by ATLAS at 13 TeV. It presents the detector acceptances, where the author of this thesis prepared the Monte Carlo re-weighting. He is also responsible for the final shape of the probability density function used in the unbinned maximum likelihood fit for extracting the parameters of interest. He also participated in the calculations of the systematic uncertainties, focusing mainly on the systematic test due to the flavour tagging. Finally, the eighth chapter presents all the important pieces of the analysis and discusses the final results.

The last chapter is devoted to the precision measurement of the B^0 meson lifetime in $B^0 \to J/\psi K^{*0}$ decays. Here, the author was the main contributor to the analysis, so he was responsible for almost all stages of the analysis - from preparing the data and the fit model to studying the systematic effects and providing the final results. Lastly, this chapter includes the determination of the average decay width Γ.

CHAPTER 1

Introduction to the Particle Physics

Mandkind always asked what the world is made of. The first concept of matter composition can be found in ancient Greece, where atomists thought that nature consists of two fundamental principles: atom, invisible and indivisible particle, and void, the space where all possible configurations of atoms can form. This theory was left as the most sophisticated until the beginning of the 19th century, when chemistry was quickly developing. One of the essential people of the era was John Dalton. He used the term "atom" to refer to the fundamental particle of any chemical substance [3], not strictly to elements as is the practice today. Today, our world is known to be composed of leptons and quarks, and all matter is held compact by the four types of forces.

1.1 History

1.1.1 Composition of the Atom

The thought that atoms are the smallest and indivisible particles was broken by the discovery of electrons by J. J. Thomson in 1897 [4]. He observed a beam of negatively charged particles (today known as electrons) emitted by the cathode, and this beam could be deflected by a magnet. Using this deflection, Thomson measured the charge-to-mass ratio of newly discovered particles and observed surprising results - the ratio was more significant than for any known ion. Thomson observed electrons and correctly assumed that these particles were a part of the atom. However, the atom was known to be electrically neutral, but the electron was observed to have a negative charge. Therefore, Thompson developed a pudding model of the atom. In this model, the atom is formed by a positively charged paste, and electrons are stationed in it.

In 1911, E. Rutherford, with his students E. Marsden and H. Geiger, disproofs Thomson's model by a gold foil experiment [5]. They directed alpha particles at the gold foil and observed their deflection. Most of the alpha particles went straight through the foil, confirming Thomson's model of the atom. However, some particles were deflected, even scattered back to the source. This observation led Rutherford to present a planetary model of the atom - central positive charge (protons) surrounded by a cloud of electrons [5]. Rutherford's model was extended by N. Bohr's implementation of quantum mechanics [6]. He claimed that the electron circle around the nuclei in a stationary orbit. The orbits can be only at given distances from the nuclei fulfilling the condition of position multiplied by angular momentum to be an integer multiple of the reduced Planck constant. The condition was proposed by W. Heisenberg in 1927 and is known as *Uncertainty Principle* [7].

Bohr expected that the nucleus of atoms heavier than hydrogen is composed of the same number of electrons and protons. However, the helium with two electrons was observed to have a mass of approximately four protons instead of two. This dilemma was resolved by J. Chadwick, who discovered a neutron by detecting unknown, electrically neutral radiation coming from the interaction of alpha particles from ^{210}Po with the beryllium target [8]. When this ionizing radiation hit the paraffin wax, protons were ejected and detected. Chadwick also measured how the new radiation impacted the atoms of various gases. He observed that the radiation is composed of particles with a mass similar to protons, but the particles are uncharged. These particles were given the name neutrons.

1.1.2 The Photon

The photon was not discovered by only one experiment or physicist; it was described and measured in stages. In the 19$^{\text{th}}$ century, the light was believed to be a wave. In 1865, J. C. Maxwell predicted that light is a form of electromagnetic wave [9], and his theory was confirmed by the detection of radio waves by H. Hertz [10]. However, some properties were still not appropriately described. For example, M. Planck was attempting to explain the so-called black-body spectrum for the electromagnetic radiation emitted by a hot object (if the light is only a wave, the total power radiated should be infinite for given frequencies of radiated photons). To fix this, Planck proposed that electromagnetic radiation is quantized [11]. Each package of light carries the energy of $E = h\nu$, where $h = 6.62607015 \cdot 10^{-34}$ J $\cdot$ s is Planck's constant and ν is the frequency of the radiation. A. Einstein extended the theory [12] by claiming that energy quantization was a property of electromagnetic radiation itself. In 1916 Einstein showed that if Planck's law of black-body radiation is accepted, the energy quanta must also carry momentum, making them valid particles [13]. Accepting both particle and wave theories at the same time led to a wave-particle duality, claiming that all bodies are both states and only certain types of measurements can favour particle or wave properties.

1.1.3 Muons, Mesons and Strange Particles

Description of the atom nucleus seemed to have all necessary building blocks - protons and neutrons. However, it was unknown what causes the attraction between protons (which should be, in fact, repelled by their electrical charge) and neutrons (which cannot be affected by the electric force due to their neutral electrical charge). This force must be obviously stronger than electromagnetic, at least at short distances. In 1934, H. Yukawa predicted a particle that carries the nuclear force holding the atom's nucleus together. Yukawa expected the mass of this new particle (called μ *meson* by Yukawa) to be 300 times the mass of the electron [14]. Two years later, C. D. Anderson and S. Neddermeyer observed particles that could match Yukawa's predictions [15]. However, the measured lifetime and other properties of the μ meson conflicted with the expected properties of the Yukawa particle. For example, the experiment carried out in Rome demonstrated that μ particle (now called *muon*) interacts with the nuclei weakly. This measurement was in contrast to the expectation of Yukawa's theory. The final answer to the question of the nuclei force mediator was presented in 1947 by C. Powel, C. Lattes, and G. Occhialini. They performed a similar experiment to Anderson's one [16] and observed a new particle decaying into an already-known muon. They called the new particle a pion π. Over the next year, the pion was proven to be the (virtual) nuclear force carrier.

By discovering the pion (and observation of antiparticles and neutrinos, see next section), it was thought that the particle world is fully understood. However, the status of the particle physics description did not last long. In December 1947, G. D. Rochester and C. C. Butler presented photographs of a cloud chamber [17] with one decay of some neutral particle decaying in two oppositely charged pions or proton and pion and another decay of some charged particle into a pion and neutral particle. These *strange particles* were later names as kaons, K^0 decaying into $\pi^+\pi^-$ (1947) and K^+ decaying into $\pi^+\pi^-\pi^+$

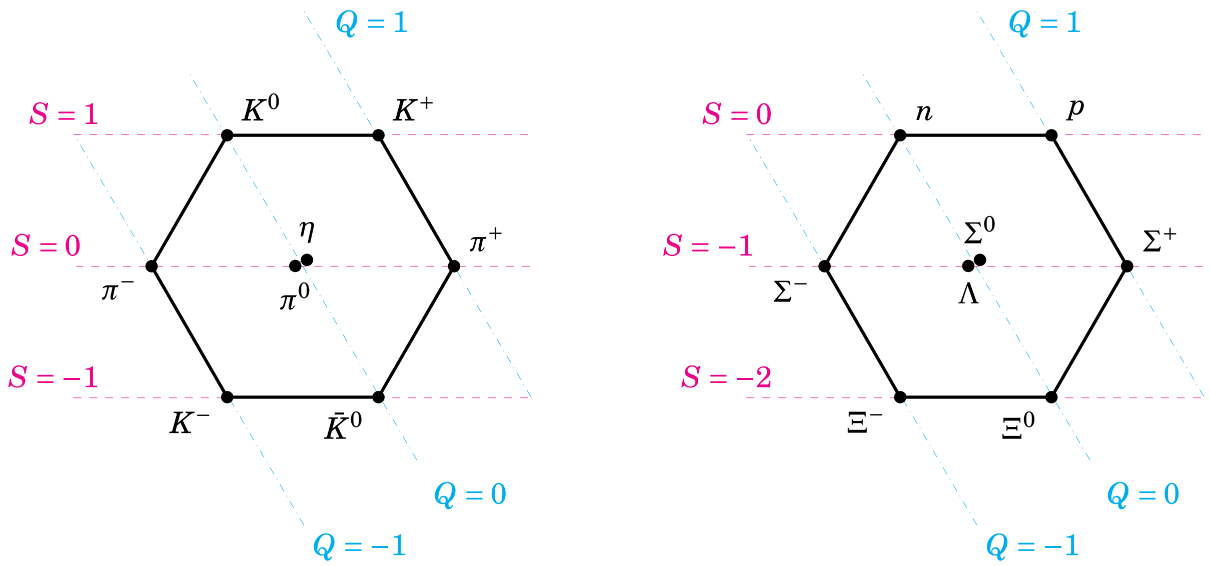

FIGURE 1.1. The meson and baryon octet organization proposed by M. Gell-Mann.

(1949) and lambda particle, $\Lambda \to p\pi^-$ (1950).

1.1.4 The Eightfold Way and Quark Model

The strange particle discovery independently led M. Gell-Mann, T. Nakano and K. Nishijima to suggest a new conserved quantum number - *the strangeness* [18–20]. The number of discovered mesons (understood today as quark-antiquark compound pair) and baryons (the state of three quarks) proliferated in the 1950s. Physicists were trying to understand the inner structure of mesons and baryons and they came up with the idea of meson and baryon organization. In 1961, Gell-Mann published a paper [21], where he presented meson and baryon octets - a weird geometrical arrangement of particles similar to that in Figure 1.1.

Gell-Mann's Eightfold Way also allowed another hadron structure, the baryon decuplet, to describe the heavier baryons (see Figure 1.2). Gell-Mann's organization of baryons and mesons is just a mathematical apparatus (the $SU(3)$ description) pretty well describing the properties of discovered particles. Still, it was unclear why hadrons fit exactly in these patterns.

The answer to this question was proposed in 1964, independently by M. Gell-Mann [22] and G. Zweig [23]. They proposed that all observed hadrons are composite particles having an inner structure. The elementary particles forming the hadrons were named *quarks*. The quarks can have three flavours: u (up) and s (strange) with fractional electric charge $2/3e$ and d (down) with electric charge $-1/3e$. The quark model claims that every baryon is composed of three quarks, and every meson is composed of quark-antiquark pair. The idea of the quark model theory was confirmed in 1968 when physicists performed deep inelastic scattering experiments at Stanford Linear Accelerator Center (SLAC) [24]. The results of the experiments demonstrated that the proton has an inner structure formed by point-like particles, the quarks.

1.1.5 November Revolution and the Third Family

The proton inner structure discovery was a striking success of the quark model theory. However, the model did not solve all open questions. One of the most important ones is the non-existence of free quarks and inconsistency with the Pauli principle (e.g.: Δ^{++}, composed of three u quarks, cannot exist unless there is another quantum number). The second question was answered a few months after the quark model presentation. O. W. Greenberg suggested another degree of freedom [25], not commuting with flavour - the colour.

In 1970, S. Glashow, J. Iliopoulos and L. Maiani invented the GIM mechanism [26] describing why the flavour-changing neutral currents (FCNC - interaction changing the flavour of quark or lepton but keeping the charge unchanged) are suppressed. This theory requires the existence of the fourth quark that was already predicted in 1964 by J. Bjorken and S. Glashow [27]. The discovery of this quark (c - charm quark) is known as

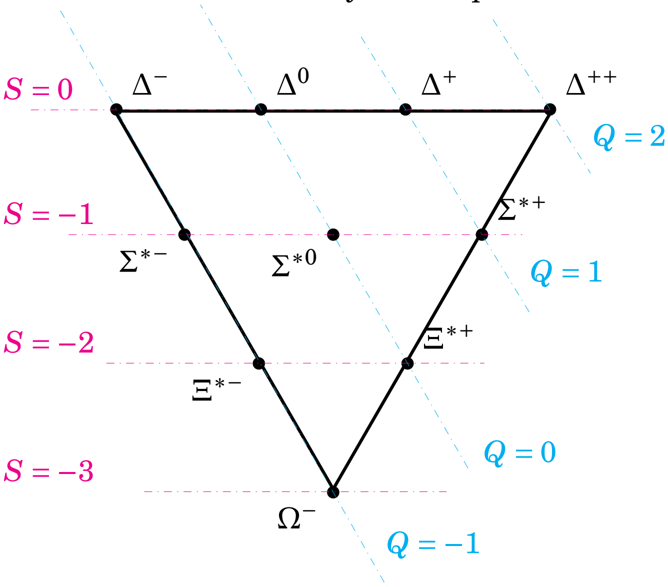

FIGURE 1.2. The baryon decuplet organization proposed by M. Gell-Mann.

the November revolution in particle physics. In November 1974, two experiments (the Brookhaven experiment led by C. C. Ting and the SLAC experiment led by B. Richter) independently announced the discovery of a new particle. Richter named it ψ [28], Ting called it J [29]. Today, it is known as a J/ψ particle, meson formed by charm quark and antiquark.

The quark model efficiently used charm quarks and formed new multiplets, predicting new particles discovered later. The GIM mechanism worked perfectly by having two families of leptons (electron with electron neutrino and muon with muon neutrino) and quarks (u-d family and s-c family). The GIM symmetry was, however, broken by the τ lepton discovery at SLAC in 1976 [30], leading scientists to predict the third family of quarks - b quark (bottom or beauty quark) and t quark (top or truth quark).

The b quark was discovered immediately after the τ observation in 1977 by the Fermilab E228 experiment led by L. M. Lederman [31]. They observed Υ particle with a mass around 9.5 GeV composed by bottom quark and antiquark.

The last piece of the quark model was the top quark discovery, announced in March 1995 by the CDF experiment [32].

1.1.6 Intermediate Vector Bosons and Higgs Boson

In 1933, E. Fermi described beta decay in [33] as a contact interaction (without mediator particle exchange). This assumption was not far from the truth, as the weak interaction (playing a dominant role in beta decay) has a short range. Fermi's theory encountered problems at higher energies and needed to be improved by introducing the mediating particle(s) for weak interaction. Additionally, the GIM mechanism introduced in the section above called for weak interaction mediators and even provided a theoretical prediction of their masses. This helped scientists build accelerators with parameters suitable for discovering these particles. The $W^{\pm}$ and Z^{0} particles were directly predicted around 1968 in a unified theory of electromagnetism and weak interactions by S. Glashow [34], S. Weinberg [35], and A. Salam [36].

In the 1970s, CERN[1] constructed the proton-antiproton collider (Super Proton Synchrotron) designed for the weak interaction mediators discovery. The discovery of the first of them, $W^{\pm}$ boson with a mass around 81 GeV/c^2 was announced to be discovered in January 1983, and its companion, Z boson with a mass of 91 GeV/c^2, was discovered in June of the same year by UA1 and UA2 experiments at the SPS collider [37, 38].

[1]European Organization for Nuclear Research (in French: **C**onseil **E**uropéene pour la **R**echerche **N**ucléaire), `www.cern.ch` .

The non-zero mass of the mediating bosons was the major obstacle for the electroweak unification theory because it predicted that the intermediate boson should have zero mass. Symmetry breaking, which can fix the problem with the non-zero mass of vector bosons, was already predicted in the 1960s. In 1964, P. Higgs [39] and R. Brout, F. Englert [40] put forward the Higgs mechanism. This mechanism is a process by which vector bosons can gain invariant mass without explicitly breaking gauge invariance as a byproduct of spontaneous symmetry breaking. It uses the Goldstone boson created by the Higgs field with four components. Three of them are absorbed by the W^+, Z^0, and W^- bosons forming their longitudinal components and the last one is the Higgs boson itself.

It took a long time to discover the Higgs boson. The Large Hadron Collider (LHC), with four major experiments (ATLAS, CMS, LHCb and ALICE), was built in 2007 to discover the Higgs boson. On 4$^{\text{th}}$ July 2012, the discovery of a new particle with a mass between $125-127$ GeV was jointly announced by ATLAS and CMS experiments [41, 42]. The observed particle behaved, interacted, and decayed in many ways predicted for Higgs particle.

1.1.7 Antiparticles and Neutrinos

The theoretical predictions and discoveries of antiparticles and neutrinos complete the history and the whole picture of particle physics.

In 1927, P. Dirac proposed an equation that describes electrons with relativistic energy [43]. This equation assumes that particles can have positive or negative energy (although the particles with only positive energy are observed). To describe the negative-energy states, Dirac assumed that particles with negative energy occupy the lowest energy states forming *Dirac sea*. Using the Pauli principle, no other electron can fall into this area and, therefore, has positive energy. However, one of the particles in the Dirac sea can be excited and lifted above sea level to have positive energy, leaving a hole in the Dirac sea that has the same properties as an electron except for the electric charge, which is the opposite. Not many physicists believed in the relevance of this theory, but it was saved by the Anderson experiment.

C. D. Anderson performed an experiment with a cloud chamber in a magnetic field. He detected particles with the same charge-to-mass ratio as electrons, but with opposite charge signs [44]. Anderson thought that he had discovered a new particle - the positron. In 1955, antiproton and antineutron were found by E. Segrè and O. Chamberlain at Berkeley [45], and other antiparticles were detected in the collisions. Nowadays, it is assumed that every particle has its antiparticle and some of the particles are their own antiparticle.

The neutrino first appeared in Pauli's proposal of beta decay description [48]. It was thought that neutron decays into proton and electron in this decay. The observed continuous energy spectrum of the electron was evidence of another particle ejected with the electron in the beta decay, conserving the total energy. Some evidence of neutrinos was observed after Pauli's prediction. However, the neutrino was not observed directly

family		symbol	name	mass	spin	charge
fermions	quarks	u	up	$2.16^{+0.49}_{-0.26}$ MeV	1/2	2/3
fermions	quarks	d	down	$4.67^{+0.48}_{-0.17}$ MeV	1/2	$-1/3$
fermions	quarks	s	strange	93^{+11}_{-5} MeV	1/2	$-1/3$
fermions	quarks	c	charm	1.27 ± 0.02 GeV	1/2	2/3
fermions	quarks	b	bottom	$4.18^{+0.03}_{-0.02}$ GeV	1/2	$-1/3$
fermions	quarks	t	top	172.76 ± 0.30 GeV	1/2	2/3
fermions	leptons	e	electron	$510.99895000 \pm 0.00000015$ keV	1/2	-1
fermions	leptons	μ	muon	$105.6583755 \pm 0.0000023$ MeV	1/2	-1
fermions	leptons	τ	tau	1776.86 ± 0.12 MeV	1/2	-1
fermions	leptons	ν_e	e-neutrino	< 1.1 eV	1/2	0
fermions	leptons	ν_μ	μ-neutrino	< 0.19 MeV	1/2	0
fermions	leptons	ν_τ	τ-neutrino	< 18.2 MeV	1/2	0
bosons	vector	γ	photon	$< 10^{-18}$ eV	1	0
bosons	vector	g	gluon	0	1	0
bosons	vector	$W^\pm$	W boson	80.379 ± 0.012 GeV	1	± 1
bosons	vector	Z^0	Z boson	91.1876 ± 0.0021 GeV	1	0
bosons	scalar	H	Higgs boson	125.25 ± 0.17 GeV	0	0
	Tensor	G	Graviton[2]	$< 5 \cdot 10^{-23}$ eV	2	0

TABLE 1.1. Particles (6 quarks and 6 leptons) and force carriers (6 bosons) in the SM [46]. The Higgs boson is a recently observed particle.

[2]The graviton is just a theoretical particle (not included in the SM nowadays), and it has not been discovered yet. However, gravitational waves (perturbations in linearized spacetime) were observed in 2016 [47].

until 1956. That year, C. L. Cowan and F. Reines detected antineutrino created in a nuclear reactor interacting with protons and producing electrons and positrons [49]. The positron immediately annihilated with one of the surrounding electrons and formed two gamma particles (photons) that were detected. The neutron was detected by capturing and releasing another photon. Powell detected the muon (anti)neutrino in the pion discovery experiment [50], and its existence explained why Powell observed a kink in the decay of pion into muon with the same charge. The decisive proof of neutrino existence is that no photon was observed in the muon decay into the electron, so the electron must be accompanied by two neutrinos (electron antineutrino and muon neutrino).

1.2 The Standard Model

The Standard Model (SM) of particles and interactions started being developed at the end of the 1970s, collecting all observed and theoretically predicted particles. Nowadays, it contains six bosons with an integer fundamental spin and 12 fermions with a half-integer fundamental spin. Details are briefly described in the sections below, and the essential properties of the Standard Model particles and force mediators are presented in Table 1.1.

interactions	**Electromagnetic**	**Weak**	**Strong**	Gravitational
gauge boson	photon γ	W^+, W^-, Z^0	gluons g	graviton
mass [GeV]	0	$m_W = 80.4$ $m_Z = 91.2$	0	?[3]
spin-parity	1^-	$1^-, 1^+$	1^-	2^+
internal symmetry	$\mathrm{U(1)_Y}$	$\mathrm{SU(2)_L}$	$\mathrm{SU(3)_C}$	-
source of charge	electric	weak	color	mass
coupling constant	$\frac{e^2}{4\pi\hbar c} = \frac{1}{137}$	$\frac{G(Mc^2)^2}{(\hbar c)} \approx 10^{-5}$	≤ 1	$\frac{G_N M^2}{4\pi\hbar c} \approx 10^{-40}$

TABLE 1.2. Fundamental interactions and their mediating particles [51].

[3]The mass of graviton is expected to be zero in four dimensions (three space and one time dimensions), but it can have nonzero mass in theories with more than four dimensions.

1.2.1 Interactions

The Standard Model is constructed as $\mathrm{SU(3)_C} \otimes \mathrm{SU(2)_L} \otimes \mathrm{U(1)_Y}$ gauge symmetry[4] describing the strong, weak and electromagnetic interactions. These interactions are realized by the exchange of the mediator bosons. In our everyday macroscopic and mundane life, the electromagnetic force is encountered, but strong and weak interactions become dominant at the distance scale of 10^{-15} m and smaller. The gravitational interaction is not included in the SM because it is described by the General Theory of Relativity and not by the relativistic quantum field theory – the consistent and predictive quantum gravity theory has not been formulated yet. However, it is included in this work to have a full description of all known interactions. The interaction properties are compared in Table 1.2.

1.2.1.1 Electromagnetic Interaction

The electromagnetic interaction between electrically charged particles is mediated by a photon exchange. This interaction includes the electrostatic force (repelling and attracting particles with the same and opposite sign of electrical charge, respectively) and a combination of electric and magnetic force that appears for charged particles moving relative to each other. The range of the electromagnetic interaction is infinite, the strength decreases with the distance between particles ($\sim 1/r$ for the electromagnetic potential), and is expressed by the coupling constant [46], also known as the fine structure constant,

$$\alpha_{\mathrm{EM}} = \frac{1}{4\pi\varepsilon_0}\frac{e^2}{\hbar c} = \frac{1}{137.035999084}, \tag{1.1}$$

where $e \simeq 1.602 \cdot 10^{-19}$ C is the electron charge magnitude, $\varepsilon_0 \simeq 8.854 \cdot 10^{-12}$ F/m is the permittivity of free space, $\hbar \simeq 1.054 \cdot 10^{-34}$ J·s is the reduced Planck constant and $c \simeq 2.998 \cdot 10^{8}$ m/s is the speed of light in vacuum [46].

Classical electrodynamics is described by Maxwell's equations [52]:

$$\partial_\mu F^{\mu\nu} = j^\nu, \tag{1.2}$$

where $j^\mu = \left(c\rho, \mathbf{j}\right)$ is the four-current density consisting of the charge density ρ, and the conventional current density $\mathbf{j}$ and $F^{\mu\nu}$ is electromagnetic tensor combining the electric

[4] $U(n)$ group of degree n is described by $n \times n$ unitary matrices. Further, the $SU(n)$ is a special $U(n)$ group with matrices determinant equal to one.

E and magnetic **B** fields into a covariant antisymmetric tensor [53]

$$F_{\mu\nu} = \begin{pmatrix} 0 & \frac{E_x}{c} & \frac{E_y}{c} & \frac{E_z}{c} \\ -\frac{E_x}{c} & 0 & -B_z & B_y \\ -\frac{E_y}{c} & B_z & 0 & -B_x \\ -\frac{E_z}{c} & -B_y & B_x & 0 \end{pmatrix}. \tag{1.3}$$

This tensor can also be written using the four-potential $A^\mu = \left(\frac{\phi}{c}, \mathbf{A}\right)$,

$$F_{\mu\nu} = \partial_\mu A_\nu - \partial_\nu A_\mu. \tag{1.4}$$

Maxwell's equations can also be derived from the Lagrangian [52],

$$\mathscr{L} = \mathscr{L}_{\text{em}} + \mathscr{L}_{\text{int}}, \qquad \mathscr{L}_{\text{em}} = -\frac{1}{4} F^{\mu\nu} F_{\mu\nu} \quad \text{and} \quad \mathscr{L}_{\text{int}} = -eJ^\mu A_\mu. \tag{1.5}$$

The classical (non-relativistic) particle can be described by the Schrodinger equation. The relativistic extension of it was made by P. Dirac (using natural units, $c = \hbar = 1$)

$$(\mathrm{i}\gamma^\mu \partial_\mu - m)\psi\left(x^\mu\right) = 0, \tag{1.6}$$

where $\psi(x^\mu)$ it the wave function of the particle with rest mass m. The Dirac equation can also be obtained from the Lagrangian [54]

$$\mathscr{L}_{\text{Dirac}} = \overline{\psi}\left(\mathrm{i}\gamma^\mu \partial_\mu - m\right)\psi. \tag{1.7}$$

Unfortunately, Dirac and Maxwell Lagrangians cannot describe electromagnetic interaction as the exchange of photons between two particles. To solve (not only) this, R. Feynman [55, 56], J. Schwinger [57] and S. Tomonaga [58] created the first quantum field theory that provided a relativistic quantum mechanical description of electromagnetism - the quantum electrodynamics.

Quantum electrodynamics (QED) The first step towards the Lagrangian of QED is the sum of Dirac and Maxwell Lagrangians. This simple sum has imperfections – it has no coupling of the field A^μ to particle ψ. A good candidate to fix this issue is the interaction term of (1.5), where the conserved current can be

$$J^\mu = -e\overline{\psi}\gamma^\mu\psi. \tag{1.8}$$

Substituting the current into the sum of Maxwell and Dirac Lagrangian, the final Lagrangian is [52]

$$\mathscr{L}_{\text{QED}} = \mathscr{L}_{\text{em}} + \mathscr{L}_{\text{int}} + \mathscr{L}_{\text{Dirac}} = -\frac{1}{4} F^{\mu\nu} F_{\mu\nu} + \overline{\psi}\left(\mathrm{i}\gamma^\mu D_\mu - m\right)\psi, \tag{1.9}$$

where $D_\mu = \partial_\mu + \mathrm{i}eA_\mu$ is the minimal coupling and describes the interactions between particles and gauge bosons, and the electromagnetic field A_μ is gauge invariant. It is defined to satisfy the Lorentz gauge invariance $\partial_\mu A^\mu = 0$. The field theory with $\mathscr{L}_{\mathrm{QED}}$ is called quantum electrodynamics (QED). It is Abelian local $U(1)$ gauge theory, conserving the coupling constant, which is the electric charge e in the case of QED.

In QED, the exchanged boson (a virtual[5] photon) is not taken as a single object. It is expected that the photon can produce electron-positron pairs, and those pairs emit further photons. This leads to the original electron being surrounded by the positrons (they are attracted), and newborn electrons are repelled away by the original electron. When getting closer to the original electron, the effect of positron shielding of electron charge is lower and lower. This means that the effective charge (and also fine structure constant (1.1)) is not constant, but it depends on the distance from electron or on the momentum transfer Q^2 – see Figure 1.3. Then, the running coupling constant is [54]

$$\alpha_{\mathrm{EM}}(Q^2) = \frac{\alpha_{\mathrm{EM}}(0)}{1 - \frac{\alpha_{\mathrm{EM}}(0)}{3\pi} \ln\left(\frac{Q^2}{m_e^2}\right)}, \tag{1.10}$$

where $\alpha_{\mathrm{EM}}(0) \approx 1/137$ and m_e is the electron mass.

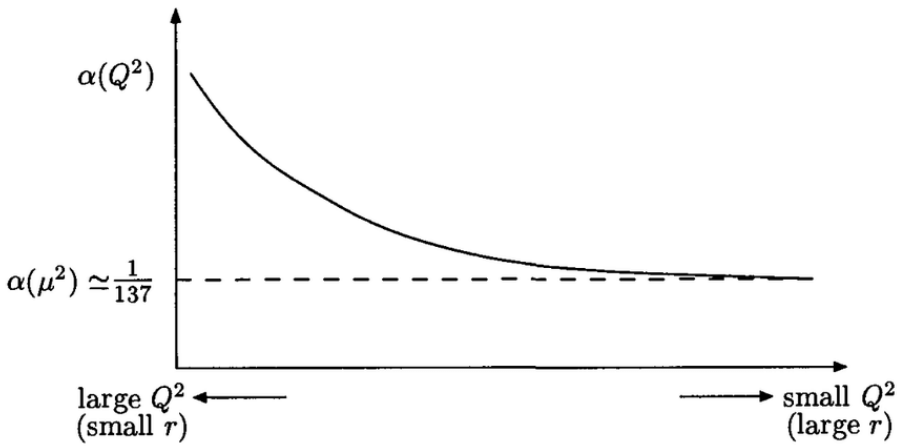

FIGURE 1.3. The running of the QED gauge coupling in the Standard Model α in dependence on the energy scale Q^2 and distance r [52].

[5]All particles have to fulfil Heisenberg's uncertainty principle. When a particle emits a photon, the photon takes some energy from the particle. To conserve the energy and uncertainty principles, the photon can live for a limited time (according to the energy), and the travelled length of the photon is minimal and unmeasurable – this leads to considering this photon as virtual.

1.2.1.2 Weak interaction

In the SM, the weak interaction is mediated through $W^{\pm}$ and Z^0 bosons. The weak interaction coupling is about 1000 times smaller than α_{EM} (1.1). It also has a very small range, $\sim 10^{-18}$ m. Using Heisenberg's uncertainty principle, the mediator must have a non-zero mass. Similarly to QED, the weak boson couplings to matter are described by current operators [53],

$$\mathscr{L}_{\mathrm{weak}} = V_\mu j^\mu, \tag{1.11}$$

where V_μ are the weak force mediator fields, and the j^μ is the current.

The weak interaction affects all fermions and also the Higgs boson. It is also the only force that can change the flavour of the fermions[6]. A good example is a β decay of a neutron inside a nucleus. Here, a neutron (udd) decays via weak interaction into a proton (uud), an electron and an electron antineutrino. This means that the quark flavour can change from *down* into *up*. This type of transformation is also called *Charged-current interaction* and is mediated via $W^{\pm}$ bosons. The charged-current Lagrangian from (1.11) is [52]

$$j^\mu_{CC} = \frac{g}{2\sqrt{2}} \sum_{l=e,\mu,\tau} \overline{\psi}_{\nu_l} \gamma^\mu \left(1-\gamma_5\right) \psi_l + \frac{g}{2\sqrt{2}} \overline{\psi}_{\overline{u},\overline{c},\overline{t}} \gamma^\mu \left(1-\gamma_5\right) V_{\mathrm{CKM}} \psi_{d,s,b} + \mathrm{h.c.}, \tag{1.12}$$

where $\gamma_5 = \mathrm{i} \prod_{\mu=0}^{3} \gamma_\mu$, ψ_{ν_l}, ψ_l are lepton wave functions, $\psi_{\overline{u},\overline{c},\overline{t}}$, $\psi_{d,s,b}$ are (anti)quark wave functions and V_{CKM} is the CKM matrix (see the section below for further details).

Z^0 particle mediates the second type of the weak interaction, the *Neutral-current interaction*, in which the flavour of the fermions is unchanged, and the current contains both left- and right-handed fermions [52]:

$$j^\mu_{NC} = \frac{g}{\cos\theta_W} \sum_f \left(\epsilon_L^{(f)} \overline{\psi}^f_L \gamma^\mu \psi^f_L + \epsilon_R^{(f)} \overline{\psi}^f_R \gamma^\mu \psi^f_R \right), \tag{1.13}$$

where $\theta_W \approx 30^\circ$ is the Weinberg angle and ψ^f_L, ψ^f_R are left- and right-handed fermion wave functions, respectively. The factors $\epsilon_L^{(f)}$ and $\epsilon_R^{(f)}$ are

$$\epsilon^{(f)}_{L,R} = T^{(f)}_{3\,L,R} - Q_f \sin^2\theta_W$$

with $T^{(f)}_{3\,L} = 1/2$ for neutrinos and u, c, t quarks, $T^{(f)}_{3\,L} = -1/2$ for changed leptons and d, s, b quarks, $T^{(f)}_{3\,R} = 0$ for all fermions and Q_f is electrical charge of fermion.

[6]The helicity is the sign of the particle spin or total angular momentum projection in the direction of the particle momentum. Weak interaction acts only on left-handed (helicity state) particles and right-handed antiparticles.

Electroweak unification S. L. Glashow, S. Weinberg and A. Salam proposed the unification mechanism of electromagnetic and weak interaction [59]. The electroweak interaction can be described by a Yang-Mills field [60] with an $SU(2)_L \otimes U(1)_Y$ (L for left-handed particles only and Y for the weak hypercharge) gauge group with the formal operations that can be applied to the electroweak gauge fields without changing the dynamics of the system. The fields are W_1, W_2, W_3 (a triplet associated with the weak isospin) and B (a singlet associated with the weak hypercharge). These fields are not physical ones unless using the Higgs mechanism and $W^{\pm}$, Z^0 are produced through the spontaneous symmetry breaking of the electroweak $SU(2)_L \otimes U(1)_Y$ symmetry into the electromagnetic symmetry $U(1)_{\text{em}}$. The electric charge is defined as the sum of the third isospin component and the weak hypercharge,

$$Q = T_3 + \frac{1}{2}Y. \tag{1.14}$$

Spontaneous symmetry breaking If the vector bosons are massive (they are observed to be massive in nature), the theory must contain a mass term that causes the breaking of gauge symmetry. The solution to this problem comes from the Higgs mechanism, which introduces the scalar fields interacting with massive bosons (and fermions). In the SM, the Higgs field is a complex scalar ϕ dictating how the system behaves, and its Lagrangian can be written as a sum of the kinetic and potential term [54]:

$$\mathscr{L} = \partial^{\mu}\phi^{\dagger}\partial_{\mu}\phi - V(\phi) = \partial^{\mu}\phi^{\dagger}\partial_{\mu}\phi - \frac{1}{2}\mu^2\phi^2 - \frac{1}{4}\lambda\phi^4, \tag{1.15}$$

where $\frac{1}{2}\mu^2\phi^2$ is the mass term and $\frac{1}{4}\lambda\phi^4$ is the interaction term of four-point vertex. The potential has $\lambda > 0$ and $\mu^2 > 0$ for vacuum state $\phi = 0$. The second possibility with $\lambda > 0$ and $\mu^2 < 0$ has the local maxima and two global minima at $\phi = \pm\sqrt{\frac{-\mu^2}{\lambda}} = \pm v$ and the potential shape is the famous "Mexican hat".

When using covariant derivative (containing the W^{μ} and B massless fields) instead of partial derivative in (1.15) and also the "Mexican hat" potential shape, the vacuum state can be chosen:

$$\phi = \frac{1}{\sqrt{2}}\begin{pmatrix} 0 \\ v + H(x) \end{pmatrix}, \tag{1.16}$$

where $H(x)$ is the Higgs field. Finally, the part of (1.15) with covariant derivatives gives with (1.16) the vector bosons mass terms:

$$\mathscr{L}_{\text{vect. boson mass}} = \left(m_W^2 W_{\mu}^{+} W^{-\mu} + m_Z^2 Z_{\mu} Z^{\mu}\right) \tag{1.17}$$

where $m_W = vg/2$, $g = e/\sin\theta_W$ and $m_Z = m_W/\cos\theta_W$. Note that the electromagnetic mediator still has zero mass.

Electroweak Lagrangian In conclusion, the electroweak Lagrangian after spontaneous symmetry breaking for the fermion fields ψ_i is [53]

$$\begin{aligned}\mathscr{L}_{EW} = &\sum_i \overline{\psi}_i \left(\mathrm{i}\gamma^\mu D_\mu - m_i - \frac{m_i H}{v} \right) \psi_i \\ &- \frac{g}{2\sqrt{2}} \sum_i \overline{\psi}_i \gamma^\mu \left(1-\gamma^5\right) \left(T^+ W_\mu^+ + T^- W_\mu^- \right) \psi_i \\ &- e \sum_i Q_i \overline{\psi}_i \gamma^\mu \psi_i A_\mu \\ &- \frac{g}{\cos\theta_W} \sum_f \left(\epsilon_L^{(f)} \overline{\psi}_L^f \gamma^\mu \psi_L^f + \epsilon_R^{(f)} \overline{\psi}_R^f \gamma^\mu \psi_R^f \right),\end{aligned} \tag{1.18}$$

where $A_\mu = B_\mu \cos\theta_W + W_\mu^3 \sin\theta_W$ is the photon field, $Z_\mu = W_\mu^3 \cos\theta_W - B_\mu \sin\theta_W$, $W^\pm = \left(W_\mu^1 \mp \mathrm{i} W_\mu^2\right)/\sqrt{2}$ are neutral and charged weak boson fields, respectively. The first term of (1.18) describes the Yukawa coupling of the Higgs field to fermions; the second term represents the charged-current weak interaction, the third term arises from the QED, and the last term describes the neutral-charged current.

The SM Lagrangian also contains the gauge part, describing the interaction of mass vector bosons, Higgs bosons and photons via the three- and four-track vertex (self)interaction, for example, $Z^0 \to W^+W^-$, $\gamma\gamma \to W^+W^-$, $Z^0\gamma \to W^+W^-$, $H \to HH$, $HH \to W^+W^-$ and many others).

1.2.1.3 Strong interaction

Unlike leptons, quarks and gluons interact via strong interaction. This force is responsible for binding quarks and gluons together, forming mesons and baryons (and other exotic states like recently observed tetraquarks and pentaquarks). The strong interaction is described within the quantum chromodynamics framework (QCD).
After observation of the three up quark system, Δ^{++} in 1952 [61], the colour quantum number has been introduced as an extra degree of freedom in the quark model in order for quarks in baryons not to violate the Pauli exclusion principle. Every quark has assigned either red (r), blue (b) or green (g) colour. Similarly, antiquarks have their anticolour (antired - $\bar{r}$, antiblue - $\bar{b}$ or antigreen $\bar{g}$). O. Greenberg [62] proposed that the non-Abelian group represented by the 3×3 unitary matrices $\mathrm{SU}(3)_C$ is the local symmetry corresponding to the gauge field of the QCD [63]. For $\mathrm{SU}(3)_C$, we obtain $N^2 - 1 = 3^2 - 1 = 8$ gluons, represented by 8 generators derived from Gell-Mann matrices

λ^a [52]:

$$\lambda^1 = \begin{pmatrix} 0 & 1 & 0 \\ 1 & 0 & 0 \\ 0 & 0 & 0 \end{pmatrix}, \quad \lambda^2 = \begin{pmatrix} 0 & -\mathrm{i} & 0 \\ \mathrm{i} & 0 & 0 \\ 0 & 0 & 0 \end{pmatrix}, \quad \lambda^3 = \begin{pmatrix} 1 & 0 & 0 \\ 0 & -1 & 0 \\ 0 & 0 & 0 \end{pmatrix},$$
$$\lambda^4 = \begin{pmatrix} 0 & 0 & 1 \\ 0 & 0 & 0 \\ 1 & 0 & 0 \end{pmatrix}, \quad \lambda^5 = \begin{pmatrix} 0 & 0 & -\mathrm{i} \\ 0 & 0 & 0 \\ \mathrm{i} & 0 & 0 \end{pmatrix}, \quad \lambda^6 = \begin{pmatrix} 0 & 0 & 0 \\ 0 & 0 & 1 \\ 0 & 1 & 0 \end{pmatrix}, \tag{1.19}$$
$$\lambda^7 = \begin{pmatrix} 0 & 0 & 0 \\ 0 & 0 & -\mathrm{i} \\ 0 & \mathrm{i} & 0 \end{pmatrix}, \quad \lambda^8 = \frac{1}{\sqrt{3}} \begin{pmatrix} 1 & 0 & 0 \\ 0 & 1 & 0 \\ 0 & 0 & -2 \end{pmatrix}.$$

Assuming that the quark field q is given in both the Dirac space and the colour space with three colour components

$$q = \begin{pmatrix} q^R \\ q^R \\ q^R \end{pmatrix}, \tag{1.20}$$

the QCD Lagrangian describing the dynamics of quarks and gluons is [52]

$$\mathscr{L} = \sum_{q,\ C=1-8} \overline{q}_a \left(i\gamma^\mu \partial_\mu \delta_{ab} - g_s \gamma^\mu t^C_{ab} G^C_\mu - m_q \delta_{ab} \right) \psi_{q,b} - \frac{1}{4} G^A_{\mu\nu} G^{A\mu\nu}, \tag{1.21}$$

where q_a are the quark field spinors for quark $q = u,d,s,c,b,t$ with the mass m_q and the colour index $a = R,G,B$ and C running from 1 to 8 stands for the number of gluons. G^C_μ describes the gluon field, and $t^C = \lambda^C/2$ correspond to Gell-Mann matrices. The quantity g_s is the QCD coupling constant and $G^A_{\mu\nu}$ is a field-strength tensor given by [52]

$$G^A_{\mu\nu} = \partial_\mu G^A_\nu - \partial_\nu G^A_\mu - g_s f_{ABC} G^B_\mu G^C_\nu, \tag{1.22}$$

where f_{ABC} are structure constants of the SU(3) group. Comparing (1.4) and (1.22), one can see gluons can interact in the Lagrangian with other gluons, in difference to photons in QED.

Strong coupling constant In analogy with QED, the strong coupling constant depends on the energy scale or the distance. However, the nature of processes is very different because gluon can decay not only into quark-antiquark pair but also into a new gluon pair (the consequence of the possibility of gluon self-interaction). Therefore the quark surrounded by the gluons is anti-screened by them. The anti-screening is also visible in the strong coupling equation:

$$\alpha_S(Q^2) = \frac{\alpha_S(\mu)}{1 - \frac{(33-2N_f)\alpha_S(\mu)}{12\pi}\ln\left(\frac{Q^2}{\mu^2}\right)}, \tag{1.23}$$

where the second term in the denominator has the opposite sign for the number of flavours $N_f = 6$. This expression can also be rewritten using the value of $Q^2 = \Lambda^2_{\mathrm{QCD}}$, for which the denominator is zero in (1.23). Then, the strong running coupling is

$$\alpha_s\left(Q^2\right) = \frac{g_s^2\left(Q^2\right)}{4\pi} \approx \frac{12\pi}{\left(33 - 12N_f\right)\ln\left(Q^2/\Lambda_{QCD}\right)} \tag{1.24}$$

and its dependence on the energy scale and distance can be seen in Figure 1.4.

1.2.1.4 Gravitational Interaction

The effects of the gravitational interaction demonstrate themselves predominantly in the macroscopic world and especially at large spatial scales, where it was observed that gravitating objects curve the spacetime around themselves. This curvature can manifest itself by exerting a force on nearby objects, or in the language of the general theory of relativity, the object follows the geodesic curves. Gravity binds objects to the surface of the Earth and holds together star clusters, galaxies and clusters of galaxies. Its coupling

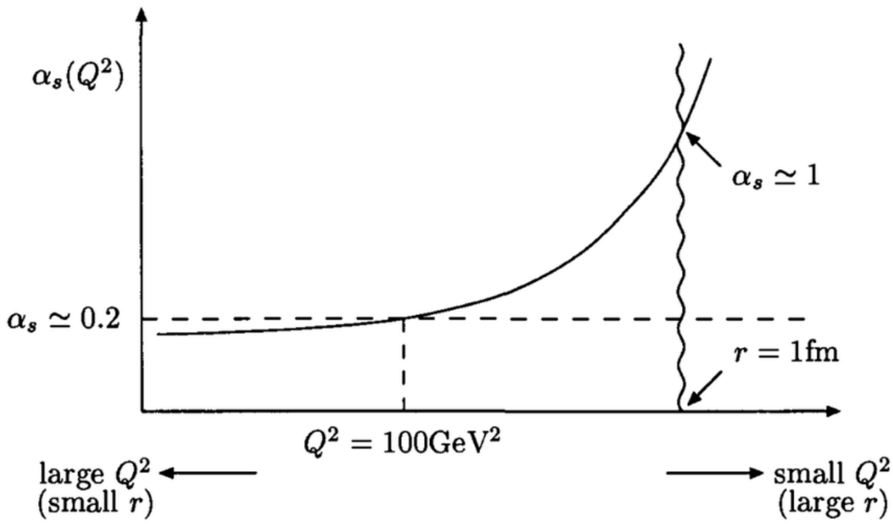

FIGURE 1.4. The running of the QCD gauge coupling in the SM α in dependence on the energy scale Q^2 and distance r [52].

strength is defined by the Newtonian constant [46]

$$G = 6.673 \cdot 10^{-11}\,\mathrm{m}^3\mathrm{kg}^{-1}\mathrm{s}^{-2}, \tag{1.25}$$

which is a constant used in the Einstein field equations of the general theory of relativity:

$$R_{\mu\nu} - \frac{1}{2} R g_{\mu\nu} + \Lambda g_{\mu\nu} = \frac{8\pi G}{c^4} T_{\mu\nu}, \tag{1.26}$$

where $R_{\mu\nu}$ is the Ricci curvature tensor, R is the scalar curvature (the Ricci scalar), $g_{\mu\nu}$ is the metric tensor, Λ is the cosmological constant (now understood to be the value of the energy density of the vacuum of space) and $T_{\mu\nu}$ is the stress-energy tensor generalising the stress tensor of Newtonian physics [64].

In the Newtonian approach, the magnitude of the force between two point particles with mass M and distance r is given by $\frac{G_N M^2}{r^2}$. When calculating the electromagnetic force strength between charged particles, e^2/r^2, we can substitute GM^2 in the definition (1.1) for e^2/ε_0 and obtain a constant [46]

$$\frac{GM^2}{4\pi\hbar c} = 5.34 \cdot 10^{-40}. \tag{1.27}$$

This value demonstrates the relative strength of gravity to electromagnetism. Compared to the fine structure constant (1.1), the gravitational interaction is negligibly small at the high energy physics scale and is not included in the SM. On the other hand, gravitational interaction is crucial at large spatial scales, such as in orbital dynamics and cosmology, because it is a long-distance interaction. Moreover, a negative gravitational charge has not been observed yet. Therefore, the gravitational force is only attractive, and it is hypothetically mediated through the graviton in the corresponding quantum field theories [65]. In the four-dimensional models, it is a massless particle with a spin of 2. As noted in the footnote of Table 1.2, the gravitational waves have been recently observed, but the graviton particle has not been observed yet.

1.2.2 Leptons

Leptons are elementary particles with half-integer spin and obey Fermi-Dirac statistics. All leptons interact via electroweak interaction, but only charged leptons can interact

Q/e	$L_e = -1$	$L_\mu = -1$	$L_\tau = -1$
0 +1	$\begin{pmatrix} \overline{\nu}_e \\ e^+ \end{pmatrix}$	$\begin{pmatrix} \overline{\nu}_\mu \\ \mu^+ \end{pmatrix}$	$\begin{pmatrix} \overline{\nu}_\tau \\ \tau^+ \end{pmatrix}$

Q/e	$L_e = +1$	$L_\mu = +1$	$L_\tau = +1$
0 −1	$\begin{pmatrix} \nu_e \\ e^- \end{pmatrix}$	$\begin{pmatrix} \nu_\mu \\ \mu^- \end{pmatrix}$	$\begin{pmatrix} \nu_\tau \\ \tau^- \end{pmatrix}$

TABLE 1.3. Charge Q/e and lepton number L of leptons.

electromagnetically. Leptons do not have a colour charge, so they cannot interact via a strong force. Leptons have baryon number $B = 0$ and they obey the conservation of lepton number L (listed in Table 1.3).

In the current status of knowledge, six leptons are known: charged stable electron e, unstable muon μ and tau τ with mean lifetimes $(2.1969811 \pm 0.0000022) \cdot 10^{-6}$ s for muon and $(290.3 \pm 0.5) \cdot 10^{-15}$ s for tau, respectively [46]. Each charged lepton has a corresponding flavour neutrino ν with zero electromagnetic charges. Neutrinos are produced in weak decay and are detected in the charged-current weak interaction, where they are associated with a specific lepton flavour. It is assumed in the Standard Model that neutrinos are massless. However, the neutrino flavour oscillation has been observed, implying that neutrinos have nonzero mass and thus the SM is incomplete.

The neutrino oscillation was first predicted in 1957 by B. Pontecorvo. Nowadays, the neutrino oscillation is described by the Pontecorvo–Maki–Nakagawa–Sakata matrix (PMNS matrix), an analogue of the CKM matrix describing the mixing of quarks (described in section 1.2.1.2 and 1.4).

1.2.3 Quarks

In the Standard Model, quarks are expected to be point-like particles and interact via the electroweak and strong interaction. There are six types of quarks: up u, down d, strange s, charm c, top t and bottom b. Quarks have various intrinsic properties, including mass, colour charge, and spin. The spin of quarks is 1/2 and they are the only known particles having noninteger electric charge: $Q = +2/3$ for u, c, t quarks and $Q = -1/3$ for d, s, b

	d	u	s	c	b	t
Q/e	$-1/3$	$2/3$	$-1/3$	$2/3$	$-1/3$	$2/3$
I	$1/2$	$1/2$	0	0	0	0
I_z	$-1/2$	$1/2$	0	0	0	0
S	0	0	-1	0	0	0
C	0	0	0	1	0	0
B	0	0	0	0	-1	0
T	0	0	0	0	0	1

TABLE 1.4. Charge Q/e, isospin I and its z-component I_z and quark flavour numbers S (strangeness), C (charm), B (bottomness), T (topness) of up, down, strange, charm, bottom and top quarks.

quarks. The charge can be obtained from the generalised Gell-Mann-Nishijima formula

$$Q = I_z + \frac{\mathscr{B} + S + C + B + T}{2}, \tag{1.28}$$

where $\mathscr{B} = 1/3$ is the baryon number for quarks and $\mathscr{B} = -1/3$ is the baryon number for antiquarks. Their z-component of isospin and quark flavours S, C, B, and T are summarized in Table 1.4. Quarks have not been observed separately but are always in a bound state of quark-antiquark or a bound state of three, except for the top quark. Also, exotic composite structures like tetraquarks and pentaquarks have been observed recently.

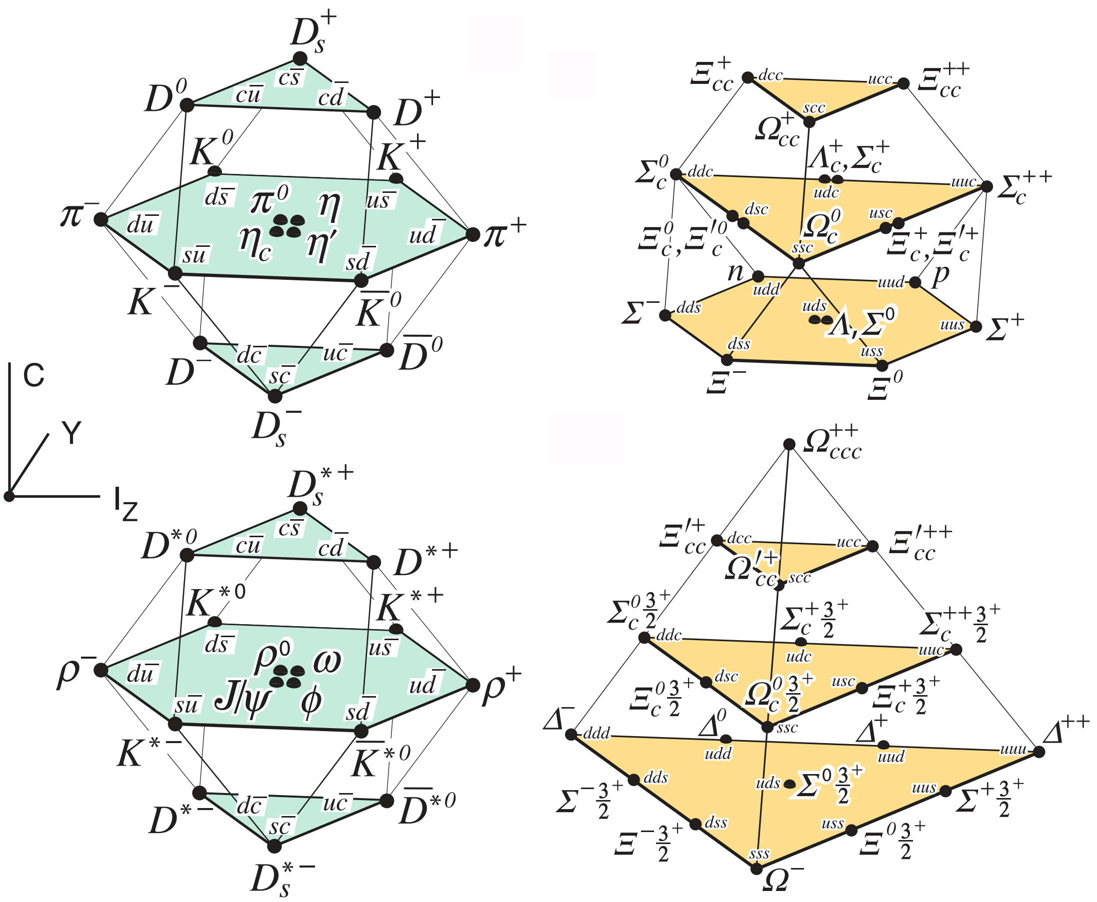

FIGURE 1.5. $SU(4)$ multiplets of baryons made of u, d, s, and c quarks - the 16-plets for the pseudoscalar meson (top left) and vector mesons(bottom left). The top right figure is for spin 1/2 baryon 20-plet with an $SU(3)$ baryon octet, and the bottom right is a plot for spin 3/2 baryon 20-plet with an $SU(3)$ baryon decuplet [46].

1.2.3.1 Mesons

Mesons have baryon number $\mathscr{B} = 0$ and integer spin; therefore they are bosons. In the quark model, they are $q\overline{q}$ bound states of quark q and antiquark $\overline{q}$ (the flavours of q and $\overline{q}$ may be different). By adding the spin of the mesons' constituent quarks, mesons can be pseudoscalar bosons (the final spin is $s = 0$) or vector bosons ($s = 1$).

Taking only three constituent quarks u, d, s, the combinations of the $q\overline{q}$ pair can be represented by an octet and a singlet:

$$3 \otimes \overline{3} = 8 \oplus 1. \tag{1.29}$$

If the fourth quark is included, the 16 mesons can be obtained, grouped into 15-plet and singlet

$$4 \otimes \overline{4} = 15 \oplus 1. \tag{1.30}$$

All mesons from the 15-plet and singlet made of the four lightest quarks can be found in Figure 1.5. The octet and the singlet of the $SU(3)$ representation in (1.29) build the middle plane in 1.5 (left).

1.2.3.2 Baryons

Baryons are composite particles made of three quarks and have baryon number $\mathscr{B} = 1$. They are fermions (the total spin of baryons is an integer multiple of 1/2).

The most ordinary baryons are made of the three lightest quarks (u, d, s), forming a group

$$3 \otimes 3 \otimes 3 = 10 \oplus 8 \oplus 8 \oplus 1. \tag{1.31}$$

Figure 1.5 (right) shows baryons made of four quarks (including charm quarks to the three lightest ones). This quark organisation can be represented by a group

$$4 \otimes 4 \otimes 4 = 20 \oplus 20 \oplus 20 \oplus 1. \tag{1.32}$$

1.2.3.3 Tetraquarks and pentaquarks

Tetraquarks and pentaquarks are new composite structures of quarks and antiquarks, which have been recently observed and cannot be classified either as mesons or baryons. In 2007, the observation of the $Z(4430)$ state, a $c\overline{c}d\overline{u}$ tetraquark candidate, was announced by the Belle experiment in Japan [66]. The observation of $Z(4430)$ was confirmed in 2014 by the LHCb experiment [67].

After this observation, it is not surprising that also pentaquark state has been observed,

namely the $J/\psi p$ resonance in $\Lambda_b^0 \to J/\psi K^- p$ decays [68]. The quark content of this pentaquark is expected to be $c\bar{c}uud$.
These new composite objects are not entirely unexpected since they have been discussed in the original Gell-Mann paper [69].

1.3 Symmetries

In classical physics, the system motion equations are determined by the Lagrangian of a given system. This Lagrangian is usually a function of several variables (like space position, angles, vector of momentum or angular momentum). Applying a transformation (e.g., Lorentz or Galilean transformation), Euler-Lagrange equations for a given Lagrangian can be the same as they have been before the transformation. In other words, the system is invariant under the transformation, and for every symmetry of a Lagrangian, there exists a conserved quantity called the constant of motion.

The transformations can be separated into continuous symmetries described by Lie groups and discrete symmetries described by finite groups.

1.3.1 Continuous Symmetries

The invariance of the system under continuous symmetry is related to the conservation laws and can be described by the Noether's theorem. Examples of continuous symmetries in classical physics are:

- Time translation. A physical system has the same features over a given time period, thus the system's energy is conserved.
- Spatial translation. The system does not change by changing the observer's location, thus the system's momentum is conserved.
- Spatial rotation. The system does not change if an observer moves on the circle or the system rotates. The conserved quantity is the angular momentum in this case.

The Standard Model (described by relativistic physics) uses gauge symmetries similar to continuous symmetries of classical physics. A good example of gauge symmetries is $U(1)$ group of quantum electrodynamics

$U(1)$ **Symmetry of QED:** The Lagrangian of QED is (1.9) and can be written as

$$\mathscr{L}_{\text{QED}} = -\frac{1}{4}F^{\mu\nu}F_{\mu\nu} + \overline{\psi}\left(\mathrm{i}\gamma^{\mu}\partial\mu - m\right)\psi + e\overline{\psi}\gamma^{\mu}A_{\mu}\psi. \tag{1.33}$$

The gauge transformation, under which the Lagrangian (1.33) is invariant, is

$$\psi \to \mathrm{e}^{-\mathrm{i}\alpha}\psi \qquad\qquad A_{\mu} \to A_{\mu} + \frac{1}{e}\partial_{\mu}\alpha, \tag{1.34}$$

where α is an infinitesimal parameter that can depend on position and time. The transformation of particle field ψ is described by the unitary matrix $U = \mathrm{e}^{-\mathrm{i}\alpha}$.

1.3.2 Discrete Symmetries

Besides the continuous symmetry, the Standard Model Lagrangian can be invariant under the discrete transformation. Examples of discrete symmetries are squared angular momentum $\hat{L}^2$ and the third component of angular momentum $\hat{L}_z$.

Unitary or anti-unitary operators represent a particular group of symmetries. The eigenvalues of these operators are 1 or -1. This group contains operators crucial for the following chapters of this work, such as the parity operator $\hat{P}$, charge conjugation operator $\hat{C}$ and time reversal operator $\hat{T}$.

1.3.2.1 The Parity

The parity or space inversion operation converts a right-handed coordinate system to a left-handed $(x, y, z \to -x, -y, -z)$

$$\hat{P}\psi(\mathbf{r}) = \psi(-\mathbf{r}). \tag{1.35}$$

Moreover, it also inverts the momentum direction but does not affect time and angular momentum. In two dimensions, the inversion of axes is equivalent to the 180° rotation. By applying twice the parity operator, the original state is obtained, which implies that the eigenvalues of the parity are ±1.

Parity conservation implies that any physical process will happen identically when viewed in a mirror image. The parity had seemed to be conserved in every physical process until 1956, when S. Wu observed a parity violation in ^{60}Co decay [70]. The radioactive cobalt nuclei were placed in the magnetic field, and their beta decay products ^{60}Ni, an electron and two photons from the deexcitation of nickel ^{60}Ni were detected. The parity would be conserved if the electron and photon were found to be emitted isotropically. However, Wu observed electrons' direction is opposite to the direction of photons. The observation showed that most electrons prefer a specific direction of decay, opposite to the nuclear spin, so the parity has been violated.

1.3.2.2 The Charge Conjugation

The charge conjugation operator $\hat{C}$ changes the sign of all quantum charges and does not affect the particle's mass, linear momentum and spin. The effect of the $\hat{C}$ implies that the operator $\hat{C}$ transforms the particle into its antiparticle,

$$\hat{C}\psi(\mathbf{r}) = \bar{\psi}(\mathbf{r}). \tag{1.36}$$

This operator is conserved in electromagnetic and strong interactions similar to parity and violated in weak interactions. The charge conjugation is violated in transforming the left-handed neutrino into the left-handed anti-neutrino, which has not been observed[7].

1.3.2.3 The Time Reversal

The time reversal operator $\hat{T}$ changes the time direction,

$$\hat{T}\psi(r,t) = \psi(r,-t). \tag{1.37}$$

The time-reversal symmetry is broken. The first direct observation of the T-symmetry violation was made at the CERN LEAR ring in 1998 [71].

1.3.2.4 CPT Invariance

The CPT theorem states that all interactions are invariant under the simultaneous application of the parity, charge conjugation and time reversal operators. The time reversal and combination of parity and charge conjugation are violated (CP violation), unlike the combination of all three symmetries. The CPT invariance in the observations of the high energy physics experiments is conserved [72–74].

1.3.3 CP Violation

The combination of parity and charge conjugation is violated. If CP were an exact symmetry, the laws of Nature would be the same for matter and antimatter. We observe that most phenomena are C- and P-symmetric, and therefore, also CP-symmetric. In particular, these symmetries were expected but not found to be respected by the gravitational, electromagnetic, strong, and weak interactions. The situation changed in 1964, when Christenson, Cronin, Fitch and Turlay were studying eigenstates of two

[7] As discussed in the previous section, only left-handed neutrino and right-handed anti-neutrino are possible in the Standard Model using the Dirac description of neutrinos.

neutral K mesons in the kaon decays, labelled short-lived and long-lived kaons, K_S^0 and K_L^0. If CP is to be conserved, the final states can only be $K_S^0 \to 2\pi$ and $K_L^0 \to 3\pi$ and mass eigenstates are also CP eigenstates. As seen, K_L^0 also sometimes decays to 2 pions, which implies the CP eigenstates are different from the mass eigenstates, and the K^0 and $\overline{K}^0$ can oscillate between each other. Thus the CP symmetry is violated in specific rare processes.

There are three ways in which the CP symmetry can be violated in the Standard Model - CP violation in decay, in mixing and in the interference of mixing and decay.

The CP violation in decay (also known as direct CP violation) is the only possible source of CP asymmetry in charged meson decays. The decay amplitude Γ of the particle M into the final state f is different from the decay amplitude of its antiparticle into its final anti-state,

$$\Gamma(M \to f) \neq \Gamma\left(\overline{M} \to \overline{f}\right). \tag{1.38}$$

The CP violation in decay is usually measured in the difference of decay width of the two charge-conjugated states

$$A_{CP} = \frac{\Gamma(M \to f) - \Gamma(\overline{M} \to \overline{f})}{\Gamma(M \to f) + \Gamma(\overline{M} \to \overline{f})} \tag{1.39}$$

The CP violation in mixing (or indirect CP violation) arises when the probability of oscillation from meson to antimeson is different from the probability of oscillation from antimeson to meson,

$$\mathrm{Prob}\left(P^0 \to \bar{P}^0\right) \neq \mathrm{Prob}\left(\bar{P}^0 \to P^0\right). \tag{1.40}$$

Thus the mass eigenstates are not CP eigenstates.

The CP violation in interference of mixing and decay occurs in case both meson and antimeson decay into the same final state, $M^0 \to f$ and $M^0 \to \bar{M}^0 \to f$. This case occurs, for example, in the decay of $B_s^0 \to J/\psi\phi$.

The key quantity to study CP violation containing meson antimeson mixing is defined by

$$\lambda_f = \frac{q\overline{A}_f}{pA_f} = |\lambda_f|\,\mathrm{e}^{\mathrm{i}\phi_f}, \tag{1.41}$$

where $\overline{A}_f$ and A_f are decay amplitudes, the q/p is the relative phase from meson-antimeson mixing. If the decay amplitudes are the same, $\overline{A}_f = A_f$, the CP violation appears if

$$\left|\frac{q}{p}\right| \neq 1. \tag{1.42}$$

This type of CP violation is also called indirect CP violation.

1.4 CKM Quark-Mixing Matrix

The CP violation also appears in the SM Lagrangian, directly in the CKM matrix (Cabibbo-Kobayashi-Maskawa matrix), which is responsible for the quark flavour mixing. The CKM matrix is part of the charged-current weak interaction as is explicitly stated in (1.12). The matrix is a product of the matrices responsible for the transformation of the mass eigenstate of quark into an interaction eigenstate:

$$d'_L = V^\dagger_{dL} d_L \qquad\qquad \overline{u}'_L = V_{uL}\overline{u}_L, \tag{1.43}$$

where V_{uL} and V_{dL} are trasformation matrices, $d' = (d', s', b')$ and $u' = (u', c', t')$ are interaction eigenstates, $d = (d, s, b)$ and $u = (u, c, t)$ are mass eigenstates of quarks. Using (1.43), the CKM matrix is $V_{\text{CKM}} = V^\dagger_{uL} V_{dL}$ and is denoted as

$$V_{CKM} = \begin{pmatrix} V_{ud} & V_{us} & V_{ub} \\ V_{cd} & V_{cs} & V_{cb} \\ V_{td} & V_{ts} & V_{tb} \end{pmatrix}. \tag{1.44}$$

1.4.1 PDG and Wolfenstein Parametrisation

The matrix (1.44) is a complex 3×3 unitary matrix. Therefore, it has 18 parameters (9 complex elements), of which only four parameters are independent - 3 Euler mixing angles and one CP-violating phase [46]. Defining $s_{ij} = \sin\theta_{ij}$, $c_{ij} = \cos\theta_{ij}$ and δ as the phase causing CP violation, the CKM matrix (1.44) can be written as a product of three matrices

$$\begin{aligned} V_{CKM} &= \begin{pmatrix} 1 & 0 & 0 \\ 0 & c_{23} & s_{23} \\ 0 & -s_{23} & c_{23} \end{pmatrix} \begin{pmatrix} c_{13} & 0 & s_{13}e^{-\imath\delta} \\ 0 & 1 & 0 \\ -s_{13}e^{\imath\delta} & 0 & c_{13} \end{pmatrix} \begin{pmatrix} c_{12} & s_{12} & 0 \\ -s_{12} & c_{12} & 0 \\ 0 & 0 & 1 \end{pmatrix} = \\ &= \begin{pmatrix} c_{12}c_{13} & s_{12}c_{13} & s_{13}e^{-\imath\delta} \\ -s_{12}c_{23} - c_{12}s_{23}s_{13}e^{\imath\delta} & c_{12}c_{23} - s_{12}s_{23}s_{13}e^{\imath\delta} & s_{23}c_{13} \\ s_{12}s_{23} - c_{12}c_{23}s_{13}e^{\imath\delta} & -c_{12}s_{23} - s_{12}c_{23}s_{13}e^{\imath\delta} & c_{23}c_{13} \end{pmatrix}, \end{aligned} \tag{1.45}$$

each describing the two-dimensional rotation. The angle θ_{12} is identified as the Cabibbo angle.

Based on the fact that $s_{13} \ll s_{23} \ll s_{12} \ll 1$, the CKM matrix in Wolfenstein parameterization [46] takes form:

$$V_{CKM} = \begin{pmatrix} 1-\frac{1}{2}\lambda^2-\frac{1}{8}\lambda^4 & \lambda & A\lambda^3(\rho-\imath\eta) \\ -\lambda & 1-\frac{1}{2}\lambda^2-\frac{1}{8}\lambda^4\left(1+4A^2\right) & A\lambda^2 \\ A\lambda^3(1-\rho-\imath\eta) & -A\lambda^2+\frac{1}{2}A\lambda^4(1-2(\rho+\imath\eta)) & 1-\frac{1}{2}A^4\lambda^4 \end{pmatrix} + \mathcal{O}(\lambda^5), \tag{1.46}$$

with the parametrization

$$\begin{aligned} s_{12} &= \lambda, \\ s_{23} &= A\lambda^2, \\ s_{13}e^{\imath\delta} &= A\lambda^3(\rho+\imath\eta). \end{aligned} \tag{1.47}$$

The values from the experimental data [46] are:

$$\begin{aligned} \lambda =& 0.22650 \pm 0.00048, \\ A =& 0.790^{+0.017}_{-0.012}, \\ \overline{\rho} =& \rho\left(1-\frac{1}{2}\lambda\right) = 0.141^{+0.016}_{-0.017}, \\ \overline{\eta} =& \eta\left(1-\frac{1}{2}\lambda\right) = 0.357 \pm 0.011. \end{aligned} \tag{1.48}$$

From these results and parametrisation (1.46) of the CKM matrix (1.44), it is demonstrable that the diagonal elements are ~ 1, whereas the non-diagonal elements (which are responsible for the the quark generation change) are smaller than 1, specifically $|V_{us}|, |V_{cd}| \sim \lambda$, $|V_{cb}|, |V_{ts}| \sim \lambda^2$ and $|V_{ub}|, |V_{td}| \sim \lambda^3$. The imaginary part is larger for the $|V_{ub}| \sim \lambda^3$ and $|V_{td}|, |V_{ts}| \sim \lambda^4$.

1.4.2 Unitary Triangles

The unitarity condition of the CKM matrix can be manifestly demonstrated by noting that $V_{CKM}V^{\dagger}_{CKM} = \mathbb{1}$ is equivalent to the orthonormality of columns or rows in V_{CKM} expressed as

$$\sum_{\alpha=u,c,t} V_{\alpha i}V^*_{\alpha j} = \delta_{ij}, \quad \sum_{i=d,s,b} V_{\alpha i}V^*_{\beta i} = \delta_{\alpha\beta}. \tag{1.49}$$

One of these unitarity triangles is

$$V_{ud}V^*_{ub} + V_{cd}V^*_{cb} + V_{td}V^*_{tb} = 0, \tag{1.50}$$

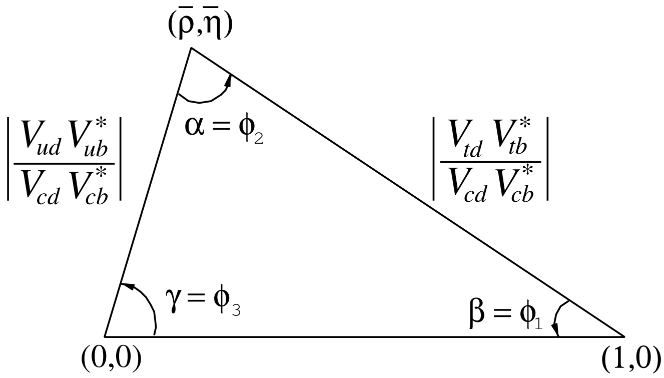

FIGURE 1.6. The unitarity triangle corresponding to the equation (1.50) [75].

interpreted as a triangle in the complex plane (see Figure 1.6).

This equation is often called B_d^0 triangle, because the angles α, β, γ from Fig. 1.6 are well measured in the B_d^0 decays. The B_s^0 triangle gives the relation

$$V_{us}V_{ub}^* + V_{cs}V_{cb}^* + V_{ts}V_{tb}^* = 0, \tag{1.51}$$

from which the small angle

$$\beta_s = \arg\left(-\frac{V_{ts}V_{tb}^*}{V_{cs}V_{cb}^*}\right) \tag{1.52}$$

can be obtained. This angle is sensitive to CP violation via the element V_{ts} (at $\mathcal{O}\left(\lambda^4\right)$), details are provided in chapter 2.

1.5 Physics Beyond the Standard Model

The Standard Model provides a perfect description of the particles and interactions. However, this theory is still incomplete (despite the Higgs particle discovery) and has some questions that have not been answered yet. The SM cannot explain:

- gravity. SM can describe three of four fundamental interactions. However, it does not include gravity (with the hypothetical particle graviton).
- Neutrino masses. The SM assumes that neutrinos are massless particles. However, it has been confirmed that they have tiny but non-zero mass.
- Matter-antimatter asymmetry. Our world is mainly composed of matter. On the other hand, the SM expects that the initial universe conditions did not involve disproportionate matter relative to antimatter.

- Lepton non-universality. Recently, the anomalous magnetic dipole moment of the muon ($(g-2)_\mu$) has been measured to disagree with the Standard Model expectation at the level of 4.2 significance level. Additionally, CDF Collaboration showed that the mass of $W^\pm$ boson is away from the SM by 7σ significance.
- Values of 19 parameters. The Standard Model has parameters whose values can be extracted only from experiments. Some theories try at least to describe the relationship between the parameters, but the SM does not include them.
- Hierarchy problem. The mass of the Higgs boson was expected to be much higher than the observed one. The mass of the Higgs gets some substantial quantum corrections due to the presence of virtual particles, and these corrections are much larger than the actual mass of the Higgs boson.
- Absence of the strong CP violation in the SM. The SM allows the appearance of the strong CP violation. However, it has never been observed, implying that the parameter describing it is very close to zero.

To describe at least some of the Standard Model inconsistencies, several theories extending or supplementing the SM have been developed. Some promising beyond the SM theories are described below: supersymmetry, grand unified theory and theory of leptoquarks. The other approaches that are not mentioned can also answer all or some of the open questions about the SM: string theory, theory of magnetic monopoles, axion theory or theory of quark and lepton compositeness. Some of the theories are also connected. For example, supersymmetry can give hints for the grand unified theory, and grand unified theories can predict the existence of a magnetic monopole.

1.5.1 Supersymmetry

Supersymmetry (SUSY) is currently the most favoured theory beyond the SM. It predicts that every particle in the SM has its superpartner. The Supersymmetry generator Q transforms the bosons into fermions and vice versa:

$$Q\,|\text{fermion}\rangle = |\text{boson}\rangle\,, \qquad Q\,|\text{boson}\rangle = |\text{fermion}\rangle\,. \tag{1.53}$$

The minimal SUSY extension to the SM is called the Minimal Supersymmetric Standard Model (MSSM). The MSSM is the SM Higgs field extension. It introduces two Higgs doublets leading to 8 degrees of freedom after the spontaneous symmetry breaking (SM has 4 degrees of freedom). Three of them are responsible for the $W^\pm$ and Z^0 masses, two

of the remaining Higgs bosons are [CP](#)-even (h and H^0), three are [CP](#)-odd ($H^{\pm}$ and A). The concept of 2 Higgs doublets is essential. Without additional Higgs bosons, the theory cannot generate masses for both up-like and down-like fermions.
The electroweak gauge bosons $W^{\pm}$ and Z^0 supersymmetric partners are binos and winos that can mix with the Higgs supersymmetric partners Higgsinos. The mass eigenstates of the binos, winos and Higgsinos are neutralinos ($\tilde{\chi}_1^0$, $\tilde{\chi}_2^0$, $\tilde{\chi}_3^0$, $\tilde{\chi}_4^0$) and charginos ($\tilde{\chi}_1^{\pm}$, $\tilde{\chi}_2^{\pm}$). The gluons also have their superpartners - gluinos. For the fermions in the SM, the MSSM contains their corresponding scalar partners: squarks and sleptons. The whole MSSM particle zoo is shown in Figure 1.8.
The Lagrangian of the MSSM no longer conserves the baryon and lepton number. On the other hand, the MSSM Lagrangian is symmetric in the R-parity that is defined as

$$R = (-1)^{2s+3B+L}\,, \tag{1.54}$$

where s is the particle spin, B is baryon number, and L is lepton number. The R-parity is always positive for the SM particles and negative for their superpartners.
As R-parity is not expected to be violated, the lightest supersymmetric particle cannot decay. If this particle exists, it is anticipated that it explains the universe's missing mass and is the candidate to be a dark matter particle. It is assumed that this particle would interact through weak and gravitational interaction. Due to this, the particle is often

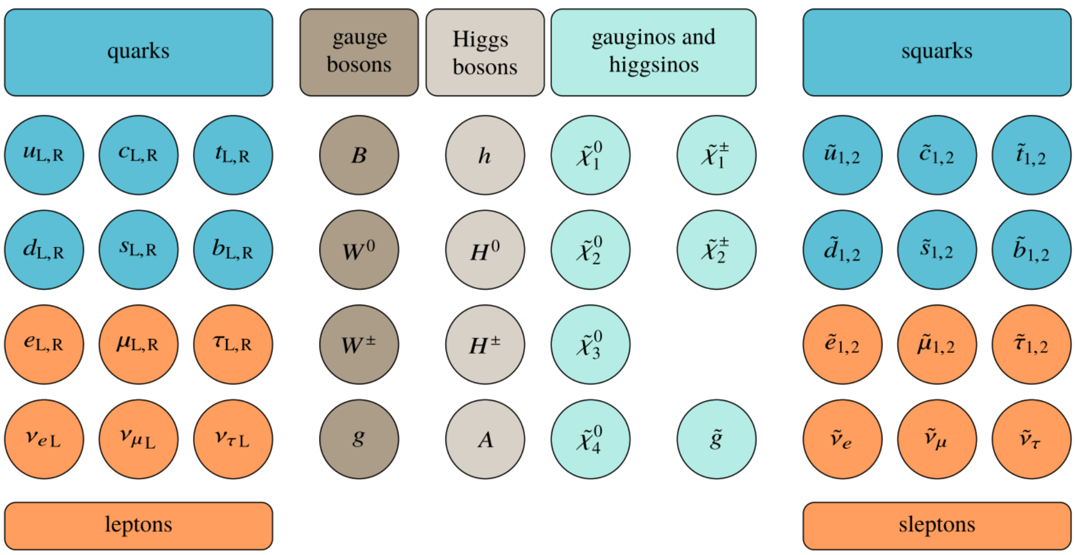

FIGURE 1.7. Particles in the Minimal Supersymmetric Standard Model. The left part is the same as the SM with the Higgs particle extensions, and the right part shows mass eigenstates of SUSY particles [76].

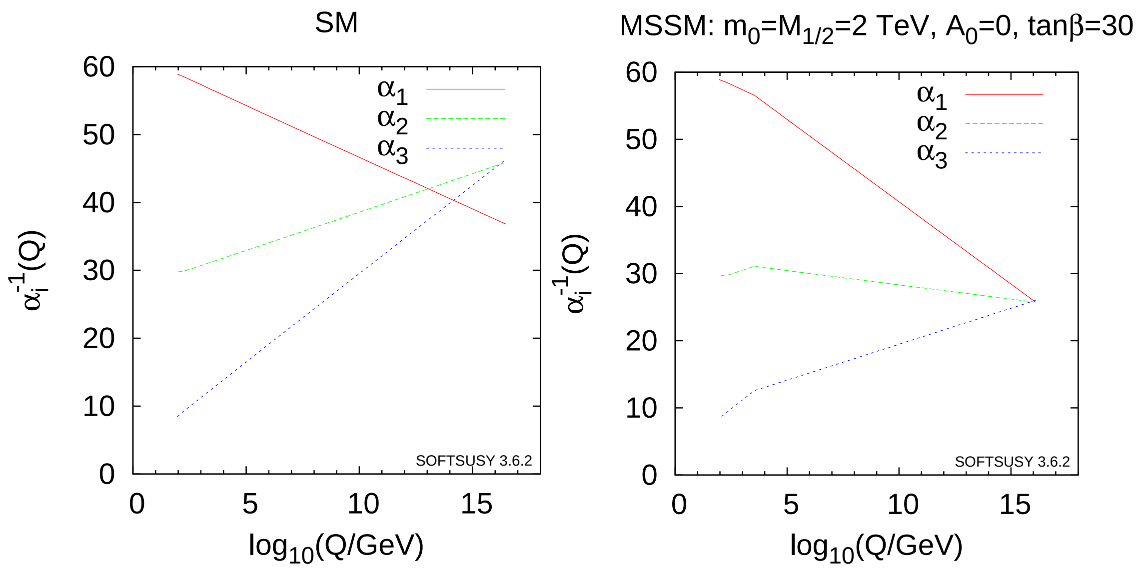

FIGURE 1.8. The running coupling of Grand Unified Theories. The left figure shows the near unification of the SM interaction running coupling, and the right figure shows the precise unification if the MSSM theory is used [46].

called a weakly interacting massive particle (WIMP).

1.5.2 Grand Unified Theories

The SM has 19 free parameters (9 charged fermion masses, three mixing angles and one CP phase in the CKM matrix, Higgs mass, quartic coupling, strong CP phase and three gauge couplings) that are extracted from the experiments, but not predicted by the SM. The primary motivation of Grand Unified Theories (GUT) is to find one large gauge symmetry that has several force carriers but only one gauge coupling. The SM interaction unification is possible due to the energy scale dependence of force coupling parameters in quantum field theory. This predicts that the three forces couplings of the SM can nearly meet at some point if the hypercharge is normalized. Due to this, the $SU(5)$ and $SO(10)$ symmetry theories are favoured to be the GUT. If the MSSM is used for the GUT, the three interaction coupling meet precisely (not only closely as for the SM), and the energy scale of this unification is expected to be at [46]

$$\Lambda_{\mathrm{GUT}} \approx 10^{16}\,\mathrm{GeV}. \tag{1.55}$$

1.5.3 Leptoquarks

The leptoquarks are hypothetical particles having non-zero lepton and baryon numbers. Therefore, they can interact with quarks and leptons. The leptoquarks are expected to be bosons with spin 0 (scalar) or 1 (vector). One of the first theories predicting the leptoquarks is the Pati-Salam model [77]. There also exist the current Grand Unified Theories that are most favoured (primarily based on $SU(5)$ and $SO(10)$ symmetries). Leptoquarks can also be connected to Supersymmetry model with R-parity violation. In all theories, the mass of the leptoquarks is expected to be at the TeV scale or even higher.

CHAPTER 2

The Physics of Neutral Open-Beauty Mesons

The mesons are bound states of quark and antiquark. The heaviest mesons are those containing at least one b quark. The state composed of the $b\bar{b}$ pair is called *bottomium*, the bound state of b quark and antiquark with zero bottomness are called B mesons.

During the last decades, it was shown that B mesons are perfect probes for the search of physics beyond the Standard Model due to their relatively large mass and long lifetimes.

2.1 Discovery of the b Quark

In 1975, two generations of quarks and two generations of leptons were known. It seemed that the particle world had been fully explained. However, the τ lepton was observed at SLAC in 1976 [30]. To include the new particle, physicists predicted the third family of quarks - and the hunt for new particles started again.

In 1976-1977, Leon Lederman and his colleagues modified an earlier dilepton experiment in the Fermilab Proton Center Laboratory. The two-arm spectrometer was modified by adding the beryllium as a hadron filter to the existing scintillator counters, drift chambers and Cherenkov counters. A newly observed particle was created in the collision of protons with energy 400 GeV with platinum or copper target:

$$p + \mathrm{Cu(Pt)} \rightarrow \mu^+\mu^- + \mathrm{anything}. \tag{2.1}$$

Name	Valence quark composition	Mass m [MeV]	Lifetime τ [ps]
B^+	$u\overline{b}$	5279.34 ± 0.12	1.638 ± 0.004
B_d^0	$d\overline{b}$	5279.66 ± 0.12	1.519 ± 0.004
B_s^0	$s\overline{b}$	5366.92 ± 0.10	1.520 ± 0.005
B_c^+	$c\overline{b}$	6274.47 ± 0.27	0.510 ± 0.009

TABLE 2.1. The lightest B mesons and their properties [46].

This particle with a composition of $b\overline{b}$ pair was named Upsilon (Υ).

2.2 B Mesons Properties

The lowest mass B mesons are pseudoscalar particles, which can be charged or neutral. The summary of pseudoscalar B mesons in the ground state is shown in Table 2.1. Surprisingly, the B meson lifetime is larger than the lifetime of charmed mesons, and their typical flight length before decaying is $c\tau \approx 0.5\,\text{mm}$.

The B_c^+ is the heaviest b-flavored mesons ground state and is also the most difficult

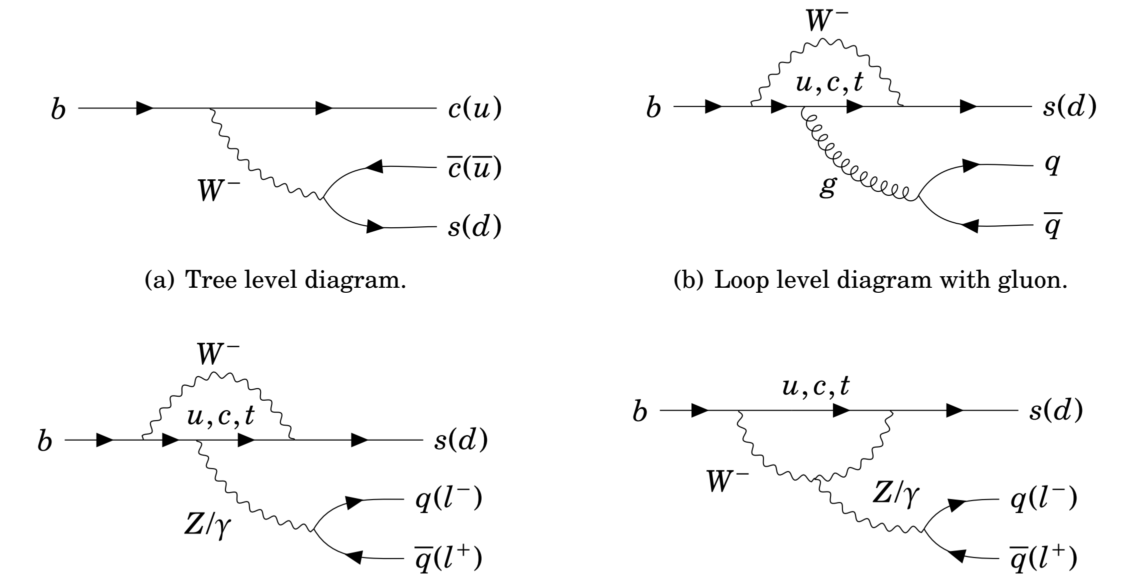

(a) Tree level diagram.

(b) Loop level diagram with gluon.

(c) Loop level diagram with photon or Z^0 boson.

(d) Loop level diagram with photon or Z^0 boson.

FIGURE 2.1. Tree level diagram (a) and loop (penguin) diagrams (b),(c),(d) of the b quark decays.

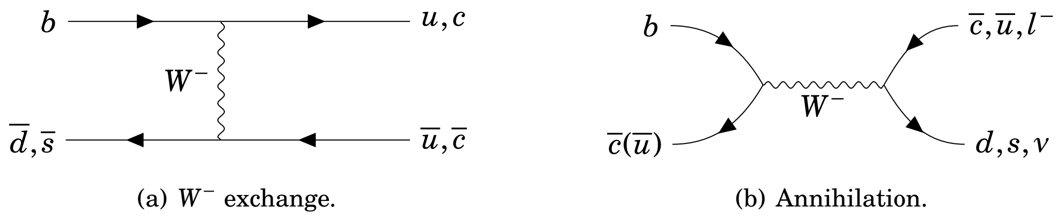

FIGURE 2.2. B meson decays via the W^- boson exchange (a) and via the annihilation (b).

to produce - it was discovered in 1998 [78], but its mass was first measured in 2006 at CDF [79].

Most of the B meson decays occur via the weak generation changing processes. As the CKM matrix is mostly diagonal, these decays are the golden channels for observing the physics beyond the SM, the flavour oscillations, large CP asymmetries or studying the loop and box diagrams. The B mesons decay can be described as a b quark decay (due to its mass compared to the other quark mass). The dominant decay mode is the *tree decay* via $b \to cW^{*\pm}$, where $W^{*\pm}$ is virtual. Also, $b \to uW^{*\pm}$ transition is allowed, but suppressed by the CKM matrix. The second b-quark decay mode is called *loop decay* (also denoted as a *penguin* decay), where the $b \to s$ and $b \to d$ transitions appear, also known as flavour-changing-neutral-current (FCNC) processes. Figure 2.1 shows the example of tree-level and loop-level b quark decays.

B meson decays are described through the b quark decay, i.e., the tree and loop diagrams. Additionally, B mesons can decay via the annihilation and the $W^\pm$ boson exchange (see Figure 2.2). They can also mix via the box diagram - detailed in the following section.

The decays through the loop diagram and annihilation are sensitive to physics beyond the Standard Model because undetected particles can be exchanged in these processes.

2.3 Oscillation of the Neutral B-Mesons

As discussed in section 1.3.3, the neutral mesons can oscillate between their particle and antiparticle states. The same applies to the neutral B mesons: B_d^0 and B_s^0 mesons. In the Standard Model, the mixing can be described by Feynman box diagrams (see Figure 2.3). An essential aspect of the B meson mixing is that both states decay into the same final state. If the B meson is created, only final states are detected, and additional analysis

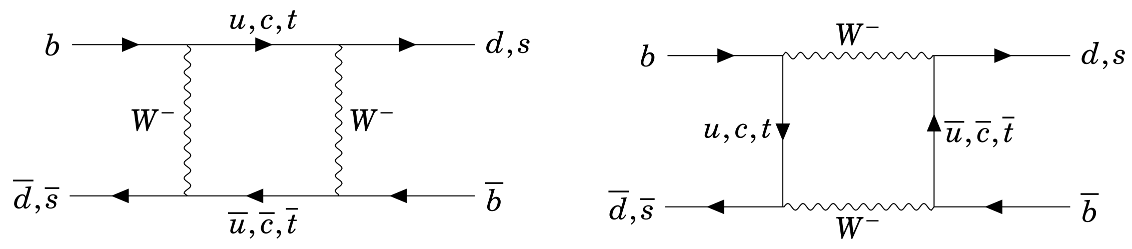

FIGURE 2.3. Neutral B meson mixing diagram.

(the flavour tagging) is needed.

The state vectors of flavour eigenstates directly at the time of creation ($t = 0$) are denoted as $|B^0\rangle$ and $|\overline{B}^0\rangle$. Charge-parity operator transforms flavour eigenstates as:

$$CP\,|B^0\rangle = \eta_{CP}\,|\overline{B}^0\rangle, \qquad |\overline{B}^0\rangle = \eta^*_{CP}\,|B^0\rangle, \tag{2.2}$$

where $\eta_{CP} = e^{\imath\xi_{CP}}$ is a complex phase factor fulfilling $|\eta_{CP}| = 1$. The flavour operator does not commute with the Hamiltonian used for the neutral B meson time evolution description. The CP operator commutes with the Hamiltonian if the CP symmetry is conserved. Then, the CP eigenstates can be considered as physical states:

$$|B_\pm\rangle = \frac{1}{\sqrt{2}}\left(e^{-\imath\xi_{CP}/2}\,|B^0\rangle \pm e^{\imath\xi_{CP}/2}\,|\overline{B}^0\rangle\right), \tag{2.3}$$

for which

$$CP\,|B_\pm\rangle = \pm\,|B_\pm\rangle\,. \tag{2.4}$$

The CP eigenstates are not CP-conjugate states - so they can have different masses and lifetimes. CP eigenstates are the physical states (eigenstates of the full Hamiltonian) if the CP symmetry holds. On the contrary, if the CP is violated, the mass eigenstates (of the full Hamiltonian) are used for theoretical description instead of the CP eigenstates. In the following text, the CP is assumed to be violated, and the description of mass eigenstates and flavour eigenstates is used.

2.3.1 Effective Hamiltonian

Due to the mixing, the neutral B meson at any time can be described as a linear combination of the flavour states:

$$|\psi\rangle = a(t)\,|B^0\rangle + b(t)\,|\overline{B}^0\rangle\,. \tag{2.5}$$

The terms $a(t)$ and $b(t)$ are complex function describing the time evolution and $|a(t)|^2 + |b(t)|^2 = 1$.
The time evolution of the neutral B meson mixing is given by the Schrödinger equation:

$$i\hbar \frac{\mathrm{d}}{\mathrm{d}t} |\psi\rangle = \boldsymbol{H} |\psi\rangle, \tag{2.6}$$

where $\boldsymbol{H}$ is the Hamiltonian of the system. The Hamiltonian can be split into a Hermitian and an anti-hermitian part:

$$\boldsymbol{H} = \boldsymbol{M} - \frac{\imath}{2}\boldsymbol{\Gamma}, \tag{2.7}$$

where both $\boldsymbol{M}$ and $\boldsymbol{\Gamma}$ are hermitian. $\boldsymbol{M}$ describes the mass terms, and $\boldsymbol{\Gamma}$ provides the exponential decay terms. If the two mesons are mixed, the Hamiltonian is 2×2 matrix:

$$\boldsymbol{H} = \begin{pmatrix} M_{11} - \frac{\imath}{2}\Gamma_{11} & M_{12} - \frac{\imath}{2}\Gamma_{12} \\ M_{21}^* - \frac{\imath}{2}\Gamma_{21}^* & M_{22} - \frac{\imath}{2}\Gamma_{22} \end{pmatrix}. \tag{2.8}$$

The diagonal terms are responsible for the non-mixing processes, while the nonzero off-diagonal terms mean the mixing between $B^0_{d,s}$ and $\overline{B}^0_{d,s}$.
The physical eigenstates of the hamiltonian (2.8) can be written in full generality as

$$|B_L\rangle = p_L |B^0\rangle + q_L \left|\overline{B}^0\right\rangle, \qquad |M_H\rangle = p_H |B^0\rangle - q_H \left|\overline{B}^0\right\rangle. \tag{2.9}$$

The coefficients are normalized by $|p_L|^2 + |q_L|^2 = 1$ and $|p_H|^2 + |q_H|^2 = 1$. Then, the flavour states are

$$|B^0\rangle = \frac{1}{q_L p_H + q_H p_L} [q_H |B_L\rangle + q_L |B_H\rangle] \tag{2.10}$$

and

$$\left|\overline{B}^0\right\rangle = \frac{1}{q_L p_H + q_H p_L} [p_H |B_L\rangle - p_L |B_H\rangle]. \tag{2.11}$$

When the hamiltonian (2.8) is diagonalized via

$$\boldsymbol{H} |B_{L,H}\rangle = \lambda_{L,H} |B_{L,H}\rangle, \tag{2.12}$$

the eigenvalues are

$$\lambda_L = H_{11} + \frac{q_L}{p_L} H_{12}, \qquad \lambda_H = H_{11} - \frac{q_H}{p_H} H_{12}. \tag{2.13}$$

Calculating $\Delta\lambda = \lambda_H - \lambda_L$, we can define:

$$\Delta m = m_H - m_L \qquad \Delta\Gamma = \Gamma_L - \Gamma_H \qquad \Gamma = \frac{1}{2}(\Gamma_L + \Gamma_H). \tag{2.14}$$

The diagonalization also leads to the definition of $\frac{q}{p}$ due to the zero off-diagonal components of diagonalized Hamiltonian:

$$\frac{q}{p} = \sqrt{\frac{q_L}{p_L}\frac{q_H}{p_H}} = \sqrt{\frac{H_{21}}{H_{12}}}. \tag{2.15}$$

In the text above, the general approach was applied. Now, additional information can be included to simplify the previous relations. Firstly, the CPT theorem can be applied, leading to the same values of the hamiltonian (2.8) diagonal terms: $H_{11} = H_{22}$. This condition suggests that the ratios of the mixing parameters q, p are the same for two physical states:

$$\frac{q_L}{p_L} = \frac{q_H}{p_H} = \frac{q}{p}, \tag{2.16}$$

resulting into the simplification of the equation (2.9):

$$|B_L\rangle = p\left|B^0\right\rangle + q\left|\overline{B}^0\right\rangle, \qquad |B_H\rangle = p\left|B^0\right\rangle - q\left|\overline{B}^0\right\rangle \tag{2.17}$$

and the eigenvalues (2.13) are (with also using equation (2.15))

$$\lambda_L = H_{11} + \frac{q}{p}H_{12} = H_{11} + \sqrt{H_{12}H_{21}}, \qquad \lambda_H = H_{11} - \frac{q}{p}H_{12} = H_{11} - \sqrt{H_{12}H_{21}}. \tag{2.18}$$

To finish the problem of the eigenvalues, the solution of the secular equation for two eigenstates

$$\left(H_{11} - \lambda_{L,H}\right)^2 - H_{12}H_{21} = 0 \tag{2.19}$$

is required to be found. The real and imaginary parts of this equation are

$$\begin{aligned} (\Delta m)^2 - \frac{1}{4}(\Delta\Gamma)^2 &= 4\left|M_{12}\right|^2 - \left|\Gamma_{12}\right|^2, \\ \Delta m \Delta\Gamma &= -4\mathrm{Re}\left(M_{12}\Gamma_{12}^*\right). \end{aligned} \tag{2.20}$$

The last expression is equivalent to

$$\Delta m \Delta\Gamma = -4\left|M_{12}\right|\left|\Gamma_{12}\right|\cos\phi_{M/\Gamma}, \tag{2.21}$$

where $\phi_{M/\Gamma} = \arg(-M_{12}/\Gamma_{12})$. Similarly, the equation (2.16) can be rewritten to

$$\frac{q}{p} = \frac{\Delta m + \frac{\imath}{2}\Delta\Gamma}{2M_{12} - \imath\Gamma_{12}}. \tag{2.22}$$

Experimentally for B meson systems, we know $\Delta\Gamma \ll \Delta m$. Additionally, the Standard Model calculations establish $|\Gamma_{12}| \ll \Delta m$. Then, equations (2.20) and (2.21) imply $|\Gamma_{12}| \ll |M_{12}|$, leading into

$$\begin{aligned} \Delta m = 2\left|M_{12}\right| \qquad & \Delta\Gamma = \left|\Gamma_{12}\right|\cos\phi_{M/\Gamma} \\ \frac{q}{p} = -e^{-\imath\phi_M}&\left(1 - \frac{1}{2}\frac{\left|\Gamma_{12}\right|}{\left|M_{12}\right|}\sin\phi_{M/\Gamma}\right). \end{aligned} \tag{2.23}$$

The ratio of mixing can be further simplified to:

$$\frac{q}{p} = -e^{-\imath\phi_M}. \tag{2.24}$$

2.3.2 Time Evolution

The time evolution of the $B^0_{d,s} - \overline{B}^0_{d,s}$ mixing is described by the Schrödinger equation (2.6). Its solution is given by the mass eigenvalues (2.13):

$$\left|B_{L,H}(t)\right\rangle = e^{-\imath m_{L,H}t-\Gamma_{L,H}t/2}\left|B_{L,H}(0)\right\rangle. \tag{2.25}$$

The flavour eigenstates can be expressed as

$$\begin{aligned}\left|B^0(t)\right\rangle &= \frac{1}{2p}\left[e^{-\imath m_L t-\Gamma_L t/2}\left|B_L(0)\right\rangle + e^{-\imath m_H t-\Gamma_H t/2}\left|B_H(0)\right\rangle\right]\\ \left|\overline{B}^0(t)\right\rangle &= \frac{1}{2p}\left[e^{-\imath m_L t-\Gamma_L t/2}\left|B_L(0)\right\rangle - e^{-\imath m_H t-\Gamma_H t/2}\left|B_H(0)\right\rangle\right]\end{aligned} \tag{2.26}$$

and the final time evolution of flavour eigenstates can be expressed using (2.26) and (2.17) as

$$\begin{aligned}\left|B^0(t)\right\rangle &= g_+(t)\left|B^0(0)\right\rangle + \frac{q}{p}g_-(t)\left|\overline{B}^0(0)\right\rangle\\ \left|\overline{B}^0(t)\right\rangle &= \frac{q}{p}g_-(t)\left|B^0(0)\right\rangle + g_+(t)\left|\overline{B}^0(0)\right\rangle,\end{aligned} \tag{2.27}$$

where

$$g_\pm(t) = \frac{1}{2}\left(e^{-\imath m_L t-\Gamma_L t/2} \pm e^{-\imath m_H t-\Gamma_H t/2}\right). \tag{2.28}$$

The time evolution functions $g_\pm(t)$ are usually expressed in terms of physical observables (mass average $m = m_H + m_L$ and those from (2.14)):

$$\begin{aligned}g_+(t) &= \frac{1}{2}\mathrm{e}^{-\imath mt-\Gamma t/2}\left[\cosh\left(\frac{\Delta\Gamma}{4}t\right)\cos\left(\frac{\Delta mt}{2}\right) - \imath\sinh\left(\frac{\Delta\Gamma}{4}t\right)\sin\left(\frac{\Delta mt}{2}\right)\right]\\ g_-(t) &= \frac{1}{2}\mathrm{e}^{-\imath mt-\Gamma t/2}\left[-\cosh\left(\frac{\Delta\Gamma}{4}t\right)\sin\left(\frac{\Delta mt}{2}\right) + \imath\sinh\left(\frac{\Delta\Gamma}{4}t\right)\cos\left(\frac{\Delta mt}{2}\right)\right].\end{aligned} \tag{2.29}$$

When the time evolution of the $B^0_{d,s} - \overline{B}^0_{d,s}$ is established, the time-dependent decay rate can be calculated. The decay rate of the produced $B_{d,s}$ meson decaying into some final state f is given by

$$\Gamma\left(B^0_{d,s}(t) \to f\right) = \frac{1}{N_B}\frac{\mathrm{d}N(B^0_{d,s}(t) \to f)}{\mathrm{d}t}, \tag{2.30}$$

where $\mathrm{d}N(B^0_{d,s}(t) \to f)$ is the number of decays of the initial meson tagged as $B^0_{d,s}$ at $t=0$ into the final state at the time between t and $t+\mathrm{d}t$. N_B is the number of total B^0 candidates produced at $t=0$. In a language of the decay amplitudes, the decay rate is

$$\Gamma\left(B^0_{d,s}(t) \to f\right) \propto N_f \langle f|\boldsymbol{H}|B^0_{d,s}\rangle, \tag{2.31}$$

with N_f being a time-independent normalization factor. For simplification, the decay amplitudes of B^0_s to the final state f at can be denoted as

$$\begin{aligned} A_f &= \langle f|\boldsymbol{H}|B^0_s\rangle & \overline{A}_f &= \langle f|\boldsymbol{H}|\overline{B}^0_s\rangle \\ A_{\overline{f}} &= \langle \overline{f}|\boldsymbol{H}|B^0_s\rangle & \overline{A}_{\overline{f}} &= \langle \overline{f}|\boldsymbol{H}|\overline{B}^0_s\rangle. \end{aligned} \tag{2.32}$$

Additionally, the parameter describing the CP violation can be defined as

$$\lambda_f = \frac{q}{p}\frac{\overline{A}_f}{A_f} = \left|\lambda_f\right| - e^{-\imath\phi_M}\frac{\overline{A}_f}{A_f}. \tag{2.33}$$

The branching ratio (decay rate) for the $B^0_s \to f$ can be thus expressed as

$$\begin{aligned} \Gamma\left(B^0_s(t) \to f\right) = & N_f|A_f|^2 \mathrm{e}^{-\Gamma t}\left[\frac{1+|\lambda_f|^2}{2}\cosh\frac{\Delta\Gamma t}{2} + \frac{1-|\lambda_f|^2}{2}\cos\Delta m t\right. \\ & \left. - \mathscr{R}e\left(\lambda_f\right)\sinh\frac{\Delta\Gamma t}{2} - 2\mathscr{I}m\left(\lambda_f\right)\sin\Delta m t\right]. \end{aligned} \tag{2.34}$$

The branching ratio for the $\overline{B}^0_s$ looks similar:

$$\begin{aligned} \Gamma\left(\overline{B}^0_s(t) \to f\right) = & N_f|A_f|^2 \mathrm{e}^{-\Gamma t}\left[\frac{1+|\lambda_f|^2}{2}\cosh\frac{\Delta\Gamma t}{2} - \frac{1-|\lambda_f|^2}{2}\cos\Delta m t\right. \\ & \left. - \mathscr{R}e\left(\lambda_f\right)\sinh\frac{\Delta\Gamma t}{2} + \mathscr{I}m\left(\lambda_f\right)\sin\Delta m t\right]. \end{aligned} \tag{2.35}$$

2.3.3 CP violation in $B^0_s \to J/\psi\phi$

Until now, formalism has been developed without any final state consideration. However, the final state is needed for further analysis. This thesis is devoted to the study of CP violation in the $B^0_s \to J/\psi\phi$ decay, so the final state taken into account is two vector mesons: J/ψ and ϕ, written in the bracket formalism as $\left|J/\psi\phi\right\rangle$. This is also CP eigenstate:

$$CP\left|J/\psi\phi\right\rangle = \eta_f\left|J/\psi\phi\right\rangle = (-1)^L\left|J/\psi\phi\right\rangle. \tag{2.36}$$

The eigenvalues $\eta_f = \pm 1$ depend on the angular momentum L of two final states. The initial particle has spin and angular momentum 0, J/ψ and ϕ have both spin 1. Following the expression for the final angular momentum $J = S + L$, the possible angular

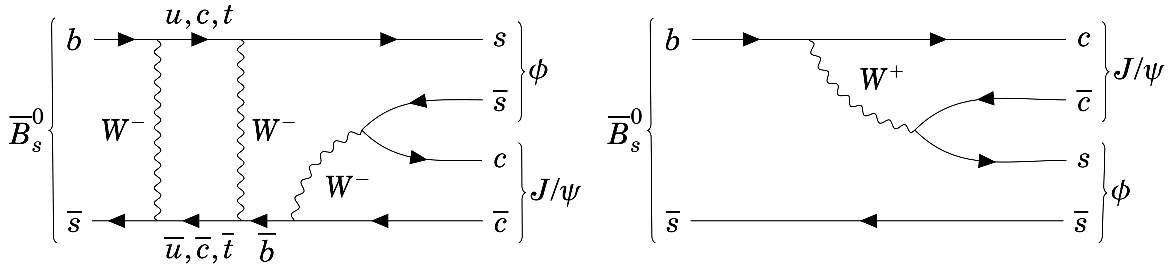

FIGURE 2.4. $B_s^0 \to J/\psi\phi$ decay diagram with (left) and without (right) initial state mixing.

momentum of the final state is $L \in (0,1,2)$. The $L=0$ and $L=2$ states are CP-odd, the $L=1$ state is CP-even.
The amplitudes (2.32) of the decay into CP final states can be written as

$$A_{f_{CP}} = \left|A_{f_{CP}}\right| e^{\imath(\delta_f - \phi_D)}, \tag{2.37}$$

where δ_f is the strong phase not affected by the CP transformation and ϕ_D a weak phase entering the decay amplitude. The amplitude of $\overline{B}^0$ decaying into the same final state can be described by:

$$\overline{A}_{f_{CP}} = \eta_{CP}\overline{A}_{\overline{f}_{CP}} = \eta_{CP}\left|A_{f_{CP}}\right| e^{\imath(\delta_f + \phi_D)}. \tag{2.38}$$

Then, the ratio of the amplitudes (2.37) and (2.38) is

$$\frac{\overline{A}_{f_{CP}}}{A_{f_{CP}}} = \eta_{CP} e^{\imath 2\phi_D}. \tag{2.39}$$

Substituting this fraction in (2.33), the phase of λ_f is

$$\phi_s = -\arg\lambda_f = \phi_M - 2\phi_D. \tag{2.40}$$

The amplitude ϕ_M describes the CP violation and is connected to the CKM matrix (1.44) (as visible in Figure 2.4) via

$$\phi_M = \arg M_{12} = \arg\left[\left(V_{tb}V_{ts}^*\right)^2\right] \tag{2.41}$$

and the phase ϕ_D is dedicated to the CP violation in the decay of $b \to c\bar{c}s$:

$$\phi_D = \arg\left(V_{cb}V_{cs}^*\right), \tag{2.42}$$

leading into the final connection between CKM matrix elements and ϕ_S phase

$$\phi_s = 2\arg\left(\frac{V_{tb}V_{ts}^*}{V_{cb}V_{cs}^*}\right) = -2\beta_s, \tag{2.43}$$

where β_s is defined in (1.52). The Standard Model weak phase includes additional contribution from the penguin diagram (the tree level decay of b quark in Figure 2.4 can be substituted by loop diagrams from Figure 2.1):

$$\phi_s^{SM} = -2\beta_s + \phi_s^{\text{penguin}} + \phi_s^{\Delta_s}. \tag{2.44}$$

The $\phi_s^{\Delta_s}$ reflects the possible contribution of the physics beyond the SM. This contribution arises from the modification of the effective hamiltonian mass terms (2.8):

$$M_{12} \to M_{12}^{SM}\Delta_s = M_{12}^{SM}\,|\Delta_s|\,e^{\imath\phi_s^{\Delta_s}}. \tag{2.45}$$

If there is no beyond SM physics, $\phi_s^{\Delta_s} = 0$.
The theoretical prediction of the SM value of ϕ_s by the CKMFitter group is [80]

$$\phi_s^{SM} = -0.0368^{+0.0006}_{-0.0009}\,\text{rad} \tag{2.46}$$

and by the UTfit Collaboration [81]

$$\phi_s^{SM} = (-0.03700 \pm 0.00104)\text{ rad}. \tag{2.47}$$

2.3.4 Helicity and Transversity Formalism

The three components of the decay amplitudes (2.32) can be distinguished through the angular analysis, where the final state is described by three angles. Usually, the angles are chosen in a helicity and transversity basis. The choice of the basis does not have any effect on the measured physical observables, but it helps determine the separation of the three decay amplitudes components).

2.3.4.1 Helicity Basis

In the helicity basis, the spin of the particles is projected on the momentum direction of the resonant vector mesons. As the mother particle, B_s^0 has zero spin, its helicity (spin projection) is also 0. The daughter particles have spin 1 and can have three possible helicity: $\lambda_{J/\psi} = -1, 0, +1$ and $\lambda_\phi = -1, 0, +1$. The helicity of the final state is constrained by the helicity (spin) of the mother particle by relation

$$\left|\lambda_{J/\psi} - \lambda_\phi\right| = \lambda_{B_s^0} \tag{2.48}$$

resulting into three possible helicity combinations of daughter particles: $(-1,-1)$, $(0,0)$ and $(+1,+1)$. Each of the amplitude components is associated with one final helicity

state: A_{-1}, A_0, A_{+1}.
The definition of the helicity basis angles $\Omega_H = \{\theta_\mu;\theta_K;\phi_H\}$ is shown in Figure 2.5. The angle ϕ_K is the angle between K^+ and the opposite B_s^0 direction of flight in the $\phi(K^+K^-)$ rest frame. Similarly, the angle ϕ_μ is the angle between μ^+ and the opposite B_s^0 direction of flight in the $J/\psi(\mu^+\mu^-)$ rest frame. The last angle ϕ_H is the angle between the $J/\psi(\mu^+\mu^-)$ and $\phi(K^+K^-)$ rest frame planes defined by the $J/\psi(\mu^+\mu^-)$ and $\phi(K^+K^-)$ daughter particles.

2.3.4.2 Transversity Basis

The transversity uses a decomposition of the decay amplitude into the three independent linear polarization of the final vector bosons. The possible polarizations are: both vectors have longitudinal polarization labelled by 0; both vectors are polarized transversally to the vector direction. There are two possible configurations of transverse polarization. The polarizations are parallel to each other (labelled by $\|$) and perpendicular to each other (labelled by $\perp$). All possible polarization combinations are shown in Figure 2.6.

The angles $\Omega_T = \{\theta_T;\psi_T;\phi_T\}$ are defined in Figure 2.7. The angle ψ_T is defined as the angle between the opposite B_s^0 direction of flight and K^+ in the K^+K^- rest frame. ϕ_T and θ_T are defined in the $\mu^+\mu^-$ rest frame, where θ_T is the polar angle, and ϕ_T is the azimuthal angle of the μ^+ with respect to the $x-y$ plane defined by the $\phi \to K^+K^-$ decay vectors.
The amplitudes in the transversity basis can be expressed by the helicity amplitudes:

$$A_0 = A_0 \qquad A_\| = \frac{A_{+1}+A_{-1}}{2} \qquad A_\perp = \frac{A_{+1}-A_{-1}}{2}. \tag{2.49}$$

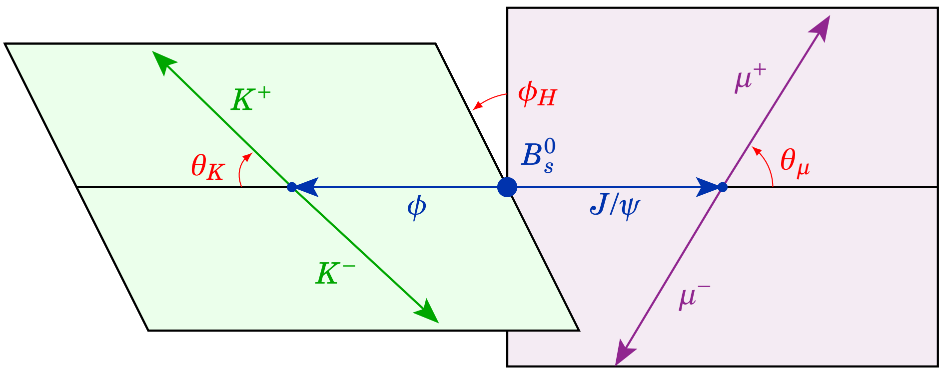

FIGURE 2.5. $B_s^0 \to J/\psi\phi$ angular description in the helicity basis.

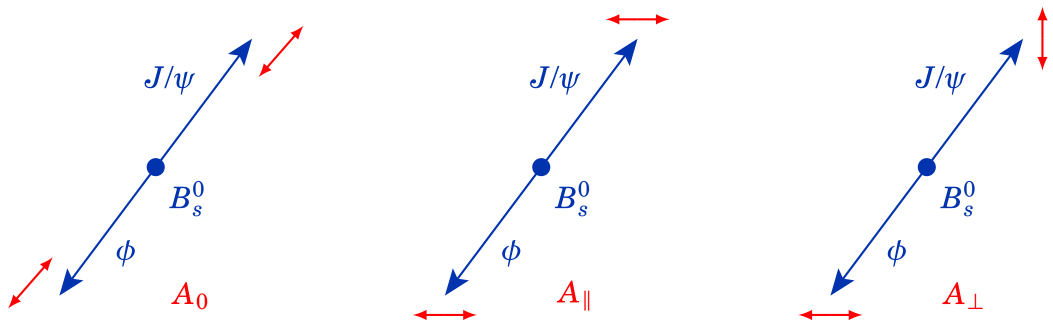

FIGURE 2.6. Polarization amplitudes of $B_s^0 \to J/\psi\phi$ decay amplitudes in the transversity basis. A_0 corresponds to the longitudinal polarization. $A_\parallel$ and $A_\perp$ correspond to transverse parallel and transverse perpendicular polarization, respectively.

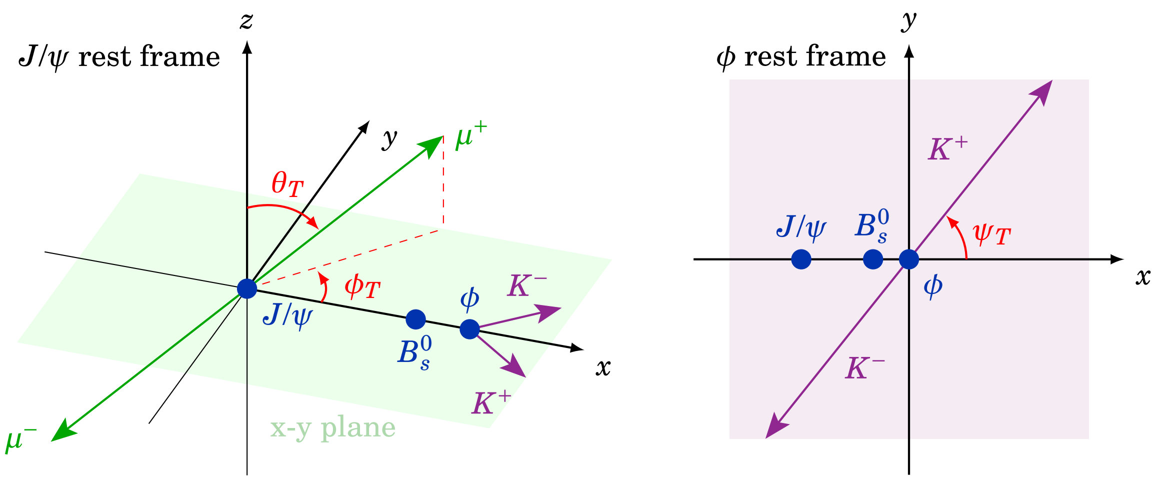

FIGURE 2.7. $B_s^0 \to J/\psi\phi$ decay in the transversity basis.

Usually, the transversity basis is often used instead of the helicity basis in the analyses. The reason for this is that the transverse formalism allows separation of the amplitude into the CP-even (A_0, $A_\parallel$) and CP-odd ($A_\perp$) amplitude. This basis is used in the analysis presented in this thesis, and its connection to the angular analysis is emphasized in the following section.

2.3.5 Angular Analysis

Considering B meson as pseudoscalar particle decaying into two vector particles with polarization four-vectors $\epsilon^*_{1,\mu}$, $\epsilon^*_{2,\mu}$, masses m_1, m_2 and momenta p_1^μ, p_2^μ, the decay in a general form can be written as

$$B(p) \to V_1(\epsilon^*_{1,\mu}, \vec{p}_1) + V_2(\epsilon^*_{2,\mu}, \vec{p}_2). \tag{2.50}$$

V_1 meson denotes the J/ψ particle and V_2 is identified as ϕ. The most general amplitude $A(t)$ from the invariant matrix element M for this decay as a sum of three terms is

$$A(t) = \epsilon^*_{1,\mu}(\vec{p}_1)\epsilon^*_{2,\mu}(\vec{p}_2)\left[a g^{\mu\nu} + \frac{b}{m_1 m_2} p_1^{\nu} p_2^{\mu} + \imath \frac{c}{m_1 m_2} \varepsilon^{\mu\nu\alpha\beta} p_{1,\alpha} p_{2,\beta} \right]. \tag{2.51}$$

The B meson decay can be considered in the J/ψ rest frame: $p^{\nu}_{J/\psi} = (m_{J/\psi}, \vec{0})^{\nu}$ and $\epsilon^*_{J/\psi,\mu} = (0, \vec{\epsilon}_{J/\psi})_{\mu}$. The J/ψ polarization vector can be decomposed into the longitudinal and transverse directions along the ϕ meson direction of motion:

$$\epsilon^*_{J/\psi}(\vec{0}) = (0, \epsilon^{*L}_{J/\psi}\hat{p}_{\phi} + \vec{\epsilon}^{\,*T}_{J/\psi}), \tag{2.52}$$

where $\hat{p}_{\phi}$ is the unit vector of ϕ four-momentum. The ϕ polarization vector in the ϕ rest frame can be written in a similar form, but when this vector is boosted in the J/ψ rest frame, one obtains:

$$\epsilon^*_{\phi}(\vec{0}) = (0, \epsilon^{*L}_{\phi}\hat{p}_{\phi} + \vec{\epsilon}^{\,*T}_{\phi}) \to \epsilon^*_{\phi}(\vec{p}_{\phi}) = (\frac{|p_{\phi}|}{m_{\phi}}\epsilon^{*L}_{\phi}, \frac{E_{\phi}}{m_{\phi}}\epsilon^{*L}_{\phi}\hat{p}_{\phi} + \vec{\epsilon}^{\,*T}_{\phi}), \tag{2.53}$$

where $E_{\phi} = \sqrt{\vec{p}^{\,2}_{\phi} + m^2_{\phi}}$ is the total energy of ϕ meson. Using (2.52) and (2.53), the general amplitude equation (2.51) can be written as

$$A(t) = A_0(t)\epsilon^{*L}_{J/\psi}\epsilon^{*L}_{\phi} - \frac{1}{\sqrt{2}}A_{\parallel}(t)\vec{\epsilon}^{\,*T}_{J/\psi}\cdot\vec{\epsilon}^{\,*T}_{\phi} - \imath\frac{1}{\sqrt{2}}A_{\perp}(t)\left(\vec{\epsilon}^{\,*T}_{J/\psi}\times\vec{\epsilon}^{\,*T}_{\phi}\right)\cdot\hat{p}_{\phi}. \tag{2.54}$$

The separated transverse polarization amplitudes are associated with the amplitudes in Figure 2.6. Only the decay of B meson to two vector particles was considered until now. To determine the J/ψ and ϕ polarization, the decay of vectors to daughter particles must also be included.

The ϕ meson is expected to decay into the KK pair (a pseudoscalar spinless pair). Thus, the ϕ linear polarization vector lies in the $x-y$ plane in the ϕ rest frame. The polarization vectors arise from the amplitude

$$A\left(\phi \to K^+K^-\right) \propto 2\vec{\epsilon}_{\phi}\cdot\vec{p}_{K^+} \tag{2.55}$$

and they can be written as

$$\begin{aligned} \vec{\epsilon}^{\,L}_{\phi} &= \left(\cos\psi_T, 0, 0\right) \\ \vec{\epsilon}^{\,T}_{\phi} &= \left(0, \sin\psi_T, 0\right). \end{aligned} \tag{2.56}$$

The J/ψ meson has a single linear polarization per each amplitude in its rest frame:

$$\begin{aligned} A_0: &\quad \vec{\epsilon}_{J/\psi} = (1,0,0) \\ A_\parallel: &\quad \vec{\epsilon}_{J/\psi} = (0,1,0) \\ A_\perp: &\quad \vec{\epsilon}_{J/\psi} = (0,0,1). \end{aligned} \tag{2.57}$$

The first polarization vector refers to the longitudinal polarization $\vec{\epsilon}^{L}_{J/\psi} = (1,0,0)$, while the last two vectors can form the transverse polarization: $\vec{\epsilon}^{T}_{J/\psi} = (0,1,1)$. Using (2.57) and (2.56), the decay amplitude (2.54) becomes

$$\vec{A}(t) = \left(A_0(t)\cos\psi, -\frac{1}{\sqrt{2}}A_\parallel(t)\sin\psi, \frac{\imath}{\sqrt{2}}A_\perp(t)\sin\psi\right). \tag{2.58}$$

The last missing piece of the puzzle is the coupling of the J/ψ meson to the $\mu^+\mu^-$ final state. Generally, the total differential decay rate of $B_s^0 \to J/\psi\phi$ is proportional to the sum over lepton polarization that leads to the tensor L_{ij}:

$$\begin{aligned} \frac{\mathrm{d}^4\Gamma\left(B_s^0 \to J/\psi\phi\right)}{\mathrm{d}t\,\mathrm{d}\cos\psi\,\mathrm{d}\cos\theta\,\mathrm{d}\phi} \equiv \frac{\mathrm{d}^4\Gamma}{\mathrm{d}t\,\mathrm{d}\vec{\Omega}} &\propto \sum_{r,s} A_i^\dagger(t)\left[\overline{u}(s)\gamma_i v(r)\right]^\dagger A_j(t)\left[\overline{u}(s)\gamma_j v(r)\right] \\ &= A_i(t)A_j(t)L_{ij} = A_i(t)A_j(t)\left(\delta_{ij} - n_i n_j\right), \end{aligned} \tag{2.59}$$

i	$T_i(t)$	$g_i\left(\vec{\Omega}\right)$
1	$\lvert A_0(t)\rvert^2$	$\cos^2\psi\left(1-\sin^2\theta\cos^2\phi\right)$
2	$\left\lvert A_\parallel(t)\right\rvert^2$	$\frac{1}{2}\sin^2\psi\left(1-\sin^2\theta\sin^2\phi\right)$
3	$\lvert A_\perp(t)\rvert^2$	$\frac{1}{2}\sin^2\psi\sin^2\theta$
4	$\mathscr{Re}\left(A_0^*(t)A_\parallel(t)\right)$	$\frac{1}{2\sqrt{2}}\sin(2\psi)\sin^2\theta\sin(2\phi)$
5	$\mathscr{Im}\left(A_0^*(t)A_\perp(t)\right)$	$\frac{1}{2\sqrt{2}}\sin(2\psi)\sin(2\theta)\cos\phi$
6	$\mathscr{Re}\left(A_\parallel^*(t)A_\perp(t)\right)$	$\frac{-1}{2}\sin^2\psi\sin(2\theta)\sin\phi$
7	$\lvert A_S(t)\rvert^2$	$\frac{1}{3}\left(1-\sin^2\theta\cos^2\phi\right)$
8	$\mathscr{Re}\left(A_0^*(t)A_S(t)\right)$	$\frac{2\sqrt{3}}{3}\cos\psi\left(1-\sin^2\theta\cos^2\phi\right)$
9	$\mathscr{Re}\left(A_\parallel^*(t)A_S(t)\right)$	$\frac{\sqrt{6}}{6}\sin\psi\sin^2\theta\sin(2\phi)$
10	$\mathscr{Im}\left(A_\perp^*(t)A_S(t)\right)$	$\frac{-\sqrt{6}}{6}\sin\psi\sin(2\theta)\cos\phi$

TABLE 2.2. Terms of the $B_s^0 \to J/\psi\phi$ differential decay rate, where $T_i(t)$ is the time-dependent product of polarization amplitudes and $f_i(\vec{\Omega})$ describes the angular distribution. The last four rows are dedicated to the contribution from the S-wave and its interference with the polarization terms.

where n_i is the i-th component of the unit vector describing the direction of the μ^+ in the J/ψ rest frame:

$$\hat{n} = \left(\sin\theta\cos\phi, \sin\theta\sin\phi, \cos\theta\right). \tag{2.60}$$

Using this notation, the equation (2.59) can be written as

$$\frac{\mathrm{d}^4\Gamma}{\mathrm{d}t\mathrm{d}\vec{\Omega}} \propto A_i(t)A_j(t)L_{ij} = \left|\vec{A}(t)\times\hat{n}\right|^2 = \sum_{i=1}^{6} T_i(t)g_i(\vec{\Omega}). \tag{2.61}$$

The $T_i(t)$ is the time-dependent product of polarization amplitudes and $g_i(\vec{\Omega})$ describes the angular distribution. All terms are detailed in Table 2.2 together with the S-wave contribution that plays an important role in the analyses.

2.3.6 S-Wave Contribution

Usually, the decay of $B_s^0 \to J/\psi\phi$ is observed via the final states - $J/\psi \to \mu^+\mu^-$ and $\phi \to K^+K^-$. The spinless kaons must form the $L = 1$ state due to the decay of vector particle ϕ. This state is also called the P-wave state. However, the detected final state can be additionally formed by the $B_s^0 \to J/\psi K^+K^-$ and $B_s^0 \to J/\psi f_0$ decays. In this case, the K^+K^- final state has the total angular momentum $L = 0$, often referred to as the S-wave. Therefore, in the final analysis, both contributions must be considered.

The S-wave contribution is CP-odd, and it has only one vector particle in the $B_s^0 \to J/\psi K^+K^-$ decay. To conserve the spin, J/ψ can have only the longitudinal polarization, implying the form of the S-wave amplitude vector to be

$$\vec{S}(t) = (A_S(t), 0, 0), \tag{2.62}$$

where $A_S(t)$ is the amplitude of the S-wave contribution. To include the S-wave, the differential decay rate (2.61) is modified to

$$\frac{\mathrm{d}^4\Gamma}{\mathrm{d}t\mathrm{d}\vec{\Omega}} \propto A_i(t)A_j(t)L_{ij} = \left|\left(\vec{A}(t)+\frac{1}{\sqrt{3}}\vec{S}(t)\right)\times\hat{n}\right|^2 = \sum_{i=1}^{10} T_i(t)g_i(\vec{\Omega}). \tag{2.63}$$

The factor $1/\sqrt{3}$ is chosen to preserve the normalization. Equation (2.63) contains four additional term due to the S-wave contribution and its interference with the P-wave. The time-dependent amplitudes from Table 2.2 can be depicted using the equations (2.35) and (2.34), leading to the differential decay rate

$$\frac{\mathrm{d}^4\Gamma}{\mathrm{d}t\mathrm{d}\vec{\Omega}} = \sum_{k=1}^{10} A_k T_k(t) g_k(\theta_T, \psi_T, \phi_T), \tag{2.64}$$

k	$g^{(k)}(\theta_T,\psi_T,\phi_T)$	$A^{(k)}$	$T^{(k)}(t)$	meaning of δ_k
1	$2\cos^2\psi_T(1-\sin^2\theta_T\cos^2\phi_T)$	$\frac{1}{2}\lvert A_0(0)\rvert^2$	$\left(1+\frac{2\lvert\lambda\rvert}{1+\lvert\lambda\rvert^2}\cos\phi_s\right)\mathrm{e}^{-\Gamma_{\mathrm{L}}^{(s)}t}+\left(1-\frac{2\lvert\lambda\rvert}{1+\lvert\lambda\rvert^2}\cos\phi_s\right)\mathrm{e}^{-\Gamma_{\mathrm{H}}^{(s)}t}$ $\pm 2\mathrm{e}^{-\Gamma_s t}\left(\frac{2\lvert\lambda\rvert}{1+\lvert\lambda\rvert^2}\sin(\Delta m_s t)\sin\phi_s+\frac{1-\lvert\lambda\rvert^2}{1+\lvert\lambda\rvert^2}\cos(\Delta m_s t)\right)$	
2	$\sin^2\psi_T(1-\sin^2\theta_T\sin^2\phi_T)$	$\frac{1}{2}\lvert A_\parallel(0)\rvert^2$		
3	$\frac{1}{\sqrt{2}}\sin 2\psi_T\sin^2\theta_T\sin 2\phi_T$	$\frac{1}{2}\lvert A_0(0)\rvert\lvert A_\parallel(0)\rvert\cos\delta_{\lvert\lvert}$		
4	$\sin^2\psi_T\sin^2\theta_T$	$\frac{1}{2}\lvert A_\perp(0)\rvert^2$	$\left(1-\frac{2\lvert\lambda\rvert}{1+\lvert\lambda\rvert^2}\cos\phi_s\right)\mathrm{e}^{-\Gamma_{\mathrm{L}}^{(s)}t}+\left(1+\frac{2\lvert\lambda\rvert}{1+\lvert\lambda\rvert^2}\cos\phi_s\right)\mathrm{e}^{-\Gamma_{\mathrm{H}}^{(s)}t}$ $\mp 2\mathrm{e}^{-\Gamma_s t}\left(\frac{2\lvert\lambda\rvert}{1+\lvert\lambda\rvert^2}\sin(\Delta m_s t)\sin\phi_s-\frac{1-\lvert\lambda\rvert^2}{1+\lvert\lambda\rvert^2}\cos(\Delta m_s t)\right)$	
5	$\frac{2}{3}\left(1-\sin^2\theta_T\cos^2\phi_T\right)$	$\frac{1}{2}\lvert A_S(0)\rvert^2$		
6	$\frac{1}{3}\sqrt{6}\sin\psi_T\sin 2\theta_T\cos\phi_T$	$\frac{1}{2}\alpha\lvert A_S(0)\rvert\lvert A_\perp(0)\rvert\sin(\delta_\perp-\delta_S)$		
7	$-\sin^2\psi_T\sin 2\theta_T\sin\phi_T$	$\frac{1}{2}\lvert A_\parallel(0)\rvert\lvert A_\perp(0)\rvert$	$\left(\mathrm{e}^{-\Gamma_{\mathrm{L}}^{(s)}t}-\mathrm{e}^{-\Gamma_{\mathrm{H}}^{(s)}t}\right)\frac{2\lvert\lambda\rvert}{1+\lvert\lambda\rvert^2}\cos\delta_k\sin\phi_s$ $+\frac{1}{2}\left(\mathrm{e}^{-\Gamma_{\mathrm{L}}^{(s)}t}+\mathrm{e}^{-\Gamma_{\mathrm{H}}^{(s)}t}\right)\frac{1-\lvert\lambda\rvert^2}{1+\lvert\lambda\rvert^2}\sin\delta_k$ $\pm 2\mathrm{e}^{-\Gamma_s t}\left(\sin\delta_k\cos(\Delta m_s t)-\frac{2\lvert\lambda\rvert}{1+\lvert\lambda\rvert^2}\cos\delta_k\cos\phi_s\sin(\Delta m_s t)\right)$	$\delta_7=\delta_\perp-\delta_{\lvert\lvert}$
8	$\frac{1}{\sqrt{2}}\sin 2\psi_T\sin 2\theta_T\cos\phi_T$	$\frac{1}{2}\lvert A_0(0)\rvert\lvert A_\perp(0)\rvert$		$\delta_8=\delta_\perp$
9	$\frac{1}{3}\sqrt{6}\sin\psi_T\sin^2\theta_T\sin 2\phi_T$	$\frac{1}{2}\alpha\lvert A_S(0)\rvert\lvert A_\parallel(0)\rvert$		$\delta_9=\frac{\pi}{2}-\delta_{\lvert\lvert}+\delta_S$
10	$\frac{4}{3}\sqrt{3}\cos\psi_T\left(1-\sin^2\theta_T\cos^2\phi_T\right)$	$\frac{1}{2}\alpha\lvert A_0(0)\rvert\lvert A_S(0)\rvert$		$\delta_{10}=\frac{\pi}{2}+\delta_S$

TABLE 2.3. Table showing the ten time-dependent functions $\mathcal{O}^k(t)=A^kT^k(t)$ and the functions of the transversity angles $g^k(\theta_T,\psi_T,\phi_T)$ [82].

where A_k are functions of the transverse polarization amplitudes and their interferences at time $t = 0$, $T_k(t)$ described the time evolution and $g^k(\theta_T, \psi_T, \phi_T)$ are the functions of the transversity angles ϕ_T, ψ_T, θ_T, see Table 2.3.

This equation is valid for both B_s^0 and $\overline{B}_s^0$ decay rate; the sign reverses in the terms containing Δm_s in the latter case.
The equation (2.64) is expressed for the tagged events. If no tagging information is available (untagged events), all terms with Δm_s are cancelled. As the terms with Δm_s in Table 2.3 also contain $\cos\phi_s$ or $\sin\phi_s$, tagged events provide higher sensitivity to the measurement of ϕ_s. Interference terms of the equation (2.64) are not represented with the real and imaginary part of the amplitudes but use the absolute values of amplitudes and their strong phases δ_k:

$$\delta_{\parallel} = \arg\left(A_{\parallel}(0)\right), \quad \delta_{\perp} = \arg(A_{\perp}(0)), \quad \delta_0 = \arg(A_0(0)), \quad \delta_S = \arg(A_S(0)), \tag{2.65}$$

where the definition $\delta_0 = 0$ is often used.

2.4 Theoretical and Experimental Status

2.4.1 CP-violating phase ϕ_s and decay width difference $\Delta\Gamma_s$

The first observation of the ϕ_s in the $B_s^0 \to J/\psi(\mu^+\mu^-)\phi(K^+K^-)$ system was provided by the DØ and CDF experiments at the Tevatron collider in 2008, showing the small discrepancy of the ϕ_s value from the Standard Model prediction [85]. The improved measurement by the same experiments was published in 2010, showing better agreement with the SM, but leaving space for more precise measurement due to the large statistical uncertainties. The first contribution to the experimental CP-violation phase value by the Large Hadron Collider (LHC) experiments at CERN (European Organization for Nuclear Research) was made by the LHCb experiment in 2010. In 2012, LHCb submitted the paper in which the ϕ_s has better precision and also the sign of the decay rate difference $\Delta\Gamma$ was firstly determined, favouring the positive sign. This confirmed the expectation that $\Gamma_L > \Gamma_H$. The LHCb results were supported by two other LHC experiments: ATLAS and CMS, both providing untagged and tagged analyses.

The overview of the experimental status from each experiment (without the most recent results of the analysis presented in this thesis) is summarized in Table 2.4 and Figure 2.8. The Figure 2.8 further shows the theoretical results of the ϕ_s and Γ_s

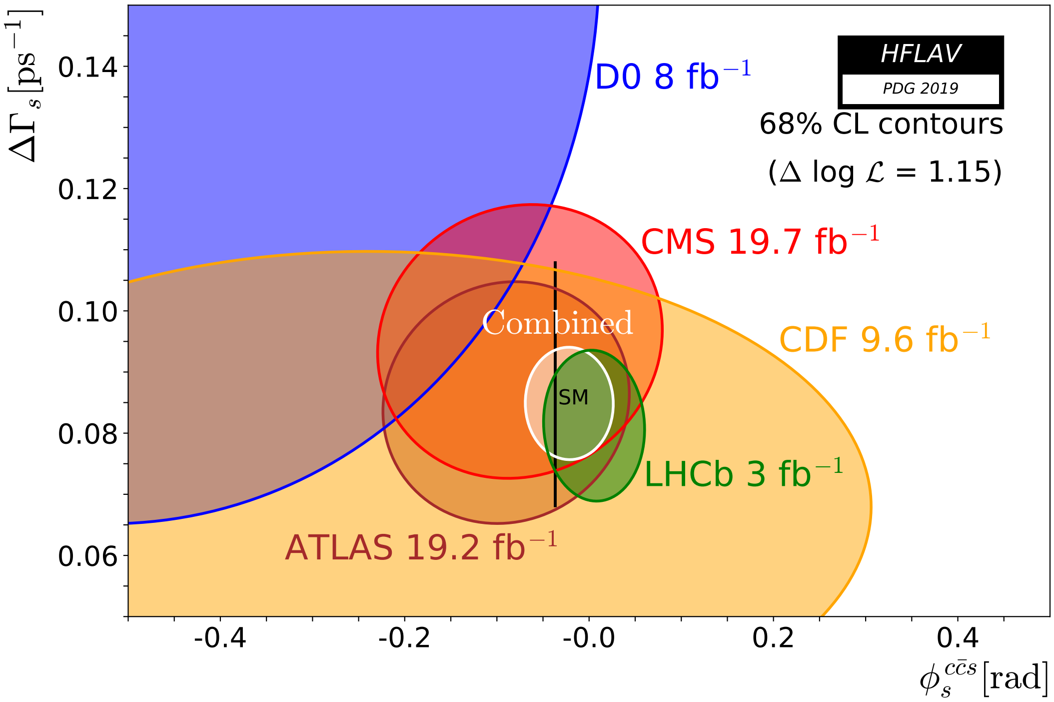

FIGURE 2.8. The ϕ_s and $\Delta\Gamma_s$ results from experiments plotted in the 2-dimensional plane [83]. Each experiment has its contour of 68% confidence level. In all contours, the statistical and systematic uncertainties are combined in quadrature. The combination contour is represented by white colour, and the thin black rectangle shows the Standard Model predictions [80, 84].

parameters, those the most current values are [80, 84]

$$\begin{aligned} \phi_s &= -0.0368^{+0.0006}_{-0.0009}\,\mathrm{rad}, \\ \Delta\Gamma_s &= (0.091 \pm 0.013)\ \mathrm{ps}^{-1}. \end{aligned} \tag{2.66}$$

2.4.2 Lifetime of B_d^0 mesons

The lifetime value of B_d^0 mesons can be estimated directly by the lifetime measurement or extracted from the analysis of the B_d^0 oscillations and mass difference. The results are provided by three groups of experiments: SLC and LEP experiments, B-factories, and Large Hadron Collider with Tevatron. Each group has different environments, obtained using substantially different techniques, providing the credibility of all measurements and the opportunity of avoiding systematic errors. All experimental results are listed in [94], and the average value of B_d^0 lifetime is presented together with the $B_d^0 - B_s^0$ lifetime

Exp.	Mode	ϕ_s [rad]	$\Delta\Gamma_s$ [ps^{-1}]	Ref.
CDF	$J/\psi\phi$	$[-0.60;+0.12]$ at 68% CL	$0.068 \pm 0.026 \pm 0.009$	[85]
DØ	$J/\psi\phi$	$0.55^{+0.38}_{-0.36}$	$0.163^{+0.065}_{-0.064}$	[86]
CMS	$J/\psi\phi$	$-0.075 \pm 0.097 \pm 0.031$	$0.095 \pm 0.013 \pm 0.007$	[87]
LHCb	$J/\psi K^+K^-$	$-0.058 \pm 0.049 \pm 0.006$	$0.0805 \pm 0.0091 \pm 0.0032$	[88]
LHCb	$J/\psi K^+K^-$	$0.119 \pm 0.107 \pm 0.034$	$0.066 \pm 0.018 \pm 0.010$	[89](a)
LHCb	$J/\psi\pi^+\pi^-$	$0.070 \pm 0.068 \pm 0.008$	—	[90]
LHCb	$\psi(2S)\phi$	$0.23^{+0.29}_{-0.28} \pm 0.02$	$0.066^{+0.41}_{-0.44} \pm 0.007$	[91]
LHCb	$D_s^+D_s^-$	$0.02 \pm 0.17 \pm 0.02$	—	[92]
ATLAS	$J/\psi\phi$	$0.12 \pm 0.25 \pm 0.05$	$0.053 \pm 0.021 \pm 0.010$	[93]
ATLAS	$J/\psi\phi$	$-0.110 \pm 0.082 \pm 0.042$	$0.101 \pm 0.013 \pm 0.007$	[82]
Combined		-0.021 ± 0.031	0.085 ± 0.006	[83]

(a) $m(K^+K^-) > 1.05$ GeV

TABLE 2.4. The experimental results of CP-violating phase ϕ_s from ATLAS, CMS, LHCb, DØ and CDF collaborations [82, 85–93] and their combinations provided by the HFLAV group [83]. Only results published before 2019 are presented.

ratio $\tau(B_s^0)/\tau(B_d^0)$ in Table 2.5.

The lifetime itself is difficult to predict by theory. On the other hand, it is easier to achieve the prediction of the lifetime ratio. The theoretical predictions of the lifetime ratio are acquired by the HQET (HQET) framework and lattice QCD. HQET permits the calculation of B-meson observables through perturbative expansion in powers of the reciprocal of the b-quark mass, m_b. Lifetime differences among the B-hadrons are almost entirely attributable to the corrections for Pauli interference and weak annihilation, both of which are enhanced by a relatively large phase space factor where they enter the expansion at the term proportional to m_b^{-3}. The largest contributions to the total

	$\tau(B_d^0)$ [ps]	$\tau(B_s^0)/\tau(B_d^0)$	Ref.
HQET	—	1.0007 ± 0.0025	[95]
Lattice QCD	—	1.00 ± 0.02	[96]
Exp. combination	1.519 ± 0.004	1.001 ± 0.004	[94]

TABLE 2.5. Theoretical predictions using HQET and lattice QCD [95, 96], and experimental results of the lifetime ratio $\tau(B_s^0)/\tau(B_d^0)$ and B_d^0 lifetime provided by the HFLAV [94].

uncertainty on the lifetime ratio, as predicted with HQET, come from the hadronic matrix elements. Predictions for $\tau(B_s^0)/\tau(B_d^0)$ have also been made in the lattice QCD framework, including next-to-leading order perturbative quantum chromodynamics corrections in the coefficient functions, and these are compared as well. The predicted value of the $B_d^0 - B_s^0$ lifetime ratio $\tau(B_s^0)/\tau(B_d^0)$ shown in Table 2.5.

CHAPTER 3

THE LARGE HADRON COLLIDER

The discoveries of new particles, the tests of many theories (mainly the Standard Model nowadays), and the improved measured precision of many parameters could not be possible without the development of the physics and technique of particle colliders and detectors. Such a collider should be capable of colliding preferred particles (usually protons, ions of gold, or lead), have systems detecting the collision output, record the produced particles in the collision and store this information for future analysis.

Today, Large Hadron Collider (LHC) has the leading role among the colliders. It is a dual-circular collider accelerating two beams of protons, ions of lead of xenon (in opposite directions), located under the CERN laboratory near Geneva, Switzerland. It is installed in a 26.7 km long tunnel, replacing the previous accelerator Large Electron–Positron Collider (LEP).

3.1 History of LHC

The Large Hadron Collider is the most powerful particle collider ever built. The first proposal for the Large Hadron Collider was presented in 1984 at the CERN and ECFA2 workshop in Lausanne, Switzerland. In this proposal, the tunnel already used for Large Electron–Positron Collider collider was chosen for the latter Large Hadron Collider. The tunnel was excavated in 1988, and the first collisions appeared at LEP in 1989. The total beam energy of the initial electron-positron collisions was 45 GeV. The particles

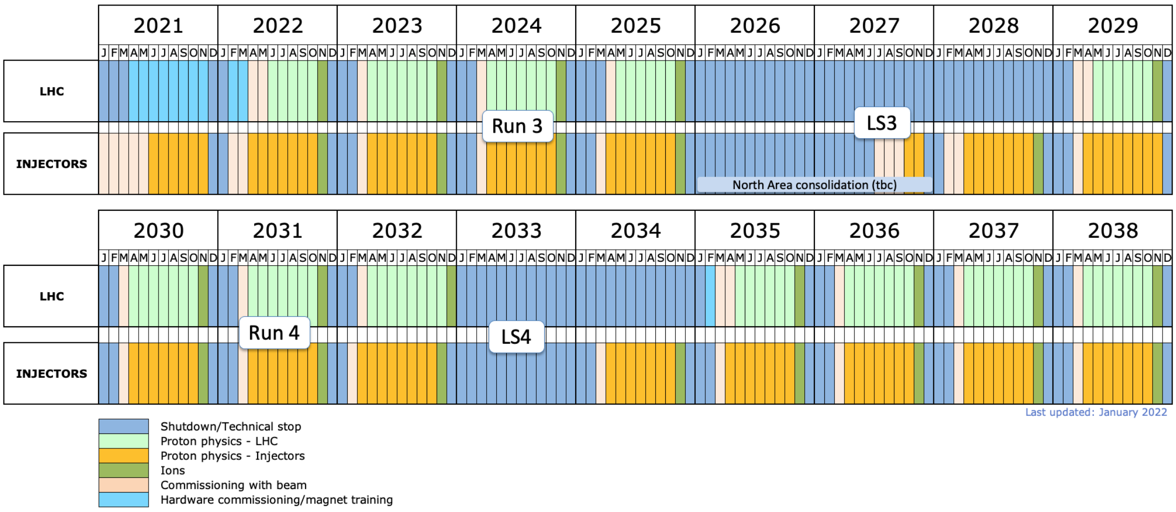

FIGURE 3.1. The outline LHC schedule out to 2038 with the LS shutdowns [98].

were injected into the LEP ring already accelerated by the Super Proton Synchrotron (SPS), the older accelerator and collider used previously as an independent accelerator of protons (later protons and antiprotons, S$p\overline{p}$S) between 1981 and 1984. The last year of the LEP operation was in 2000, with a collision energy of 209 GeV.

The CERN council approved the construction of the Large Hadron Collider in 1994, and the design report of the LHC was published in 1995, the finalised technical design report in 2003 [97]. The ATLAS, CMS and ALICE experiments were approved in 1997, and the LHCb experiment a year later.

The LHC operation was launched on September 10$^{\text{th}}$ 2008. A week later, an unpleasant accident happened: a fault forcing a shutdown occurred in the magnet electrical bus connection, and the helium from the cooling system was explosively released. After several fixes, the LHC was restarted in November 2009. A month later, the new world record with the highest collision energy of 2.36 TeV was set. This period from the start of LHC to December 2012 is often denoted as LHC Run1.

The continuous data taking with the beam energy of 3.5 TeV (7 TeV centre-of-mass energy) started in 2011, and the energy was increased to 8 TeV in 2012. A period between January 2013 and March 2015 was reserved for the Long Shutdown 1 (LS1), followed by the Run2, lasting between 2015 and 2018. The Run2 operation used protons with a beam energy of 6.5 TeV. The Long Shutdown 2 (LS2) recently ended, and the Run3 is ongoing these days with the record centre-of-mass energy of 13.6 TeV, and its expected stop is in December 2025. The overview of the LHC schedule between the years 2021 ad

2038 is in Figure 3.1.

The primary function of the LHC are the proton–proton ($p-p$) beams collisions, but it can also collide ions. Each year, the nuclei of lead are collided at the energy of 5.02 TeV during the last month of operation. Additionally, the xenon nuclei were collided at the energy of 5.44 TeV in 2017.

3.2 Accelerator Parameters

Each high-energy collider uses key parameters that describe the quality of the beam. The most crucial ones are beam energy, luminosity, emittance, pile-up, and beam crossing angle.

3.2.1 Instantaneous and Integrated Luminosity

The Large Hadron Collider was built to create new particles in $p-p$ collisions. For LHC to be efficient, the collision rate must be high. The LHC collides protons with a frequency of 40 MHz (every 25 ns). Additionally, the rate of created particles needs to be large. This rate can be expressed as

$$R_{\text{event}} = \sigma_{\text{event}} \int \mathscr{L}(t)\mathrm{d}t, \tag{3.1}$$

where σ_{event} is the cross-section for the event under the study, and L is the instantaneous luminosity with dimension $m^{-2}s^{-1}$. With a given frequency of collision f_{col} and the number of particles in collided bunches N_1 and N_2, the instantaneous luminosity for

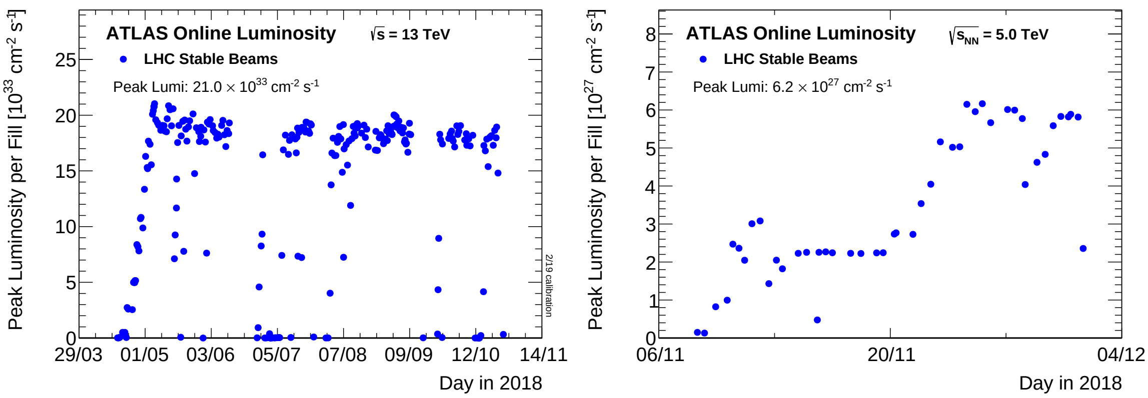

FIGURE 3.2. Peak luminosity for proton–proton (left) and lead-lead (right) collisions recorded during 2018 by ATLAS [99].

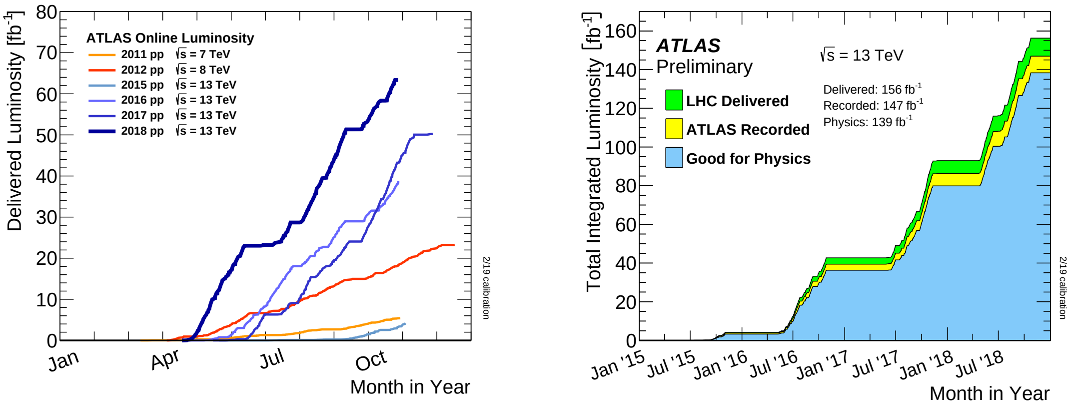

FIGURE 3.3. Integrated luminosity recorded by ATLAS per each year of LHC operation and during the Run2 period [99].

gaussian-shaped beams at the interaction point is [100]

$$\mathscr{L} = f_{\mathrm{col}} N_b \frac{N_1 N_2}{4\pi \Sigma_x \Sigma_y}. \tag{3.2}$$

The parameters Σ_x and Σ_y are beam profile parameters, describing the inverse of the beam overlap in x a y direction. The denominator of (3.2) is often expressed by the cross-sectional area of the beams A assuming perfect overlap of the beams. If the beam profiles are considered to have a identical Gaussian transverse profile, the parameters Σ_x and Σ_y correspond to the standard deviation σ_x and σ_y.

The instantaneous luminosity can be expressed in terms of beam emittance ε and amplitude functions $\beta(s)$ [100]:

$$\mathscr{L} = f_{\mathrm{col}} N_b \frac{N_1 N_2 \gamma}{4\pi \sqrt{\varepsilon_x \beta_x^* \varepsilon_y \beta_y^*}} F, \tag{3.3}$$

where γ is the relativistic factor, ε_x and ε_y are transversal beam emittance constants, and β_x^* and β_y^* are the values amplitude modulation functions $\beta(s)$ near the interaction point (the beams are expected to be the most squeezed here). The parameter F is the geometric luminosity reduction due to the crossing angle θ_c at the interaction point [101]:

$$F = \left(1 + \left(\frac{\theta_c \sigma_z}{2\sigma_x}\right)^2\right)^{-1/2}, \tag{3.4}$$

the parameter σ_z is the length of the bunch.

The instantaneous luminosity is time-dependent, and the integrated luminosity expressing the amount of collected data is used:

$$L = \int \mathscr{L}(t)\mathrm{d}t. \tag{3.5}$$

Both instantaneous and integrated luminosities recorded by ATLAS are in Figures 3.2 and 3.3.

3.2.2 Amplitude function $\beta(s)$

The Large Hadron Collider is a circular collider that needs magnets to bend, focus and squeeze the beams to have fruitful collisions. Both bending and focusing can be described by Hill's equation [46, 102]:

$$\begin{aligned} \frac{\mathrm{d}^2x}{\mathrm{d}s^2} + K_x x = 0, \quad & K_x = \frac{q}{p}\frac{\partial B_y}{\partial x} + \frac{1}{\rho^2} \\ \frac{\mathrm{d}^2y}{\mathrm{d}s^2} + K_y y = 0, \quad & K_y = -\frac{q}{p}\frac{\partial B_y}{\partial x} \\ \frac{\mathrm{d}z}{\mathrm{d}s} + \frac{x}{\rho} = 0, \quad & \end{aligned} \tag{3.6}$$

where $B_y(s)$ is the magnetic field along the path s in the y direction (only), q and p are the charge and momentum of the accelerated particles, respectively. $\rho = p/(qB_y)$ is the radius of the curvature. The special linear case solution of (3.6) is [102, 103]

$$x(s) = \sqrt{\varepsilon}\sqrt{\beta(s)}\cos\left(\psi(s)+\phi\right). \tag{3.7}$$

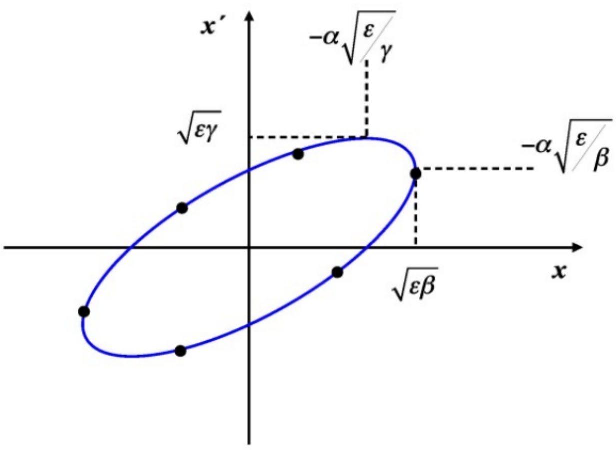

FIGURE 3.4. The phase space ellipse describing the transverse displacement of the beam in the x direction and its derivative x' as a solution (3.7) [103].

The amplitude modulation function $\beta(s)$ varies with distance s to the minimum given by

$$\beta(s) = \beta^* \left(1 + \left(\frac{s}{\beta^*}\right)^2\right). \tag{3.8}$$

β^* is a value of the beta function at the Interaction Point (IP), where the beam optics are designed to produce the narrowest possible focus. The value of β^* for the LHC varies between 0.2-1 m.

3.2.3 Emittance ε

The emittance is defined as the amplitude or spread of the transverse beam size in the momentum-position phase space (see Figure 3.4). Unlike the physical dimensions, the emittance is invariant concerning the location in an accelerator. In phase space Figure 3.4, beam dimension is given as the projection of the phase space ellipse onto the x axis. The emittance is kept as small as possible to increase the probability of interactions (luminosity). The usual values at the LHC are $\varepsilon \approx 2-5\ \mu m$.

3.2.4 Crossing angle

The crossing angle θ_c is the angle between the interacting bunches. To reduce the value of β^* and increase the luminosity, the bunches are rotated before entering the interaction point. The collision with rotated bunches is called the crab crossing [104]. The schematic draw of the crab crossing can be seen in Figure 3.5.

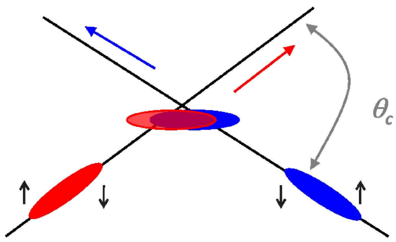

FIGURE 3.5. Schematic view of crab crossing of beams [104].

3.2.5 Pile-up

The Large Hadron Collider collides bunches of protons (or heavy ions). With the desire to have luminosity as large as possible, the beam size is tiny, resulting in many inelastic proton–proton interactions. The number of interactions per bunch collision follows the

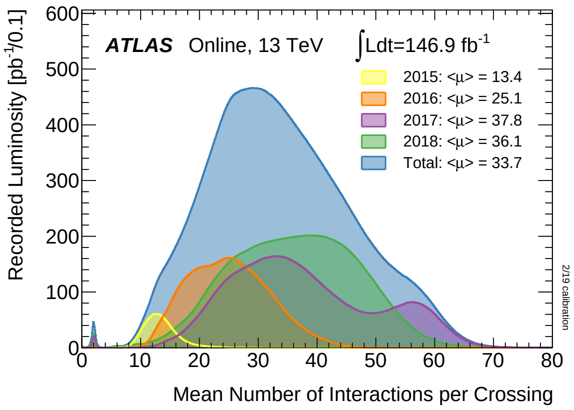

FIGURE 3.6. The mean number of interactions per bunch crossing recorded in Run2 by the ATLAS detector [99].

Poison distribution, and its mean value is referred to as the mean number of interactions per bunch crossing or pile-up. Its value at a given interaction point can be calculated using the delivered luminosity to the interaction point $\mathscr{L}$ and the inelastic cross-section σ_{inel} [106]

$$\langle\mu\rangle = \frac{\mathscr{L}\sigma_{\text{inel}}}{N_b f}. \tag{3.9}$$

Here, N_b is the number of bunches colliding at the frequency f. The pile-up distribution for Run2 operation period is shown in Figure 3.6.

3.3 LHC Injection Chain

The LHC uses already pre-accelerated bunches from the system of the accelerators. The whole CERN accelerator complex is shown in Figure 3.7.

Firstly, the hydrogen atoms are stripped of their electrons by applying an electric field. The protons (from hydrogen) continue to the linear accelerator Linac4, where they are formed into bunches and accelerated to 50 MeV. The bunches are sent to Proton Synchrotron Booster (PSB). After reaching the energy of 1.4 GeV, the protons enter the Proton Synchrotron (PS). The bunches are accelerated to 26 GeV in PS and transferred to the Super Proton Synchrotron (SPS). The beams get the energy of 450 GeV by SPS before entering two rings of the LHC. The final acceleration is provided by the LHC itself, accelerating the protons to the energy of 3.5 TeV, 4 TeV (Run1), 6.5 TeV (Run2), or 6.8 TeV (Run3).

The lead ions start their journey in Linac3, where they are formed into bunches and get the energy of 4.2 MeV per nucleon. The next step is the Low Energy Ion Ring (LEIR) which accelerates the lead ions to 72 MeV. Then, the bunches are sent to PS (5.9 GeV per nucleon), SPS (177 GeV per nucleon) and LHC. The final energy of lead ions in the LHC ring was 1.38 TeV per nucleon in Run1 and 2,51 TeV per nucleon in Run2. The expected energy per nucleon in Run3 is 2.75 TeV [108].

The LHC rings are filled in steps. Filling the LHC requires 12 cycles of SPS, and one fill to SPS needs 3-4 cycles of PS. The PS and SPS cycling times are 21.60 s and 3.60 s, respectively, yielding the final filling time to LHC of 4 minutes. The acceleration in the LHC ring lasts about 20 minutes. The full description of designed filling schemes for various LHC operation modes can be found in [109].

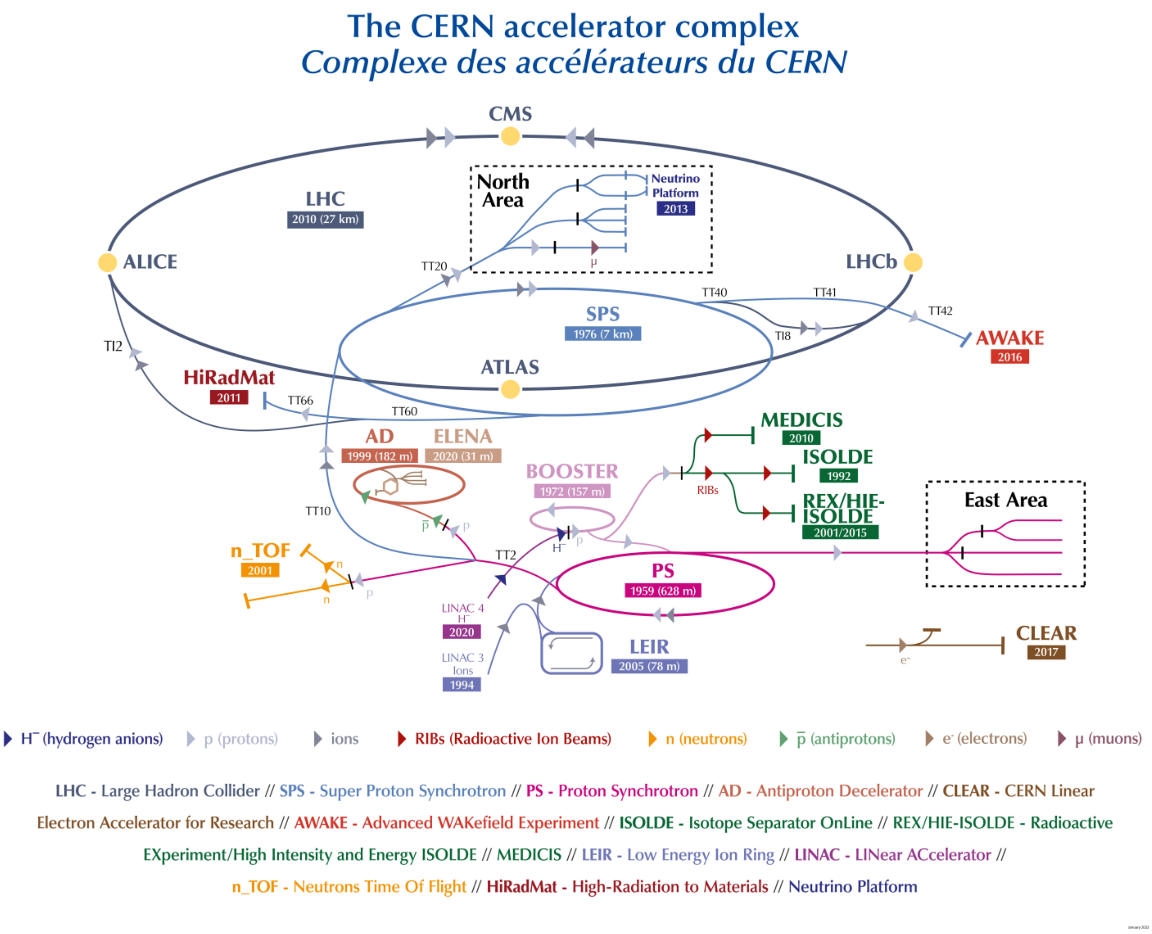

FIGURE 3.7. The CERN accelerator complex [105].

3.4 LHC Layout

A schematic layout of the Large Hadron Collider is shown in Figure 3.8. The LHC has eight arcs and eight straight sections. Each section has an Interaction Point (IP) in the middle. The LHC arcs are made of 23 modules, each having length of 106.9 m. The straight sections in the tunnel are approximately 528 m long. Totally, the LHC consists of 1232 dipole segments. Additionally, over 6000 multipole magnets are used to shape the bunches and remove undesired beam imperfections.

Two interaction points are occupied by the high luminosity detectors: ATLAS (IP 1) and CMS (IP 5). LHCb, the experiment mainly studying the B physics, is placed in IP 8. The detector for heavy ion collisions, ALICE, is located at IP 2. The last two IPs are also areas where beams enter the LHC ring from Super Proton Synchrotron. Four remaining IPs are not occupied by large experiments but serve as beam collimating systems (IP 3 and 7); the acceleration cavities at IP 4, and IP 6 is used for beam dump.

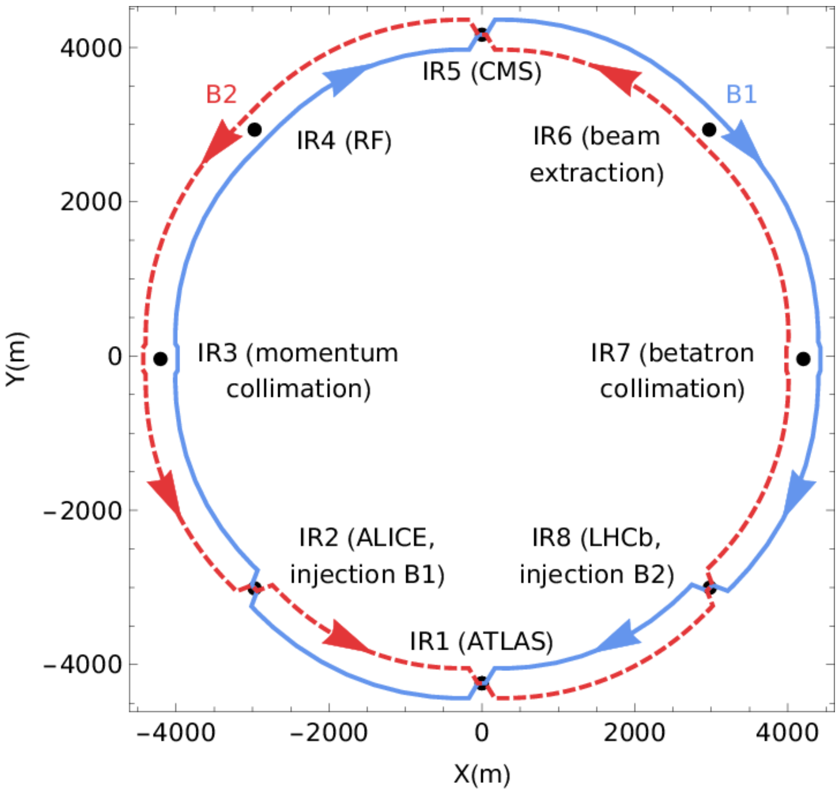

FIGURE 3.8. The LHC ring layout [107].

3.5 Experiments at the LHC

The Large Hadron Collider has four Interaction Points occupied by seven experiments. Each experiment has its collaboration, and the physics decisions are made independently of each other (the decisions concerning the beam setup are made in cooperation of experiments and accelerator experts). There are experiments outside of the LHC ring at CERN, but they are irrelevant in this thesis.

3.5.1 ATLAS

A **T**oroidal **L**HC **A**pparatu**S** is a multi-purpose detector. It is built to study particle physics beyond the Standard Model. ATLAS was built to discover the basic block of matter, and to investigate properties of the Higgs boson or the asymmetry between the behaviour of matter and antimatter. The following chapter provides a detailed description of the ATLAS detector.

3.5.2 CMS

The **C**ompact **M**uon **S**olenoid was built with a similar purpose as ATLAS. The main goals of this experiment are the same as the goals of ATLAS, but CMS and ATLAS use different technical solutions and designs for their calorimeter detectors and magnet system. The calorimeters and muon chambers are built around a huge solenoid magnet generating the field of 4 T. The tracker and the calorimeter are inside the magnet (ATLAS has calorimeters outside the solenoid magnet). The outermost system of CMS is composed of muon detectors.

3.5.3 ALICE

A **L**arge **I**on **C**ollider **E**xperiment (ALICE) was built to study heavy ion collisions. The quark-gluon plasma, which probably was formed a few milliseconds after Big Bang, is created in these collisions for a short time. ALICE aims to study its properties alongside the quark deconfinement, quark-gluon plasma expansion and the final rehadronisation.

3.5.4 LHCb

Large **H**adron **C**ollider **b**eauty (LHCb has different scheme from the other large Large Hadron Collider experiments. It is a single-arm spectrometer designed to study the difference between matter and antimatter. LHCb provides precise measurements of *CP* violation, mainly in the rare decays of beauty and charm mesons. The spectrometer is built to study the created particles in the forward direction (alongside the beam pipe), in which the created mesons are expected to be more probably observed.

3.5.5 TOTEM

TOTal **E**lastic and diffractive cross section **M**easurement is experiment sharing the interaction point with CMS. It focuses on measuring the total cross-section, elastic scattering and diffraction dissociation. It consists of eight Roman Pots (inserted directly into the beam vacuum pipe) located in the cylindrical vessels and two particle telescopes (charged particle trackers measuring the created particles in inelastic scattering).

3.5.6 LHCf

Large **H**adron **C**ollider **f**orward is a detector system studying the created particles travelling in the forward directions. The cosmic ray interactions and decays are simulated by the Large Hadron Collider particles. Similar decay cascade to the cosmic rays is created in the LHC environment. This experiment shares the Interaction Point with the ATLAS experiment.

3.5.7 MoEDAL

the **Mo**nopole and **E**xotics **D**etector **A**t the **L**HC is a system located near the LHCb experiment. I was designed for direct search for the magnetic monopole (state/particle having either a "north" or a "south" magnetic charge instead of having both of the charges) and for the Stable Massive Particles (SMPs), predicted by theories beyond the Standard Model.

3.6 Current LHC Performance

The Large Hadron Collider was designed to collide beams at the energy of $\sqrt{s} = 14$ TeV, peak luminosity of $\mathscr{L} = 1 \times 10^{34}$ cm^{-2}s^{-1} and frequency of 40 MHz. However, the operation condition in Run1 and Run2 were not fulfilled, so different energies and frequencies were used.

In Run1, the accelerating magnets were not sufficiently trained, so collision energy of $\sqrt{s} = 7$ TeV and $\sqrt{s} = 8$ TeV in 2011 and 2012 were reached, respectively. Additionally, the proton beams were collided at 20 MHz. Long Shutdown 1 in 2013 and 2014 provided space for improvements. The progress of magnet training was not optimal, so designed energy could not still be reached, but it was increased up to $\sqrt{s} = 13$ TeV. The collision rate was also improved to the nominal value of rate 40 MHz. However, the operation conditions were changing during the Run2, leading to several on-flight changes. In 2016, Super Proton Synchrotron suffered from a vacuum leak. This limited the number of injected bunches to LHC to 144 bunches per injection. The filling scheme has been changed to optimize the functionality of LHC. A new Bunch Compression Merging and Splitting (BCMS) [110] was developed. It keeps the same beam intensity, but provides improvement by reducing the beam emittance. This scheme was used in the rest of Run2 except for a short period in 2017 when the higher beam-loss probability was observed due to the exchange of one of the accelerating magnets. When fixing the higher beam losses, the filling scheme 8b4e (8 filled bunches and four empty bunches period) was used. The peak luminosity in 2017 and 2018 exceed the nominal value by factor 2.

The beam parameters for all years of LHC operation can be found in Table 3.1. Comparing the current values to the designed ones, the LHC largely reached the designed values, but there is still a place for improvements.

	E_b [TeV]	t_b [ns]	N_b -	N_p [10^{11}]	$\mathscr{L}$ [cm^{-2}s^{-1}]	$<\mu>$ -	ε [μm]	β^* [m]	θ_c [rad]
Des.	7	25	2808	1.15	1.0×10^{34}	20	3.75	0.55	285
2011	3.5	50	1380	1.45	0.37×10^{34}	17	2.50	1.00	–
2012	4	50	1380	1.65	0.75×10^{34}	35	2.50	0.60	290
2015	6.5	25	2244	1.10	0.5×10^{34}	13	3.50	0.80	290
2016	6.5	25	2220	1.10	1.4×10^{34}	25	2.20	0.40	370–280
2017	6.5	25	2556	1.15	2.1×10^{34}	38	2.20	0.3–0.4	300–240
2018	6.5	25	2556	1.15	2.1×10^{34}	37	1.90	0.25–0.3	320–260

TABLE 3.1. LHC designed (Des.) and real performance in Run1 and Run2 with the beam energy E_b, number of bunches N_b with time spacing t_b. Each bunch contains N_p number of protons. The peak luminosity $\mathscr{L}$ and average pile-up $<\mu>$ were reached in the collision with the beam setup of emittance ε, the optimal beta function at the start of collision β^* and crossing angle θ_c [110–112].

	E_b [TeV]	t_b [ns]	N_b -	N_p [10^{11}]	$\mathscr{L}$ [$\mathrm{cm^{-2}s^{-1}}$]	ε [μm]	β^* [m]	θ_c [rad]
Nominal	7	25	2808	1.15	1×10^{34}	3.75	0.55	290
2022	6.8	25	2748	1.4	2×10^{34}	1.8–2.5	0.6	320
2023	6.8	25	2748	1.8	2×10^{34}	1.8–2.5	0.6–1.2	320
2024	6.8	25	2496	1.8	2×10^{34}	1.8–2.5	0.6–1.2	320

TABLE 3.2. Expected LHC performance in Run3 with the beam energy E_b, number of bunches N_b with time spacing t_b. Each bunch contains N_p number of protons. The expected peak luminosity $\mathscr{L}$ was reached in the collision with the beam setup of emittance ε, the optimal beta function β^* and crossing angle θ_c at the start of collisions [113].

3.7 Presence and Future of LHC

Currently (October 2022), the Run3 is ongoing after the Long Shutdown 2 in 2019-2021. The collision energy was increased to $\sqrt{s} = 13.6$ TeV, and an almost nominal value is achieved. Many systems upgraded their trigger system (ALICE, LHCb, ATLAS) and exchanged detector subsystems (e. g. Small Wheels for ATLAS). The expected beam parameters for Run3 are illustrated in Table 3.2. The expected luminosity recorded during Run3 is approximately 200 fb^{-1} [113].

Quadrupoles are expected to withstand a maximum of $400-700$ fb^{-1}. This can be reached at the end of Run3. So next Long Shutdown (LS3, see Figure 3.1) will be used to exchange these magnets. Moreover, the cooling power of the magnet will be upgraded. This will remove the limitation of peak luminosity. The designed peak luminosity in

	E_b [TeV]	t_b [ns]	N_b -	N_p [10^{11}]	$\mathscr{L}$ [$\mathrm{cm^{-2}s^{-1}}$]	ε [μm]	β^* [m]	θ_c [rad]
Nominal	7	25	2808	1.15	1×10^{34}	3.75	0.55	290
HL-LHC (standard)	7	25	2760	2.20	5×10^{34}	2.50	0.15–1.2	500
HL-LHC (BCMS)	7	25	2744	2.20	5×10^{34}	2.50	0.15–1.2	500

TABLE 3.3. Expected LHC performance in HL-LHC for standard and Bunch Compression Merging and Splitting (BCMS) schemes with the beam energy E_b, number of bunches N_b with time spacing t_b. Each bunch contains N_p number of protons. The expected peak luminosity $\mathscr{L}$ was reached in the collision with the beam setup of emittance ε, the optimal beta function β^* and crossing angle θ_c at the start of collisions [114].

Run4 is $\mathscr{L} = 5 \times 10^{34}$ cm^{-2}s^{-1}. Due to the peak luminosity increase, the LHC Run4 and later are often denoted as HL-LHC (HL-LHC). The standard expectation of the beam parameters for HL-LHC (and for different bunch injection mechanisms) are presented in Table 3.3. The pile-up is expected to reach a doubled value of Run3 during the HL-LHC operation.

CHAPTER 4

The ATLAS Experiment

The ATLAS detector [115] is the multi-purpose hybrid detector, the largest of the LHC detector systems. It is located at the Interaction Point 1. Its physics program is broad, covering Higgs discovery pursuit and measurement of its properties, vector boson scattering, decays of B mesons, tests of the Standard Model, searches of hypothetical SUSY or Dark Matter particles, testing theories beyond the SM and many others.

The ATLAS detector was designed with radiation-sensitive sensors with quick readout (particles are collided every 25 ns at IP1). High granularity of subsystems is necessary due to many interactions per bunch crossing. To detect as many created particles as possible, large geometrical acceptance of the whole system is needed.

The ATLAS collaboration consists of over 5500 members and almost 3000 scientific authors, affiliated with 181 institutes from 42 countries. The main executive power is held by ATLAS management (Spokesperson, Deputy Spokesperson, Technical Coordinator and Resource Coordinator), the Executive Board (directing communication between the ATLAS management and the ATLAS Systems) and the ATLAS Systems (Inner Detector, Magnets, Liquid Argon Calorimeter, Tile Calorimeter, Muon Spectrometer, Shielding, Trigger). The ATLAS Spokesperson is the main responsible for all of the ATLAS Execution and future collaboration goals. Last but not least, conveners play an important role in physics analyses. They are elected from relevant institutions for two years.

One of the ATLAS goals was achieved in 2012 by the Higgs particle discovery [41],

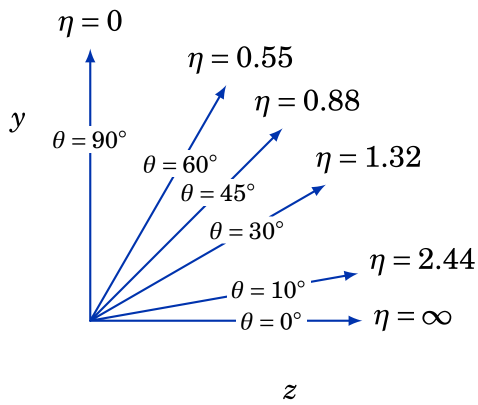

FIGURE 4.1. Definition of pseudorapidity η in term of the polar angle θ in the cartesian system with y and z axes.

opening space for new analyses studying its properties and interactions with other particles. The rest of the physics goals are still under investigation - by precise measurements in the electro-weak sector, studying CP violation not only in B meson decay and searches for new particles. ATLAS still has large space for confirming or rejecting theoretical predictions and setting the limits in hunting for Supersymmetry or Dark Matter particles.

4.1 ATLAS Coordinate System

The ATLAS detector uses a common coordinate system used by many large particle physics detectors. The cartesian system is used for demonstration purposes, but the created tracks in the ATLAS volume are described in the spherical system. This system uses two angles, the polar angle θ defined as the angle from the beam axis (positive z) and the azimuthal angle ϕ defined around the beam axis. Additionally, the position coordinate z is used, determining the distance from the centre of the ATLAS detector) alongside the beam pipe.

To achieve the Lorentz invariant (important for the particle description), pseudorapidity is used instead of the polar angle θ, given by the relation

$$\eta = -\ln \tan\left(\frac{\theta}{2}\right). \tag{4.1}$$

The graphical representation of the relation (4.1) is shown in Figure 4.1. Pseudorapidity

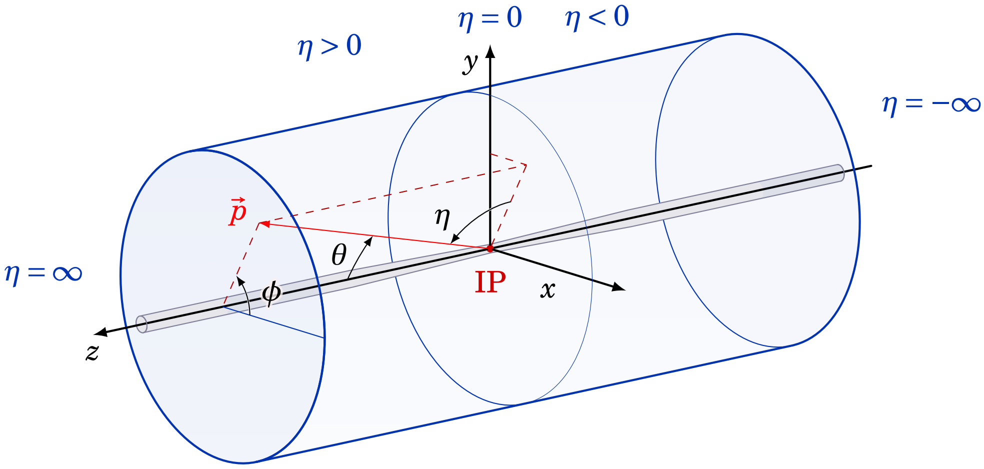

FIGURE 4.2. ATLAS coordinate system describing the particle with momentum $\vec{p}$ by the polar angle θ, azimuthal angle ϕ, pseudorapidity η and cartesian position along the z axis. x and y axes from the cartesian coordinate system are also visible to understand the angles' definitions better. The centre of ATLAS detector is defined by the interaction point IP.

can also be expressed in terms of the particle momenta components as

$$\eta = \frac{1}{2}\ln\left(\frac{|\vec{p}| + p_z}{|\vec{p}| - p_z}\right), \tag{4.2}$$

where p_z is the momentum component in the z direction. The pseudorapidity definition in equation (4.2) is similar to the rapidity definition

$$y = \frac{1}{2}\ln\left(\frac{E + p_z}{E - p_z}\right). \tag{4.3}$$

However, the simple angle description is often easier to obtain (pseudorapidity depends only on a polar angle, not energy E), favouring the pseudorapidity instead of rapidity, especially for massive relativistic particles. Furthermore, the rapidity and pseudorapidity are identical for the massless particles. The graphical depiction of the ATLAS coordinate system is shown in Figure 4.2.

4.2 General Layout

The ATLAS detector is placed in the UX15 cavern located at the CERN Meyrin site in Switzerland, surrounding the Interaction Point 1. The cavern is 92 m below the surface, providing sufficient radiation shielding. ATLAS shape is a cylinder with a length of 44 m

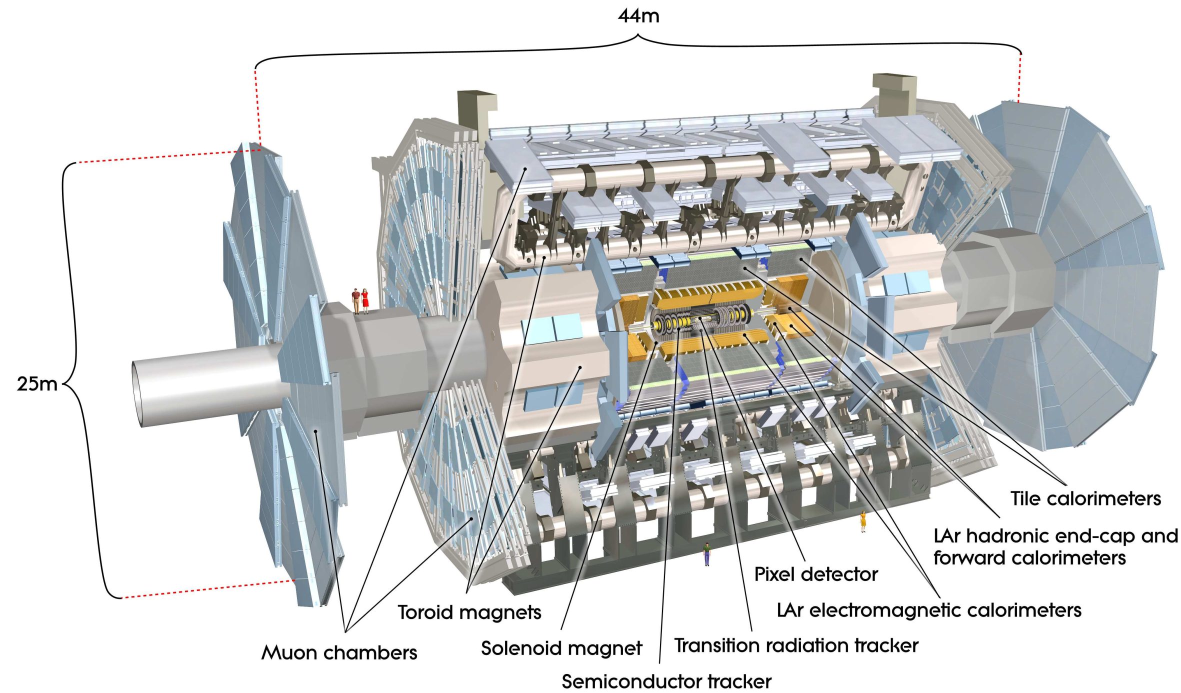

FIGURE 4.3. The ATLAS detector layout with its subsystems displayed [115].

and a diameter of 25 m. The weight of this complex system is estimated to be around 7000 tonnes.

ATLAS consists of several detecting subsystems with a different pseudorapidity coverage (the largest coverage is $|\eta| < 4.9$) and magnets structured in layers, see Figure 4.3. The innermost system is the Inner Detector (ID), responsible for the precise measurement of trajectories and momenta of charged particles. The ability to measure these variables is secured by the barrel magnet surrounding the ID. The next layers are Electromagnetic Calorimeter and Hadronic Calorimeter (ECAL and HCAL), providing a measurement of the energy of passing particles that are created in the collisions. By this measurement, most of the particles are absorbed, only neutrinos and muons pass both calorimeters due to the low interaction cross-section. Neutrinos are generally hard to detect, but the momentum of muons can be measured by the outermost ATLAS detector system: Muon Spectrometer (MS). The MS and Calorimeters are also used to trigger interesting events. Each subsystem is described in the sections below.

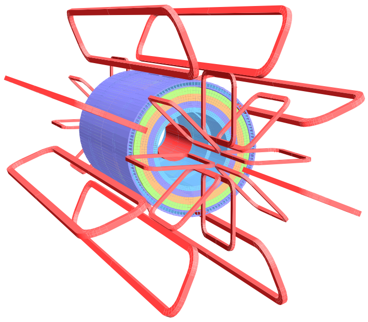

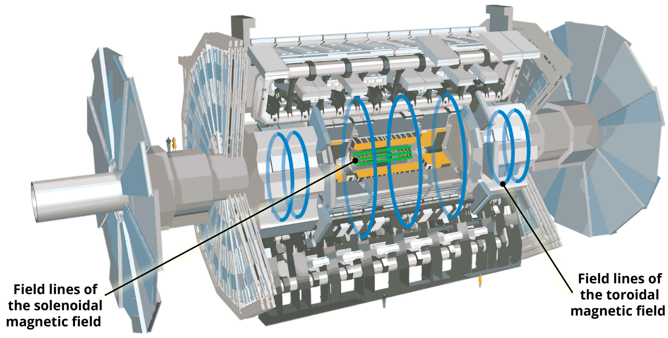

FIGURE 4.4. Left: Geometry of the ATLAS magnet system. Mutual position with barrel ECAL shown for understanding the location of the magnets in the ATLAS volume [115]. Right: Magnetic field line created by the solenoid and endcap toroid magnets shown in the ATLAS detector [116].

4.3 Magnet System

The ATLAS magnet system provides the opportunity to measure the momentum of charged particles by bending their trajectories. The unique magnet system comprises four superconducting magnets: a central solenoid, a barrel toroid and two end-cap toroids. The magnets are made of the coil based on winding a pure Al-stabilised NbTi (solenoid) and Nb/Ti/Cu (toroids) superconductors [115]. To secure the superconductivity, all magnets are cooled to the temperature of 4.6 K. The general magnet layout and the magnetic field lines created by the solenoid and toroids are shown in Figure 4.4.

4.3.1 Central Solenoid

The central solenoid, placed between the Inner Detector and Electromagnetic Calorimeter, provides a field of 2 T inside the ID. To lower the material budget, the solenoid and ECAL share the common cryostat. The solenoid is 5.8 m long with inner and outer diameter of 2.46 m and 2.56 m, respectively. The magnet weighs 5400 kg and can store the magnetic energy of 40 MJ. The solenoid can be charged to the nominal current of 7.73 kA in 30 minutes [115].

4.3.2 Barrel and End-cap Toroids

The barrel and end-cap toroids produce a magnetic field of approximately 4 T for the track measurement by the Muon Spectrometer. The barrel toroid system consists of eight coils with a size of 25.3 m in length and 9.4/20.1 m in inner/outer diameter. The current ramp to the nominal value of 20.5 kA takes 2 hours. The stored energy at the peak current is 1.1 GJ.

The end-cap toroids are also composed of eight coils with a similar layout of coils, providing a similar magnetic field for MS in end-caps, just the dimensions of the coils are smaller. The end-cap toroid coils are rotated with respect to the barrel toroid coils by 22.5°.

4.4 Inner Detector

Thousands of particles are created every 25 ns in a typical proton–proton bunch collision. To be able to detect the charged particle tracks and measure their momenta, high-granularity sensors are required. The Inner Detector (ID) covers the pseudorapidites of $|\eta| < 2.5$. The solution to the precise tracking and momentum and vertex resolution required for physics analysis is using the segmented semiconductor detectors in combination with the straw tubes of the Transition Radiation Tracker. The layout of the ID is shown in Figure 4.5.

In total, the ID is 6.2 m long and its radius is 2.1 m. It can be separated into two parts - the barrel section with a length of 3.5 m and the end-cap section covering the large pseudorapidity regions. The sensors in each sector have different orientations of sensors to satisfy requirements for the perfect transverse momentum resolution, see Figure 4.6. The barrel sensors are arranged in layers parallel to the beam pipe, while the end-cap sensors are formed in the discs perpendicular to the beam pipe.

The ID uses 4 four different sensors to reach the aim of the high-precision. The Pixel Detector and Insertable B-Layer are silicon detectors measuring the momentum and providing tracking. Additionally, the Pixel Detector improves the vertex position resolution, and Insertable B-Layer provides additional spacetime coordinate for vertexing in the reconstruction of B mesons and $\tau^{\pm}$ leptons. The Semiconductor Tracker formed by silicon strip sensors contributes to precise momenta measurements. The outermost TRT is comprised of straw tubes supporting the silicon sensors in tracking. Further, the Transition Radiation Tracker introduces a pattern of electron identification complementary to the Electromagnetic Calorimeter.

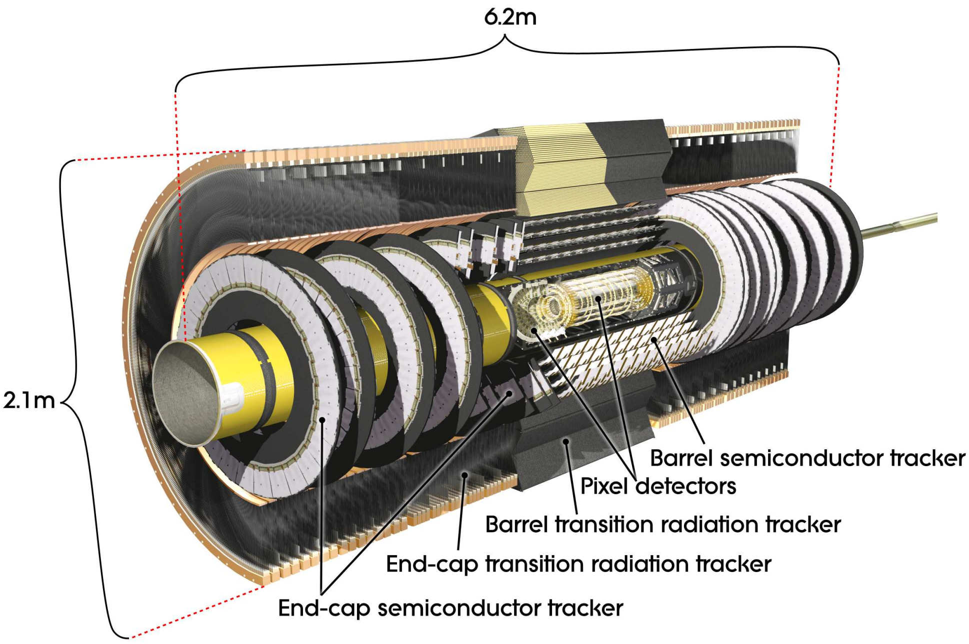

FIGURE 4.5. Schematic layout of the ATLAS Inner Detector [115].

4.4.1 Pixel Detector

The Pixel Detector (PIX) is a high-granularity semiconductor tracker installed closest to the beam pipe [115]. It consists of sensor elements with an identical structure for all detector regions. Detection elements, called pixels, are produced by the planar silicon sensor technology - the sensor is fabricated on the n-type wafer. The n^+ layer for readout is implanted to one side of the wafer, the opposite side has a layer of p^+ implants. Each sensor is connected to the front-end readout electronics using the bump bonding technology. Most of the pixels have an area of 50×400 μm^2 and thickness 250 μm, the rest of the pixels with an area 50×600 μm cover the gaps between front-end readout chips [115]. The PIX has 1744 pixel modules, each containing group of over 47000 pixels). The PIX has 80.4 million readout channels in total, each providing the intrinsic position resolution of 10 μm in the $R-\phi$ plane and 115 μm in the z plane [115].

The pixel modules are organised into three layers in the barrel region and overlap each other. They are inclined with an azimuthal angle of 20° to each other to secure full-angle coverage. The modules are mounted on the supporting structure, the staves. Each of the end-cap discs is formed by eight sectors. Figure 4.6 depicts the layers and discs composition.

The sensors produce heat during the operation and require cooling. Cooling is also

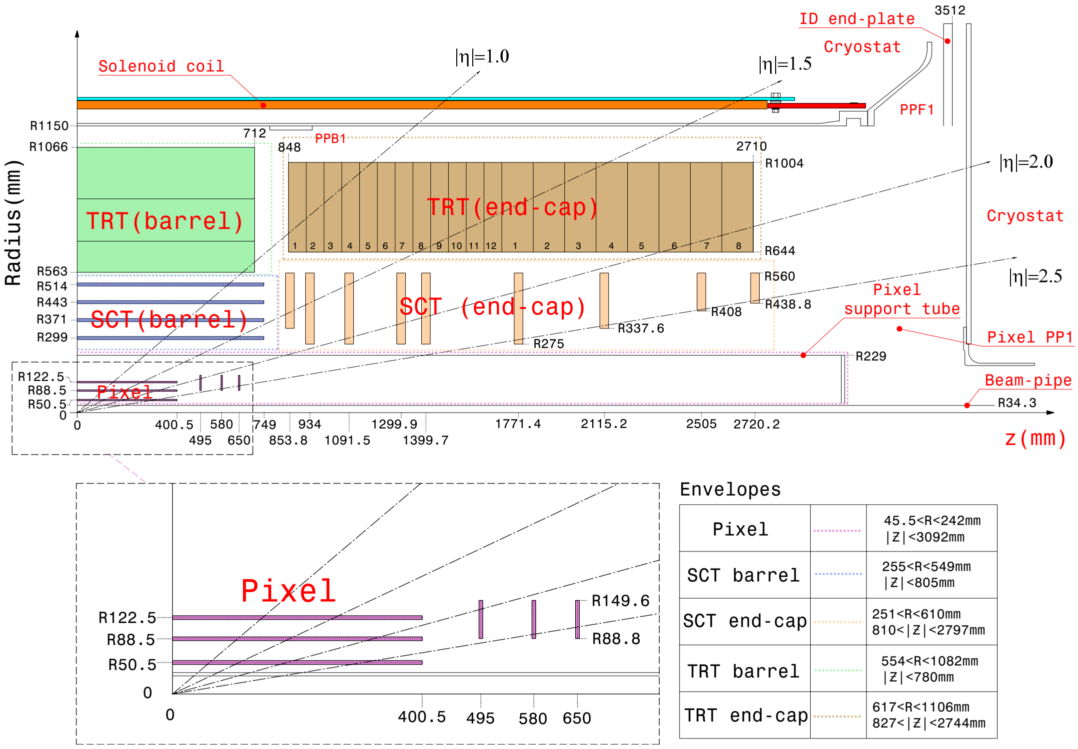

FIGURE 4.6. Plan view of a quarter-section of the ATLAS Inner Detector showing each major detector element: Pixel Detector, Semiconductor Tracker, Transition Radiation Tracker. The PP1, PPB1 and PPF1 denote the ID support services [115].

required to reduce thermal noise and leakage current, especially after irradiation. The PIX is operated at the temperatures between −5 °C and −10 °C, ensured by the non-flammable and electrically non-conductive C_3F_8 coolant [115]. Additionally, the PIX is placed into the dry nitrogen environment with a temperature range −7–0 °C to avoid condensation in the cold surfaces. The dry nitrogen does not provide sensor cooling.

4.4.2 Insertable B-Layer

A new Insertable B-Layer (IBL) was installed during the Long Shutdown 1 and became the innermost layer of the Inner Detector [118], see Figure 4.7. The IBL consists of 14 staves with 20 hybrid pixel detector modules at each stave. Some of the IBL pixel modules are made in a similar way that the PIX modules are, but they are accompanied by the 3D n^+-in-p 3D modules (outermost modules) [119]. The area of each sensor is $50 \times 250\ \mu\text{m}^2$, providing finer granularity. The IBL pixels use new front-end readout electronics with increased radiation hardness. In total, additional 12 million readout channels were included. Due to the lower leakage current and less heat produced, the cooling requirements of the IBL are smaller than that of the Pixel Detector. The CO_2 gas is used as a coolant to maintain the sensor at the temperature of −10 °C [120].

4.4.3 SemiConductor Tracker

The Semiconductor Tracker (SCT) is a set of silicon strip sensors providing precise tracking at larger radii. The principle of particle detection is very similar to the Pixel Detector. The SCT has eight barrel region layers and nine end-cap discs. The overall geometry is presented in Figures 4.6 and 4.7. The strip modules are 6.4 cm long with the distance between strips of 80 μm and the sensor thickness is 285 μm. The SCT contains 15912 single-sided sensors (to reduce the cost). The end-cap sensors are back-to-back glued in pairs. Strips run radially with an angle of 40 mrad between two strips to give the required resolution. The nominal SCT hit position resolution is 17 μm in the lateral plane ($R-\phi$) and 580 μm in the longitudinal plane (z or R). The whole SCT has

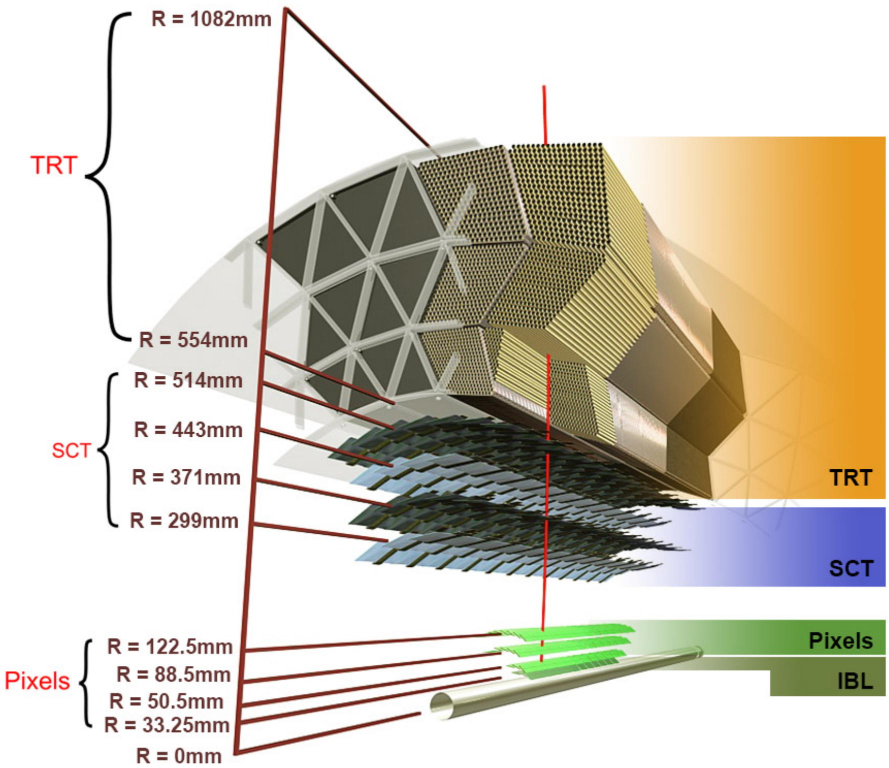

FIGURE 4.7. Schematic view of the ATLAS ID with the Insertable B-Layer (IBL) included [117].

approximately 6.2 million of readout channels.

The SCT share the same dry nitrogen environment to reduce the humidity, and the same coolant as PIX is used to achieve the working point temperatures.

4.4.4 Transition Radiation Tracker

The Transition Radiation Tracker (TRT) is the outer tracker using a different technology than PIX and SCT. It uses the transition radiation that is created by the relativistic charged particles particle traversing the edge of the two materials with different dielectric constants. The ATLAS uses the polyimide drift straw with the wall thickness of 35 μm and tungsten wire plated with 0.5 μm layer of gold operating as an anode in the centre of each straw. The straws are filled by the gas mixture of 70% Xe, 27% CO_2 and 3% O_2 with 10 mbar over-pressure. Each straw is 4 mm in diameter, and the maximum length is 144 cm in the barrel and 37 cm in the end-cap region.

The TRT provides the $|\eta| < 2.0$ coverage with an intrinsic resolution of 130 μm per straw. The barrel TRT is made of 73 layers of straws separated into three layers. Each end-cap side of the TRT contains 160 straw planes, separated into 20 wheels of radially aligned straws. On average, a particle track with transverse momentum $p_{\mathrm{T}} > 0.5$ GeV and $|\eta| < 2.0$ traverse 36 straws. Besides the tracking, the TRT also has a supplementary

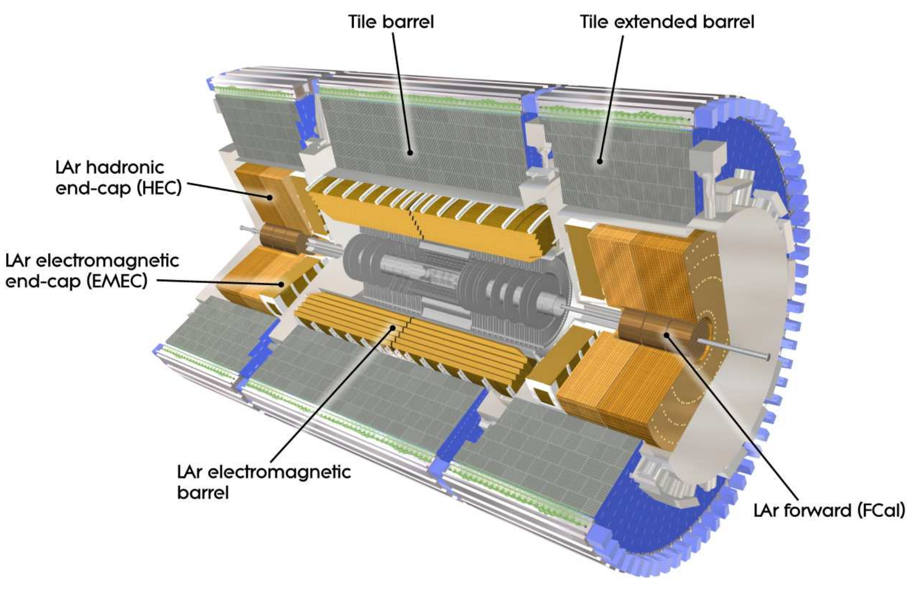

FIGURE 4.8. Schematic drawing of the ATLAS Electromagnetic Calorimeter and Hadronic Calorimeter [115].

role in electron identification. The electrons are known to produce more transition radiation thanks to their low mass compared to charged pions and kaons.

The TRT can operate at room temperature. The temperature is kept stable by cooling by the C_6F_{14}. The same coolant at the same temperature is also used for front-end electronics. The TRT is in the CO_2 envelope to avoid pollution from gas permeation through the straw walls.

4.5 Calorimetry

The ATLAS Calorimeter [115] is a system of sampling detectors that is large enough to absorb the traversing particle and measure its energy via the detection of the secondary particles created by absorbing the particle. In addition, the traversing particle leaves secondary particles along its path in the detector while losing a fraction of its energy. The secondary particles are usually called a *shower*. The properties of the absorbing material creating the shower are expressed with the radiation length X_0, defined as the length of the particle path, where it loses $1/e$ of its energy until the particle's energy is small enough to be fully absorbed.

The general calorimeter is designed to measure the kinematic properties of the relativistic particle. Additionally, it can measure the missing energy (of undetected neutrinos). The momentum directions of the two colliding protons are opposite, and the total momentum and energy of the collision are conserved. The missing energy is extracted by subtracting all measured energy from the collision energy.

The ATLAS Calorimeter envelopes the barrel solenoid and is formed by Electromagnetic Calorimeter (ECAL), which detects the electromagnetic showers and Hadronic Calorimeter (HCAL), which detects the hadronic showers, both shown in Figure 4.8. The ATLAS Calorimeters cover a larger pseudorapidity region than the Inner Detector, reaching the value of $|\eta| < 4.9$.

4.5.1 Electromagnetic Calorimeters

The Electromagnetic Calorimeter [115] is designed to stop the electromagnetically interacting particle while creating the secondary particles: electrons and photons. These particles can have sufficient energy to create other secondary particles. This happens until the shower evolution is stopped. The minimal thickness of the ECAL is $> 22\ X_0$ in the barrel region and $> 24\ X_0$ in the end-caps. The thickness provides good energy resolution that is given by the formula

$$\frac{\sigma_E}{E} = \frac{a}{\sqrt{E}} \oplus \frac{b}{E} \oplus c, \tag{4.4}$$

where $a = 10\% \sqrt{\text{GeV}}$ is the stochastic term, $b = 0.17\%$ GeV is the noise term and $c = 0.2\%$ is the constant term. The $\oplus$ symbol denoted the sum in quadratures.

The detection system used for the ECAL is based on the Liquid Argon (LAr) technology with kapton electrodes for readout and lead used as the absorber (to reduce the material budget to stop energetic particles by increasing the probability of particle interaction with the calorimeter). The ECAL parts are located in three separate cryostats with the temperature of -183 °C [115]. The barrel ECAL covers a region of $|\eta| < 1.475$, and two end-cap calorimeters (EMEC) measure the energy of the particle in the pseudorapidity region of $1.375 < |\eta| < 3.2$. The coverage in the $3.1 < |\eta| < 4.9$ is secured by the Forward Calorimeter, which also serves as the hadronic calorimeter. The second layer of the ECAL cells has the most precise granularity of $\Delta\eta \times \Delta\phi = 0.025 \times 0.025$ [115].

4.5.2 Hadronic Calorimeters

The Hadronic Calorimeter (HCAL) ensures the measurement of the energy of hadrons like pions, kaons, protons and neutrons. To absorb a hadron, a denser environment is required. Then, the shower development is similar to the Electromagnetic Calorimeter. The resolution of HCAL is worse in comparison to the ECAL, the stochastic term of equation (4.4) is $a = 50\% \sqrt{\text{GeV}}$, $b = 3\%$ GeV and $c = 0\%$. The HCAL consists of three separate systems: Tile Calorimeter, LAr hadronic end-cap calorimeter and LAr Forward Calorimeter.

4.5.2.1 Tile Calorimeter

The Tile Calorimeter (TileCal) is placed directly outside the ECAL. In barrel, it covers the region $|\eta| < 1.0$, while two extended barrels the range $0.8 < |\eta| < 1.7$. The scintillating tiles are used as the sampling material, and the absorber is made of steel. The barrel part and extended barrel parts are formed into three layers parallel to the beam line.

The signal from active material (tiles) is led from the area by the wavelength-shifting fibres to the photomultipliers that read out the signal.

4.5.2.2 LAr hadronic end-cap calorimeter

The LAr hadronic end-cap calorimeter (HEC) forms two wheels behind the ECAL, sharing the same cryostat. It covers the rapidity range of $1.5 < |\eta| < 3.2$. Each wheel is built of 32 identical modules and is divided into two in-depth segments. The wheels are placed around the Forward Calorimeters and are surrounded by the extended TileCal; see Figure 4.8.

4.5.2.3 LAr Forward Calorimeter

LAr Forward Calorimeters (FCAL) can measure electromagnetic and hadron showers. With LAr active volume and copper/tungsten absorber plates, it is very close to the beam pipe in pseudorapidity of $3.1 < |\eta| < 4.9$. Compared to the TileCal, it has worse energy resolution (4.4) with the parameters $a = 100\% \sqrt{\text{GeV}}$, $b = 10\%$ GeV and $c = 0\%$.

4.6 Muon Spectrometer

Unlike the other particles, muons have smaller energy losses in materials and typically pass the Inner Detector and Calorimeters without being absorbed. To detect them and measure their momenta, the ATLAS outermost detector system is Muon Spectrometer (MS). It provides muon tracking and event triggering by using four different sensors: Cathode Strip Chambers and Monitored Drift Tubes are designed to provide precise detection of muon trajectory, and Resistive Plate Chambers and Thin Gap Chambers are the detectors with fast readout used by the ATLAS trigger system. Additionally, the field of the barrel and end-cap toroids are used to bend the muon trajectories to increase the momentum resolution. The resolution of the muon with transverse momentum $p_\text{T} = 1$ TeV is $\sigma_{p_\text{T}}/p_\text{T} = 10\% \cdot p_\text{T}$.

The MS has three layers of detectors in the barrel region and three layers orthogonal to the beam axis in the end-caps. The total ATLAS MS view with all subsystems depicted can be seen in Figure 4.9.

4.6.1 Monitored Drift Tubes

The Monitored Drift Tubes (MDT) basic elements are aluminium drift tubes with a diameter 29.97 mm and length in a range $0.9 - 6.2$ mm. The tubes are filled by gas composed of 93% Ar and 7% CO_2 operating at a pressure of 3 bar. The electrons from ionized gas (produced by traversing muons) are collected by the tungsten-rhenium wire

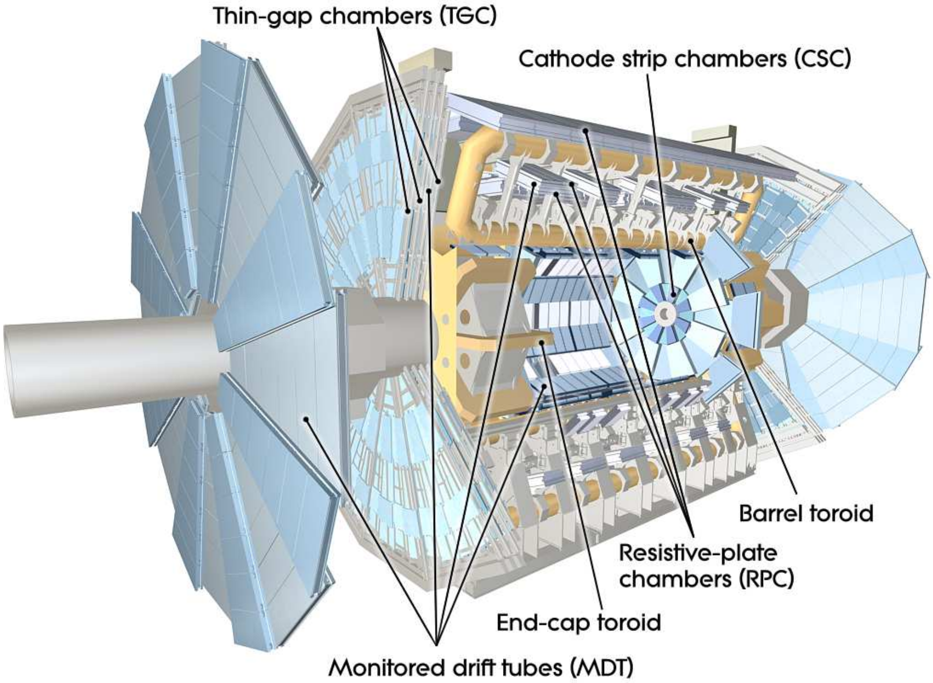

FIGURE 4.9. Schematic drawing of the ATLAS Muon Spectrometer [115].

at the centre of each tube. The wires are connected to the voltage of 3080 V to create a high potential for electrons to drift towards the central wire.

The MDT tubes provide muon precision track measurement within mostly the whole Muon Spectrometer volume ($|\eta| < 2.7$). The layers of MDT modules are used in the barrel ($|\eta| < 1.4$), and three wheels of MDT modules are located in each end-cap ($1.4 < |\eta| < 2.7$).

4.6.2 Cathode Strip Chambers

The Monitored Drift Tubes operate at a limited rate 150 Hz/cm^2 in the region of $|\eta| > 2$ due to the thermalized neutrons coming from the Calorimeters. The Cathode Strip Chambers (CSC) provides supplementary muon track measurement in this region. The modules are made of the multi-wire proportional chambers with strip readout. The chambers are filled by 80% Ar/20% CO_2 gas. The whole system form two discs with eight chambers each.

4.6.3 Resistive Plate Chambers

The trigger system in the barrel is secured by the Resistive Plate Chambers (RPC), covering the pseudorapidities of $|\eta| < 1.05$. The barrel middle layer of the Monitored Drift Tubes is enveloped by two layers of RPC. The third RPC is placed next to the outermost MDT layer. The geometry overview can be seen in Figure 4.10.

The RPC is made of two parallel phenolic-melamine plastic laminate plates at the distance of 2 mm. One of the plates is settled by metallic strips that serve as a readout of created electrons. Due to the electric field of 4.9 kV/mm, the traversing muon creates an avalanche of electrons in the filling gas mixture of $C_2H_2F_4$ (94.7%), Iso-C_4H_{10} (5%) and SF_6 (0.3%).

4.6.4 Thin Gap Chambers

The Thin Gap Chambers (TGC) is the second system used for event triggering, and it covers the end-caps ($1.05 < |\eta| < 2.4$). The TGC also provides muon precise azimuthal angle measurement in the pseudorapidity region of $1.05 < |\eta| < 2.7$. The TGC and

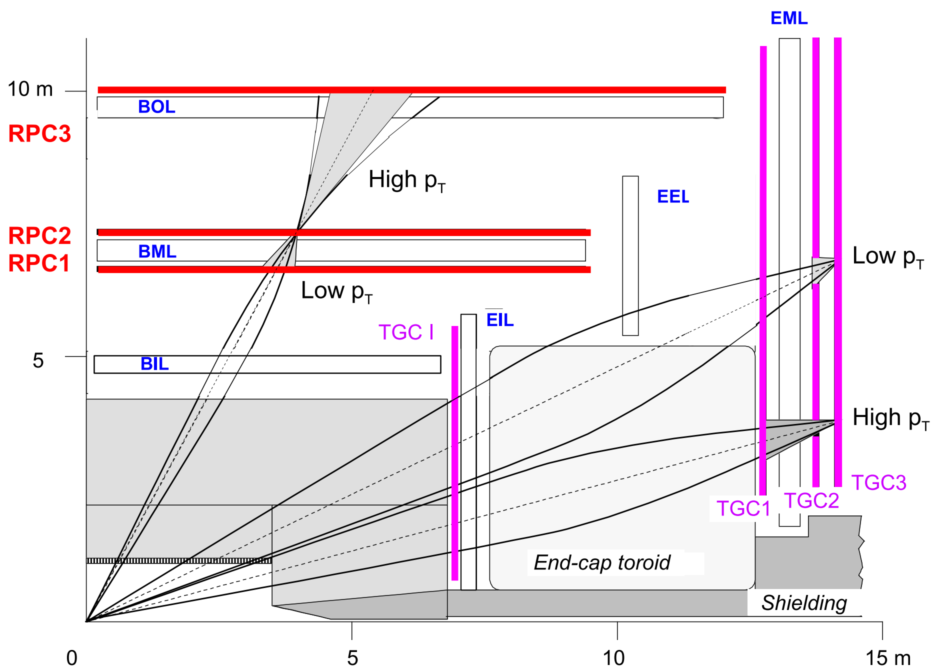

FIGURE 4.10. Schematic of ATLAS muon trigger system [115]. The Resistive Plate Chambers neighbour the Monitored Drift Tubes (denoted as BIM, BML, BOL) in the barrel and the Thin Gap Chambers layers are in front and behind the second MDT wheel.

Monitored Drift Tubes mutual position is shown in Figure 4.10. They do not touch each other as in the case of Resistive Plate Chambers, the TGC has its own support system or uses a support system of the barrel toroid coils.

The TGC is made of multi-wire proportional chambers with a wire-to-cathode distance of 1.4 mm. The cells are filled with a mixture of 55% CO_2 and 45% n-C_5H_{12} (n-pentane).

4.7 Forward Detectors

The large pseudorapidities are not covered by the primary ATLAS detector systems. They are referred to as Forward detectors. Their main function is to measure luminosity and to study the $p-p$ diffraction. Ordered by the distance to the Interaction Point 1, the first system is the Cherenkov detector LUCID at a distance of 17 m from IP. The second detector system is the ZDC detector, located at 170 m. The last system is the ALFA detector at a distance of 240 m. All Forward detectors are shown in Figure 4.11 and described in the following sections.

4.7.1 LUCID Detector

The LUminosity measurement using Cerenkov Integrating Detector (LUCID) is the set of the Cherenkov detectors. They are made of aluminium and filled by the C_4F_{10} gas at the constant pressure of $1.2-1.4$ bar. The traversing particle creates light in the medium.

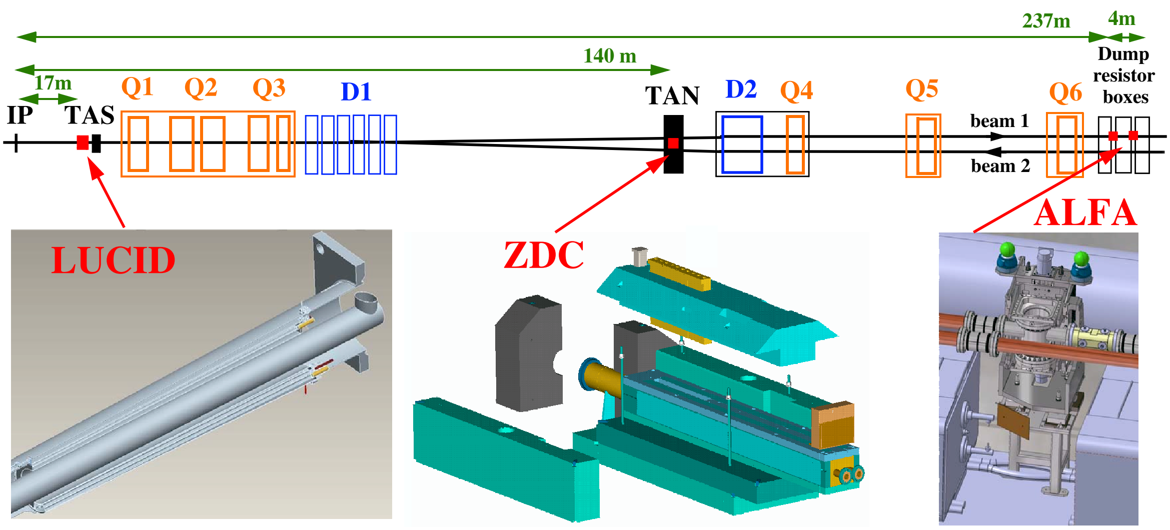

FIGURE 4.11. The ATLAS Forward detectors LUCID, ALFA and ZDC [115].

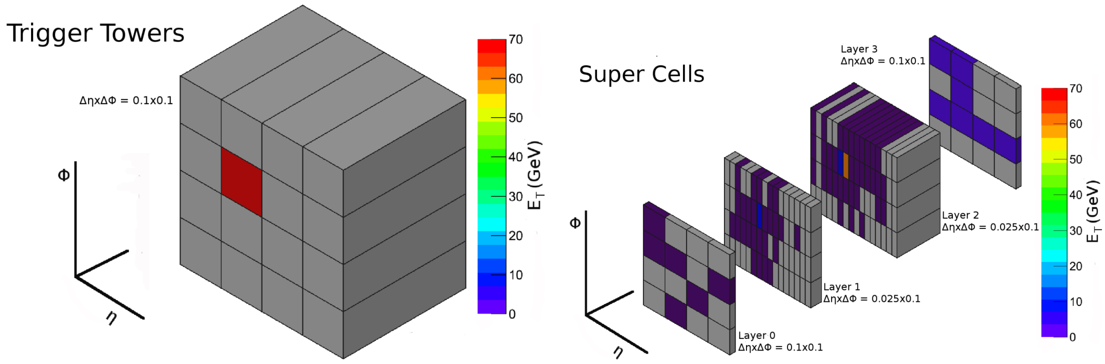

FIGURE 4.12. An electron (with 70 GeV of transverse energy) as seen by the Run2 Level-1 Calorimeter trigger electronics (left) and by the Run3 trigger electronics (right) [121].

This light is delivered to the photomultipliers, which are read out by a front-end card containing a fast amplifier and a differential line driver.

The LUCID is the only detector that can measure luminosity by detecting the inelastic proton–proton scattering in forward regions. LUCID also measures both integrated luminosity with designed uncertainty lower than 5%. It can also be used for diffractive physics studies.

4.7.2 ZDC Detector

The Zero Degree Calorimeter (ZDC) at each side is placed in two arms near beam pipe 140 m from the Interaction Point. It covers the pseudorapidity region $|\eta| > 8.3$. The ZDC plays an important role in heavy ion collisions; it is used to determine the collision centrality correlated with forward neutrons. The ZDC is the calorimeter composed of one electromagnetic and three hadronic modules in each arm. The tungsten and steel plates are used as absorbers, and quartz rods are the active sensing material. The created showers are read out by the multianode phototubes.

4.7.3 ALFA Detector

Absolute Luminosity For ATLAS (ALFA) detector is used for the luminosity measurement using the optical theorem that connects the elastic scattering amplitude in the forward region and the total cross section that can be used to extract luminosity. The ALFA is located 240 meters from the Interaction Point in the Roman pots (specialized retractable devices allowing to have the detector in the primary vacuum of the beam pipe). The

ALFA detectors are not very close to the beam pipe during the injection and the energy ramp-up. When stable conditions are reached, the ALFA is moved close to the beam axis until it reaches a distance of 1–2 mm from the beam. The detector itself is made of square-shaped scintillating fibres, read out by multi-anode photo-multiplier tubes.

4.8 Run3 and HL-LHC Upgrade

The Run2 ended in 2018 and was followed by Long Shutdown 2 period. In this shutdown, the detector improvement was made to prepare for the High Luminosity Large Hadron Collider era. The upgrade impacted four systems: the New Small Wheel detector, the liquid argon (LAr) calorimeter front-end electronics, the new muon detectors in the barrel and the Trigger and Data Acquisition system.

The New Small Wheel system (NSW) covers the pseudorapidity region $1.3 < |\eta| < 2.7$ [122]. Each wheel is formed by two external small strip thin gap chambers (sTGC) and two internal MicroMesh Gaseous Structure (Micromegas) wedges. The new setup reduces the muon triggers due to the electronic noise. In addition to the New Small Wheels, the new Resistive Plate Chambers were installed in the region $1.0 < |\eta| < 1.3$ to extend the NSW detection and reduce the muon trigger rate.

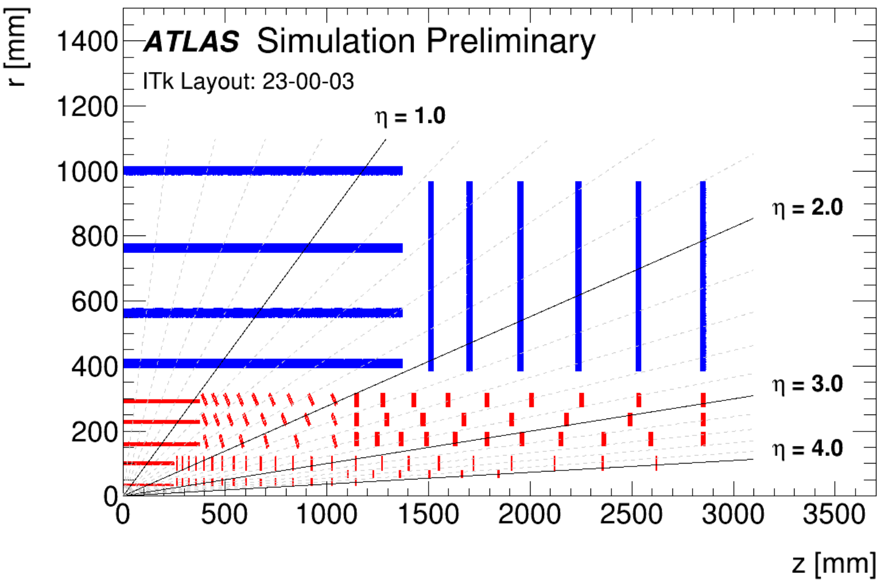

FIGURE 4.13. The ATLAS designed tracking system ITk (Inner Tracker Detector) for HL-LHC runs with pixel (red) and strip (blue) sensors [123].

The LAr calorimeter system has new front-end and back-end electronic boards [121, 122]. This upgrade improves the trigger tower granularity from $\Delta\eta \times \Delta\phi = 0.1 \times 0.1$ to $\Delta\eta \times \Delta\phi = 0.025 \times 0.1$ with the same trigger efficiency (see Figure 4.12). This setup will maintain a similar performance even for higher pile-ups.

The last upgrade is connected to the ATLAS TDAQ that is described in detail in the following chapters. The L1Topo triggers with specific topological algorithms on the calorimeter and muon data have been installed. A new readout system is based on the server-based system FELIX (Front End LInk eXchange) system. The common ATLAS software Athena was upgraded for High Level Trigger into the multithread version to exploit a large number of computer cores and reduce the CPU usage [124].

The next Long Shutdown is planned to start at the beginning of 2026. The current Inner Detector cannot be used for further physics runs due to the large radiation damages. The new all-silicon tracking system ITk (Inner Tracker Detector) will be installed to maintain tracking performance in the high occupancy environment and to cope with the increase of approximately a factor of ten in the integrated radiation dose [123]. The designed ITk layout is shown in Figure 4.13. Additionally, the Calorimeter and Muon systems will be upgraded to satisfy HL-LHC radiation requirements. Finally, the ATLAS TDAQ will have further improvements to hold a larger amount of data. For example, a single-level hardware trigger will be expected to reach a maximum rate of 1 MHz, an order of magnitude improvement over Run3.

CHAPTER 5

THE ATLAS COMPUTATIONAL AND RECONSTRUCTION TOOLS

Every 25 ns, bunches of protons are collided in the center of the ATLAS detector. The created particles in the collision travel through the ATLAS detector sensors and modules (fully described in chapter 4). Due to the readout and trigger limitation, not all collisions are recorded. The recording rate is only a few hundred Hz on average to collect information from all parts of the ATLAS detector before another collision can be recorded. Therefore, the data (signal in the detector) is triggered by two stages: hardware-based Level-1 Trigger and software-based High Level Trigger. The latter also secures the online reconstruction during the decision-making process and helps store the data. The recorded data are finally stored and processed to reconstruct the tracks of particles, fit the vertices, reconstruct the clusters in the Calorimeters, and provide muon tracking in Muon Spectrometer. ATLAS has its own software used for High Level Trigger trigger, tracking and vertexing.

5.1 Trigger and Data Acquisition System

Technical limitations do not allow recording all collisions (also referred to as events) due to the large flow of data estimated to be 1 PB/s. To reduce the amount of data, the events are evaluated, and only those with interesting physics signatures are stored. The decision is taken by the ATLAS Trigger and Data Acquisition system (TDAQ). TDAQ

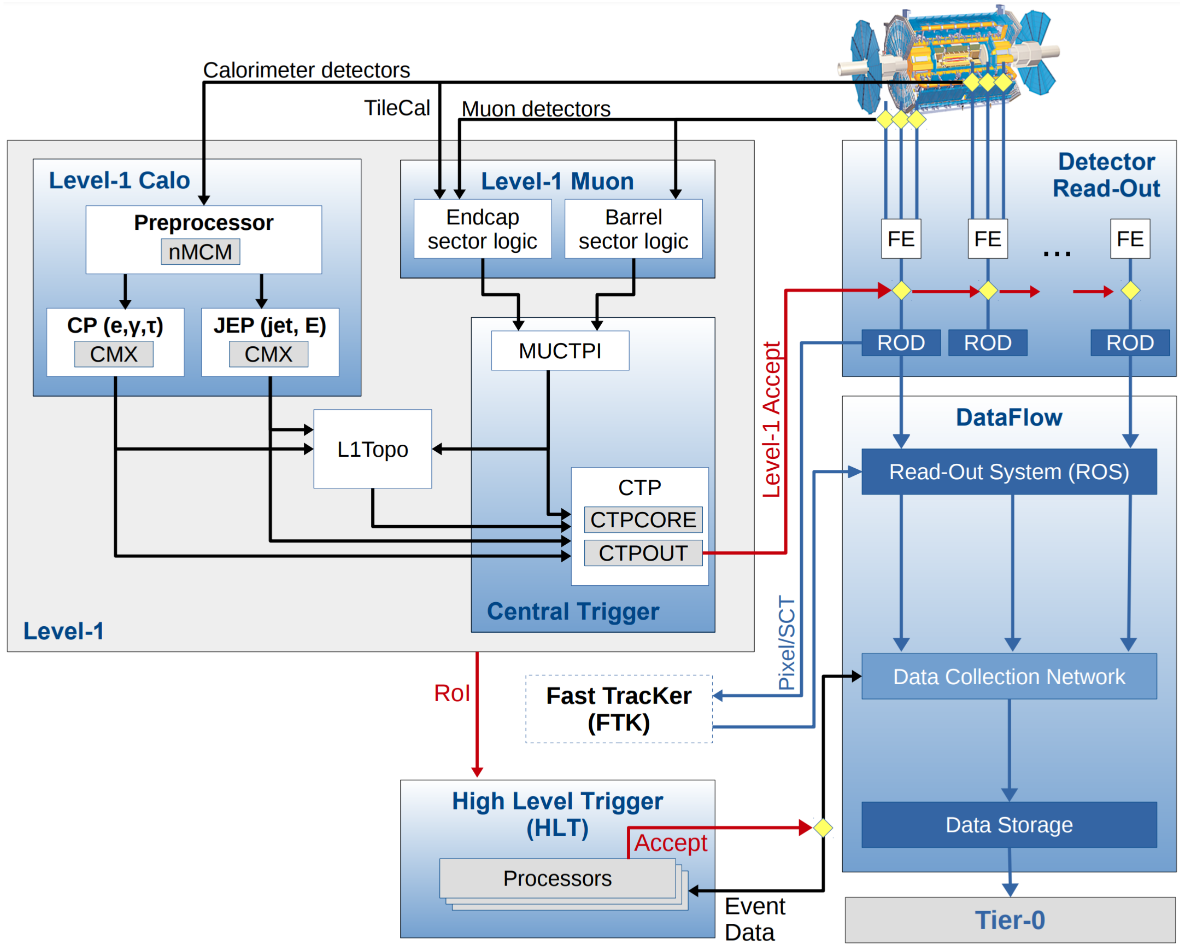

FIGURE 5.1. The architecture of ATLAS TDAQ in Run2 [125].

has two levels: Level-1 Trigger (L1) and High Level Trigger (HLT). When the event is accepted, the ATLAS detector is fully read out; the information is collected to by the Read-out System. Events recorded with the minimum possible selection are referred to as *minimum-bias events*. The last step is storing the data in the CERN Worldwide LHC Computing Grid. The ATLAS TDAQ schematic is shown in Figure 5.1.

5.1.1 Level-1 Trigger

When a particle travelling through the ATLAS detector creates hits in detector modules, the Level-1 Trigger starts. It is the hardware-based system triggering reduced granularity information by the custom electronics. Only the information from Electromagnetic Calorimeter, Hadronic Calorimeter (Calorimeters) and Resistive Plate Chambers, Thin

Gap Chambers are used in the L1 decision process. No information from the Inner Detector is available due to the relatively slow readout and reconstruction.

The L1 Calorimeter trigger (L1Calo) uses the preprocessor to digitise the analogue detector signal. Then, the Cluster Processor (CP) tries to identify signatures of electrons, τ leptons and photons. In parallel, the Jet/Energy-sum Processor (JEP) estimates the sum of missing energy and performs the jet identification.

The L1 Muon trigger (L1Muon) reconstructs the track by forming the hit pattern in the Muon Spectrometer and compares it to the hit pattern from a muon with infinite momentum. The different logic is applied in the barrel and in the end-caps. The information from L1Muon and L1Calo is sent to the Central Trigger Processor (CTP) through the L1Muon Central Trigger Processor Interface (MUCTPI) and the L1 topological (L1Topo) trigger. The final L1 decision is made in the CTP. The CPT also applies the dead time when the detectors are read out to minimize the probability of overlap of two L1 windows and FE buffer overflowing.

In general, L1 considers the muon transverse momentum, total energy or other quantities that can be obtained from RoI. Besides, the L1Topo combines the geometric or kinematic information from L1Calo and L1Muon and considers the topological quantities like invariant masses or distances of reconstructed objects.

The L1 uses roughly reconstructed tracks and creates the regions of interest (RoIs, the detector region with possible interesting physics). If the RoIs are accepted, the front-end (FE) detector electronics read out the event data for all systems. Firstly, the information is sent to ReadOut Drivers (RODs) that perform the data processing and formatting. Then, data are buffered in ReadOut System (ROS) and sent to High Level Trigger. The L1 output rate is up to 100 kHz.

5.1.2 HLT Trigger

If the event is accepted by the Level-1 Trigger, it is then sent to the High Level Trigger (HLT) for further processing. The HLT is a software-based system using thousands of trigger algorithms. The algorithms are CPU-consuming and are similar to the offline reconstruction algorithms. They perform the process of accepting/rejecting the event with full information from the detector parallel to each other. The decision of each algorithm takes a few hundred milliseconds, and it is stored together with data. The recording rate of each of the HLT chains is 1.2 kHz, and 1.2 GB of data is stored every second.

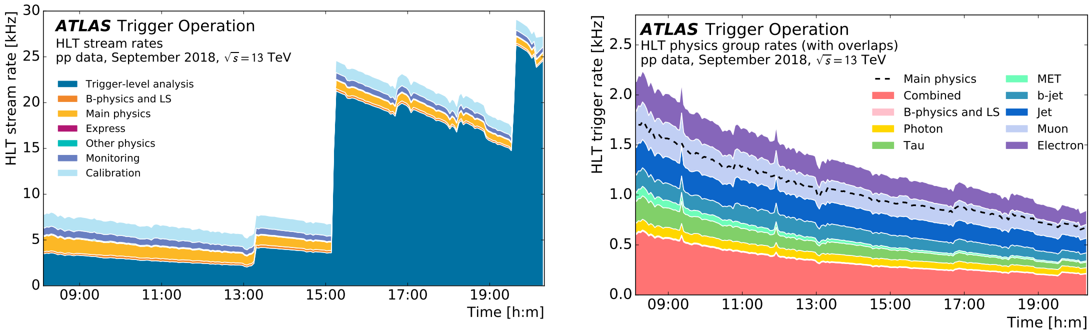

FIGURE 5.2. Trigger stream rates at the HLT as a function of time in a fill taken in September 2018 [126]. The right plot shows separated physics program streams that are shown in the left plot as Main physics.

5.1.2.1 Trigger Menu

The algorithms run in the HLT can be grouped by their purpose, while the full list of the algorithms is called *Trigger Menu* [125]. The menu for the pp collisions consists of

- Primary triggers which are used for physical analyses,
- Support triggers, which are used for efficiency and performance studies, background estimates and monitoring,
- Alternative triggers, which are usually meant as a test for the future trigger algorithms and run along the current triggers,
- Backup triggers, with tighter selections and lower processing or output rate, are used when the CPU usage is overloaded,
- Calibration triggers, which are used for detector calibrations.

Figure 5.2 (left) shows HLT rates for common Large Hadron Collider collisions. The right plot of Figure 5.2 shows the trigger signatures separately. The main physics signature contains mostly all of them; just B-physics and light states physics (BLS) are treated in a separate stream. ATLAS also has other types of runs; for example, the special runs have different trigger menus with setups for special LHC modes of operations and calibration, such as van der Meer scans, β^* levelling and other calibrations, scans and tests.

The trigger names originate in their thresholds on the transverse momentum [125]. For example, L1_MU6 denotes the L1 trigger searching muons with transverse momen-

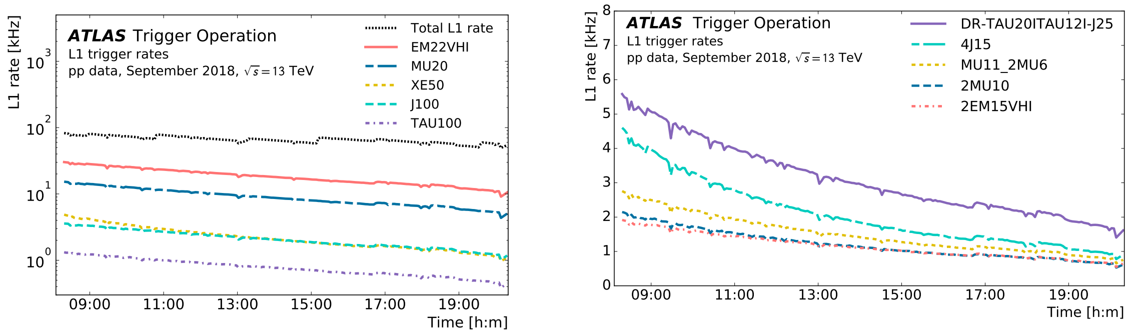

FIGURE 5.3. Level-1 (L1) physics trigger rates as a function of time in a fill taken in September 2018 [125, 126]. These single trigger items (left) and multi items (right) are based on such objects as electromagnetic clusters (EM), muon candidates (MU), jet candidates (J), missing transverse energy (XE) and tau candidates (TAU). The letters following the threshold values refer to details of the selection: separation in η and ϕ (DR), variable thresholds (V), hadronic isolation (H), and electromagnetic isolation (I).

tum greater than 6 GeV. The example of several L1 trigger names and their rates can be seen in Figure 5.3.

5.2 ATLAS Offline Software

The ATLAS experiment uses the Athena framework [127] as the environment for the High Level Trigger, the data preparation and the analyses. The Athena framework consists of more than 2000 packages itself and 100 packages with dependencies on external packages like Geant4 or Monte Carlo generators. The majority of the physical analyses at ATLAS are made with C++ and python programming languages with ROOT toolkit.

5.2.1 Athena

Athena is the Atlas Control Framework based on the common Gaudi architecture [128], originally developed by LHCb. Nowadays, it is used commonly by the ATLAS and LHCb experiments. It is the object-oriented control framework, mainly written in C++ and python and can be compiled by CMake. It uses the C++ classes that can be compiled separately and called by the python configuration scripts.

Athena provides various services and tools that can be used online and offline. For online data handling, Athena is used for the High Level Trigger configuration and trigger monitoring. Offline, it plays a dominant role in the tracks and vertices reconstruction, particle identification, physical simulations and all kind of analyses. The main components of Athena are: the Application Manager providing the core services for framework operation; the Algorithms developed as the basic data processing class; Tools providing similar options as Algorithms but can be run several times per event processing; messaging service providing a series of macros for printing messages to the screen or log; the performance monitoring to control the output of the Algorithms and help identify the problem; StoreGate passing the data to Algorithms and Tools.

Athena is still being developed. The Run2 data were recorded and processed by the Athena releases 20 and 21. The ongoing Run3 uses the most current release 22 [129]. This release has been migrated into a multi-threaded version to handle jobs in parallel. This configuration also reflects the development of the architecture of consumer computer hardware. Athena also can be installed on any Linux distribution with limitations depending on the Linux version and distribution.

5.2.2 ROOT

ROOT [130] is an object-oriented framework originally designed at CERN by René Brun and Fons Rademakers. It has a C/C++ interpreter (CINT) and C/C++ compiler (ACLIC) and can be used as an interactive environment or executing scripts. Its advantage is the ability to handle large files by parallel data processing, make multi-dimensional histograms, perform model fits to data and store the analysis results as ROOT files. ROOT also provides the Virtual Monte Carlo interface to simulation engines such as Geant4 and can be used to develop an application providing the detector geometry or the particle path visualisation. ROOT also has RooFit and RooStat packages implemented.

The RooFit package [131] was originally developed for the BaBar collaboration at Stanford Linear Accelerator Center. It can perform fits using the normalized probability density functions (PDFs). It has better CPU usage not only in fitting procedures than pure ROOT. It also provides a better description and a larger possibility to describe any function. It also can perform multidimensional fits by using binned or per-candidate fit procedures with correct computation of the correlations between parameters. Lastly, it provides better data handling by storing them in a dataset. This can potentially reduce the file size by order of 10.

The RooStat [132] provides advanced statistical tools. It is built on top of the RooFit package. It provides tools for multivariate analyses, hypothesis testing, PDF morphing and other calculations. RooStat is still being developed by a joint team of people from all Large Hadron Collider experiments and ROOT developers.

5.3 ATLAS Data Representation and Distribution

The data acquisition at ATLAS is tightly interconnected with the trigger system into a common Trigger and Data Acquisition system. The connection can be seen in Figure 5.1. The data are stored in several formats depending on the stage of the reconstruction and also analysis needs. Usually, the simulated hits or events are requested in the physical analyses by using the Monte Carlo simulation package Pythia. Due to the huge sizes of the data sample, a special extensive computing and storage system Worldwide LHC Computing Grid was developed, connecting sites with data storage space from all around the world.

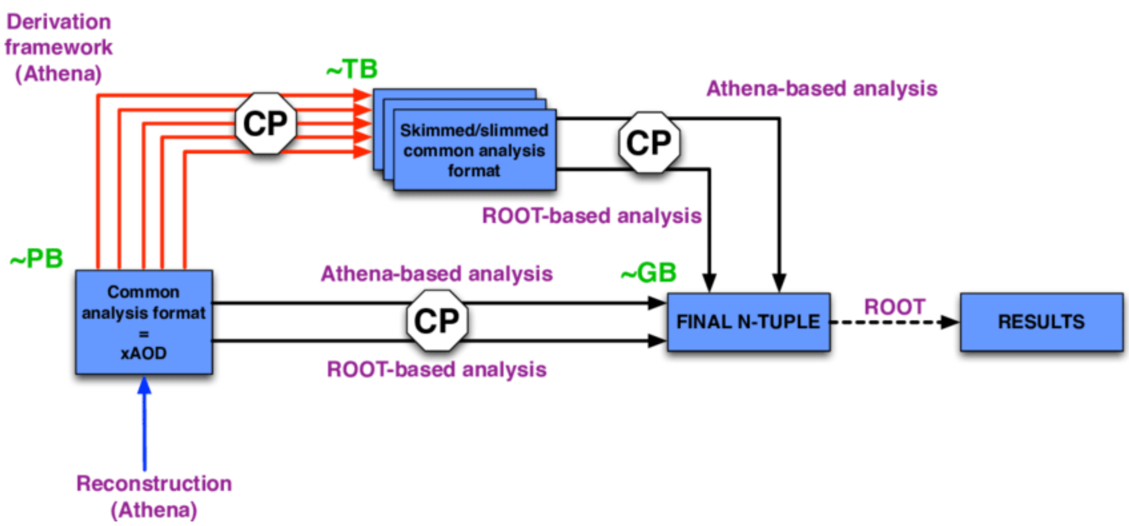

FIGURE 5.4. The ATLAS Run-2 analysis model consisting of xAOD, a centralized reduction framework (Derivation Framework, DAOD), and dual-use tool infrastructure for applying combined performance (CP) group recommendations [133].

5.3.1 ATLAS Event Data Model

If the event is accepted by the Level-1 Trigger, the hits information from detector sensors is passed from Front-the End (FE) detector electronics to the ReadOut Drivers (RODs) [134]. RODs perform initial data processing and formatting and send the data to Read-Out System (ROS) via the optical link. The data buffered in the ROS are investigated by the High Level Trigger. After all HLT algorithms are finished, the final step is to store the accepted data in local data storage and around the world through the Worldwide LHC Computing Grid. The RAW format is used to store the data.

The RAW format contains only information about hits and the information provided by the L1 and HLT [135]. The RAW data are reconstructed using the Athena framework, and the data are stored in the xAOD format. This format is ROOT-readable. The xAOD files do not contain the full detector reconstructed information - it holds only the physics objects interesting to specific ATLAS physics groups. The combined performance (CP) group applies all the recommended prescriptions [133, 136]. In the next stage, the xAOD is slimmed and skimmed (see Figure 5.4) at the request of each analysis team. The final stage is the production of the NTUPLEs[1] stored as the ROOT file. This is the final file used in the analysis.

5.3.2 Monte Carlo Simulation

Monte Carlo (MC) generators are popular in the physicist community. Its application is wide - from detector simulation to physics simulation with desired products of the collisions and their kinematic properties. The produced data by the simulations are essentially the list of detector hits, tracks and vertices positions, particles with their properties and/or the particle decay history (decay products, particle parents, daughters, kinematic variables).

To produce the MC sample, several steps are needed to be followed. Firstly, the particles are generated with mutual relations, and the output is stored in the EVNT[2] file. There are several MC generators. The most common ones are Pythia [137], and Herwig2 [138]. Additionally, specific packages can be included, e. g. EvtGen [139] for B-meson decays, which is relevant to this thesis. The $b\bar{b}$ pairs are created only in ~ 1% pp collisions. PythiaB [140] increases the production of b quarks. After each parton development, the products are checked for the presence of $b\bar{b}$ quarks. Only events

[1] A generic data format arranged as an event-by-event table.

[2] format containing the full reconstruction information such as tracks and their hits in sensors, calorimeter clusters etc.

with these pairs undergo the hadronisation process. To save CPU time, the collision generation is omitted in case of events with desired quarks, and the events with b quarks are clones. The hadronization of each clone is calculated separately.

The generated particles are used in the next step, where the detector response to the particles is simulated. To simulate the passage of particles through the detector, the simulation toolkit Geant4 [141] is used. It uses EVNT files as input and provides information about deposited energy, position and time. The output of the algorithms is stored in the format HITS.

The HITS data are digitized by simulating the electronic response to the deposited energy. The effect of pile-up can also be accounted for in this step. The digitization output has the same format of data as the real data format, so the simulation output is reconstructed by the same tools the data are reconstructed and stored in the xAOD files, and the derivations and NTUPLEs can be produced similarly to data production.

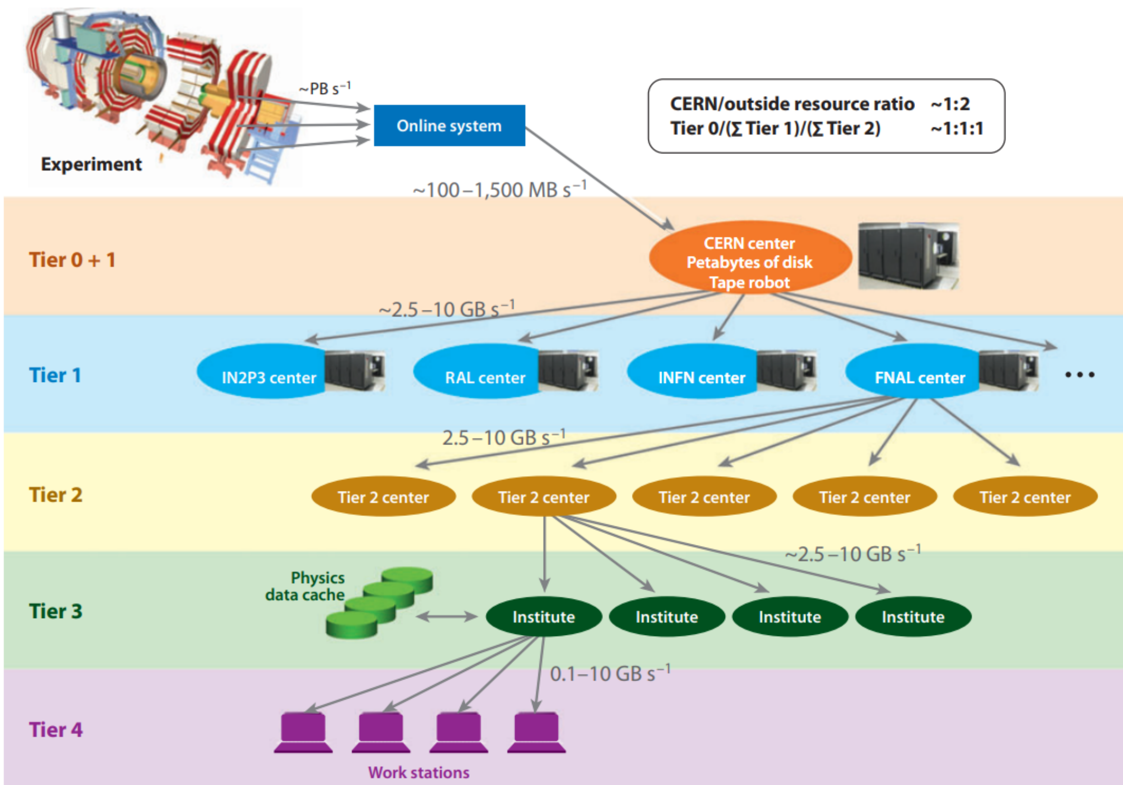

FIGURE 5.5. The model of LHC computing. Data flow outward from Tier 0 to the distributed Tier 1 sites and then to Tier 2 [142].

5.3.3 Worldwide LHC Computing Grid

It is necessary for the data from the detector and the MC samples to be stored and made available for further analyses to the community from around the world. In addition, the reconstruction and simulation require computing farms that provide the CPU and storage space. The system fulfilling the requirements was developed and is known as Worldwide LHC Computing Grid (WLCG) [142–145]. WLCG is an international collaboration providing approximately 170 computing centres in more than 42 countries. In total, 900 000 computer cores are linked into a single network. The main elements of WLCG are Tiers of computer centres, each having specific roles and responsibilities. The overall structure of the WLCG Tiers connection is shown in Figure 5.5.

Tier-0 is composed of the centres: the CERN Data Centre in Geneva, Switzerland and the Wigner Research Centre for Physics in Budapest, Hungary. They are connected by the 100 Gbit/s optical links. Tier-0 is responsible for storing the data in RAW format. Moreover, the initial event reconstruction is performed here. Only $\sim 20\%$ of data can be reprocessed in Tier-0 due to the time limitation, the reconstruction for monitoring is performed, and the data for the full reconstruction is sent to the Tier-1 computer via the fibre optics links.

Tier-1 is used as the data backup. It also provides the main computing capacity for central data production tasks such as large-scale reprocessing and simulation jobs. Tier-1 is also responsible for the further distribution of data to and between sites of the WLCG.

Universities or institutes typically operate tier-2 sites. They can store data (the derivations DAODs are stored at Tier-2) and provide satisfactory power for simulations and physical analyses. The set of Tiers-2 (cloud) is connected only to one Tier-1 site. To use and transfer data from one Tier-2 site to another, the Tiers-1 communicate with each other and provide the interface for data transmission between Tiers-2 from different clouds.

5.4 Physics Object Reconstruction

Reconstructed objects are the pattern recognised by the Athena algorithms from the digital hits from the detector (or, in the case of Monte Carlo, from the digitisation process). The hit patterns are assigned to the particles according to their detector signatures. The pattern formation process is called tracking, and the pattern assignment to the physical

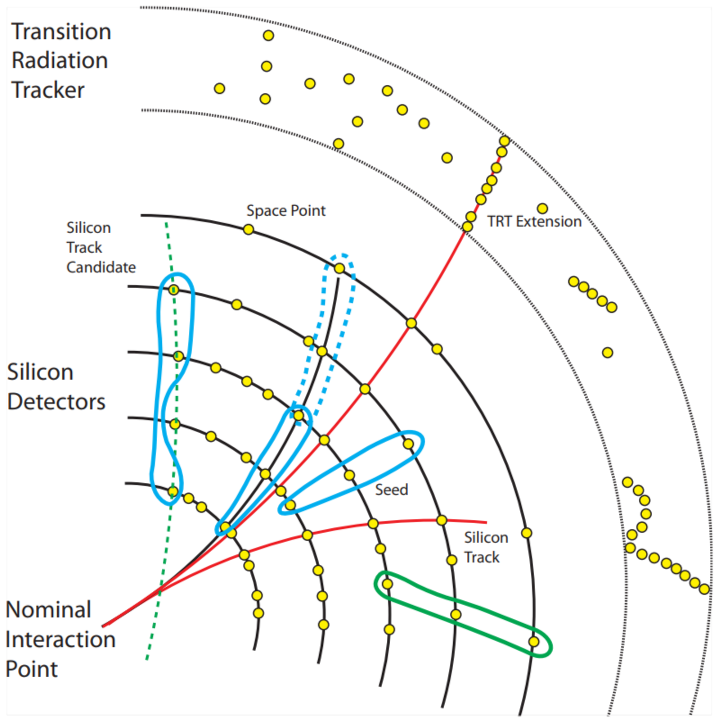

FIGURE 5.6. The ATLAS tracking [146]. The yellow point represents the hits in the ID sensors. The initial seeds for the tracking algorithms are shown as blue and green boundaries. Red curves show the successfully reconstructed tracks.

objects (like muon, electron or jet) is called reconstruction. The reconstructed objects with very close origins are then combined into sets of tracks. The sets are called vertices.

5.4.1 Tracking

The ATLAS tracking uses the hit from the Inner Detector. It is based on local and global pattern recognition algorithms, and the inside-out track finding is usually used. The ID tracking consists of several consecutive steps [147, 148]: data preparation and space point formation, space point seeded track finding, ambiguity solving, and TRT extension.

Space point formation: Charged-particle tracking in the ID starts with assembling clusters from the RAW data. A connected component analysis (CCA) [148] searches for cells with a common edge or corner in the pixel and strip detectors. The formed clusters are transformed into the 3D space point by applying the coordinate transformation from the measured local (sensor) to the global coordinate system (ATLAS coordinates). The space points are shown as yellow circles in Figure 5.6.

Space point seeded track finding: The tracking starts with creating the set of three ID subdetector space points - the seed. The algorithm starts forming the seeds only in the Semiconductor Tracker, then in Pixel Detector only, and finally, mixed-detector seeds are created. The seeds must pass several selection requirements. The selected seeds are used as an output of the track-finding algorithm - the combinatorial Kalman filter [149] is usually used. The filter creates multiple track candidates per seed if the seed fulfils the tracking requirements. Figure 5.6 shows the seed by blue and green lines. The red curves picture the reconstructed tracks.

Ambiguity solving: The track-finding algorithm reconstruct true tracks, but also the fake tracks formed by the random combination of seeds. The ambiguity-solving method determines the track score, whose calculation is based on the track fit quality, missing hits in the seeds, and the transverse momentum of the track. The ambiguity-solver requirements are: transverse momentum is $p_{\mathrm{T}} > 400$ MeV, transverse impact parameter calculated with respect to the measured beam-line position is smaller than 2 mm, minimum of 7 PIX and SCT clusters are used for the track, and no more than two holes appear in the combined PIX and SCT clusters.

TRT extension: The tracks passing the ambiguity-solving stage are extended into the Transition Radiation Tracker. By this extension, a small number of tracks are rejected, and the passing tracks have significantly increased momentum resolution.

5.4.2 Muon Reconstruction

The muon reconstruction is firstly done separately in the Inner Detector and Muon Spectrometer. The information from the other tracking detector systems is then combined to form a fully reconstructed muon. The reconstruction in the ID is done using algorithms for all charged tracks. The muon reconstruction in the MS starts with forming the segments in each muon chamber. The segments are used as seeds for the muon track reconstruction algorithm. It starts in the middle MS layer, where more hits per segment are provided. The search in the extended inner and outer layer follows, and the full muon track in the MS is formed.

5.4.2.1 Combined Muon Reconstruction

The combined muon reconstruction procedure uses different algorithms depending on the information provided by the ID, MS and ECAL. Four types of muons are defined depending on the provided subdetector tracks: combined muons, segment-tagged muons, calorimeter-tagged muons and stand-alone muons.

Combined (CB) muons: The track is fitted independently in the ID and MS, then the global refit procedure using the hits from both systems form the combined track. The outside-in tracking pattern is used, where the hits from MS are seeded in the first place, and the track from the MS is extrapolated into the ID. To improve the fit quality, some hits not corresponding to the final track reconstructed in the MS can be removed.

Segment-tagged (ST) muons: This category of muons is reconstructed with the inside-out technique with a limited number of hits in the MS. The tracks are formed in the ID and then extrapolated to the MS, where only one hit can be used (e. g. muon hit only the first layer of MS and then leave the volume where it can be detected).

Calorimeter-tagged (CT) muons: If the track from the ID cannot be connected with the MS hits and the ECAL detect the energy deposit compatible with a minimum-ionizing particle, the muon can be still reconstructed. The CT muons have the lowest purity and are only used in the regions where the full MS details cannot be delivered.

Stand-alone (SA) muons: At least two layers of MS chambers are required reconstruct SA muons. The information from the ID is not provided for the SA muon reconstruction, only the compatibility of MS hits with the Interaction Point is tested. The SA muons are usually reconstructed only in the regions not covered by the ID.

5.4.2.2 Muon Identification

Muon identification is performed by applying the set of requirements on the number of hits in the PIX, SCT and in the MS chambers, the maximum number of holes in the ID. Five muon identification qualities are provided to fulfil the specific needs of the analyses [150]: Tight, Medium, Loose, High-p_{T} and Low-p_{T}.

Medium muons: The Medium identification criteria provide the default selection for muons in ATLAS. They are selected to minimize the systematic uncertainties associated with muon reconstruction and calibration. This identification considers only CB and SA muons. To identify muon as the medium muon, the CB muons must satisfy the condition of at least two hits on at least two layers of Monitored Drift Tubes, and the SA muons require at least three hits in each of the three layers of MDT or CSC [150].

Tight muons: This quality of muons optimises their purity. The tight identification requires fulfilling the medium CB muons together with the additional cuts on the normalized χ^2 of the combined track fit and on the compatibility between the momenta measured in the ID and MS [150].

Loose muons: The loose muon criteria maximises the reconstruction efficiency while having worse purity but still providing good quality muon tracks. All types of muons can be used, but CT and ST muons must be in the region of $|\eta| \approx 0$, where the CB muon reconstruction is less efficient due to the MS coverage gap [150].

High-p_{T} muons: This identification of muons maximises the momentum resolution for muons with transverse momentum above 100 GeV. Only CB muons passing the medium identification are considered. These muon tracks must also have at least three hits in three MS segments [150].

Low-p_{T} muons: Low-p_{T} muons pass the loose identification requirements. Further, the muon transverse momentum is above 2.5 GeV and below 4 GeV [150].

5.4.3 Vertexing

The input to the vertexing algorithms is the collection of the charged tracks in the Inner Detector. To consider the tracks in the vertexing, they must pass the following requirements [152]:

- Transverse momentum is above 400 MeV,
- Pseudorapidity of the track is in the region $|\eta| < 2.5$,
- At least one hit occurs in the first two PIX layers,
- The maximum allowed number of holes in the SCT is 1,
- Number of silicon hits is at least 9.

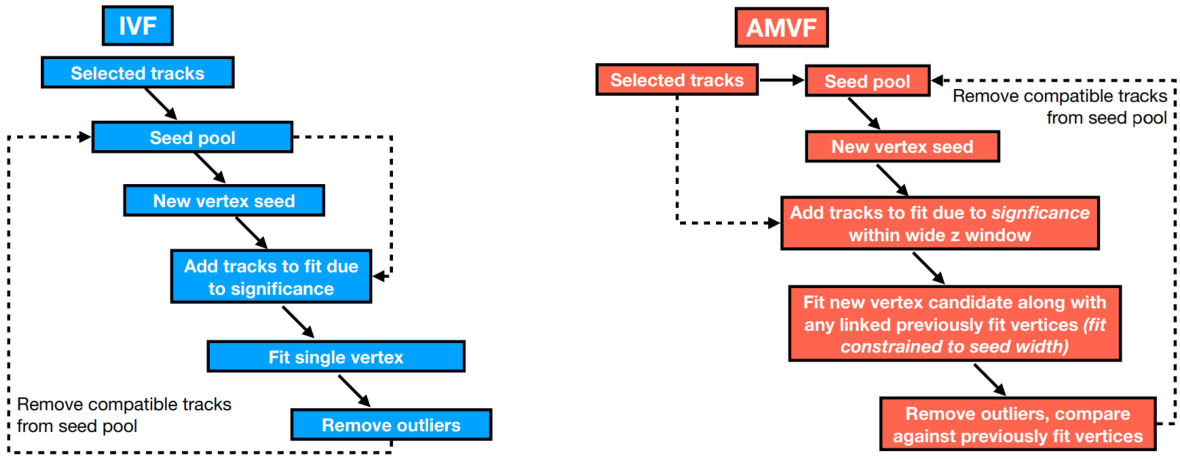

FIGURE 5.7. Comparison of the Iterative Vertex Finder (IVF) and Adaptive Multi-Vertex Finder (AMVF) logic [151].

If the collection of tracks contains at least one track, the vertex finding and fitting procedure can start. After tracks pass the selection criteria, the first vertex seed is selected. At ATLAS, the Gaussian track density seed finder is usually used. The finder uses the longitudinal Gaussian function to calculate seed finding weights, and the transverse Gaussian function is used as independent quality control. The fit of the vertex position is performed with input information about the seed and track. The tracks

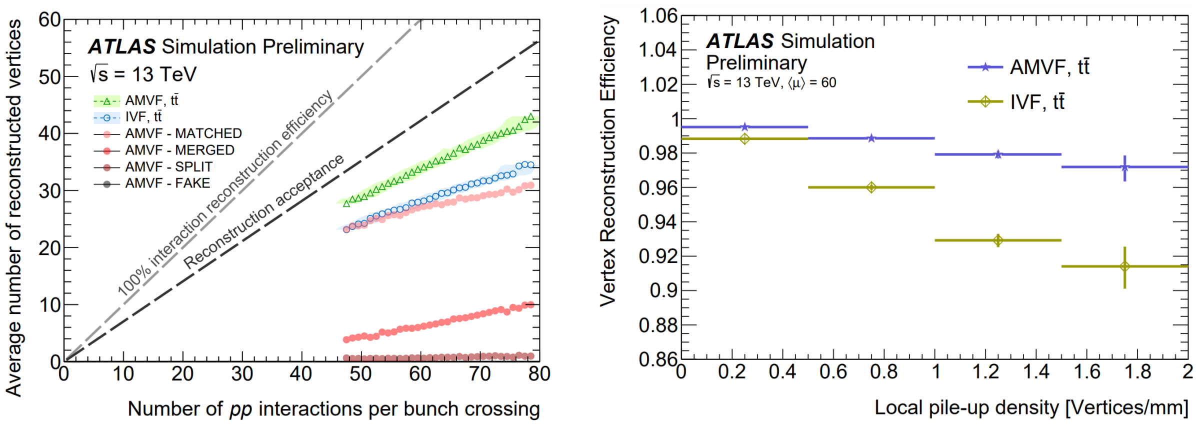

FIGURE 5.8. Left: average number of vertices reconstructed as a function of the number of pp interactions per bunch crossing $<\mu>$ in simulated $t\bar{t}$ events [151]. Right: comparison of IVF and AMVF vertex reconstruction efficiency as a function of local pile-up density [151].

incompatible with the vertex fit results are removed from the current vertex and can be used in the next iteration. The process is repeated with the tracks not used in the current iteration until no tracks available for vertexing are left.

The ATLAS vertex reconstruction uses two vertex finder algorithms: Iterative Vertex Finder (IVF) and Adaptive Multi-Vertex Finder (AMVF). The IVF and AMVF algorithms are similar to each other (see Figure 5.7) with some key differences. Both of them use the Gaussian track density seed finder as the input. Then, the vertex is fitted by the single vertex fitter (IVF) or the simultaneous vertex fitter (AMVF) if any previously fit vertices share tracks with the vertex candidate currently being fit. The consequence of the vertex fitter strategy is that each track is used only for one vertex fitting in the IVF. On the other side, AMVF can use each track more than once. Due to the parallel AMVF fitting of the vertex, it provides better performance for high pile-ups than the IVF does (see Figure 5.8) [151].

When all vertices are fitted, the Primary Vertex (PV) is chosen by requiring the vertex to have at least three tracks. Additionally, the selection criteria $\textsc{max}\sum p_{\mathrm{T}}^2$ must be satisfied. The $\textsc{max}\sum p_{\mathrm{T}}^2$ calculates the sum of the squares of the constituent tracks transverse momenta $\sum p_{\mathrm{T}}^2$ and selects the vertex with the highest values as the PV.

CHAPTER 6

B Physics Program at ATLAS

ATLAS has a well-defined program studying the B mesons properties. Because B mesons are heavy particles (with respect to particles made only of u, b or c quarks), they are used as a probe for the Beyond Standard Model (BSM) processes. The ATLAS B-Physics (also called Beauty Physics) program includes the searches for new particles, Quantum chromodynamics studies by studying the beauty quark production mechanisms, increasing the precision of the SM parameters and searches for BSM hints.

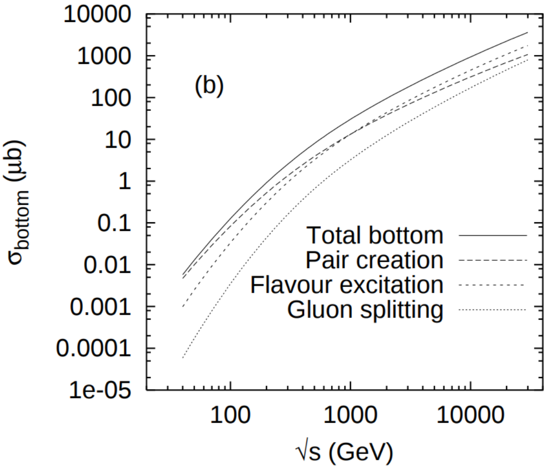

FIGURE 6.1. The bottom quark production cross-section for the proton-proton collisions as the function of the collision energy. The contributions from pair creation, flavour excitation and gluon splitting are shown separately [153].

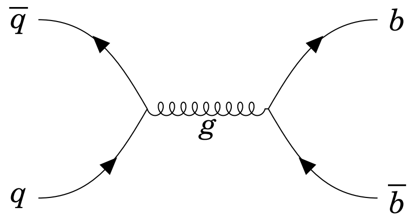

(a) Leading order pair production.

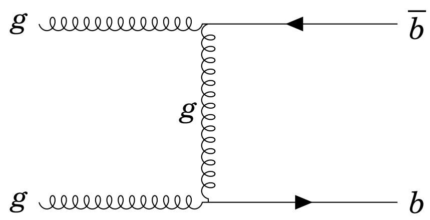

(b) Leading order pair production.

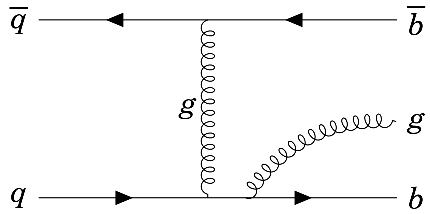

(c) Next-to-leading order pair production.

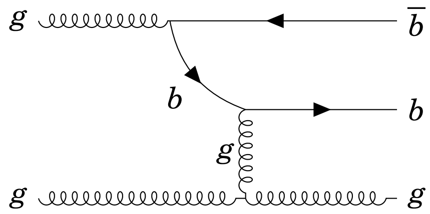

(d) Flavour excitation.

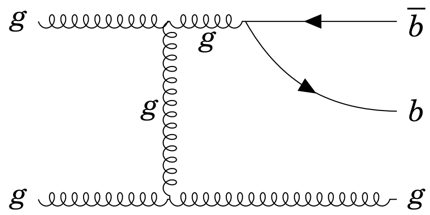

(e) Gluon splitting.

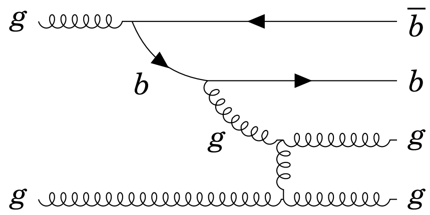

(f) Gluon splitting of flavour-excitation character.

FIGURE 6.2. Examples of Leading Order (LO) and Next-to-Leading Order (NLO) heavy-flavour production diagrams [154].

6.1 Production Mechanism of B Mesons at the LHC

At the Large Hadron Collider, B mesons are produced during the hadronization of b and $\overline{b}$ quarks. The b quark production is described within perturbative Quantum chromodynamics calculations as an expansion in a series of the coupling constant α_s. Heavy flavour events can be subdivided into three production classes: pair creation, flavour excitation and gluon splitting. The cross-section of b quark pairs to be created in the proton-proton collisions is shown in Figure 6.1. The Leading Order (LO) and Next-to-Leading Order (NLO) Feynman diagrams of each heavy-flavour production can be seen in Figure 6.2.

Pair creation: The hard processes can generate the $b\overline{b}$ pairs [154]. This can be described by $\mathcal{O}(\alpha_s^2)$ leading-order (LO) graphs, $gg \to b\overline{b}$ and $q\overline{q} \to b\overline{b}$ (see Figure 6a and 6b). To understand the minor effects of the cross-section calculation, the $\mathcal{O}(\alpha_s^3)$ next-to-leading (NLO) processes are approximated by the parton shower calculations. This approach allows describing the produced pair creation events $q\overline{q} \to b\overline{b}g$ (Figure 6.2c), where the quarks do not have back-to-back geometry.

Flavour excitation: In this hard scattering NLO process, the heavy flavour from the parton distribution scatters with the gluon from another parton. If the heavy quark is not valence, it must come from the gluon decaying into quark pair, and the virtuality of the process must be larger than for the pair creating, $Q^2 > m_b^2$ [154]. Effectively, the process can be described as $gq \to b\overline{b}q$ or $gg \to b\overline{b}g$ (also see Figure 6.2d. The additional possibility of further emissions is also included in this contribution.

Gluon splitting The last NLO process describes the gluon splitting into quark pair, $g \to b\overline{b}$ [154], where the created quarks do not undergo the hard scattering with other quarks (Figure 6.2e). It can happen that the created quark scatters on a gluon or emits a gluon. Then, the process is similar to the flavour excitation, but no flavour enters the hard scattering, so this process is considered to be a gluon splitting process (Figure 6.2f).

6.2 B-Physics Trigger

The ATLAS Trigger and Data Acquisition system is described in chapter 5. B-physics triggers are based on the B-hadron identification through their decay chain with dimuon final state. This means that B-physics uses the Level-1 Trigger object identified as a single muon. These muons can be used in the topological trigger to search for the muon pairs, each having transverse momentum p_{T} larger than 4 GeV, 6 GeV or 11 GeV [155]. The High Level Trigger uses cut on transverse momentum $p_{\mathrm{T}} > 6$ GeV to remove most of the background accepted by L1. The HLT triggers use the muon or dimuon information from the L1 topological information. In addition, it can use more tracks reconstructed in the Inner Detector to form the candidate for physical analysis.

Primary B-physics triggers searches for the $B \to J/\psi(\mu^+\mu^-)X$ and $B \to \mu^+\mu^-$, good examples are: HLT_MU6_MU4_BMUMUXV2, HLT_MU6_MU4_BJPSIMUMU or HLT_MU11_MU6_BDIMU. The first one searches B hadron with two muons in the final state with the cut on muons $p_{\mathrm{T}} > 6$ GeV and $p_{\mathrm{T}} > 4$ GeV. The second example

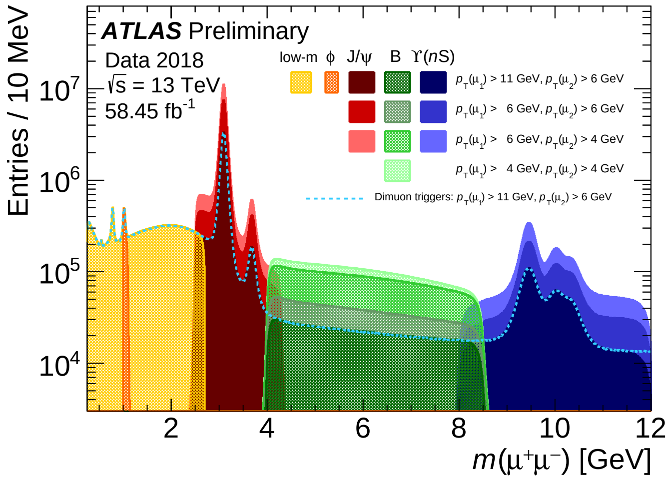

FIGURE 6.3. The invariant mass distribution of dimuon tracks collected by the B-Physics triggers in 2018 [126].

trigger is similar to the first one, it just further requires that two muons must form J/ψ that originates from the B hadron. The last mentioned trigger is usually used for the rare decay of B mesons to a pair of muons [156]. Figure 6.3 shows the invariant mass distribution of dimuon tracks collected by the B-Physics triggers in 2018.

6.3 ATLAS B-Physics and Light States Working Group

The ATLAS B-physics and Light States (BLS) working group is well established and is organised into three subgroups: Rare decays group, $B \to J/\psi X$ physics group, and Onia production and $b\bar{b}$ cross-section group. They all use B-physics triggers described in the previous section. Thanks to the large B meson production rate and long lifetimes, BLS focuses on the studies of the Standard Model boundaries, searches for beyond the SM, and probes to the Quantum chromodynamics.

This thesis presents two analyses performed within the ATLAS BLS group. One is dedicated to the measurement of the CP-violating phase ϕ_s in the $B_s^0 \to J/\psi\phi$ with a large contribution from the $B^\pm \to J/\psi K^\pm$ flavour tagging. The second analysis focuses on the high-precision measurement of B_d^0 meson lifetime in $B^0 \to J/\psi K^{*0}$ decay. In addition to the above-mentioned analyses, the three latest analysis overviews from the ATLAS B-physics group are presented below.

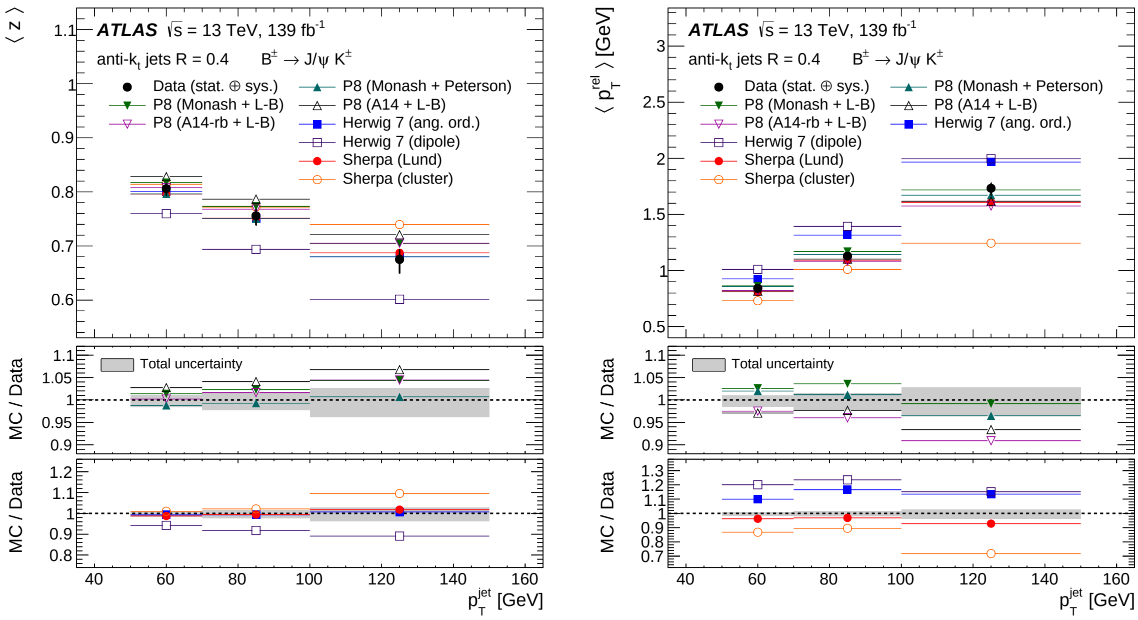

FIGURE 6.4. Average values of the longitudinal and transverse profiles $< z >$, $< p_{\mathrm{T}}^{rel} >$ as a function of the jet $p_{\mathrm{T}}^{\mathrm{jet}}$, compared with MC predictions [157].

6.3.1 Measurement of b-quark fragmentation properties in jets using the decay $B^{\pm} \to J/\psi K^{\pm}$

Understanding the b quark fragmentation is crucial for understanding the Quantum chromodynamics as well as for Higgs studies. The lastest ATLAS measurement was performed with data from 139 fb^{-1} of pp collisions at $\sqrt{s} = 13$ TeV [157]. Only charged B mesons were studied: the $B^{\pm} \to J/\psi K^{\pm}$ final stated was the only one considered. The analysis also uses jets reconstructed with the anti-k_{T} algorithm [158] with the radius parameter $R = 0.4$. After reconstructing all objects, $B^{\pm}$ candidates are matched to the jets. The longitudinal and transverse momentum profiles are known to be sensitive to the fragmentation function and are defined with the $B^{\pm}$ momentum $\vec{p}_B$ and jet momentum $\vec{p}_j$:

$$z = \frac{\vec{p}_B \cdot \vec{p}_j}{\left|\vec{p}_j\right|^2}, \quad p_{\mathrm{T}}^{rel} = \frac{\left|\vec{p}_B \times \vec{p}_j\right|}{\left|\vec{p}_j\right|^2}. \tag{6.1}$$

Figure 6.4 shows the average values of the longitudinal and transverse profiles dependent on the jet momentum $\vec{p}_j$ together with several MC simulations. The data were corrected for detector resolution effects using an iterative Bayesian algorithm. The discrepancies between data and MC can be accounted to the modelling of the gluon splitting $g \to b\bar{b}$ in

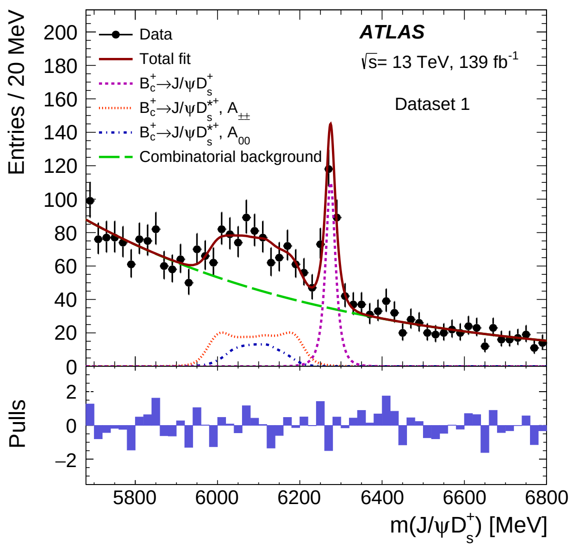

FIGURE 6.5. The projections of the mass m (left) and $\cos\theta'(\mu)$ (right) for the selected $B_c^+ \to J/\psi D_s^{(*)+}$ candidates [159].

the parton shower algorithms.

6.3.2 Study of $B_c^+ \to J/\psi D_s^+$ and $B_c^+ \to J/\psi D_s^{*+}$ decays

The B_c^+ meson is the heaviest B meson. It is known to be produced with a low cross-section. The study of the B_c^+ meson can provide a better understanding of various theoretical approaches used to describe its production and decay.

The ATLAS collaboration performed a measurement of the $B_c^+ \to J/\psi D_s^+$, $B_c^+ \to J/\psi D_s^{*+}$ and $B_c^+ \to J/\psi \pi^+$ branching rations and the measurement of the transverse polarization fraction using the 139 fb^{-1} of pp collisions at $\sqrt{s} = 13$ TeV [159]. A multivariate analysis based on boosted decision trees (BDTs) was utilised to reduce the background. The branching ratios were obtained from the extended mass unbinned maximum likelihood.

The measurement of the transverse polarization ratio uses a two-dimensional fit, where the $\cos\theta'(\mu)$ distribution was fitted along the B_c^+ candidate mass. The parameter $\theta'(\mu)$ is the helicity angle defined in the rest frame of the muon pair as the angle between the μ^+ and the D_s^+ candidate momenta.

The fit projections of the mass m and $\cos\theta'(\mu)$ are shown in Figure 6.5 and the branching ratio results are:

$$R_{D_s^+/\pi^+} = \frac{\mathscr{B}\left(B_c^+ \to J/\psi D_s^+\right)}{\mathscr{B}\left(B_c^+ \to J/\psi \pi^+\right)} = 2.76 \pm 0.33\,(\text{stat.}) \pm 0.29\,(\text{syst.}) \pm 0.16\,(\text{ext.}),$$

$$R_{D_s^{*+}+/\pi^+} = \frac{\mathscr{B}\left(B_c^+ \to J/\psi D_s^{*+}\right)}{\mathscr{B}\left(B_c^+ \to J/\psi \pi^+\right)} = 5.33 \pm 0.61\,(\text{stat.}) \pm 0.67\,(\text{syst.}) \pm 0.32\,(\text{ext.}),$$

$$R_{D_s^{*+}+/D_s^+} = \frac{\mathscr{B}\left(B_c^+ \to J/\psi D_s^{*+}\right)}{\mathscr{B}\left(B_c^+ \to J/\psi D_s^+\right)} = 1.93 \pm 0.24\,(\text{stat.}) \pm 0.09\,(\text{syst.}),$$

where the first uncertainty is statistical, the second is systematic, and the third corresponds to the uncertainty in the branching fraction of the $D_s^+ \to \phi(K^+K^-)\pi^+$ decay. The transverse polarization fraction is

$$\frac{\Gamma_{\pm\pm}}{\Gamma} = 0.70 \pm 0.10\,(\text{stat.}) \pm 0.04\,(\text{syst.}).$$

6.3.3 Study of the rare decays of B_s^0 and B^0 mesons into muon pairs

The direct decay of B^0 and B_s^0 is highly suppressed in the Standard Model, the predicted branching ratios are

$$\mathscr{B}(B^0 \to \mu^+\mu^-) = (1.06 \pm 0.09) \times 10^{-10}, \mathscr{B}(B^0 \to \mu^+\mu^-) = (3.65 \pm 0.23) \times 10^{-10},$$

The experimental deviations from these values will suggest the existence of NP using the decays via a loop diagram.

The ATLAS experiment provides the branching ratio measurements using data from the pp collisions at $\sqrt{s} = 13$ TeV collected between years 2015 and 2016 corresponding to 36.2 fb^{-1} [160]. The results are combined with the Run1 results using proton-proton collision data at $\sqrt{s} = 7,8$ TeV.

The branching ratios are calculated using the formula:

$$\mathscr{B}\left(B_{(s)}^0 \to \mu\mu\right) = N_{d(s)} \frac{\mathscr{B}\left(B^\pm \to \mathrm{J}/\psi K^\pm\right) \times \mathscr{B}\left(\mathrm{J}/\psi \to \mu\mu\right)}{N_{\mathrm{J}/\psi K^\pm} \frac{\varepsilon_{\mu\mu}}{\varepsilon_{\mathrm{J}/\psi K^\pm}}} \frac{f_u}{f_{d(s)}} \tag{6.2}$$

where $\mathscr{B}\left(B^\pm \to \mathrm{J}/\psi K^\pm\right)$ and $\mathscr{B}\left(\mathrm{J}/\psi \to \mu\mu\right)$ are branching ratios known from PDG [46], $f_u/f_{d(s)}$ from HFLAV [94], $\varepsilon_{\mu\mu}/\varepsilon_{\mathrm{J}/\psi K^\pm} = 0.1176 \pm 0.0009(\text{stat.}) \pm 0.0047(\text{syst.})$ relative reconstruction efficiencies estimated from MC and $N_{d(s)}$ and $N_{\mathrm{J}/\psi K^\pm}$ are yields of $B_{(s)}^0 \to \mu\mu$ and reference channel $B^\pm \to \mathrm{J}/\psi K^\pm$ extracted from unbinned ML fit.

The continuum background is rejected by a 15-variable Boosted Decision Tree (BDT) which is trained and tested on data sidebands and simulated signal events.

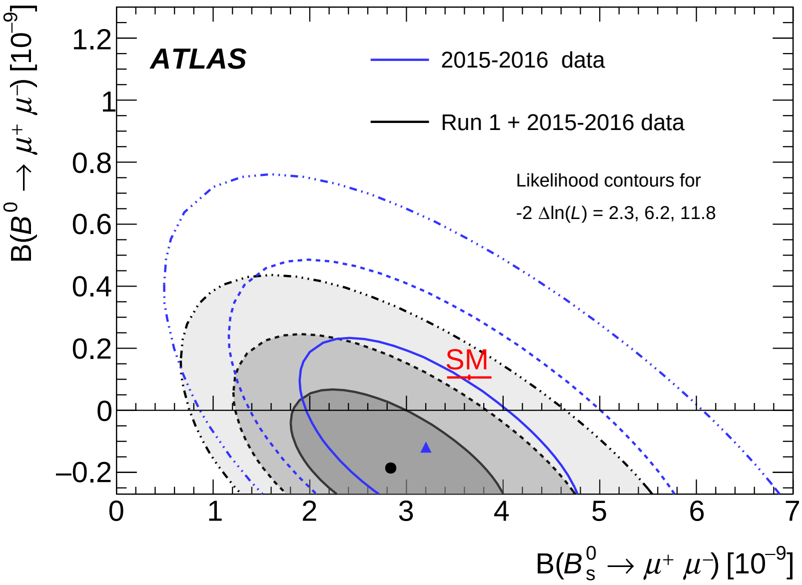

FIGURE 6.6. Likelihood contours for the combination of the Run1 and 2015-2016 Run2 $B^0_{(s)} \rightarrow \mu\mu$ results (shaded areas) [160]. The contours are obtained from the combined likelihoods of the two analyses for values of $-2\Delta\ln(L)$ equal to 2.3, 6.2 and 11.8. The empty contours represent the result from 2015-2016 Run 2 data alone. The SM prediction with uncertainties is indicated.

The other background contributions arise from partially reconstructed B-hadrons and miss-reconstruction ($B^0_{(s)} \rightarrow hh$ decays, where both hadrons are identified as muons. An unbinned ML fit to the mμμ distribution is performed in four BDT intervals of constant signal efficiency to extract the signal yield. Due to the limited mass resolution, the peaks of $B^0_{(s)} \rightarrow \mu\mu$ overlap and are statistically separated in the fit. The results were combined with ATLAS Run1 measurements, resulting in branching ratios [160]

$$\mathscr{B}\left(B^0_s \rightarrow \mu\mu\right) = \left(2.8^{+0.8}_{-0.7}\right) \cdot 10^{-9}$$
$$\mathscr{B}\left(B^0 \rightarrow \mu\mu\right) < 2.1 \cdot 10^{-10} \text{at } 95\% \text{ CL}$$

The resulting contour of two branching ratios is shown in Figure 6.6.

The combined results are further combined with results obtained by the CMS and LHCb experiments with data collected between 2011 and 2016, leading to the values[161]

$$\mathscr{B}\left(B^0_s \rightarrow \mu\mu\right) = \left(2.69^{+0.37}_{-0.35}\right) \cdot 10^{-9}$$
$$\mathscr{B}\left(B^0 \rightarrow \mu\mu\right) < 1.9 \cdot 10^{-10} \text{at } 95\% \text{ CL.}$$

CHAPTER 7

Flavour Tagging in the Charged B-mesons Decays

The analysis studying the CP-violating phase ϕ_s in the $B_s^0 \to J/\psi\phi$ decay can concurrently provide a measurement of the B_s^0 meson lifetime properties that are tightly connected to the oscillations of B_s^0 mesons. The lifetime parameters can be obtained even without knowing the initial flavour of the B_s^0, but the statistical uncertainty is significantly larger. In order to have precise measurements, the initial B_s^0 meson flavour determination shall be performed. The method to infer the initial flavour is called *Flavour Tagging*. Analysis in the following chapter applies the flavour tagging in the ϕ_s and lifetime parameters extraction by using the flavour tagging calibration curve. This curve is acquired from studying flavour tagging in the self-tagged channel $B^\pm \to J/\psi K^\pm$. The study is presented in this chapter, together with the explanation of flavour tagging theory. The application of the calibration curve to the B_s^0 flavour inference is also provided in this chapter.

7.1 Flavour Tagging Algorithms

The algorithms for inferring the initial flavour of the signal neutral B-mesons come in two categories: Same-Side Tagging (SST) and Opposite-Side Tagging (OST). The SST exploits the tag information from the particle accompanying the B_s^0 candidate. This particle is expected to contain a strange quark having the same origin as the s quark forming the B_s^0 meson, assuming that the s quarks were created in pairs, and the initial flavour of the signal B_s^0 is therefore also known. Figure 7.1 shows the signal candidate and the same-side (SS) kaon as the example of the SST.

The OST uses the fact that b quarks are created in pairs at the Large Hadron Collider. One of the created quarks hadronises into the B_s^0 candidate that is detected via the decay into $J/\psi(\mu^+\mu^-)$ and $\phi(K^+K^-)$. The second bottom quark forms a not necessarily identified or reconstructed B hadron. A set of fragment tracks from this opposite B hadron is required to be reconstructed in order to provide the OST information. If no track is associated with the opposite side meson, the OST cannot be performed.

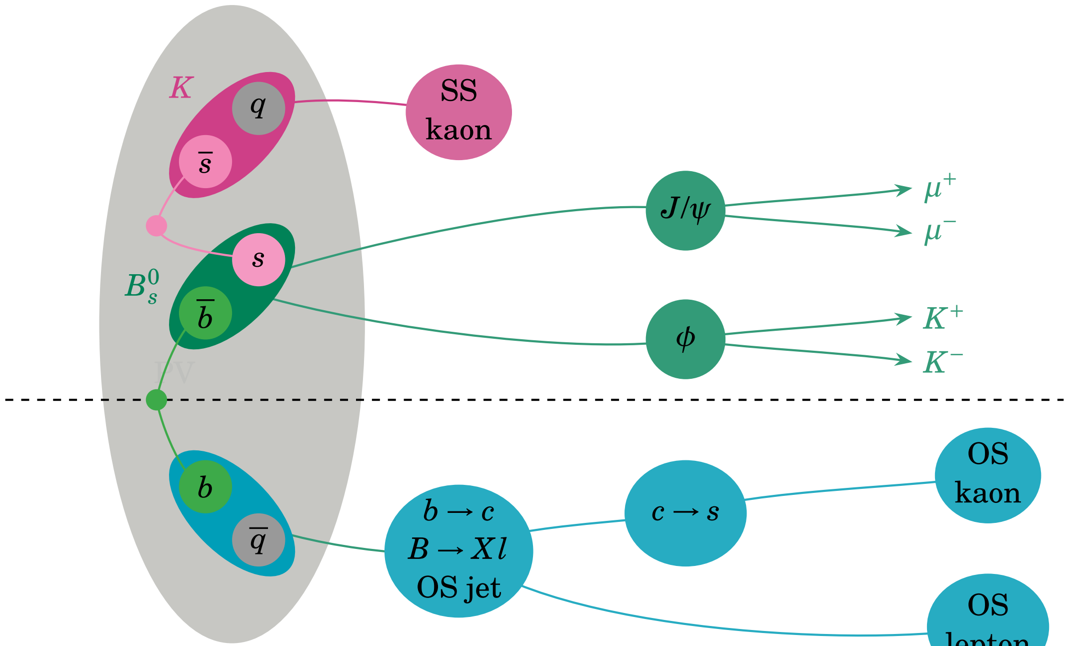

FIGURE 7.1. The schematic overview of the underlying principles of flavour tagging algorithms to infer the initial B_s^0 flavour. Both algorithms for same-side (SS) and opposite-side (OS) tagging are shown.

The SST and OST algorithms cannot work for neutral meson without any training or calibration. The analysis presented in the next chapter uses the calibration curves from the $B^\pm \to J/\psi K^\pm$ candidates. This decay channel is known to have similar kinematics to the $B_s^0 \to J/\psi\phi$. Further, it is a non-oscillating channel, so the initial flavour immediately corresponds to the charge of the opposite side tagger. The following sections are denoted to the tagging performance in the $B^\pm \to J/\psi K^\pm$ channel and to creating the calibration for the $B_s^0 \to J/\psi\phi$. Finally, the procedure of applying the calibration to the B_s^0 candidates and exploiting the B_s^0 tag probability is described.

7.2 Flavour Tagging Parameters

The OST in the $B^\pm \to J/\psi K^\pm$ channel uses four tagging methods: tight muons, low-p_T muons, electrons and jets. The performance of each method must be validated and the purest tagging is desired. The efficiency, dilution and tag power are used to quantify each tag method performance, and the calibration curves are extracted from the $B^\pm$ tag probabilities.

7.2.1 Efficiency, Dilution and Tag Power

Not all candidates can use the information from the OST. To estimate the fraction of tagged events, the efficiency ε_tag is defined as

$$\varepsilon_\mathrm{tag} = \frac{N_r + N_w}{N_{B^\pm}}, \tag{7.1}$$

where N_r is the number of correctly tagged events (the charge of tagger corresponds to the initial flavour), N_w is the number of wrongly tagged events and $N_{B^\pm}$ is the number of all candidates. The N_w is non-zero due to the possible $b \to c$ transition of the opposite-side meson, so the tagging is not actually pure. The purity of the tagger is given by the dilution

$$D_\mathrm{tag} = \frac{N_r - N_w}{N_r + N_w} = 1 - 2w_\mathrm{tag}, \tag{7.2}$$

where w_tag is the fraction of wrongly tagged events with respect to the total number of tagged events. The dilution of the purest sample is close to 1.

The combination of efficiency and dilution is called tag power and is defined as

$$P_\mathrm{tag} = \sum_i \varepsilon_{tag}^{(i)} \left(D_{tag}^{(i)}\right)^2, \tag{7.3}$$

where the sum runs over the bins of a given distribution. The tag power is a figure of merit to compare the different tagging methods between experiments and it is not directly used in the calibration to B_s^0 sample.

7.2.2 Tag Method and Tag Probability

To improve the tagging performance, the cone charge parameter is used instead of the signal lepton or jet charge. The cone charge is defined as the weighted sum of charges of tracks around the lepton:

$$Q_x = \frac{\sum_i^{N\text{ tracks}} q_i \cdot (p_{\mathrm{T}i})^\kappa}{\sum_i^{N\text{ tracks}} (p_{\mathrm{T}i})^\kappa} \tag{7.4}$$

where $x = \{\mu, e, \text{jet}\}$ refers to the muon, electron, or jet charge, respectively, and the summation is made using the charge of the track, q_i, and its $p_{\mathrm{T}i}$, over a selected set of tracks, including the leading lepton or jet, in a cone of size $\Delta R = \sqrt{(\Delta\phi)^2 + (\Delta\eta)^2}$ around the lepton or jet direction. The value of the parameter κ is optimised for each OST method. The cone charge value of the specific event is equivalent to the probability $P(Q|B^+)$.

The probability of B^+ tagging for each passed event is calculated using the formula

$$P(B|Q_x) = \frac{P(Q_x|B^+)}{P(Q_x|B^+) + P(Q_x|B^-)}, \tag{7.5}$$

where $P(Q_x|B^+)$ is the cone charge value of the B^+ for the specific event with tag method x and the $P(Q|B^-)$ is the cone charge value of the B^- for the same event. There is no need to construct the probability distribution function for B^- tagging, because these two probabilities are related by $P(\bar{B}|Q_x) = 1 - P(B|Q_x)$. The dilution (7.2) can be expressed using the tag probability $P(B|Q_x)$:

$$D_{\text{tag}} = 2P(B|Q_x) - 1. \tag{7.6}$$

7.3 $B^\pm \to J/\psi K^\pm$ Event Selection

The analysis presented in the following chapter uses the $B^\pm \to J/\psi K^\pm$ candidates extracted from the data collected by the ATLAS detector during 2015–2017 at centre-of-mass energy $\sqrt{s} = 13$ TeV. In total, 80.5 fb^{-1} of data was used. The sections below describe the selection criteria for the $B^\pm \to J/\psi K^\pm$ candidates and for each tag method object.

7.3.1 $B^\pm \to J/\psi K^\pm$ Candidates

To identify an event with the $B^\pm \to J/\psi K^\pm$ candidate, several conditions are applied. First, J/ψ candidates are selected from oppositely charged muon pairs, each muon is required to have $p_{\mathrm{T}} > 4$ GeV and $|\eta| < 2.5$. Only dimuon candidates with invariant mass $2.8 < m(\mu^+\mu^-) < 3.4$ GeV are retained for further analysis. The invariant mass is determined from the re-fitted track parameters of the dimuon vertex.

In order to form the $B^{\pm}$ candidate, an additional track is required. This track must not be identified as an electron or muon and must pass the assigned charged-kaon mass hypothesis. The final $B^{\pm}$ candidate is the combination of track and dimuon using a vertex fit, performed with the mass of the dimuon pair constrained to the PDG J/ψ mass. Prompt background contributions are suppressed by the requirement on the proper decay time of the $B^{\pm}$ candidate with $\tau > 0.2$ ps.

The tagging probabilities are determined from B^{+} and B^{-} signal events. These signal yields are derived from fits to the invariant mass distribution, $m(J/\psi K^{\pm})$, and performed in intervals of the cone charge.

7.3.2 Opposite side leptons and jets

After selecting the $B^{\pm}$ candidate, the OST tag methods are required to pass additional selection criteria.

Only muons with the Tight or Low-p_{T} qualities are considered. The muon rapidity must belong to the region of pseudorapidity $|\eta| < 2.5$, and $|\Delta z_0| < 5$ mm, where Δz_0 is the difference in z between the primary vertex and the longitudinal impact parameter of the ID track associated with the muon. To reject the muons associated with the signal, all tracks from the cone $\Delta R < 0.5$ around the $B^{\pm}$ candidate are excluded in the calculation of the cone charge. Electrons must fulfil the same kinematic and Δz_0 requirements. Instead of rejecting the electrons using the cone around the signal candidate, the cosine of the angle between the electron and the signal candidate is required to be $\cos\zeta > 0.93$.

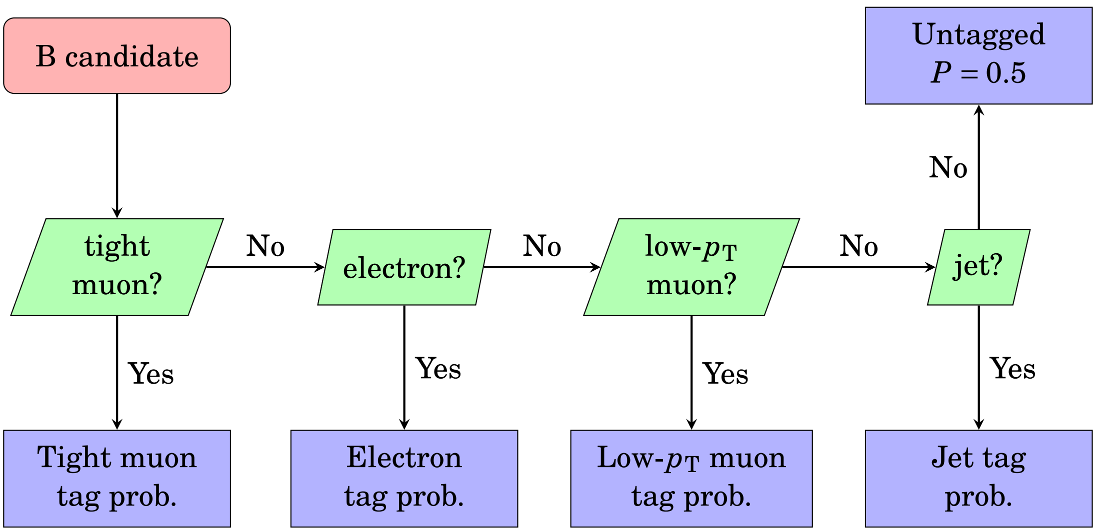

FIGURE 7.2. Diagram for the OST method selection.

The jet tagger containing a b-hadron is used in the absence of leptons. Jets are reconstructed using the anti-k_{T} algorithm [158] with a radius of $\Delta R < 0.4$. The identification of a b-tagged jet uses a multivariate algorithm [162] utilising boosted decision trees (BDT). Only jets with a BDT classifier value larger than 0.56 are considered for the OST.

The tracks in the cones around the leptons and jets must have $p_{\mathrm{T}} > 0.5$ GeV and $|\eta| < 2.5$. Tracks associated with the decay of a B meson signal candidate are excluded from the sum.

The $B^{\pm}$ candidate can have more than one tag method. In that case, the tag method with better precision is prioritised, following the diagram in Figure 7.2.

7.4 $B^{\pm} \to J/\psi K^{\pm}$ Mass Fit

To fit the invariant mass distribution for all $B^{\pm} \to J/\psi K^{\pm}$ candidates, an extended binned likelihood fit is performed using the RooFit toolkit.

The signal mass peak is described by a double-Gaussian with a common mean, and

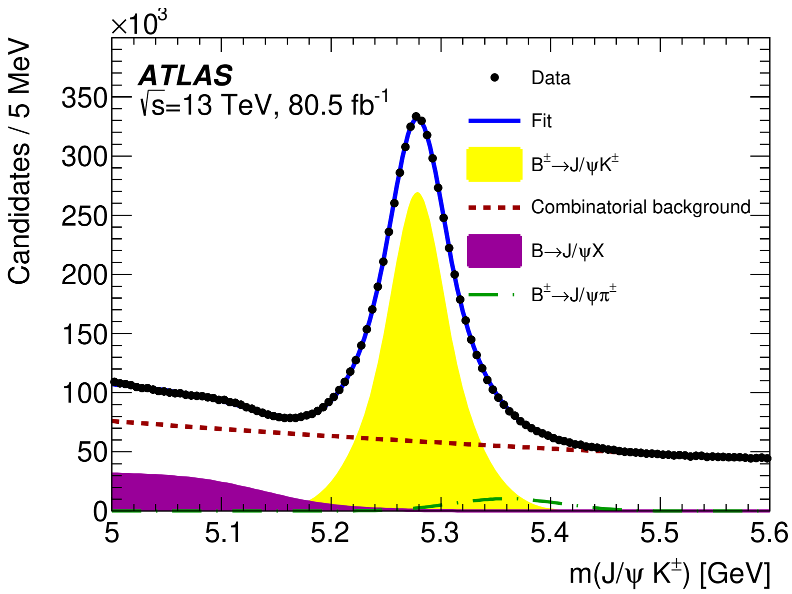

FIGURE 7.3. The invariant mass distribution for selected $B^{\pm} \to J/\psi K^{\pm}$ candidates. Data are shown as points, and the overall result of the fit is given by the blue curve. The contributions from the combinatorial background component are indicated by the red dotted line, partially reconstructed b-hadron decays by the purple shaded area, and decays of $B^{\pm} \to J/\psi\pi^{\pm}$, where the pion is misassigned as a kaon, by the green dashed line.

free parameters for the mass, resolution and yields. For the background, three contributions are considered: the combinatorial background from J/ψ candidates combined with a non-signal track; the contribution from partially or misreconstructed B-decays that manifests at the lower mass region, and a small contribution from $B^{\pm} \to J/\psi\pi^{\pm}$, where the pion is miss-assigned the kaon mass.

The background is modelled by an exponential to describe the combinatorial background and a hyperbolic tangent function to parameterize the low-mass contribution from incorrectly or partially reconstructed B decays. A Gaussian function is used to model the $B^{\pm} \to J/\psi\pi^{\pm}$ contribution, with mean fixed at the world average 5359.68 MeV [46], and width of 49.2 MeV, the yield is left free in the fit. The contributions of non-combinatorial backgrounds are found to have a negligible effect on the tagging procedure. Figure 7.3 shows the invariant mass distribution of B candidates for all rapidity regions overlaid with the fit result for the combined data. In total, 4.3 million signal events are found.

7.5 ATLAS $B^{\pm} \to J/\psi K^{\pm}$ Flavour Tagging Performance

The cone charge distributions for each tag method were split into bins. In each bin, the extended maximum-likelihood mass fit was performed with a hyperbolic tangent shape fixed from the total mass fit. In each bin, the fitted number of B^{+} and B^{-} candidates yields were used to calculate the efficiency, dilution and tag power. Table 7.1 shows the final tagging performance for each tag method. The efficiency ($\varepsilon_{\mathrm{tag}}$) and tagging power ($T_{\mathrm{tag}}$) are each determined by summing over the individual bins of the cone charge distribution. The effective dilution (D_{tag}) is obtained from the measured efficiency and tagging power. For the efficiency, effective dilution, and tagging power, the corresponding uncertainty is determined by combining the appropriate uncertainties in the individual bins of each charge distribution. By definition, there is no overlap between lepton-tagged and jet-charge-tagged events. The overlap between events with a muon (either Tight or Low-p_{T}) and events with an electron corresponds to around 0.6% of all tagged events.

To extract the best tagging performance, the size of the cone with tracks ΔR and the parameter κ in equation (7.4) has been varying independently on each other. The final values are $\Delta R < 0.5$ for each tag method, $\kappa = 1.1$ for muons and jets, and $\kappa = 1$ for electrons. Additionally, the tag method Δz_0 selection cut was optimised to reach the best tagging performance. Further, the tagger p_{T} dependence of efficiency, dilution and tag power has been checked; see Figure 7.4. The dilution appears to have a plateau around

Tag method	ϵ_{tag} [%]	D_{tag} [%]	T_{tag} [%]
Tight muon	4.50 ± 0.01	43.8 ± 0.2	0.862 ± 0.009
Electron	1.57 ± 0.01	41.8 ± 0.2	0.274 ± 0.004
Low-p_{T} muon	3.12 ± 0.01	29.9 ± 0.2	0.278 ± 0.006
Jet	12.04 ± 0.02	16.6 ± 0.1	0.334 ± 0.006
Total	21.23 ± 0.03	28.7 ± 0.1	1.75 ± 0.01

TABLE 7.1. Summary of opposite-side tagging performances for the different flavour tagging methods on the sample of $B^{\pm}$ signal candidates, as described in the text. Uncertainties shown are statistical only.

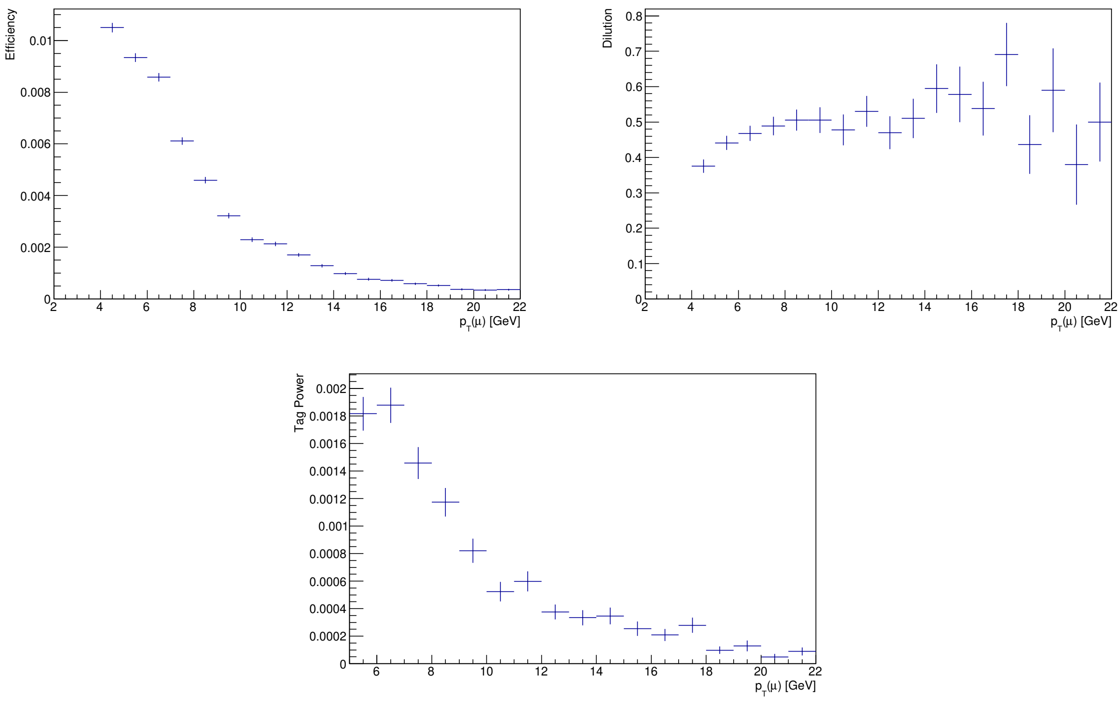

FIGURE 7.4. The dependence of OS Tight muon efficiency, dilution and tag power on its transverse momentum p_{T}.

50% from $p_{\text{T}} > 10$ GeV, the efficiency and tag power are higher for low p_{T} tagging muons.

The optimisation of the b-tag weight cut for the jet tagger is performed as a scan over possible b-tag cut values, and the value that maximises the overall tagging power is selected. From Table 7.2, it can be seen that for a rather broad range of BDT values, the tagging power is constant (within the statistical uncertainties), with the optimal value of BDT cut of 0.56 selected for the analysis.

The last output of the mass fits in the bins of the cone charges is the signal discrete

Rank	BDT	p_{T} [GeV]	D_{tag} [%]	$\varepsilon_{\mathrm{tag}}$ [%]	T_{tag} [%]
0	0.56	15.00	16.6	12.04 ± 0.02	0.3335 ± 0.0062
1	0.54	15.00	16.4	12.31 ± 0.02	0.3327 ± 0.0062
2	0.50	15.00	16.1	12.85 ± 0.02	0.3320 ± 0.0062
3	0.58	15.00	16.8	11.77 ± 0.02	0.3316 ± 0.0062
4	0.48	15.00	15.9	13.12 ± 0.02	0.3309 ± 0.0062
5	0.64	15.00	17.4	10.94 ± 0.02	0.3294 ± 0.0061
6	0.40	15.00	15.2	14.20 ± 0.02	0.3285 ± 0.0062
7	0.70	15.00	18.0	10.09 ± 0.02	0.3258 ± 0.0060
8	0.52	15.00	16.1	12.56 ± 0.02	0.3253 ± 0.0060
9	0.77	15.00	18.9	9.05 ± 0.02	0.3243 ± 0.0060

TABLE 7.2. Jet opposite-side tagging optimisation. The top ten working points of BDT cut value and p_{T} are shown, with corresponding dilution, efficiency, and tagging power.

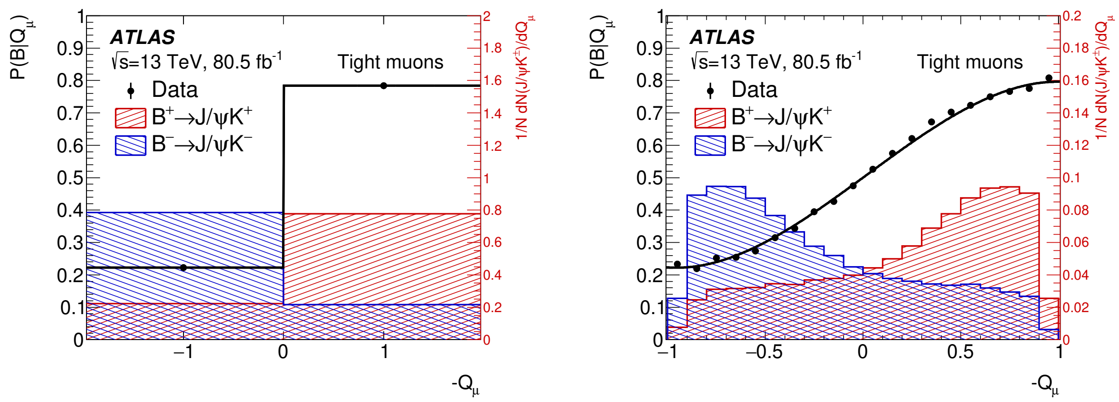

FIGURE 7.5. Cone charge distributions, $-Q_{\mu}$, for Tight muons, shown for cases of discrete charge (left), and for the continuous distribution (right). For each plot, in red (blue), the normalised B^{+} (B^{-}) cone charge distribution is shown (corresponding to the right axis scale). A B^{+} (B^{-}) candidate is more likely to have a large negative (positive) value of Q_{μ}.

(with no additional track around the lepton or jet, or all tracks have the same charge) and continuous cone charge distributions. Figures 7.5, 7.6, 7.7 and 7.8 shows the B^{+} (B^{-}) cone charge distributions.

The distribution of the tagging probability, $P(B|Q_{\mu})$, as a function of the cone charge, is derived from a data sample of $B^{\pm} \to J/\psi K^{\pm}$ decays, and it is defined as the probability

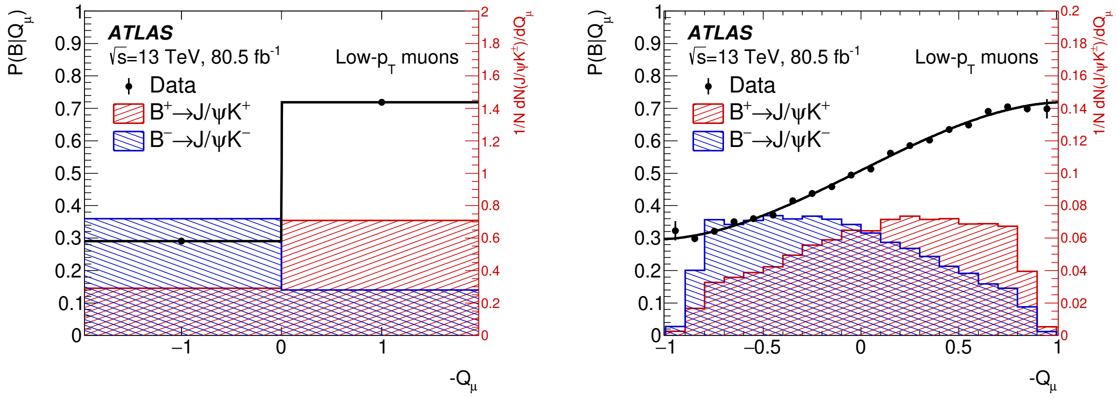

FIGURE 7.6. Normalised cone charge distributions (shown against the right axis scale), $-Q_\mu$, for B^+ (B^-) events shown in red (blue) for Low-p_T muons, for cases of discrete charge (left), and for the continuous distribution (right). Superimposed is the distribution of the tagging probability, $P(B|Q_\mu)$.

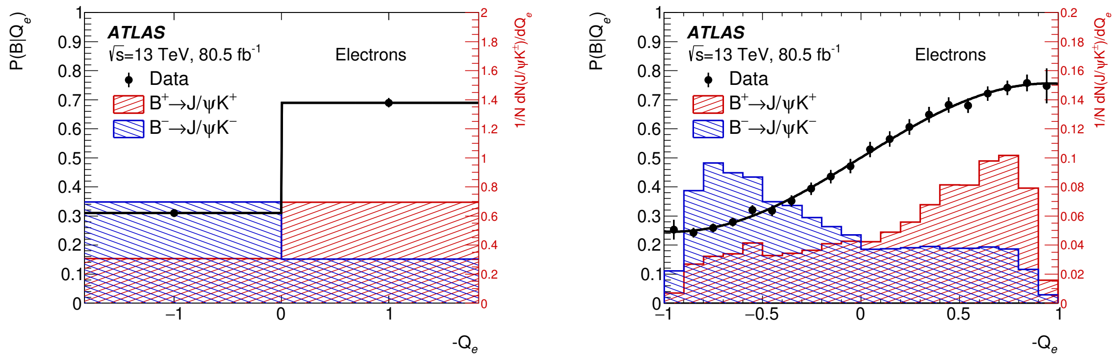

FIGURE 7.7. Normalised cone charge distributions (shown against the right axis scale), $-Q_e$, for B^+ (B^-) events shown in red (blue) for electrons, for cases of discrete charge (left), and the continuous distribution (right). Superimposed is the distribution of the tagging probabilities, $P(B|Q_e)$.

to have a B^+ meson (on the signal-side) given a particular cone charge Q_μ. The fitted parameterisation, shown in black, is used as the calibration curve to infer the probability of B_s^0 initial flavour. The calibration distributions for each tag method are shown in Figures 7.5, 7.6, 7.7 and 7.8. The tight muon, low-p_T muon and jet distribution of the tagging probability are described by the fit using the third-order polynomial function

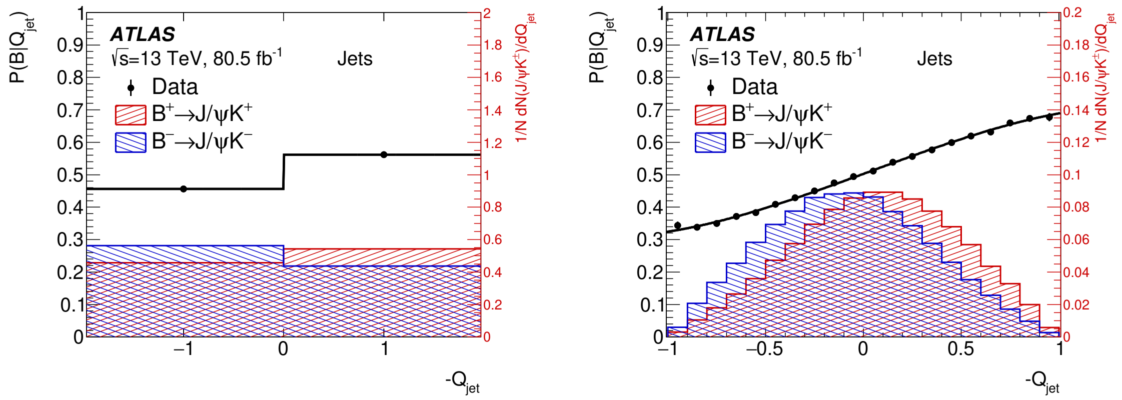

FIGURE 7.8. Normalised cone charge distributions (shown against the right axis scale), $-Q_{\text{jet}}$, for B^+ (B^-) events shown in red (blue) for jets, for cases of discrete charge (left), and the continuous distribution (right). Superimposed is the distribution of the tag probability, $P(B|Q_{\text{jet}})$.

(continuous) and the sum of two constant functions (discrete distribution). The electron distribution of the tagging probability from the discrete cone charges is fitted by the sum of two constant functions, while the continuous electron calibration is described by the sine function.

7.6 Opposite Side Tagging in $B_s^0 \to J/\psi\phi$

The selection of the B_s^0 candidate follows the criteria described in the chapter below. The selection criteria of four tag methods (tight muons, low-p_{T} muons, electrons and jets) are the same as in the case of the $B^\pm \to J/\psi K^\pm$ tagging. The cone charge distribution 7.4 is produced for each tag method. The cases of no additional track around the tagger (discrete tagging) and at least one track around the tagger (continuous tagging) are treated separately.

7.6.1 Continuous Tag Probabilities

For the continuous tagging, the calibration curves in Figures 7.5, 7.6, 7.7 and 7.8 are applied to events with the corresponding tag method and the B_s^0 initial flavour probability is derived in the form of the tag probabilities. To describe the different behaviour of tag probabilities for B_s^0 signal and background, the corresponding tag probabilities are needed to be extracted.

From the calibrations and calculated B_s^0 candidate cone charge, the B_s^0 initial flavour probability is derived. It is directly used in the fit. However, the distributions of tag probabilities for the signal and background are expected to be different irreducible

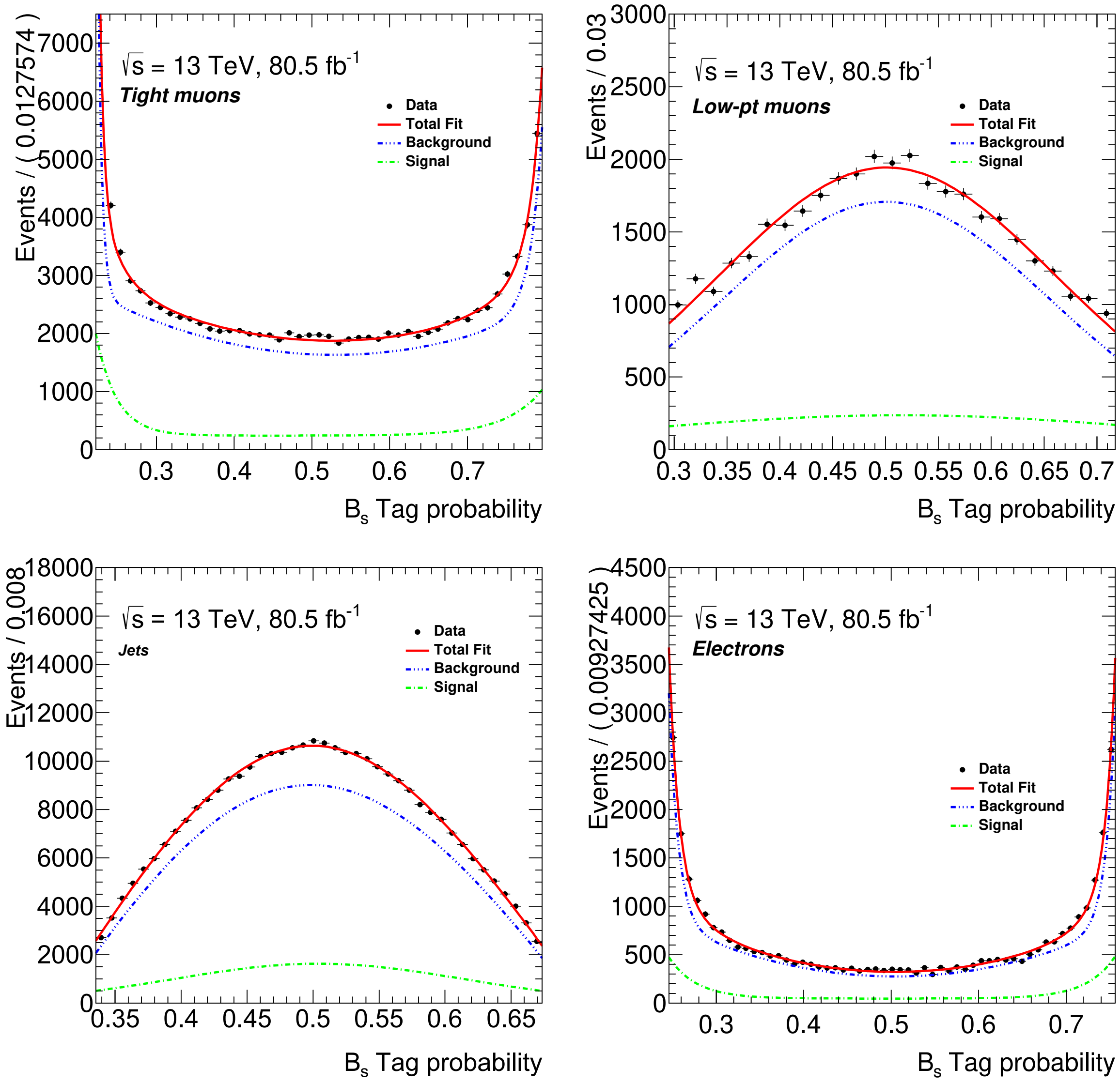

FIGURE 7.9. The tag probability distribution for Tight muons, Low-p_T muons, electrons and jets. The signal $P(B|Q_x)$ function is presented by a green curve, the background $P(B|Q_x)$ function by a blue curve and the sum of the functions (red curve) fits data.

discrepancies between signal and background. Firstly in the mass sideband regions, $5.150 < m(J/\psi K^+K^-) < 5.317$ GeV and $5.417 < m(J/\psi K^+K^-) < 5.650$ GeV, unbinned maximum likelihood fits to the $P(B|Q_x)$ distributions are performed to extract the background description tag probability. For the signal, fits are performed to the $P(B|Q_x)$ distributions, using all events in the $m(B_s^0 \to J/\psi K^+K^-)$ distributions to extract the signal. In these fits, the parameters describing the background functions are fixed to their previously extracted values, as is the relative normalisation of signal and background, extracted from a fit to the $m(J/\psi K^+K^-)$ distribution. Different functions for fitting these sideband distributions are used for different tagging methods. The sum of two exponential and the second-order polynomial function are used for tight muons and electrons signal and background. The Gaussian function is used for signal and background low-p_T muons and signal jets, while the eight-order polynomial function describes the jet sideband data. The tag probability distributions for each tag method with the signal and background separation are shown in Figure 7.9.

Tag method	Signal		Background	
	f_{+1} [%]	f_{-1} [%]	f_{+1} [%]	f_{-1} [%]
Tight muon	6.9 ± 0.3	7.5 ± 0.3	4.7 ± 0.1	4.9 ± 0.1
Electron	20 ± 1	19 ± 1	16.8 ± 0.2	17.3 ± 0.2
Low-p_T muon	10.9 ± 0.5	11.6 ± 0.5	7.0 ± 0.1	7.5 ± 0.1
Jet	3.60 ± 0.15	3.54 ± 0.15	3.05 ± 0.03	3.17 ± 0.03

TABLE 7.3. Fractions f_{+1} and f_{-1} of B_s^0 events with cone charges of +1 and −1, respectively, for signal and background events and for the different tagging methods. Only statistical uncertainties are given.

Tag method	Signal efficiency [%]	Background efficiency [%]
Tight muon	4.06 ± 0.06	3.21 ± 0.01
Electron	1.86 ± 0.04	1.48 ± 0.01
Low-p_T muon	2.95 ± 0.05	2.70 ± 0.01
Jet	12.1 ± 0.1	9.41 ± 0.02
Untagged	79.1 ± 0.3	83.20 ± 0.05

TABLE 7.4. Fractions of signal and background events tagged using the different methods. The efficiencies include both continuous and discrete contributions. Only statistical uncertainties are quoted.

7.6.2 Discrete Tag Probabilities

The tag probabilities of discrete tagging provide tag inferring of the initial flavour of B_s^0, but the signal and background separation is performed using the fractions of discrete-tag events (fractions of spikes). The procedure is very similar to the one used for continuous tagging - simple event counting is performed where the number of signal and background events is evaluated using sideband subtraction. The resulting signal and background fractions of spikes for each tag method are shown in Table 7.3. Finally, the fractions of signal and background events tagged using the different OST methods are found using a similar sideband-subtraction method and are summarised in Table 7.4.

CHAPTER 8

Measurement of the CP-Violating Phase ϕ_s in Neutral B-mesons Decays

The theoretical concept of the CP violation in neutral B mesons is provided in chapter 2. The CP violation in the $B_s^0 \to J/\psi\left(\mu^+\mu^-\right) + \phi\left(K^+K^-\right)$ channel was already measured in Run1 by the ATLAS collaboration. The experimental results were combined with the results of other experiments, shown in Figure 2.8. It can be seen that the combined results are consistent with the SM prediction; however, additional measurements are needed to exclude the Beyond the Standard Model contribution.

8.1 Reconstruction and Data Selection

The analysis presented in this chapter uses 80.5 fb^{-1} of LHC proton–proton data collected by the ATLAS detector during 2015–2017 at a centre-of-mass energy $\sqrt{s} = 13$ TeV.

The reconstructed B_s^0 candidate needs to fulfil several conditions. Each event must pass the trigger condition. The triggers are based on the $J/\psi \to \mu^+\mu^-$ decay identification with muon transverse momentum thresholds of either 4 GeV or 6 GeV. Each event must contain at least one reconstructed primary vertex for four tracks - two oppositely charged muons and two oppositely charged kaons K^+, K^-. The muon pair is refitted to a common vertex, and it must fulfil the fit quality χ^2/n.d.o.f. < 10. The ATLAS detector has various mass resolutions in different parts of the detector depending on the pseudorapidity coordinate. For this reason, the refitted $J/\psi(\mu^+\mu^-)$ candidates are selected in the mass windows according to the pseudorapidity of muons:

- both muons have $|\eta| < 1.05$: $m_{J/\psi} \in (2.959 - 3.229)$ GeV
- both muons have $1.05 < |\eta| < 2.5$: $m_{J/\psi} \in (2.913 - 3.273)$ GeV
- one muon has $|\eta| < 1.05$ and the second has $1.05 < |\eta| < 2.5$: $m_{J/\psi} \in (2.959 - 3.229)$ GeV.

The $\phi \to K^+K^-$ are reconstructed from pair of tracks not identified as muons and fulfil kinematic conditions $p_\mathrm{T} > 1$ GeV, $|\eta| < 2.5$ and the invariant mass must lie in a range of $(1.0085 - 1.0305)$ GeV. Then, the B_s^0 candidates are fitted using all combinations of the J/ψ and ϕ candidates with a common vertex. The B_s^0 candidate is accepted and used in the analysis if the B_s^0 vertex fit quality is χ^2/n.d.o.f. < 3 and the transverse momentum of B_s^0 is greater than 10 GeV. In total, 2 977 526 B_s^0 candidates are collected within the mass range of $(5.15 - 5.65)$ GeV in Run 2. The lifetime of the B_s^0 meson is the proper decay time t estimated by the relation

$$t = \frac{L_{xy} m_B}{p_{\mathrm{T}B}}, \tag{8.1}$$

where the transverse decay length, L_{xy}, is the displacement in the transverse plane of the B_s^0 meson decay vertex relative to the primary vertex, projected onto the direction of the B_s^0 transverse momentum. The B_s^0 candidate mass and transverse momentum are denoted as m_B and $p_{\mathrm{T}B}$, respectively. No lifetime cut is used in order to allow precise determination of the properties of the background events.

Due to the large pile-up in Run2 (the average number of interactions per bunch crossing between 2015 and 2017 is 30), the number of B_s^0 candidates are formed to be the primary vertex (PV). Several approaches to the candidate selection to be the best PV can be used. The commonly used MAX$\sum p_\mathrm{T}^2$ and MINA0. MAX$\sum p_\mathrm{T}^2$ select the best candidate as the PV with the highest sum of the squares of the constituent tracks' transverse momenta $\sum p_\mathrm{T}^2$. MINA0 select the best PV with the lowest three-dimensional impact parameter a_0, which is calculated as the minimum distance between each primary vertex candidate and the line extrapolated from the reconstructed B_s^0 meson vertex in the direction of the B_s^0 momentum.

8.2 Muon Trigger Proper Decay Time-Dependent Efficiency

The ATLAS trigger strategy uses no minim cut of the transverse impact parameter d_0 but applies the maximum cut $d_0 < 10$ mm in the triggers (full trigger list is shown in appendix chapter C. The applied cut results in inefficiencies at larger values of the proper decay time. This effect was studied by using the MC with 10^8 B_s^0 candidates. In this sample, the B_s^0 proper decay time distribution of an unbiased sample was compared with the distribution obtained after including the trigger. The final trigger efficiency distributions are fitted for each year by the function

$$\frac{1}{w_{\text{trigger}}} = \epsilon = p_0 \left[1 - p_1 \left(\text{Erf}\, \frac{t - p_3}{p_2} \right) + 1 \right], \tag{8.2}$$

where Erf denotes the error function and $p0$, $p1$, $p2$ and $p3$ are parameters determined in the fit to MC events. The function is normalized to obtain $w_{\text{trigger}}(0) = 1$, and the final weights $w_{\text{trigger}}(t)$ are applied to the B_s^0 data. The data and MC from the years 2015 and 2017 do not indicate triggers with extra lifetime bias, while significant bias is observed in the early 2016 data (before the run number 302737). The example of the lifetime correction for biased 2016 (before the run number 302737) triggers and unbiased 2017 triggers can be seen in Figure 8.1.

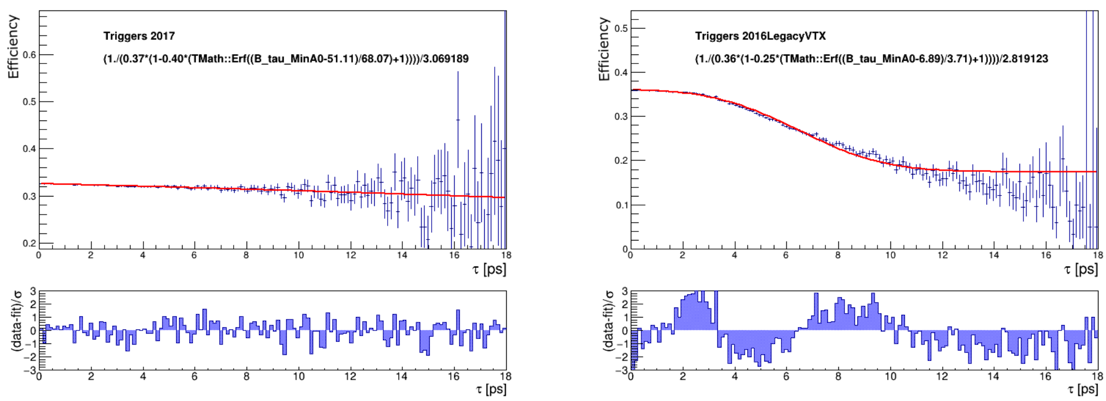

FIGURE 8.1. The time-dependent inefficiency with the respective fit curves. The lifetime corrections for the 2017 trigger group (left) and the correction applied to the biased triggers (right) are shown.

8.3 Detector Acceptance

The signal $B_s^0 \to J/\psi\left(\mu^+\mu^-\right) + \phi\left(K^+K^-\right)$ angular description (applied in the section 8.5.1) must be corrected for the detector acceptance. Signal acceptances are built in the form of a 4-dimensional matrix: 3 dimensions are angles $\Omega = (\theta_T, \psi_T, \phi_T)$ and the fourth dimension is p_{T} of the B_s^0 meson.

Acceptances were determined using MC events. It takes into account triggers and their prescales, reconstruction and selection cuts. $B_s^0 \to J/\psi\phi$ signal is generated in Pythia with flat angular distributions. These distributions remain flat when no p_{T} or eta cuts are present and are flat in 3D dimensional space of signal angles, θ_T, ψ_T and ϕ_T, and also in B_s^0 p_{T}. After simulating triggers, offline reconstruction and event selections, the angle distributions became shaped, and these shapes are different in different B_s^0 p_{T} intervals. In the simulated, reconstructed and selected MC events, the values of

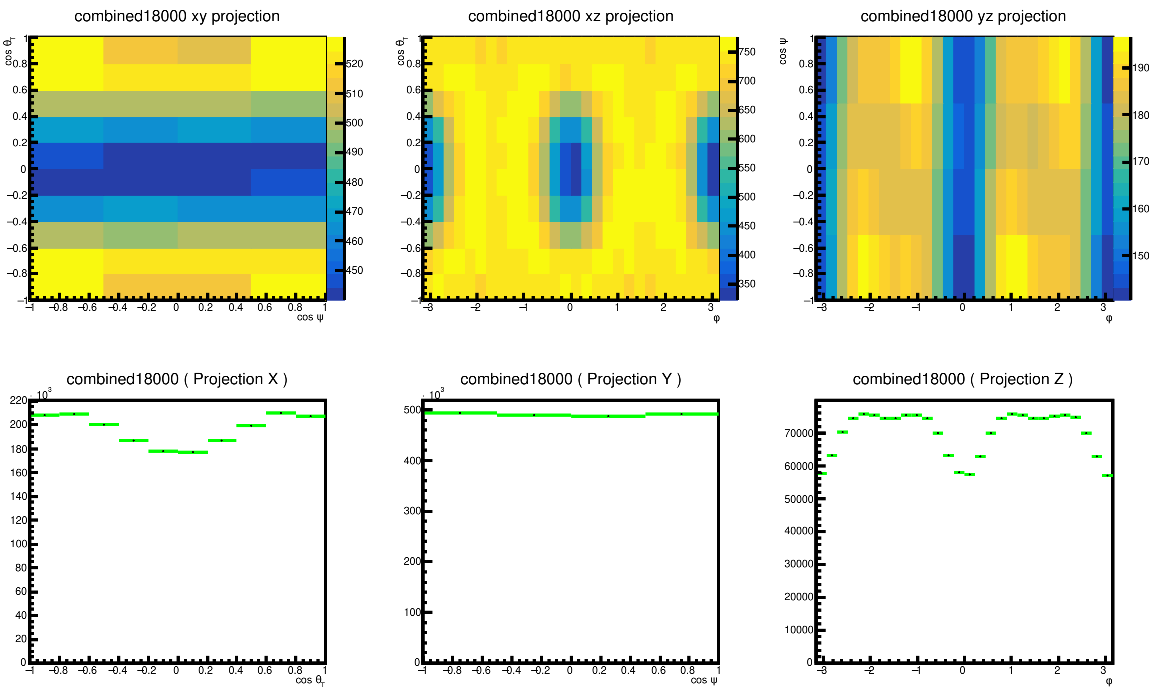

FIGURE 8.2. 2D (top) and 1D (bottom) projections of the 4-dimensional signal acceptance maps. Three plots on the top row from left to right are made for $(\cos\psi_T : \cos\theta_T)$, $(\ \phi_T : \cos\theta_T)$ and $(\ \phi_T : \cos\psi_T)$, the color depicts the number of events in each bin. The bottom row shows number of candidates in each bin of angular distributions. Only acceptance maps for the $p_{\mathrm{T}} \in (18;22)$ GeV bin are shown here.

each candidate angles and the p_{T} are used to make p_{T} dependent maps - effectively a 4-dimensional histogram. These acceptances are used to weigh data in the fit.

To account for the differing trigger menus and pre-scales during the data taking, the total luminosity is calculated (using data from lumicalc[1]) for each unique trigger menu relevant to presented analysis. The generated MC sample is then split in proportion to the size of each unique trigger menu collected. Events are rejected from each sub-sample in a way that emulates the effect of the trigger pre-scaling for that period of data taking. Weighting terms are applied to confirm p_{T} and η distributions to match data.

2D and 1D projections of the 4-dimensional acceptance maps produced by this method are shown in Figure 8.2.

The shape of the background detector angular acceptance describes the detector and kinematic effects for background events and is modelled by Legendre polynomial

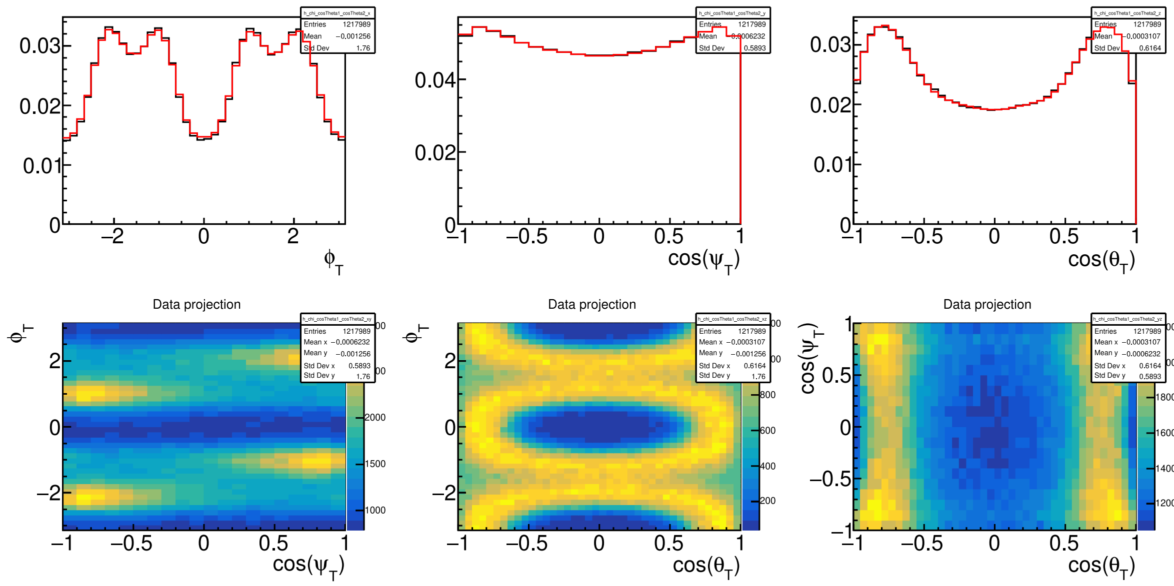

FIGURE 8.3. 1D (top) and 2D (bottom) projections of the 4-dimensional combinatorial background acceptance maps. The top row shows normalized number of candidates in each bin of angular distributions. Three plots on the bottom row from left to right are made for ($\cos\psi_T : \cos\theta_T$), ($\phi_T : \cos\theta_T$) and ($\phi_T : \cos\psi_T$), the color depicts the number of events in each bin. Only acceptance maps for the $p_{\mathrm{T}} < 15$ GeV bin are shown here.

[1]A website-available tool for luminosity calculation: https://atlas-lumicalc.cern.ch/.

functions

$$
\begin{aligned}
Y_l^m(\theta_T) &= \sqrt{(2l+1)/(4\pi)}\sqrt{(l-m)!/(l+m)!}P_l^{|m|}(\cos\theta_T), \\
P_k(x) &= \frac{1}{2^k k!}\frac{\mathrm{d}^k}{\mathrm{d}x^k}(x^2-1)^k, \\
P_b(\theta_T,\psi_T,\phi_T) &= \sum_{k=0}^{6}\sum_{l=0}^{6}\sum_{m=-l}^{l}
\begin{cases}
a_{k,l,m}\sqrt{2}Y_l^m(\theta_T)\cos(m\phi_T)P_k(\cos\psi_T) & \text{where } m>0 \\
a_{k,l,m}\sqrt{2}Y_l^{-m}(\theta_T)\sin(m\phi_T)P_k(\cos\psi_T) & \text{where } m<0 \\
a_{k,l,m}\sqrt{2}Y_l^{0}(\theta_T)P_k(\cos\psi_T) & \text{where } m=0.
\end{cases}
\end{aligned}
\tag{8.3}
$$

The coefficients $a_{k,l,m}$ are adjusted to give the best fit to the angular distributions for events in the B_s^0 mass sidebands (between 5.150 and 5.650 GeV excluding the signal mass region $|(m(B_s^0) - 5.366\text{ GeV})| < 0.110$ GeV). Similarly to the signal, the combinatorial background angular distributions are sensitive to the p_{T} of B_s^0, so the Legendre polynomial functions calculation is performed in several p_{T} intervals: (10––15) GeV, (15–20) GeV, (20–25) GeV, (25–30) GeV, (30–35) GeV and $p_{\mathrm{T}} > 35$ GeV. 1D and 2D projections for the first p_{T} bin are shown in Figure 8.3.

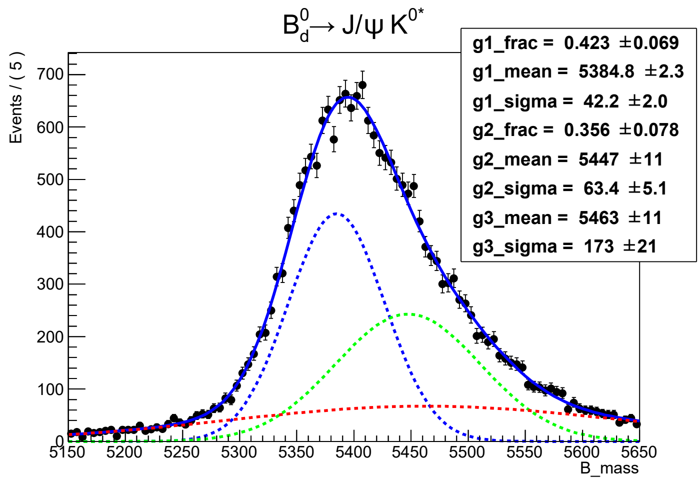

FIGURE 8.4. Fitted mass distribution of $B_d^0 \to J/\psi K^{*0}$ decay after B_s^0 selection cuts and a wrong mass assignment. three Gaussian components are shown separately in plot.

8.4 B_d^0 and Λ_b Physics Backgrounds

The B_s^0 selected sample is not pure due to the possible $\pi^{\pm}$ and p misidentification as $K^{\pm}$. The considered contaminating peaking backgrounds are $B_d^0 \to J/\psi K^{*0}$ and $\Lambda_b \to J/\psi p K^{-}$.

8.4.1 $B_d^0 \to J/\psi K^{*0}$ Background

The $B_d^0 \to J/\psi K^{*0}$ peaking background, also referred to as B_d reflections, contaminates the signal due to the B_d being reconstructed as a B_s^0 meson. Therefore, it lies within the B_s meson mass window rather than in the usual B_d mass range.

To describe this background, a sample of fully simulated $B_d^0 \to J/\psi K^{*0}$ decay and the respective decays of their $\overline{B}_d$ mesons were generated with the transversity amplitude parameters measured by LHCb [163]. These events were then mis-reconstructed as $B_s^0 \to J/\psi \phi$ decays (including a wrong mass assignment of kaon mass to a final state pion). This procedure distorted the shapes of the generated B_d mass and transversity angles, and the resulting shapes were fitted by specific functions. Parameters of these functions were fixed in the main B_s^0 fit. The mass was described by a sum of 3 independent Gaussian distributions, the plot with fit results is shown in Figure 8.4.

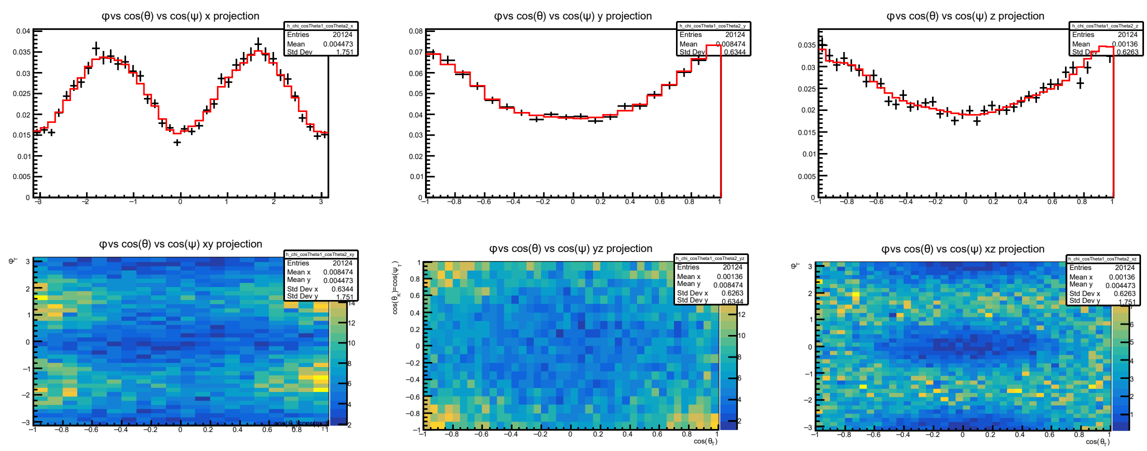

FIGURE 8.5. 1D (top) and 2D (bottom) projections of the 3-dimensional $B_d^0 \to J/\psi K^{*0}$ acceptance maps. The top row shows normalized number of candidates in each bin of angular distributions. Three plots on the bottom row from left to right are made for ($\cos\psi_T : \cos\theta_T$), ($\phi_T : \cos\theta_T$) and ($\phi_T : \cos\psi_T$), the color depicts the number of events in each bin.

The transversity amplitude parameters measured by LHCb [163] are used to generate the B_d angles. Using the generated MC, fiducial, trigger and B_s^0 selection cuts (after a wrong mass assignment) were applied to produce 3-D angular distributions of $B_d^0 \to J/\psi K^{*0}$ and that were then fitted by Legendre polynomial functions (8.3). The projections are shown in Figure 8.5.

The fraction of the $B_d^0 \to J/\psi K^{*0}$ contamination in the B_s^0 sample is estimated as follows:

$$f_{B_d} = \frac{f_d}{f_s} \frac{\mathscr{B}(B_d^0 \to J/\psi K^{*0})\mathscr{B}(K^{*0} \to K^+\pi^-)}{\mathscr{B}(B_s^0 \to J/\psi\phi)\mathscr{B}(\phi \to K^+K^-)} \times \frac{\varepsilon_{sel}^{bkg}}{\varepsilon_{sel}^{sig}}, \tag{8.4}$$

where f_d/f_s is the ratio of fragmentation fractions of B_d and B_s hadrons taken from LHCb[164] measurements. The branching ratios $\mathscr{B}(B_s^0 \to J/\psi\phi)$ and $\mathscr{B}(\phi \to K^+K^-)$ are taken from [46]. ε_{sel}^{bkg} and ε_{sel}^{sig} are the selection efficiencies for background and signal decays multiplied by the acceptance. They are estimated using samples of fully simulated $B_d^0 \to J/\psi K^{*0}$ decay and analysis selection cuts. The final fraction of B_d contamination in the B_s^0 sample is $f_{B_d} = (3.77 \pm 0.45)\%$.

8.4.2 $\Lambda_b \to J/\psi p K^-$ Background

The background contribution to the B_s^0 sample follows the same procedure as for the B_d contamination. Firstly, the mass shape model was extracted from the fit to MC mass distribution, see Figure 8.6.

The 3-D angular distributions were obtained from the flat-generated MC. Fiducial, trigger and B_s^0 selection cuts (after a wrong mass assignment) were applied to produce

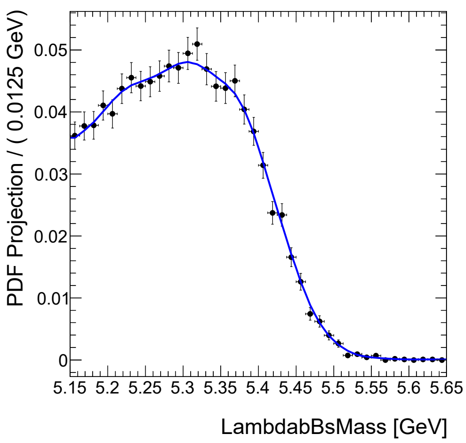

FIGURE 8.6. Fitted mass distribution of $\Lambda_b \to J/\psi p K^-$ decay after B_s^0 selection cuts and a wrong mass assignment.

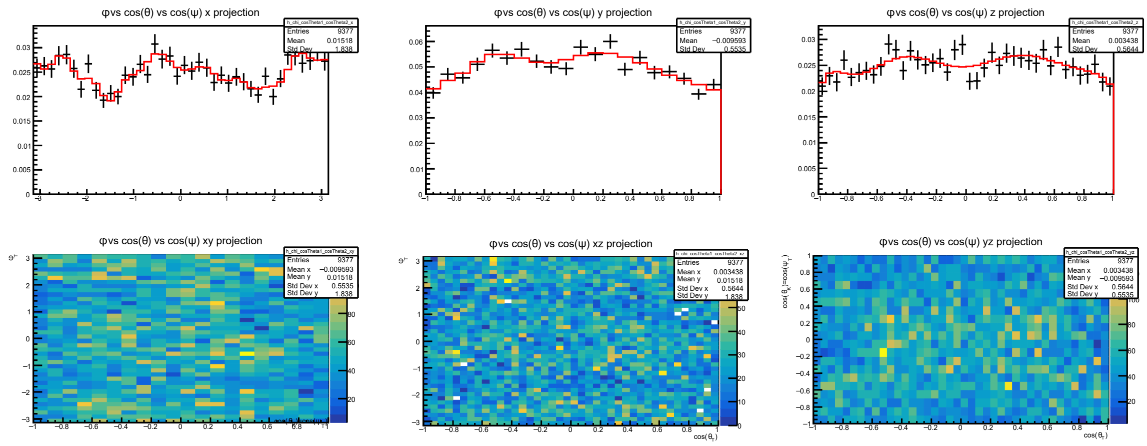

FIGURE 8.7. 2D (top) and 1D (bottom) projections of the 3-dimensional $\Lambda_b \to J/\psi p K^-$ acceptance maps. The top row shows normalized number of candidates in each bin of angular distributions. Three plots on the bottom row from left to right are made for ($\cos\psi_T : \cos\theta_T$), ($\phi_T : \cos\theta_T$) and ($\phi_T : \cos\psi_T$), the color depicts the number of events in each bin.

3-D angular distributions of $\Lambda_b \to J/\psi p K^-$ that were then fitted by Legendre polynomial functions (8.3). The projections are shown in Figure 8.7.

The relative fractions of Λ_b events within the B_s^0 fit are given as follows:

$$\frac{N_{\Lambda_b}}{N_{B_s^0}} = \frac{f_{\Lambda_b}}{f_s} \frac{\mathscr{B}(\Lambda_b \to J/\psi p K^-)}{\mathscr{B}(B_s^0 \to J/\psi\phi)\mathscr{B}(\phi \to K^+K^-)} \frac{\epsilon_{\Lambda_b}}{\epsilon_{B_s^0}} \tag{8.5}$$

With f_{Λ_b}/f_s and $Br(\Lambda_b \to J/\psi p K^-)$ taken from recent LHCb results [165, 166]. $\epsilon_{\Lambda_b} = (0.001969 \pm 0.000143)$ and $\epsilon_{B_s^0} = (0.086210 \pm 0.000673)$ have been determined from the MC. The final fraction of Λ_b events in the B_s^0 sample is $N_{\Lambda_b}/N_{B_s^0} = (2.1 \pm 0.6)\%$.

8.5 Maximum Likelihood Fit

An unbinned maximum likelihood (ML) fit is performed on the selected events to extract the parameter values of the $B_s^0 \to J/\psi\left(\mu^+\mu^-\right) + \phi\left(K^+K^-\right)$ decay. The fit uses information about the reconstructed mass, m_i, the measured proper decay time, t_i, the measured mass uncertainty, σ_{m_i}, the measured proper decay time uncertainty, σ_{t_i}, the measured transverse momentum, p_{T}, the tagging probability, $P(B|Q_x)$, and the transversity angles, Ω, of each $B_s^0 \to J/\psi\phi$ decay candidate. The measured value of the proper decay time uncertainty, σ_t, is calculated from the covariance matrix associated with the vertex fit for each candidate event. The transversity angles $\Omega = (\theta_T, \psi_T, \phi_T)$ are defined in Figure 2.7 in chapter 2.

The likelihood function is a combination of signal and background probability density functions,

$$\begin{aligned} L = \sum_{i=1}^{N} w_i \ln \Big[& f_s F_s\left(m_i, t_i, \sigma_{t_i}, \Omega_i, p_{\mathrm{T}_i}, P(B|Q)\right) + f_s f_{B^0} F_{B^0}\left(m_i, t_i, \sigma_{t_i}, \Omega_i, p_{\mathrm{T}_i}, P(B|Q)\right) \\ & + f_s f_{\Lambda_b} F_{\Lambda_b}\left(m_i, t_i, \sigma_{t_i}, \Omega_i, p_{\mathrm{T}_i}, P(B|Q)\right) \\ & + \left(1 - f_s(1 + f_{B^0} + f_{\Lambda_b})\right) F_{bkg}\left(m_i, t_i, \sigma_{t_i}, \Omega_i, p_{\mathrm{T}_i}, P(B|Q)\right) \Big], \end{aligned} \tag{8.6}$$

where N is a number of events, f_s is the signal fraction, f_{B^0} and f_{Λ_b} are the fraction of B_d and Λ_b wrongly identified as the B_s^0 candidate (these fractions are obtained from the Monte Carlo analysis and are set to be constant in this fit). The F_s, F_{B^0}, F_{Λ_b} and F_{bkg} are the probability density function (PDF) describing the signal, B_d^0 background, Λ_b background and other background distributions. The F_{B^0}, F_{Λ_b} probability density functions are modelled by fitting the MC and fixed in the main fitting procedure (see section 8.4). The fractions of B_d, Λ_b events are calculated in the section 8.4 and are fixed during the main fit. The trigger inefficiencies are corrected by the efficiency weight w_i calculated per event using the formula (8.2). The PDFs for signal and combinatorial background are detailed in the sections below.

8.5.1 Signal PDF

The signal PDF is modelled by the function

$$\begin{aligned} F_s(m_i, t_i, \sigma_{m_i}, \sigma_{t_i}, \Omega_i, P_i(B|Q_x), p_{\mathrm{T}_i}) = & P_s(m_i|\sigma_{m_i}) \cdot P_s(t_i, \Omega_i|\sigma_{t_i}, P_i(B|Q_x)) \\ & \cdot P_s(\sigma_{m_i}|p_{\mathrm{T}_i}) \cdot P_s(\sigma_{t_i}|p_{\mathrm{T}_i}) \cdot P_s(P_i(B|Q_x)) \\ & \cdot A(\Omega_i, p_{\mathrm{T}_i}) \cdot P_s(p_{\mathrm{T}_i}), \end{aligned} \tag{8.7}$$

which contains contributions from the description of mass, proper decay time, angles, tagging information, proper decay time error and transverse momentum distributions. The detector acceptances are modelled before the fit and enter the signal PDF as a correction term (see section 8.3 for further details).

The mass is described by the Gauss function with the per-candidate mass errors σ_{m_i}:

$$P_s(m_i|\sigma_{m_i}) \equiv \frac{1}{\sqrt{2\pi} S_m \sigma_{m_i}} \cdot \mathrm{e}^{\frac{-(m_i - m_{B_s})^2}{2(S_m \sigma_{m_i})^2}}, \tag{8.8}$$

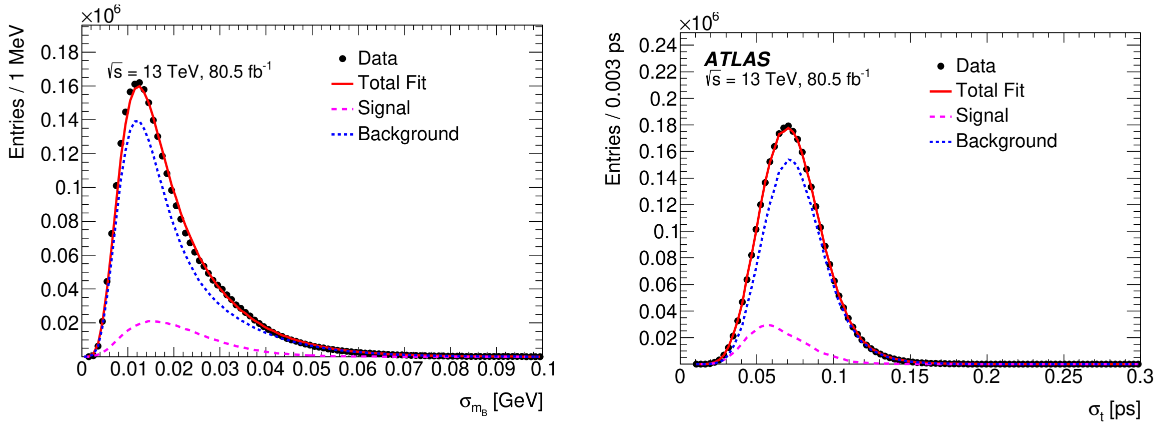

FIGURE 8.8. The proper decay time (right) and mass (left) uncertainty distributions for data (black), and the fits to the background (blue) and the signal (purple) contributions. The total fit is shown as a red curve.

where m_{B_s} is the expected PDG [46] mass of B_s^0, σ_{m_i} is the per-candidate mass error calculated from the covariance matrix associated with the four-track vertex fit of $B_s^0 \to J/\psi\phi$ candidate and S_m is the scale factor to account for any mismeasurements. Following the rules of conditional probability, the total signal PDF contains the term $P_s(\sigma_{m_i}|p_{\mathrm{T}_i})$ that define the mass uncertainty distribution. It is p_{T}-dependent, so an additional term $P_s(p_{\mathrm{T}_i})$ for transverse momentum distribution is included in equation (8.7). The signal and background overall components of mass uncertainty distribution are shown in Figure 8.8.

The proper decay time and angle distributions are described in equation (8.7) by $P_s(t_i, \Omega_i|\sigma_{t_i}, P_i(B|Q_x))$. It combines the proper decay time and angle by the relation (2.64), whose components are provided in Table 2.3. Chapter 2 provides detailed theoretical background of this relation. The proper decay time has three corrections. Firstly, the term (2.64) is smeared by the resolution function

$$R(t^{'} - t_i, \sigma_{t_i}) \equiv \frac{1}{\sqrt{2\pi}\, S_t\, \sigma_{t_i}} \cdot e^{\frac{-(t_i^{'}-t_i)^2}{2(S_t \sigma_{t_i})^2}}. \tag{8.9}$$

Here, S_t is a scale factor (a parameter of the fit), and σ_{t_i} is the per-candidate uncertainty on proper decay time t_i (similarly to the signal mass distribution). This convolution is performed numerically on an event-by-event basis, and the value σ_{t_i} is measured for each B_s^0 candidate, based on the tracking error matrix of the four final state particles (see Figure 8.8). The proper decay time angular description (2.64) is extended to include the information about the B_s^0 initial flavour:

$$P_s(t_i,\Omega_i|\sigma_{t_i},P_i(B|Q_x)) = \frac{\mathrm{d}^4\Gamma}{\mathrm{d}t\mathrm{d}\Omega} = \sum_{k=1}^{10} A_k \left(P(B|Q)T_k + (1-P(B|Q))\overline{T}_k\right) g_k(\theta_T,\psi_T,\phi_T), \tag{8.10}$$

where T_k and $\overline{T}_k$ differs in the sign of terms with $\pm$ in Table 2.3. Due to the different shapes of signal and background tag probability distributions (see Figure 7.9, further details provided in chapter 7), the equation (8.10) is multiplied by $P_s(P_i(B|Q_x))$ in (8.7).

8.5.2 Background PDF

The combinatorial background PDF is modelled by

$$\begin{aligned} &F_{bkg}(m_i,t_i,\sigma_{t_i},\Omega_i,P(B|Q),p_{\mathrm{T}_i}) = \\ &\quad = P_b(m_i|\sigma_{m_i})\cdot P_b(t_i|\sigma_{t_i})\cdot P_b(P(B|Q))\cdot P_b(\Omega_i)\cdot P_b(\sigma_{m_i})\cdot P_b(\sigma_{t_i})\cdot P_b(p_{\mathrm{T}_i}), \end{aligned} \tag{8.11}$$

where $P_b(\sigma_{t_i})$ and $P_b(p_{\mathrm{T}_i})$ are modelled by gamma functions, $P_b(P(B|Q))$ is the term describing the B_s^0 tag probability, $P_b(m_i)$ is an exponential function with a constant term added, $P_b(t_i|\sigma_{t_i})$ is parametrised as a prompt peak modelled by a Gaussian distribution (modelling the combinatorial background events, which are expected to have reconstructed lifetimes distributed around zero), two positive exponential functions (representing a fraction of longer-lived backgrounds with non-prompt J/ψ, combined with hadrons from the primary vertex) and a negative exponential function (taking into account events with poor vertex resolution). The background shapes of $P_b(\sigma_{t_i})$ and $P_b(\sigma_{m_i})$ distributions are shown in Figure 8.8 and are fixed in the main fit procedure. $P_b(\Omega_i)$ describes the background angles calculated by the Legendre polynoms (8.3) (shown in Figure 8.3) and is also fixed.

The terms F_{B^0}, F_{Λ_b} in (8.6) follow a similar description as the combinatorial background PDF (8.11) with differences of angles and mass modelling that is detailed in section 8.4.

8.5.3 Parameters of interests

The full simultaneous unbinned maximum-likelihood fit contains nine physical parameters: $\Delta\Gamma_s$, ϕ_s, Γ_s, $|A_0(0)|^2$, $|A_\parallel(0)|^2$, $\delta_{||}$, $\delta_\perp$, $|A_S(0)|^2$ and δ_S. The parameter δ_0 was set to 0. Other parameters in the full fit are signal fraction f_s, terms describing the B_s^0 mass, decay time, and decay time uncertainty distributions. In addition, there are also 353 nuisance parameters describing the background and acceptance functions that are

	ϕ_s [mrad]	$\Delta\Gamma_s$ [ns^{-1}]	Γ_s [ns^{-1}]	$\|A_\parallel(0)\|^2$ [10^{-3}]	$\|A_0(0)\|^2$ [10^{-3}]	$\|A_S(0)\|^2$ [10^{-3}]	$\delta_\perp$ [mrad]	$\delta_\parallel$ [mrad]	$\delta_\perp-\delta_S$ [mrad]
Tagging	19	0.4	0.3	0.2	0.2	1.1	17	19	2.3
ID alignment	0.8	0.2	0.5	< 0.1	< 0.1	< 0.1	11	7.2	< 0.1
Acceptance	0.5	0.3	< 0.1	1.0	0.9	2.9	37	64	8.6
Time efficiency	0.2	0.2	0.5	< 0.1	< 0.1	0.1	3.0	5.7	0.5
Best candidate selection	0.4	1.6	1.3	0.1	1.0	0.5	2.3	7.0	7.4
Background angles model:									
Choice of fit function	2.5	< 0.1	0.3	1.1	< 0.1	0.6	12	0.9	1.1
Choice of p_T bins	1.3	0.5	< 0.1	0.4	0.5	1.2	1.5	7.2	1.0
Choice of mass window	9.3	3.3	0.2	0.4	0.8	0.9	17	8.6	6.0
Choice of SB intervals	0.4	0.1	0.1	0.3	0.3	1.3	4.4	7.4	2.3
Dedicated backgrounds:									
B_d	2.6	1.1	< 0.1	0.2	3.1	1.5	10	23	2.1
Λ_b	1.6	0.3	0.2	0.5	1.2	1.8	14	30	0.8
Alternate Δm_s	1.0	< 0.1	< 0.1	< 0.1	< 0.1	< 0.1	15	4.0	< 0.1
Fit model:									
Time res. sig frac	1.4	1.1	0.5	0.5	0.6	0.8	12	30	0.4
Time res. p_T bins	0.7	0.5	0.8	0.1	0.1	0.1	2.2	14	0.7
S-wave phase	0.3	< 0.1	< 0.1	< 0.1	< 0.1	0.2	8.0	15	37
Fit bias	5.7	1.3	1.2	1.3	0.4	1.1	3.3	19	0.3
Total	22	4.3	2.2	2.3	3.8	4.6	55	88	39

TABLE 8.1. Summary of systematic uncertainties assigned to the physical parameters of interest.

fixed at the time of the fit. Parameters Δm_s and $|\lambda|$ in Table 2.3 are fixed in the fitting procedure to the PDG [46] values $\Delta m_s = (17.757 \pm 0.021)$ ps^{-1} and $|\lambda| = 1$.

8.6 Systematic Uncertainties

To detect the external effect on extracted results (like tag probabilities, detector acceptances, B^0 and Λ_b backgrounds and others), several tests were performed. Also, the effects of PDF modelling, event reconstruction or MC limitation were examined. These tests show no significant bias, as well as no systematic underestimation of the statistical errors reported from the fit to data. The list of all systematics is provided below, the tagging systematic uncertainties are described in detail in the next sections. The systematic uncertainties are listed in Table 8.1.

Flavour tagging: Several sources contribute to the systematic uncertainty due to flavour tagging. Firstly, the effect of the OST calibration precision is estimated by changing the models used to parameterise the probability distribution (shown in Figures 7.5, 7.6, 7.7 and 7.8). A set of alternative functions was used: first-order and fifthorder polynomial and sine functions. The calibration procedure described in chapter 7 was tested by producing the calibrations from the B_s^0 and $B^\pm$ simulated samples. The variations between the curves from these two samples are propagated to the calibration curves derived from the data, and the fit is performed and compared to the nominal one. The potential dependencies on the pile-up distribution were also tested by splitting the sample into the three pile-up bins with equivalent data sizes. The calibrations were produced, and the fit was performed for each set of data. Lastly, the variations of B_s^0 tag probability parameterisation are considered by using histograms instead of parameterization. For each test, differences between the nominal and the modified fit for the parameters of interest are taken as a systematic uncertainty. A detailed description of each contribution to the systematic uncertainty due to the flavour tagging is in appendix B.

ID alignment: To study a potential effect of the ID misalignments on the fit results, the systematic test was done by multiplying the B_s^0 proper-decay times and p_{T} values by a coefficient (1+ δ), where δ is equal to 0.0005 (observed radial distortion in [167]). Differences in the fit parameters between the default fit and the alternative fit, taking into account the ID distortions, are taken as systematic uncertainties.

Angular acceptance method: The detector acceptances (see section 8.3) are calculated as a binned fit to MC simulated data. The different binning, different acceptance functions and different numbers of p_{T} bins are used to produce new sets of acceptance. These are used in the alternative fits, and their deviations from the nominal fit are considered systematic uncertainty.

Time efficiency: The efficiencies are produced from the MC for each year. To estimate systematic uncertainties connected with this procedure, several alternative fits are performed. Firstly, different binning of the efficiencies are used to produce the efficiency function (8.2). Secondly, the triggers are split into smaller groups (not years) that can reflect trigger differences.

Best candidate selection: The sample for the nominal fit uses the best χ^2 selection in a case of multiple candidates per event (5% of events). To account for the possible systematic shift of parameters due to this selection, all candidates from events were used in the alternative fit.

Background angular distribution model: The shape of the background angular distribution is calculated by Legendre polynomial functions (8.3) with $l = 14$ and $k = 14$ orders. The alternative fit uses the $k = 16$ and $l = 16$ orders, and the differences in the parameters between nominal and alternative fit are taken as systematic uncertainties. In addition, the background angular distributions are produced in p_{T} bins. The systematic uncertainties due to the choice of p_{T} bins are accounted for by varying the bins. Lastly, the Legendre polynomial function was fitted to the sideband sample. The definition of the sidebands uses exclusion of signal mass regions: $|(m(B_s^0) - 5.366\text{ GeV}| > 0.110$ GeV. Alternative fits use different mass windows for signal exclusion.

B_d and Λ contributions: This test account for the wrong estimation of the fraction of the B_s^0 contamination from B_d and Λ_b. Studies are performed by varying the fraction of B_d and Λ_b within the fraction uncertainty. Further, the mass model parameters were also varied to provide slightly different models. The alternative fractions and models were used in the fit, and the fit results differences from the nominal ones are considered systematic uncertainties.

Alternate Δm_s: The systematic uncertainty due to fixing the parameter Δm_s to the PDG value was estimated by running an alternative fit where the default model was altered by releasing Δm_s within a Gaussian constraint.

Fit model mass and lifetime: To estimate the systematic uncertainties due to the signal B_s^0 mass model, the default signal model was altered by adding a second Gaussian function with the same mean as the first Gaussian function in the default model. To test the sensitivity of the part of the fit model describing the lifetime, two systematic tests are performed. The determination of signal and background lifetime errors is sensitive to the choice of p_{T} bins that were varied, and the alternative fit was performed. The fit is also sensitive to the determination of the signal fraction. The fit is repeated by varying this fraction within one standard deviation of its uncertainty, and differences are included in the systematic uncertainty.

Fit model S-wave phase: The proper decay time and angular description in Table 2.3 contains the parameter α that reflect the mass-dependent variations in absolute amplitude and phase of the two amplitudes within the interval $(1.0085 - 1.0305)$ GeV in $m(K^+K^-)$. The value of α is 0.51 ± 0.08 and was calculated from the hypothesis of uniformity of the S-wave amplitude. The α uncertainty is systematic, and it is due to:

mass detector resolution and mass scale uncertainties, uncertainties in the description of the $\phi \to K^+K^-$ resonance (mass, width, and shape descriptions as relativistic Breit-Wigner or Flatté parameterisation), and to uncertainties in the description of the shape and phase variation of the S-wave amplitude. The alternative fit uses the α value shifted according to its uncertainty, and the deviations from the nominal results are taken as systematic uncertainties.

Fit bias: The fit model is complex and can be sensitive to nuisance parameters. This sensitivity can produce a bias in the fit results. To determine the bias, a set of data from the pseudo-experiment (ToyMC) was generated with the model PDF and fitted with the same PDF. The parameter results of the fit to ToyMC samples are expected to form Normal Gaussian distributions (their means are expected to be 0 and the standard deviation to be 1). The differences between the mean of the Gaussian distribution and the default fit results are assumed to be systematic uncertainties.

Parameter	Value	Statistical uncertainty	Systematic uncertainty
ϕ_s [rad]	-0.081	0.041	0.022
$\Delta\Gamma_s$ [ps^{-1}]	0.0607	0.0047	0.0043
Γ_s [ps^{-1}]	0.6687	0.0015	0.0022
$\lvert A_\parallel(0)\rvert^2$	0.2213	0.0019	0.0023
$\lvert A_0(0)\rvert^2$	0.5131	0.0013	0.0038
$\lvert A_S(0)\rvert^2$	0.0321	0.0033	0.0046
$\delta_\perp - \delta_S$ [rad]	-0.25	0.05	0.04
Solution (a)			
$\delta_\perp$ [rad]	3.12	0.11	0.06
$\delta_\parallel$ [rad]	3.35	0.05	0.09
Solution (b)			
$\delta_\perp$ [rad]	2.91	0.11	0.06
$\delta_\parallel$ [rad]	2.94	0.05	0.09

TABLE 8.2. Fitted values for the physical parameters of interest with their statistical and systematic uncertainties. For variables $\delta_\perp$ and $\delta_\parallel$, the values are given for the two solutions (a) and (b). For the rest of the variables, the values for the two minima are consistent. The same is true for the statistical and systematic uncertainties of all the variables. The presented systematic uncertainties were obtained by summing the contributions from Table 8.1 in quadratures.

8.7 Final Results of *CP* Violation in $B_s^0 \to J/\psi\phi$

The fit with the model (8.6) was performed using 80.5 fb^{-1} of LHC proton–proton data collected by the ATLAS detector during 2015–2017 at a centre-of-mass energy $\sqrt{s} = 13$ TeV. The fit results and the mass, proper decay time and angular projections of the fit are also presented. The third part of this section presents the combination of the results with the results from ATLAS Run1.

	$\Delta\Gamma$	Γ_s	$\lvert A_{\parallel}(0)\rvert^2$	$\lvert A_0(0)\rvert^2$	$\lvert A_S(0)\rvert^2$	$\delta_{\parallel}$	$\delta_{\perp}$	$\delta_{\perp}-\delta_S$
ϕ_s	−0.080	0.017	−0.003	−0.004	−0.007	0.007	0.004	−0.007
$\Delta\Gamma$	1	−0.586	0.090	0.095	0.051	0.032	0.005	0.020
Γ_s		1	−0.125	−0.045	0.080	−0.086	−0.023	0.015
$\lvert A_{\parallel}(0)\rvert^2$			1	−0.341	−0.172	0.522	0.133	−0.052
$\lvert A_0(0)\rvert^2$				1	0.276	−0.103	−0.034	0.070
$\lvert A_S(0)\rvert^2$					1	−0.362	−0.118	0.244
$\delta_{\parallel}$						1	0.254	−0.085
$\delta_{\perp}$							1	0.001

TABLE 8.3. Fit correlations between the physical parameters of interest, obtained from the fit for solution (a).

	$\Delta\Gamma$	Γ_s	$\lvert A_{\parallel}(0)\rvert^2$	$\lvert A_0(0)\rvert^2$	$\lvert A_S(0)\rvert^2$	$\delta_{\parallel}$	$\delta_{\perp}$	$\delta_{\perp}-\delta_S$
ϕ_s	−0.084	0.019	−0.011	−0.003	−0.006	0.007	0.005	−0.006
$\Delta\Gamma$	1	−0.586	0.090	0.096	0.057	−0.029	−0.010	0.021
Γ_s		1	−0.116	−0.048	0.071	0.070	0.017	0.015
$\lvert A_{\parallel}(0)\rvert^2$			1	−0.338	−0.110	−0.444	−0.106	−0.052
$\lvert A_0(0)\rvert^2$				1	0.269	0.080	0.017	0.070
$\lvert A_S(0)\rvert^2$					1	0.291	0.060	0.251
$\delta_{\parallel}$						1	0.235	0.097
$\delta_{\perp}$							1	0.056

TABLE 8.4. Fit correlations between the physical parameters of interest, obtained from the fit for solution (b).

8.7.1 Fit Results

In total, 2 977 526 B_s^0 candidates (both signal and background) were used for the fit. From the fit result signal fraction, 453 570±740 candidates were identified as signals. The fit results values of the parameters of interest are shown in Table 8.2.

For most of the physics parameters, including ϕ_s, $\Delta\Gamma_s$ and Γ_s, the fit determines a single solution with Gaussian behaviour of the projection of the log-likelihood $-\ln L$. The

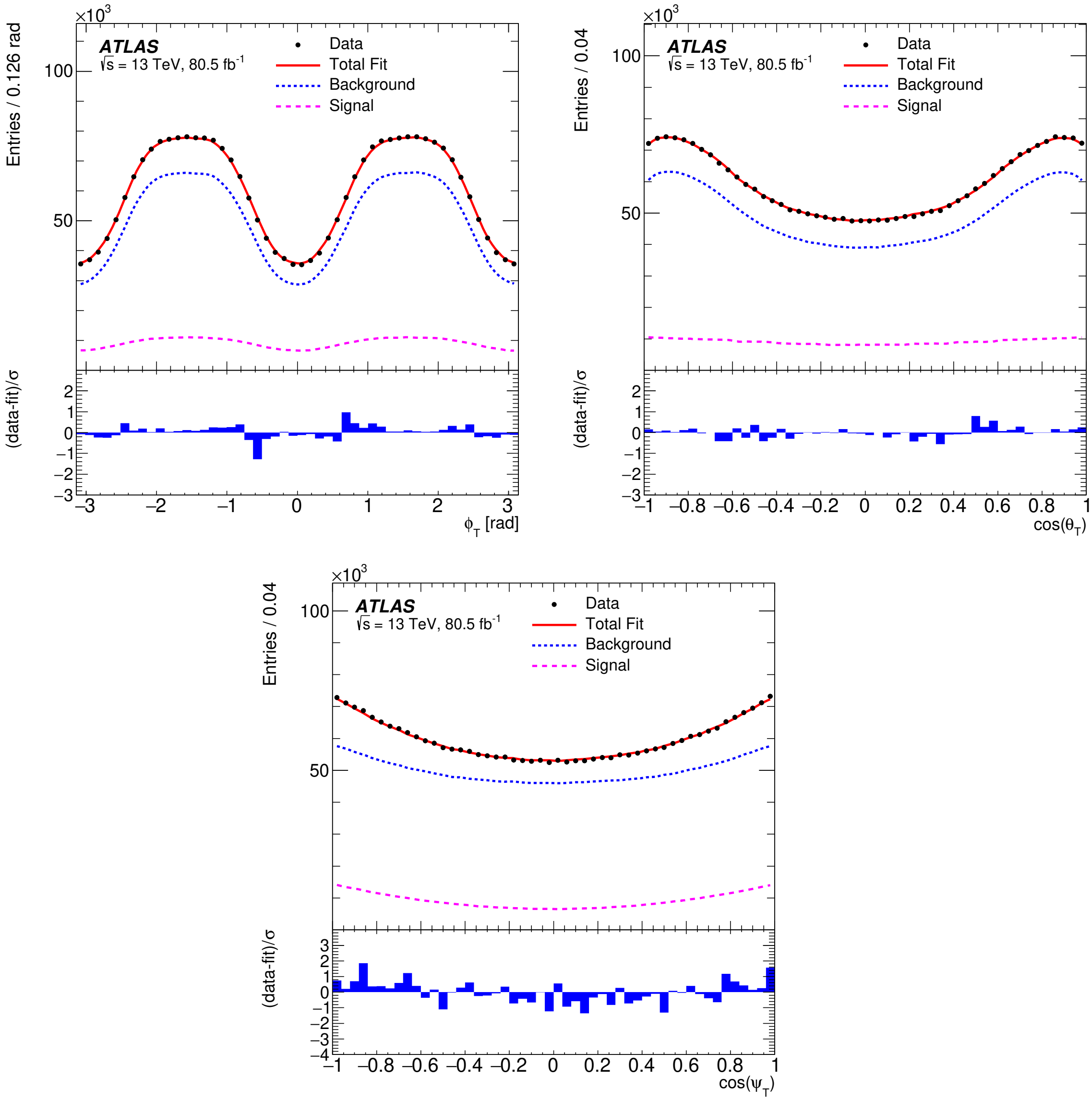

FIGURE 8.9. Fit projections for the transversity angles ϕ_T (top left), $\cos(\theta_T)$ (top right), and $\cos(\psi_T)$ (bottom). In all three plots, the solid red line shows the total fit, the $B_s^0 \to J/\psi + \phi$ signal component is shown by the magenta dashed line, and the blue dotted line shows the contribution of all background components.

likelihood profile for strong phases has two minima. The difference in $-2\Delta\ln(L)$ between the two solutions is 0.03. The correlation tables for solution (a) and solution (b) are shown in Tables 8.3 and 8.4, respectively.

The model of the fit contains direct *CP* related parameter $|\lambda|$ (see (8.10) and Table 2.3) that is fixed by default to $|\lambda| = 1$. The test with releasing this parameter was performed,

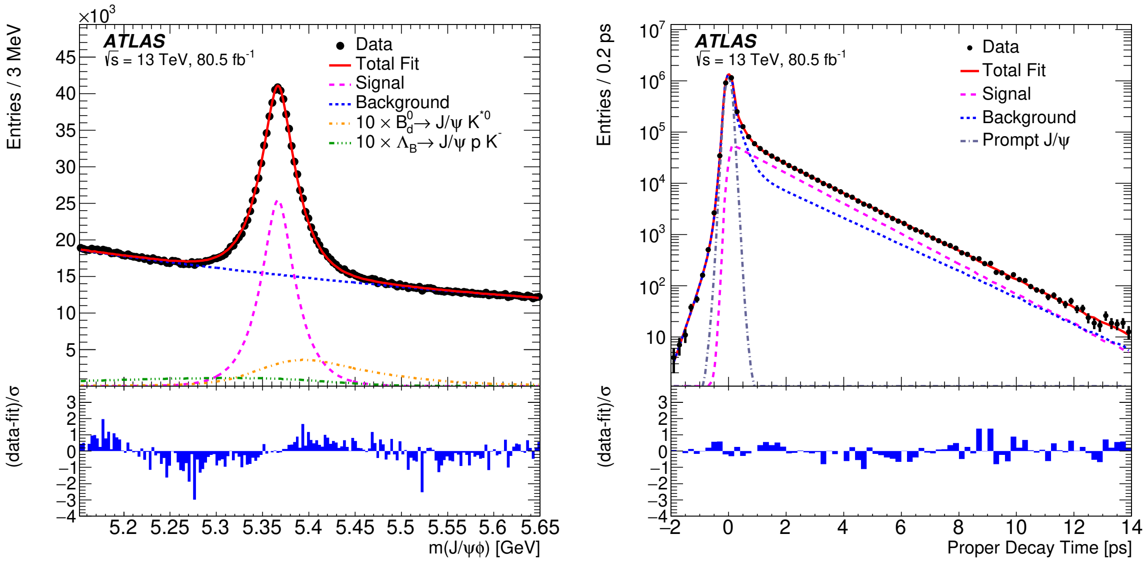

FIGURE 8.10. Mass (left) and lifetime (right) fit projection for the $B_s^0 \to J/\psi\phi$ sample. The red line shows the total fit, the short-dashed magenta line shows the $B_s^0 \to J/\psi + \phi$ signal component, the combinatorial background is shown as a blue dotted line, the orange dash-dotted line shows the $B_d \to J/\psi K^{0*}$ component, and the green dash-dot-dot line shows the contribution from $\Lambda_b \to J/\psi p K^-$ events.

and the fit result value is compatible within the statistical precision with unity as well as with the results of other experiments. The change of other physical parameters is negligible due to their small correlations with $|\lambda|$.

The mass and proper decay time default fit projections are shown in Figure 8.10, and the three angles projections are in Figure 8.9. Each plot projection also shows the ratio plots (pulls), defined for each projection bin as the difference between data and fit divided by the statistical and systematic uncertainties summed in quadrature in a given bin. The deviations of ratio plots are within 2σ, so any discrepancies between the data and the fit model are covered.

8.7.2 Likelihood Scans

The unbinned maximum likelihood fit has two well-separated maxima for the strong phases with a difference of likelihood in the maxima $-2\Delta\ln(L) = 0.03$. Figure 8.11 shows results of the 2D log-likelihood scan in the $\delta_{||}$, $\delta_{\perp}$ plane, revealing two minima. These minima are represented by two-dimensional contours at the level of $-\,2\Delta\ln(L) =$

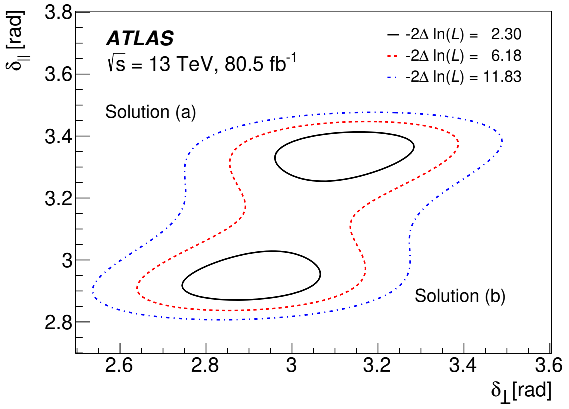

FIGURE 8.11. Two-dimensional constraints on the values of $\delta_{||}$ and $\delta_{\perp}$ for solutions (a) and (b) at the level of $-2\Delta\ln(L) = 2.30, 6.18$, and 11.83 respectively created using a full 2D scan. The minimum of the solution (b) is $-2\Delta\ln(L) = 0.03$ higher than the minimum of the solution (a).

2.30, 6.18, and 11.83, where $-2\Delta\ln(L) = 2(\ln(L^i) - \ln(L^a))$ is the difference between the likelihood values (L^i) of the fit in which the two strong phases are fixed to the values shown on the horizontal and vertical axis, and L^a which is the likelihood value for solution (a) of the fit. The rest of the parameters have a single minimum in the likelihood scans (see Figure 8.12).

The two minima for the strong phases appear due to the symmetry of the signal PDF. The decay rate with parameters in Table 2.3 is symmetric under the transformation:

$$\{\delta_{\parallel},\ \delta_{\perp},\ \delta_S\} \to \{2\pi - \delta_{\parallel},\ \delta_{\perp} + 2(\pi - \delta_{\parallel}),\ \delta_S + 2(\pi - \delta_{\parallel})\}. \tag{8.12}$$

The two local maxima of the likelihood determined in this analysis satisfy the relation of equation (8.12) very accurately for $\delta_{\parallel}$ and ($\delta_{\perp}$ - δ_S), and within the statistical uncertainty in the transformation for $\delta_{\perp}$. The difference in the log-likelihoods, $-2\Delta\ln(L)$, between the two solutions is equal to 0.03, favouring (a) but without ruling out (b). As discussed in Section 8.7.1, the two-fold nature of the likelihood maxima for the strong phases has a negligible effect on all the other variables.

8.7.3 Combination with 7 TeV and 8 TeV Results

The measurement of the *CP* violation in the $B_s^0 \to J/\psi\phi$ decay was also measured by ATLAS in Run1 [82]. The results from Run1 analyses (with collision energy $\sqrt{7}$ TeV and $\sqrt{8}$ TeV) and the current analysis are combined by using the Best Linear Unbiased

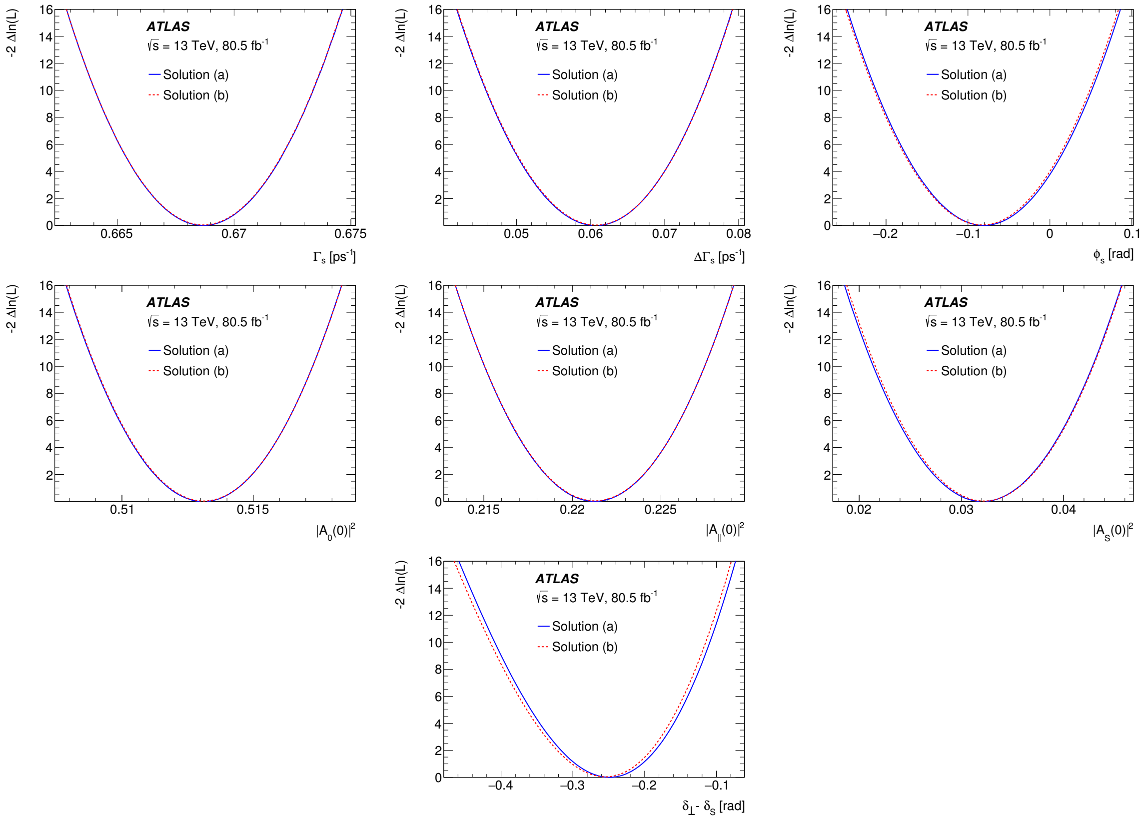

FIGURE 8.12. 1D log-likelihood scans of all other variables of the fit for the solution (a) (blue) and the solution (b) (dashed red). The variable on the vertical axis, $-2\Delta\ln(L) = 2(\ln(L^a) - \ln(L^i))$, is the difference between the likelihood values of the default fit, (L^a), and of the fit in which the physical parameter is fixed to values shown on the horizontal axis.

Estimator (BLUE). Statistical correlations for individual measurements provided by the fits to $\sqrt{7}$ TeV, $\sqrt{8}$ TeV, and $\sqrt{13}$ TeV data are given in papers [82] and [93] and Tables 8.3 and 8.4 respectively. Other correlations between the parameters for both the statistical and systematic uncertainties are estimated as follows:

- There is no correlation between statistical uncertainties as the events recorded at $\sqrt{7}$ TeV, $\sqrt{8}$ TeV and $\sqrt{13}$ TeV are considered to be different,
- In all three measurements, the correlation between them is assumed to be zero, and therefore, the systematic correlations between parameters are summed in quadrature.
- The correlations between systematic effects were categorized into groups: system-

atic uncertainties without correlations (i.e., background angles model function, the S-wave phase, the best candidate selection) and those with correlation set to 25% (the choice of p_{T} bins and B_d, Λ backgrounds). The checks with 0, 10, 25, 50, 75, and 100% were performed, and no difference in the final results was observed.

Solution (a) and solution (b) are treated separately, leading to the two sets of combined results, as shown in Table 8.5. The two-dimensional likelihood contours in the $\phi_s - \Delta\Gamma$ plane for the ATLAS result based on $\sqrt{7}$ TeV and $\sqrt{8}$ TeV data, the solution (a) of the $\sqrt{13}$ TeV measurement, and the combined result for the solution (a) are shown in Figure 8.13. The contour contains the combined statistical and systematic uncertainties in quadrature and also reflects the correlation between the two parameters. The contour plot is valid for both solutions as there are no preferences in the ϕ_s and $\Delta\Gamma_s$ results.

8.7.4 Comparison of ATLAS Results to LHCb and CMS Run2 Results

The *CP* violation not only in $B_s^0 \to J/\psi\phi$ decay was also studied by the LHCb and CMS experiments. They differ from the analysis in this thesis by using various methods and

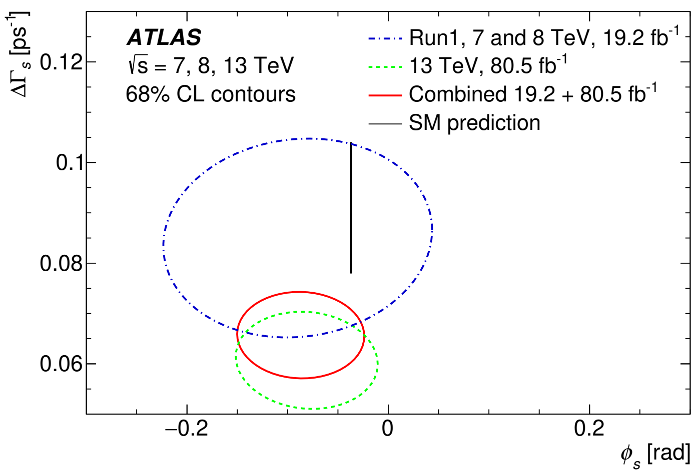

FIGURE 8.13. Contours of 68% confidence level in the $\phi_s - \Delta\Gamma$ plane, showing ATLAS results for $\sqrt{7}$ TeV and $\sqrt{8}$ TeV data (blue dashed-dotted curve), for $\sqrt{13}$ TeV data (green dashed curve) and for $\sqrt{13}$ TeV data combined with $\sqrt{7}$ TeV and $\sqrt{8}$ TeV (red solid curve) data. The Standard Model prediction [80, 84] is shown as a very thin black rectangle. In all contours, the statistical and systematic uncertainties are combined in quadrature and correlations are taken into account.

	Solution (a)		
Parameter	Value	Statistical uncertainty	Systematic uncertainty
ϕ_S [rad]	−0.087	0.036	0.021
$\Delta\Gamma_s$ [ps^{-1}]	0.0657	0.0043	0.0037
Γ_s [ps^{-1}]	0.6703	0.0014	0.0018
$\lvert A_\parallel(0)\rvert^2$	0.2220	0.0017	0.0021
$\lvert A_0(0)\rvert^2$	0.5152	0.0012	0.0034
$\lvert A_S\rvert^2$	0.0343	0.0031	0.0045
$\delta_\perp$ [rad]	3.22	0.10	0.05
$\delta_\parallel$ [rad]	3.36	0.05	0.09
$\delta_\perp - \delta_S$ [rad]	−0.24	0.05	0.04

	Solution (b)		
Parameter	Value	Statistical uncertainty	Systematic uncertainty
ϕ_S [rad]	−0.087	0.036	0.021
$\Delta\Gamma_s$ [ps^{-1}]	0.0657	0.0043	0.0037
Γ_s [ps^{-1}]	0.6704	0.0014	0.0018
$\lvert A_\parallel(0)\rvert^2$	0.2218	0.0017	0.0021
$\lvert A_0(0)\rvert^2$	0.5152	0.0012	0.0034
$\lvert A_S\rvert^2$	0.0348	0.0031	0.0045
$\delta_\perp$ [rad]	3.03	0.10	0.05
$\delta_\parallel$ [rad]	2.95	0.05	0.09
$\delta_\perp - \delta_S$ [rad]	−0.24	0.05	0.04

TABLE 8.5. Values of the physical parameters extracted in the combination of solution (a) and solution (b) of 13 TeV results with those obtained from 7 TeV and 8 TeV data.

procedures. For example, both LHCb and CMS subtract most of the background from the dataset before analysing it. The analyses delivered by both collaborations benefit from sample purity and particle identification, so they could use same side tagging along with opposite side tagging. Two-dimensional likelihood contours in the $\phi_s - \Delta\Gamma$ plane are shown in Figure 8.14 for this ATLAS result, the result from CMS [168] using the $B_s^0 \to J/\psi\phi$ decay, the result from LHCb [169] using the $B_s^0 \to J/\psi K^+K^-$ decay and finally the LHCb result including all B_s^0 channels [90, 169–172]. The contours are obtained by interpreting each result as a two-dimensional Gaussian probability distribution in the $\phi_s - \Delta\Gamma$ plane. All results are consistent with each other, and with the Standard Model [80, 84].

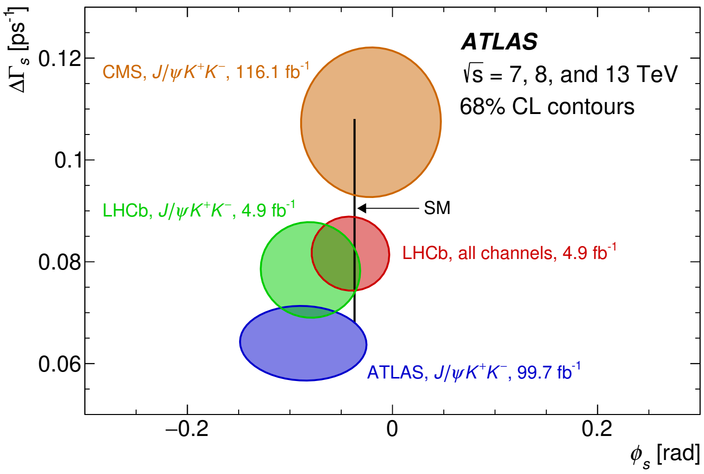

FIGURE 8.14. Contours of 68% confidence level in the $\phi_s - \Delta\Gamma$ plane, including results from CMS (orange) and LHCb (green) using the $B_s^0 \to J/\psi K^+K^-$ decay only and LHCb (red) for all the channels. The blue contour shows the ATLAS result for $\sqrt{13}$ TeV combined with $\sqrt{7}$ TeV and $\sqrt{8}$ TeV. The Standard Model prediction [80, 84] is shown as a very thin black rectangle. In all contours, the statistical and systematic uncertainties are combined in quadrature.

CHAPTER 9

B_d LIFETIME MEASUREMENT

The measurement of *CP* violation in $B_s^0 \to J/\psi\phi$ provides also the measured value of average decay width Γ_s. This result is inconsistent with the measurements of LHCb and CMS experiments at the level of 2.4σ, as shown in Figure 9.1. To validate the lifetime properties of B mesons at ATLAS, a measurement of the lifetime of the B^0 meson is reported by the ATLAS experiment using 139 fb^{-1} of proton-proton

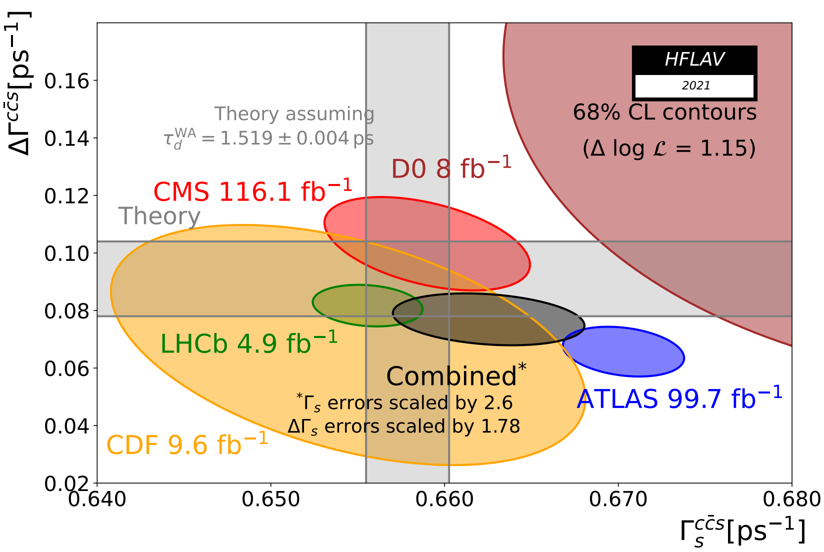

FIGURE 9.1. The individual 68% confidence-level contours of ATLAS, CMS, CDF, DØ and LHCb, their combined contour (solid black line and shaded area), as well as the Standard Model predictions (grey regions) [94].

collision data recorded at $\sqrt{s} = 13$ TeV during the period of 2015–2018 at the Large Hadron Collider. The meson is characterised through combined mass and lifetime reconstructions of the channel $B^0 \to J/\psi K^{*0}$. The measured ratio of the B^0 meson lifetime with respect to the ATLAS-measured B_s^0 meson average decay width Γ_s) [1], taken from the 2015–2017 dataset, is also reported. The effective lifetime is related to the width Γ through [173]

$$\tau = \frac{1}{\Gamma}\frac{1}{1-y^2}\left(\frac{1+2Ay+y^2}{1+Ay}\right), \tag{9.1}$$

where for the difference $\Delta\Gamma = \Gamma_L - \Gamma_H$ between the heavy and light eigenstate rates, $y = \Delta\Gamma/(2\Gamma)$. The parameter A, which depends on the final state f, is defined by the expression

$$A \equiv \frac{R_H^f - R_L^f}{R_H^f + R_L^f}, \tag{9.2}$$

where the summed decay rate of the members of the system to final state f is [173]

$$\langle\Gamma(B(t))\rangle \equiv \Gamma(B(t)) + \Gamma\left(\overline{B}(t)\right) = R_H^f \exp(-\Gamma_H t) + R_L^f \exp(-\Gamma_L t). \tag{9.3}$$

9.1 Data and Event Selection

Firstly, events are required to pass the trigger selections - the list of triggers is provided in appendix C. The selected events must contain at least one reconstructed candidate formed by one pair of oppositely charged muon candidates and at least two additional tracks. To reconstruct the J/ψ candidate, the oppositely charged muon pairs are re-fitted to a common vertex, and the pair is accepted if the quality of the fit is $\chi^2/(\text{ndof}) < 10$ The ATLAS detector has various mass resolutions in different parts of the detector depending on the pseudorapidity coordinate. For this reason, the refitted $J/\psi(\mu^+\mu^-)$ candidates are selected in the mass windows according to the pseudorapidity of muons, see section 8.1 for further details. The $K^{*0} \to K^\pm\pi^\mp$ decay candidates are reconstructed from all tracks that are not identified as muons. Only oppositely charged tracks passing the $p_T(K^{*0}) > 3.5$ GeV, $p_T(K^\pm) > 1$ GeV, $p_T(\pi^\pm) > 0.5$ GeV and $|\eta| < 2.5$ criteria are used, and the invariant mass of the $K^{*0} \to K^\pm\pi^\mp$ candidate is expected to be in a range of 846 MeV $< m(K^\pm\pi^\mp) <$ 946 MeV.

The $B^0 \to J/\psi K^{*0}$ candidate is formed by fitting the common vertex of the $J/\psi \to \mu^+\mu^-$ and $K^{*0 \to K^\pm\pi^\mp}$ combinations. The vertex fit uses the constraint to the dimuon invariant mass to the J/ψ mass value from [46]. The candidate with refitted vertex must pass the vertex quality requirement $\chi^2/(\text{ndof}) < 3$. In case of multiple candidates per event passing the selection criteria, the one with the lowest χ^2/ndof is selected only. The total number of 10 559 554 B^0 candidates are selected within the mass range of (5.00 − 5.65) GeV. This range is chosen to give enough background events in the sidebands of the mass distributions to allow precise determination of the properties of the background events. Each selected candidate has assigned proper decay time that is defined in (8.1). The data have assigned weights according to the trigger inefficiencies, see section 8.2 for a full description.

9.2 Maximum Likelihood Fit Model

The lifetime of B^0 meson is extracted from the two-dimensional unbinned maximum likelihood fit describing both signal and background. The signal model describes the $B^0 \to J/\psi K^{*0}$ decay. The background is composed of several contributions, including J/ψ from prompt production in proton-proton collisions combined randomly with any K^{*0} candidates in the event. Using this background in the fit model ensures that no proper decay lifetime cut is applied to B^0 candidates. Another background is formed from a J/ψ from other B hadron decays combined with K^{*0} candidates as in the previous case. Finally, backgrounds formed by J/ψ and K^{*0} candidates both coming from the same B meson include kinematic reflections or partially reconstructed B hadrons.

The mass and proper decay time are simultaneously fitted using the likelihood function:

$$\begin{aligned}\ln L = \sum_{i=1}^{N} w_i \ln\Big[& f_{\text{sig}} \mathscr{M}_{\text{sig}}(m_i)\mathscr{T}_{\text{sig}}(\tau_i, \sigma_{t_i}, p_{\text{T}_i}) \\ & + (1-f_{\text{sig}}) f_{\text{prompt}} \mathscr{M}_{\text{prompt}}(m_i)\mathscr{T}_{\text{prompt}}(\tau_i, \sigma_{t_i}, p_{\text{T}_i}) \\ & + (1-f_{\text{sig}})(1-f_{\text{prompt}}) \mathscr{M}_{\text{bkg}}(m_i)\mathscr{T}_{\text{bkg}}(\tau_i, \sigma_{t_i}, p_{\text{T}_i}) \Big]\end{aligned} \tag{9.4}$$

where f_{sig} is the fraction of signal events in the total number of events, N. $\mathscr{M}_{\text{sig}}$ and $\mathscr{M}_{\text{bkg}}$ are probability density functions (PDF) modelling signal and background mass distributions. The terms $\mathscr{T}_{\text{sig}}$ and $\mathscr{T}_{\text{bkg}}$ describe the decay time distributions of the signal $B^0 \to J/\psi K^{*0}$ and backgrounds $b\bar{b} \to J/\psi X$. The $pp \to J/\psi X$ mass and lifetime background is modelled by $\mathscr{M}_{\text{prompt}}$ and $\mathscr{T}_{\text{prompt}}$ respectively. The input variables to the maximum likelihood fit extracted from the data are the proper decay time τ_i, its uncertainty σ_{τ_i} in p_{T} bins, the mass m_i for each B^0 candidate passing the selections.

9.2.1 The invariant mass PDFs

The $\mathcal{M}_{\text{sig}}$, $\mathcal{M}_{\text{bkg}}$ and $\mathcal{M}_{\text{prompt}}$ are probability density functions which model the B^0 signal, background and prompt J/ψ background mass shapes in the fitted mass range. For the signal, the mass is modelled with a Johnson S_U-distribution [174]:

$$M_{\text{sig}}(m_i) \equiv \frac{\delta}{\lambda\sqrt{2\pi}\sqrt{1+\left(\frac{m_i-m_B}{\lambda}\right)^2}} \exp\left[-\frac{1}{2}\left(\gamma+\delta\sinh^{-1}\left(\frac{m_i-\lambda}{\lambda}\right)\right)^2\right] \tag{9.5}$$

where λ, γ, δ and λ are the parameters of the Johnson S_U-distribution (λ cannot be directly assigned to B^0 mass m_B because it is not the mean value of the Johnson distribution). The prompt J/ψ background mass distribution is described by the constant function, and for the combinatorial background, the mass distribution is modelled with two exponential functions:

$$\mathcal{M}_{\text{bkg}}(m_i) = \frac{f_{\text{bkg1}}}{\lambda_{\text{bkg1}}} \exp\left(\frac{-m_i}{\lambda_{\text{bkg1}}}\right) + \frac{1-f_{\text{bkg1}}}{\lambda_{\text{bkg2}}} \exp\left(\frac{-m_i}{\lambda_{\text{bkg2}}}\right), \tag{9.6}$$

where λ_{bkg1} and λ_{bkg2} are the slopes of exponential functions and f_{bkg1} is a fraction between them.

On account of partially reconstructed B mesons and kinematic reflections, no attempt is made to model the background far from the B^0 mass region. In the selected mass regions $(5000-5650)$ MeV and for the B^0, an approximation of the background by two exponential functions is adequate within the available statistics.

9.2.2 The proper decay time PDFs

The PDF terms describing proper decay time are composed of two terms:

$$\mathcal{T}_{\text{j}}(\tau_i, \sigma_{\tau_i}, p_{\text{T}_i}) = \text{P}_j\left(\tau_i|\sigma_{\tau_i}, p_{\text{T}_i}\right)\cdot \text{P}_j\left(\sigma_{\tau_i}, p_{\text{T}_i}\right) \tag{9.7}$$

where j stands for signal, prompt and combinatorial background, respectively.

The term $\text{P}_j\left(\tau_i|\sigma_{\tau_i}, p_{\text{T}_i}\right)$ assumes the lifetime to be smeared by the lifetime resolution, so each of the proper decay time distribution models is convoluted with the sum of Gaussian functions:

$$R(\tau_i'-\tau_i, \sigma_{\tau_i}) \equiv \sum_{k=1}^{3} f_{\text{res}}^{(k)} \frac{1}{\sqrt{2\pi}\, S^{(k)}\, \sigma_{\tau_i}} \exp\left(\frac{-(\tau_i'-\tau_i)^2}{2(S^{(k)}\,\sigma_{\tau_i})^2}\right). \tag{9.8}$$

$S^{(k)}$ are the scale factors (parameters of the fit), and σ_{τ_i} is the per-candidate uncertainty of τ_i. Parameters $f_{\text{res}}^{(k)}$ are the relative fractions of each Gaussian function fulfilling the normalization condition $\sum f_{\text{res}}^{(k)} = 1$.

The proper decay time distribution of the B^0 candidates is modelled as an exponential function $E(\tau_i, \tau_{B_d}) = \frac{1}{\tau_{B_d}} \exp(-\tau_i/\tau_{B_d})$ for $\tau \geq 0$, with B^0 lifetime τ_{B_d} which is extracted from the fit, convolved with the proper decay time resolution function.

$$P_{\mathrm{sig}}\left(\tau_i | \sigma_{\tau_i}, p_{\mathrm{T}_i}\right) = E(\tau_i, \tau_{B_d}) \otimes R(\tau_i' - \tau_i, \sigma_{\tau_i}). \tag{9.9}$$

The proper decay time distribution of the promptly produced J/ψ is described by the resolution function R:

$$P_{\mathrm{prompt}}\left(\tau_i | \sigma_{\tau_i}, p_{\mathrm{T}_i}\right) = \delta_{Dirac}(\tau_i') \otimes R(\tau_i' - \tau_i, \sigma_{\tau_i}) = R(\tau_i, \sigma_{\tau_i}). \tag{9.10}$$

The proper decay time PDF, P_{prompt}, for the background candidates from non-prompt J/ψ production, consists of the sum of four exponential functions, each convolved with the resolution function R:

$$P_{\mathrm{bkg}}\left(\tau_i | \sigma_{\tau_i}, p_{\mathrm{T}_i}\right) = \left[\sum_{j=1}^{4} b_j \prod_{k=1}^{j-1} (1 - b_k) E(\tau_i', \tau_{\mathrm{bkg}_j})\right] \otimes R(\tau_i' - \tau_i, \sigma_{\tau_i}) \tag{9.11}$$

where τ_{bkg_j} are different lifetimes describing four components of the non-prompt J/ψ induced background, and the factors b_j (fitted parameter) correspond to the relative fraction of the four background contributions.

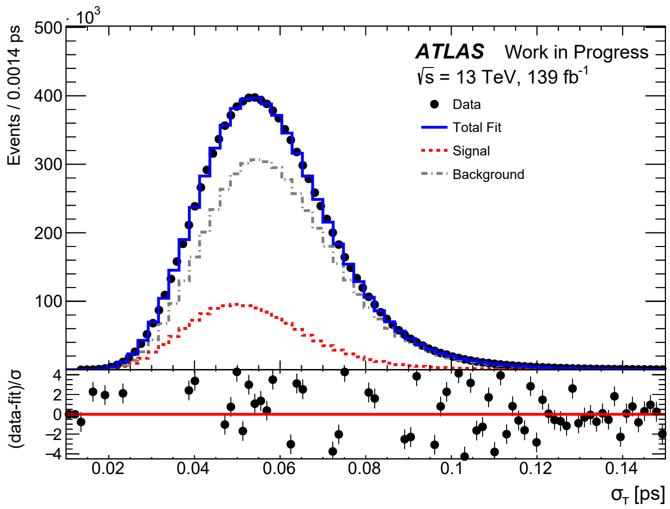

FIGURE 9.2. The projection of the B^0 proper decay time uncertainty. The blue line shows the total fit, while the short-dashed red line shows the total signal. The combinatorial and prompt J/ψ background is shown as a dash-dotted grey line. Below the figure, a ratio plot shows the difference between each data point and the total fit line divided by the statistical uncertainty.

Source of uncertainty	Systematic uncertainty [ps]
Momentum bias	0.00080
Choice of mass window	0.00084
Choice of primary vertex	<0.00001
Time efficiency	0.00109
Mass fit model	0.00058
Fit model test with ToyMC	0.00016
Total	0.0016

TABLE 9.1. Summary of systematic uncertainties assigned to the value of B^0 lifetime.

The probability terms $P_j\left(\sigma_{\tau_i}, p_{T_i}\right)$ are two-dimensional histograms introduced to describe the difference between signal, prompt and non-prompt background (the Punzi terms in appendix A) for the values of the per-candidate time error that divided into the several p_T bins. The *sPlot* technique [175] is used to separate the signal and background proper decay time and p_T distributions. The projection of the proper decay time uncertainty is shown in Figure 9.2.

9.3 Systematic Uncertainties

The systematic uncertainties of the B^0 lifetime arise from several sources. The uncertainties determination is based on a comparison of nominal and modified fit results or on observed fit biases in modified pseudo-experiments. A summary of all sources of uncertainty that contribute to the analysis is presented in Table 9.1, where the total systematic uncertainty is obtained by adding all of the contributions in quadrature. Each of the systematic uncertainty is described below:

Momentum bias: The largest possible inner detector misalignment prevails for the momentum of B^0 candidate. Since the momentum bias is propagated to the J/ψ invariant mass, the sensitivity of the lifetime fit value is tested by alternative fit to the data without constraining the J/ψ mass to its PDG value. The difference between default and alternative fit results is considered a systematic uncertainty.

Choice of mass window: By default, the events with B^0 candidate mass in the interval of (5000 – 5650) MeV are used in the analysis. The datasets with alternative mass windows were considered, and the fit was performed for each alternative window.

The largest deviation from the nominal fit values is taken as the systematic uncertainty due to the choice of the mass window.

Choice of primary vertex: Majority of events has more than one primary vertex reconstructed. The variable used to identify the primary vertex originating the B^0 candidate is the impact parameter a_0. It is calculated as a distance between the line extrapolated from the reconstructed B^0 meson vertex in the direction of the B^0 momentum and each reconstructed primary vertex candidate. By default, the chosen PV is the one with the smallest a_0. The alternative approach is to use the PV with the highest sum of the squares of the constituent tracks' transverse momenta $\sum p_{\mathrm{T}}^2$. The difference between B^0 fitted lifetime value using the default and an alternative PV selection is accounted as the systematic uncertainty due to the choice of the primary vertex.

Time efficiency: The time efficiency correction can suffer from the statistics of the efficiency distributions and from the statistical uncertainty of the fit to the distributions. To understand the size of this effect on the B^0 fitted lifetime, the time efficiency functions are smeared within their uncertainties, a new function is produced, and the B^0 lifetime fit is performed. This test is repeated 50 times. Finally, a plot is made from the differences between resulting lifetimes and lifetimes before smearing the input data. Deviation of pull distribution from zero is included in the systematic uncertainties of the measurement.

Mass fit model: To estimate the mass mismodelling effect on the fitted B^0 lifetime, two approaches were considered. Firstly, the mass pulls (deviations of the fit function from the data in each mass bin divided by the stat. uncertainty of each bin) from the default fit were used as weights for the data, and an alternative fit with these weights was performed. In addition, the pull weights were artificially generated according to analytic function, and the fit to the weighted data was repeated. The largest difference between default fit and alternative fits is included in the final systematic uncertainty. Secondly, the mass signal was tested by running alternative fits with different mass signal models - a double-sided Crystal-Ball function and two single-sided Crystal-Ball functions. The largest deviation from the default fit is considered as a contribution to the systematic uncertainty.

Fit model test with ToyMC: The fit model is complex and can be sensitive to nuisance parameters. This sensitivity can produce a bias in the fit results. To determine the bias, a set of data from the pseudo-experiment (ToyMC) was generated with the model PDF and fitted with the same PDF. The parameters' results of the fit to ToyMC samples are expected to form Normal Gaussian distributions (their means are expected to be 0 and the standard deviation to be 1). The differences between the mean of Gaussian distribution and the default fit results are assumed to be the systematic uncertainties

9.4 Results

The lifetime of B^0 meson is extracted from the two-dimensional unbinned maximum likelihood fit (see appendix A) describing both signal and background. The B^0 lifetime result is then used to determine the average decay width Γ and its ratio to the average decay width Γ_s.

9.4.1 Lifetime Results

The lifetime value using the statistics of total 2368503 ± 2175 B^0 signal candidates is found to be

$$\tau_{B^0} = 1.5174 \pm 0.0012\,(\text{stat.}) \pm 0.0016\,(\text{syst.})\,\text{ps}. \tag{9.12}$$

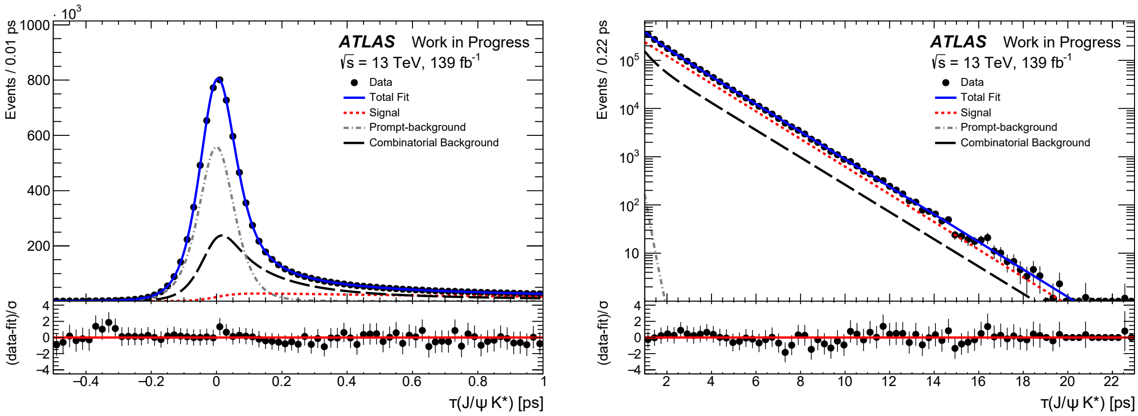

FIGURE 9.3. Proper decay time fit projection for the $B^0 \to J/\psi K^{*0}$ sample. The blue line shows the total fit, while the short-dashed red line shows the total signal. The combinatorial background is shown as a long-dashed black line, and the dash-dotted grey line shows the prompt J/ψ background component. Below each figure is a ratio plot that shows the difference between each data point and the total fit line divided by the statistical uncertainty.

The fitted value of the $B^0 \to J/\psi K^{*0}$ lifetime agrees with the world average value [46]. The lifetime projections of two-dimensional maximum likelihood fit are shown in Figure 9.3. The plots include the ratio plots showing the difference between each data point and the total fit line divided by the statistical uncertainty. The likelihood scan in Figure 9.4 of the B^0 lifetime parameter τ shows perfect parabolic behaviour.

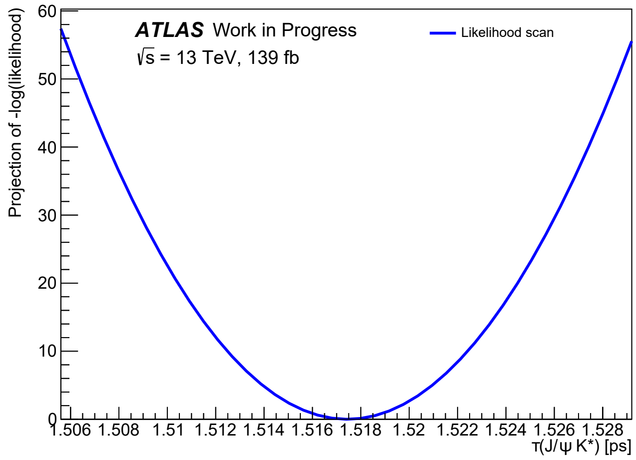

FIGURE 9.4. Proper decay time fit projection of the negative likelihood function for the $B^0 \to J/\psi K^{*0}$ sample. The blue line shows the value of the maximum-likelihood function for each value of the proper decay time.

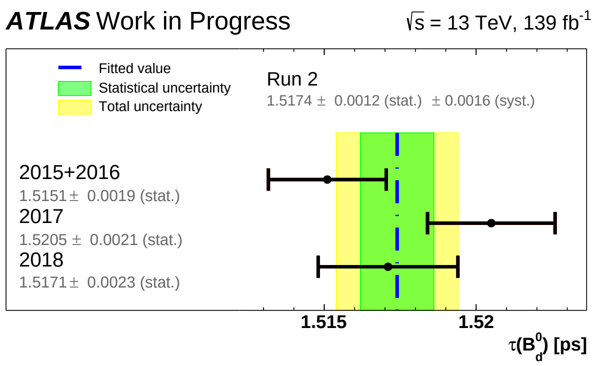

FIGURE 9.5. The $B^0 \to J/\psi K^{*0}$ fitted lifetime value for 2015+2016, 2017 and 2018 subsamples compared to the value from the whole sample. The blue dash-dotted line shows the Run2 lifetime fit result with the statistical and total uncertainty shown by the green and yellow boxes, respectively. The B^0 lifetime value for each year is shown by the black point with error bars showing their statistical uncertainty.

To test the stability of the fit, the B^0 was fitted in separated data samples. divided into the subsample according to the year of recording. Figure 9.5 shows perfect agreement of each year's results with the overall Run2 result.

9.4.2 Determination of B^0 average decay width Γ and of the Γ/Γ_s ratio

To extract the average decay width Γ from our measured effective lifetime τ_{B^0}, equation (9.1) is used. The parameters R_H^f and R_L^f from equation (9.2) are connected with the polarisation amplitudes $|A_i|^2$, where $i = 0, \perp, \parallel$, by:

$$R_H^f = |A_\perp|^2 \tag{9.13}$$
$$R_L^f = |A_0|^2 + |A_\parallel|^2. \tag{9.14}$$

The polarisation amplitudes were reached from the world average values for the $B^0 \to J/\psi K^{*0}$ channel [94]:

$$|A_0|^2 = 0.571 \pm 0.007$$
$$|A_\perp|^2 = 0.211 \pm 0.008$$
$$|A_\parallel|^2 = 0.218 \pm 0.011$$

Using these values in the equations (9.14) and (9.2), the value of (9.2) is $A = -0.578 \pm 0.0136$. This parameter value, together with the fitted effective lifetime (**??**) and the value of y [94]

$$\frac{\Delta\Gamma_d}{\Gamma_d} = 2y = 0.001 \pm 0.010, \tag{9.15}$$

enter the modified equation (9.1) for average decay width

$$\Gamma = \frac{1}{\tau}\frac{1}{1-y^2}\left(\frac{1+2Ay+y^2}{1+Ay}\right) \tag{9.16}$$

resulting in the value

$$\Gamma = (0.6586 \pm 0.0005\ (\text{stat.}) \pm 0.0007\ (\text{syst.}))\ \text{ps}^{-1}.$$

To separate these measurement uncertainties and the external HFLAV uncertainties, the statistical and systematic uncertainties contains only contribution from the lifetime uncertainties, and the external uncertainty is introduced. It is ruled by the uncertainty propagation of y and A and dominates the overall uncertainty:

$$\Gamma = 0.6586 \pm 0.0005\ (\text{stat.}) \pm 0.0006\ (\text{syst.}) \pm 0.0038\ (\text{ext.})\ \text{ps}^{-1}.$$

The uncertainties σ_Γ were calculated using the law of uncertainty propagation:

$$\sigma_\Gamma = \sqrt{\sum_{k=A,y,\tau} \left(\frac{\partial \Gamma_d}{\partial k}\right)^2 \sigma_k^2}. \tag{9.17}$$

The statistical uncertainty σ_Γ uses A, y, τ statistical uncertainties, the systematic σ_Γ uses only τ systematic uncertainty.

The calculation of the Γ/Γ_s ratio follows a similar procedure - all uncertainties were calculated from the input values of average decay widths:

$$\frac{\Gamma}{\Gamma_s} = 0.9825 \pm 0.0022\ (\text{stat.}) \pm 0.0028\ (\text{syst.}) \pm 0.0057\ (\text{ext.}).$$

The external uncertainty contains a contribution from the Γ external one, the Γ_s does not have such uncertainty. The input systematic uncertainties do not cancel as each analysis

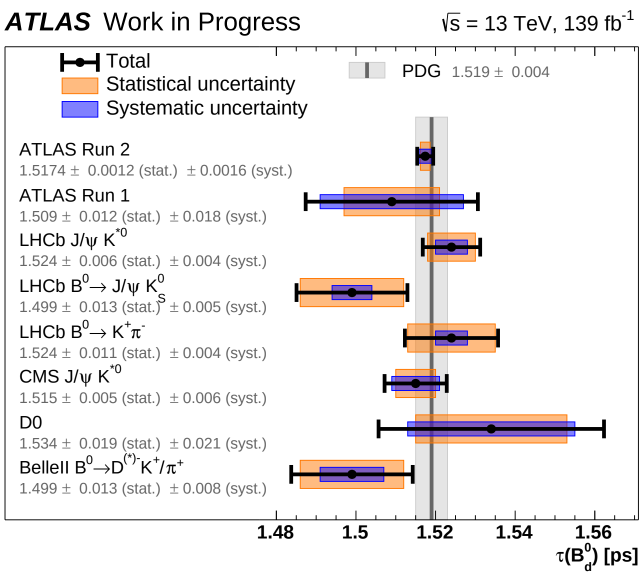

FIGURE 9.6. The $B^0 \to J/\psi K^{*0}$ fitted lifetime value compared to ATLAS Run1 and other experiment results [176–181]. The PDG value [46] is shown by grey colour. The results are shown with the black points and lines for combined uncertainties. The statistical and systematic uncertainties are shown as orange and blue boxes, respectively.

has different sources of systematic uncertainties. In addition, the Γ_s is extracted from the sample between 2015 and 2017, while the Γ value was obtained from the full Run2 sample. Therefore, the trigger effects also cannot be neglected.

9.4.3 Comparison of ATLAS Results with Other Experiments

The measurement of τ_{B^0} by ATLAS experiment is consistent with previous results, results from other experiments [176–181] and their combination in PDG [46]. The comparison presented in Figure 9.6 shows that the lifetime value presented in this thesis is the most precise one.

The value of Γ is in good agreement with the theoretical predictions [182]. Comparing the current result of the ratio Γ_s/Γ_d to theory predictions [182], and the experimental average [46], we find tensions at the level of 3σ, driven by tensions of Γ_s described in the previous chapter.

Conclusions

This thesis presents a measurement of the CP asymmetry parameters in $B_s^0 \to J/\psi(\mu^+\mu^-)\phi(K^+K^-)$ decays using the 80.5 fb^{-1} data sample of pp collisions collected by the ATLAS detector during the 13 TeV LHC run between years 2015 and 2017. This measurement uses initial flavour determination from the self-tagged $B^\pm \to J/\psi K^\pm$ channel. The supplementary measurement of the B^0 meson lifetime using the $B^0 \to J/\psi(\mu^+\mu^-)K^{*0}(\pi^\pm K^\mp)$ decay in the 139 fb^{-1} data sample of pp collisions collected with the ATLAS detector during the 13 TeV LHC run between years 2015 and 2018 is presented. The following sections summarise the results and outcomes of the two analyses [1, 2] and of tagging in $B^\pm$ that is included in [1].

Flavour Tagging in the $B^\pm \to J/\psi K^\pm$ Decay

The opposite side tagging was studied in the $B^\pm \to J/\psi K^\pm$ decay using the ATLAS data from the pp collisions at the LHC. The flavour tagging calibrations were inferred from the opposite side muons, electrons, and jets. The tagging performance was found to be (1.75 ± 0.01) %. The $B^\pm$ tag probabilities extracted from cone charge distributions were created for each of the opposite side tagging methods and they are shown in Figures 7.5, 7.6, 7.7, and 7.8. Consequently, the B_s^0 tag probabilities were yielded from the B_s^0 cone charge distributions by applying the calibration curves. The B_s^0 tag probabilities were separated into the signal and background distributions. These were fitted as shown in Figure 7.9 and included in the main fit model used in the measurement of CP violation in the $B_s^0 \to J/\psi\phi$ decay.

CP Violation in the $B_s^0 \to J/\psi\phi$ Decay

The CP violation, lifetime properties and polarisation amplitudes were used to describe the $B_s^0 \to J/\psi(\mu^+\mu^-)\phi(K^+K^-)$. The fit model describes the mass, lifetime and angular distributions and the unbinned maximum fit provides the values of nine physical parameters. A large number of systematic contributions was included in the result values. The results were combined with those from ATLAS Run1 and their values are:

$$\begin{aligned}
\phi_s &= -0.087 \pm 0.036 \text{ (stat.)} \pm 0.021 \text{ (syst.) rad},\\
\Delta\Gamma_s &= 0.0657 \pm 0.0043 \text{ (stat.)} \pm 0.0037 \text{ (syst.) ps}^{-1},\\
\Gamma_s &= 0.6703 \pm 0.0014 \text{ (stat.)} \pm 0.0018 \text{ (syst.) ps}^{-1},\\
\left|A_{\parallel}(0)\right|^2 &= 0.2220 \pm 0.0017 \text{ (stat.)} \pm 0.0021 \text{ (syst.)},\\
|A_0(0)|^2 &= 0.5152 \pm 0.0012 \text{ (stat.)} \pm 0.0034 \text{ (syst.)},\\
|A_S(0)|^2 &= 0.0343 \pm 0.0031 \text{ (stat.)} \pm 0.0045 \text{ (syst.)},\\
\delta_{\perp} &= 3.22 \pm 0.10 \text{ (stat.)} \pm 0.05 \text{ (syst.) rad},\\
\delta_{\parallel} &= 3.36 \pm 0.05 \text{ (stat.)} \pm 0.09 \text{ (syst.) rad},\\
\delta_{\perp} - \delta_S &= -0.24 \pm 0.05 \text{ (stat.)} \pm 0.04 \text{ (syst.) rad}.
\end{aligned}$$

The analysis with the combined results was published in the EPJC journal [1]. The result of the average decay width Γ_s shows 3σ tension with other experiments as shown in Figure 9.1. Other parameters are in good agreement with other experiments and theoretical predictions, so there are no hints for the physics Beyond the Standard Model. The combined results from all measurements are shown in Figure 9.7.

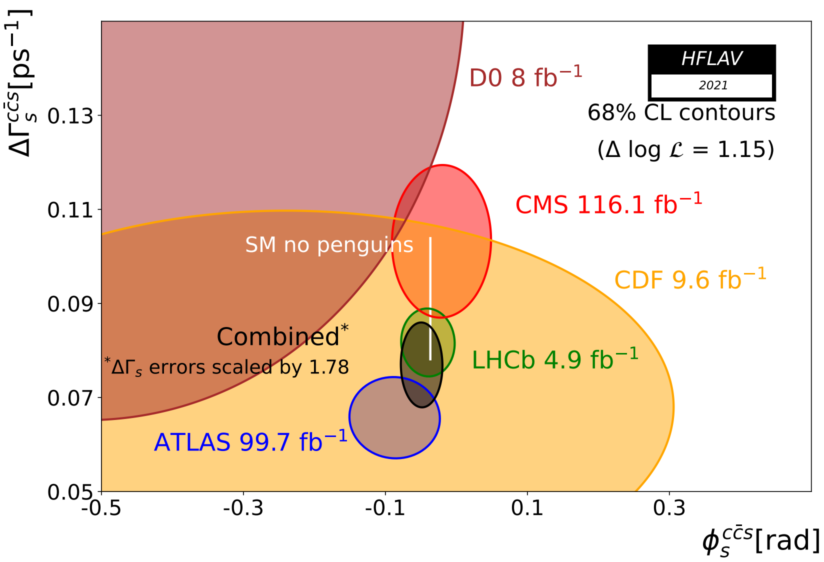

FIGURE 9.7. The individual 68% confidence-level contours of ATLAS, CMS, CDF, DØ and LHCb, their combined contour (solid white line and shaded area), as well as the Standard Model predictions (black box) [94].

B^0 Lifetime in the $B^0 \to J/\psi K^{*0}$ Decay

The tension of 3σ of the ATLAS Γ_s combined value [1] raised questions about the detector and software effects on the measured lifetime properties of mesons. To validate the B mesons measurements at ATLAS, a measurement of the lifetime of the B^0 meson is reported by the ATLAS Experiment using 139 fb^{-1} of proton-proton collision data recorded at $\sqrt{s} = 13$ TeV during the period of 2015–2018 at the Large Hadron Collider. To extract the B^0 effective lifetime value, the unbinned maximum likelihood fit with the mass-lifetime model was used. The data were corrected to the effect of the trigger and reconstruction inefficiencies and the proper decay time uncertainty enters the fit as the per-event information. The measured value

$$\tau_{B^0} = 1.5174 \pm 0.0012\,(\text{stat.}) \pm 0.0016\,(\text{syst.})\,\text{ps}$$

is the most precise measurement within statistical uncertainty, but driven by systematic uncertainty. In addition, the value of average decay width was extracted, and its value is

$$\Gamma = 0.6586 \pm 0.0005\,(\text{stat.}) \pm 0.0006\,(\text{syst.}) \pm 0.0038\,(\text{ext.})\,\text{ps}^{-1}.$$

Combining this value with the average decay width Γ_s, their ratio is

$$\frac{\Gamma}{\Gamma_s} = 0.9825 \pm 0.0022\,(\text{stat.}) \pm 0.0028\,(\text{syst.}) \pm 0.0057\,(\text{ext.}).$$

The uncertainty is driven by the external uncertainties used in the equation (9.4.2).

The lifetime and Γ values show perfect agreement with the world average values [46] and theoretical predictions [182]. The 3σ tension of the Γ/Γ_s ratio is driven by the tension of the Γ_s [1].

APPENDIX A

Statistical Data Analysis

The analysis of the recorded data usually uses the statistical technique to exploit the values of parameters of interest. These values are not sharp but are provided with some uncertainty - the statistical one in this case. A system which cannot be predicted with complete certainty is called to have random characteristics. In general, any measurement always comes with random measurement errors.

A.1 Random Variable

A degree of randomness can be expressed in a term of probability. Considering a set of (all possible) elements is called **sample space** S. The **probability** of subset A is then called a number $P(A)$ if it follow the three axioms:

- For every subset A: $P(A) \geq 0$
- For two disjoint subsets A and B, the probability of union of A and B is $P(A \cup B) = P(A) + P(B)$
- The probability assigned to the sample space is $P(S) = 1$.

A **random variable** then takes on a specific value for each element of the set S.

The **conditional probability** $P(A|B)$ is defined in the sample space S ($A, B \in S$) as

$$P(A|B) = \frac{P(A \cap B)}{P(B)}. \tag{A.1}$$

From this relation, the **Bayes' theorem** can be defined by

$$P(A|B)P(B) = P(B|A)P(A). \tag{A.2}$$

A.2 Probability density function

If the sample space corresponds to the set of possible values of the continuous random variable, the probability of observing a specific value in the interval $(x; x + \mathrm{d}x)$ is

$$P\left(x_0 \in (x; x + \mathrm{d}x)\right) = f(x)\mathrm{d}x, \tag{A.3}$$

where the function $f(x)$ is called **probability density function (PDF)**. The PDF can also be defined for the discrete random variable, but it is normalised to follow the axioms of probability. The PF can be dependent on at least one parameter θ. Consider a sample of random variable measurements $\vec{x} = (x_1, \ldots, x_N)$, where x_i can also be a set of measured parameters (i.e.: mass, momentum, energy, ...), and set of unknown parameters $\vec{\theta} = (\theta_1, \ldots, \theta_M)$, both described by the joint PDF $f(x_i, \theta_k)$. The measurements x_i are independent, so their joint PDF is **likelihood** defined as [183]

$$L(\theta) = \prod_{i=1}^{N} f(x_i, \theta), \tag{A.4}$$

where only one parameter is assumed as a simplification. The measured random variable x_i is treated as fixed in the likelihood function. It is easier to work with the logarithm of likelihood due to converting the product into the sum:

$$\ln L(\theta) = \sum_{i=1}^{N} \ln\left(f(x_i, \theta)\right) \tag{A.5}$$

The advantage of working with $\ln L(\theta)$ is visible in the parameter estimation procedure.

A.3 Maximum Likelihood Estimation

To extract the value of parameter θ from the sample $\vec{x} = (x_1, \ldots, x_N)$, the maximum likelihood method is used. It is based on an attempt to maximise the probability (likelihood) of measuring the θ with a given sample. The maximum can be found by [183]

$$\frac{\partial \ln L(\theta)}{\partial \theta} = 0 \tag{A.6}$$

and it provides an estimate of the parameter mean value. To evaluate the statistical uncertainty of the estimate, the Rao-Cramer-Frechet (RCF) method is used to extract the covariance matrix V_{ij} [183]:

$$V_{ij} = -\left(\frac{\partial^2 \ln L(\theta)}{\partial\theta_i \partial\theta_j}\right)^{-1}, \tag{A.7}$$

where the diagonal terms correspond to the squared statistical uncertainty of the estimate.

A.4 Punzi Terms

The maximum likelihood estimation usually uses the determination of the class proportion and the properties, a good example is separating the data into the signal and background by the fit model. For example, the proper decay time resolution or mass resolution can have different behaviour for signal and for background. To better understand the problem, consider a simplified situation with two types of events (A and B). With a given fraction f of A events and probability functions of A and B,

$$\begin{aligned} p(x|A) &= N(0,\sigma) \\ p(x|B) &= N(1,\sigma), \end{aligned} \tag{A.8}$$

the likelihood function is

$$L(f) = \prod_i \Big[f N(x_i, 0, \sigma) + (1-f) N(x_i, 1, \sigma) \Big], \tag{A.9}$$

where $N(x,\mu,\sigma)$ is the Gaussian function in observable x, which is considered to have constant resolution. If the measurement has a different resolution for each event (per-event resolution), the likelihood in the first approach takes a form

$$L(f) = \prod_i \Big[f N(x_i, 0, \sigma_i) + (1-f) N(x_i, 1, \sigma_i) \Big]. \tag{A.10}$$

However, this likelihood provides biased measurements of variable f [184]. The likelihood cannot be treated as a function with one parameter but two. Then, the PDF depends on both parameters, and the likelihood is

$$L(f) = \prod_i \Big[f p(x_i, \sigma_i | A) + (1-f) p(x_i, \sigma_i | B) \Big]. \tag{A.11}$$

The PDFs $p(x_i, \sigma_i|A)$ can be rewritten as a conditional probability:

$$p(x_i, \sigma_i|A) = p(x_i|\sigma_i, A)p(\sigma_i|A), \tag{A.12}$$

and the final likelihood is

$$L(f) = \prod_i \Big[fN(x_i, 0, \sigma_i)p(\sigma_i|A) + (1-f)N(x_i, 1, \sigma_i)p(\sigma_i|B) \Big]. \tag{A.13}$$

where $p(\sigma_i|A)$ and $p(\sigma_i|B)$ are the probability density functions of σ_i, also called the Punzi terms. Note that the $p(\sigma_i|A)$ and $p(\sigma_i|B)$ are distributions, but σ_i is just the number in the Gaussian function. In the case of $p(\sigma_i|A) = p(\sigma_i|B)$, the Punzi terms can be factorised out, and the likelihood (A.13) becomes (A.10).

A.5 Combination of Results

The measurements can be combined with the older ones to reach higher precision of the measured parameter. When combining two equivalent measurements, the Best Linear Unbiased Estimator (BLUE) [185, 186].

In this method, the combined result for parameter α from n estimates y_i is given by

$$\hat{x}_\alpha = \sum_{i=1}^{n} \lambda_{\alpha i} y_i, \tag{A.14}$$

where $\lambda_{\alpha i}$ are the weights assigned to each estimate. The variance of each parameter is given by

$$\mathrm{var}(\hat{x}_\alpha) = \sum_{i=1}^{n} \sum_{j=1}^{n} \lambda_{\alpha i} \mathcal{M}_{ij} \lambda_{\alpha j}. \tag{A.15}$$

In the simple case of combining two measurements of two parameters, e.g. a_1, a_2, b_1, b_2, the matrix $\mathcal{M}$ can be written as

$$\mathcal{M} = \begin{pmatrix} \mathrm{cov}(a_1, a_1) & \mathrm{cov}(a_1, a_2) & \mathrm{cov}(a_1, b_1) & \mathrm{cov}(a_1, b_2) \\ \mathrm{cov}(a_2, a_1) & \mathrm{cov}(a_2, a_2) & \mathrm{cov}(a_2, b_1) & \mathrm{cov}(a_2, b_2) \\ \mathrm{cov}(b_1, a_1) & \mathrm{cov}(b_1, a_2) & \mathrm{cov}(b_1, b_1) & \mathrm{cov}(b_1, b_2) \\ \mathrm{cov}(b_2, a_1) & \mathrm{cov}(b_2, a_2) & \mathrm{cov}(b_2, b_1) & \mathrm{cov}(b_2, b_2) \end{pmatrix}. \tag{A.16}$$

It is also possible to split the matrix $\mathcal{M}$ into a sum of statistical and systematic correlation matrices $\mathcal{M}_{(\mathrm{stat.})}$ and $\mathcal{M}_{(\mathrm{syst.})}$ respectively

$$\mathcal{M} = \mathcal{M}_{(\mathrm{stat.})} + \mathcal{M}_{(\mathrm{syst.})}. \tag{A.17}$$

The BLUE technique involves finding the values of $\lambda_{\alpha i}$ that minimize $\mathrm{var}(\hat{x}_\alpha)$. The measured values and uncertainties of the parameters in question, as well as the correlations between them are required.

APPENDIX B

Tagging Systematic Tests in the CP Violation Measurement

Several sources contribute to the systematic uncertainty due to flavour tagging. This chapter provides a detailed description of each contribution to.

B.0.1 Systematic Uncertainty Due to Jet p_{T}

To access the possible effect of different calibration curves for different intervals of jet p_{T}, the following check is performed. The $B^{\pm}$ sample is separated into four intervals

	Δ	Δ/σ
ϕ_s [rad]	0.0033040	0.0844
$\lvert A_0(0)\rvert^2$	-0.0000162	0.0123
$\lvert A_S(0)\rvert^2$	-0.0001638	0.0490
$\lvert A_{\parallel}(0)\rvert^2$	0.0003423	0.0176
$\Delta\Gamma_s$ [ps^{-1}]	-0.0000291	0.0063
Γ_s [ps^{-1}]	-0.0000101	0.0072
$\delta_{\parallel}$ [rad]	0.0028357	0.0321
$\delta_{\perp}$ [rad]	-0.0009726	0.0125
$\delta_{\perp}-\delta_S$ [rad]	-0.0000005	0.0269

TABLE B.1. Systematic uncertainties due to jet p_{T}. The relative difference Δ/σ as a difference between nominal and alternative fit values divided by the statistical uncertainties of the nominal fit is presented.

of jet-p_T, and calibrations curves are defined in the usual manner. These curves are parameterised using third-order polynomials for the continuous distribution. The main likelihood fit is rerun, where for each jet-tagged event the appropriate calibration curve is selected. In Table B.1, the results of the tests are shown for the main fit parameters (only the largest difference from all tests presented), and the difference Δ is taken as the contribution to the systematic uncertainties due to the tagging. The largest shift is, as expected, in ϕ_s, to the order of $\approx 8.5\%$ of the statistical uncertainty. Other parameters are shifted by less than half this. Therefore, no effect is observed on the tagging due to the p_T of the jet within these uncertainties.

B.0.2 Systematic Uncertainty Due to Calibrations

The contributions to the fit uncertainties due to the statistical precision of the calibration sample used for flavour tagging and the systematic shifts due to the modelling parametrisations to define the calibration are assessed and presented here.

In order to assess the uncertainty from tagging in the final result, two distinct sources are considered here. Firstly, the contribution of uncertainty due to the statistical uncertainty in the calibration sample is considered, and secondly, the systematic contribution due to the choices of parameterisation chosen for the calibration curves. These components are assessed by generating new tag-probability vs tag-charge histograms, varying each bin according to its uncertainty, and refitting the calibration curve.

	Δ	Δ/σ	Δ_{stat}
ϕ_s [rad]	0.000093	0.068295	0.000036
$\lvert A_0(0)\rvert^2$	0.000124	0.039035	0.000230
$\lvert A_S(0)\rvert^2$	0.000348	0.076827	0.000277
$\lvert A_{\parallel}(0)\rvert^2$	0.000139	0.095812	0.000048
$\Delta\Gamma_s$ [ps^{-1}]	0.000096	0.020871	0.000103
Γ_s [ps^{-1}]	0.009198	0.223276	0.001248
$\delta_{\parallel}$ [rad]	0.045781	0.194559	0.046941
$\delta_{\perp}$ [rad]	0.018021	0.119387	0.023532
$\delta_{\perp} - \delta_S$ [rad]	0.000676	0.018947	0.000623

TABLE B.2. Table of systematic shifts Δ for the calibration parametrisations. Also, the relative shifts with respect to the nominal statistical uncertainties Δ/σ are shown. The last column shows the contribution to statistical uncertainties Δ_{stat} originating from the standard deviations of parameter distribution from the 115 tests.

For the statistical uncertainty, the nominal curve is fitted to the newly generated $B^{\pm}$ tag probabilities, and the full fit is repeated. This part of the study is called Test-N. For the systematics, a set of curves are fitted, and maximum up and down deviations that are obtained from Test-U and Test-D, which are done in a similar way as Test-N, are used.

The procedure described above is repeated one hundred fifteen times. The spread of Test-N determines the statistical contribution to the uncertainty; the shift of the mean between Test-N and Test-U/Test-D components conservatively accounts for the systematic contributions. The standard deviations of the distribution of fitted parameters under the nominal case are used to assess the statistical component; the shift in means between nominal and the large of up and down are used to define the systematic contribution.

B.0.3 Systematics due to Tag Probability Functions

The effect of the B_s^0 tag probability function modelling is taken into account. The nominal signal and background functions are examined to have a bias on the final B_s^0 fit results. The functions are varied within the statistical uncertainties of their parameters, and the alternative fit is performed with these new tag probabilities. In addition, the tag probability distribution is separated to signal, and background distributions using the sPlot technique and the main fit is run with the distributions as signal and background tag probabilities. The systematic uncertainty is estimated by comparison of the baseline fit and the fits with alternative tag probabilities. The impacts of this test are shown in Table B.3.

B.0.4 Stability of Tagging with Pile-up

To test the stability of the tagging calibration against pile-up (and other time-dependent effects), the following test is performed. First, subsets of data are created according to the value of μ for each event (see Figure B.1). For each subset, independent calibration curves are created for the continuous and discrete parts. Lastly, the default fit is run, and comparisons are made between the fit using the single calibration curves vs. those where, for each pile-up subsample, the appropriate calibration curve is used, depending on the value of μ for that event. Given that sub-dividing the data reduces the statistical precision for each curve, the effects of statistical fluctuations may be considerable. The largest differences between alternative and default fits are shown in Table B.4.

	Δ	Δ/σ
ϕ_s [rad]	0.001643	0.034
$\|A_0(0)\|^2$	0.000044	0.022
$\|A_S(0)\|^2$	0.000102	0.022
$\|A_{\|\|}(0)\|^2$	0.000027	0.011
$\Delta\Gamma_s$ [ps^{-1}]	0.000116	0.018
Γ_s [ps^{-1}]	0.000129	0.067
$\delta_{\|\|}$ [rad]	0.001283	0.021
$\delta_\perp$ [rad]	0.004995	0.032
$\delta_\perp - \delta_S$ [rad]	0.000187	0.008

TABLE B.3. Results of the fitting procedure under the variation of signal and background tag probability terms. The values in the third column are obtained by division of the difference by the statistical uncertainty from Table 8.2.

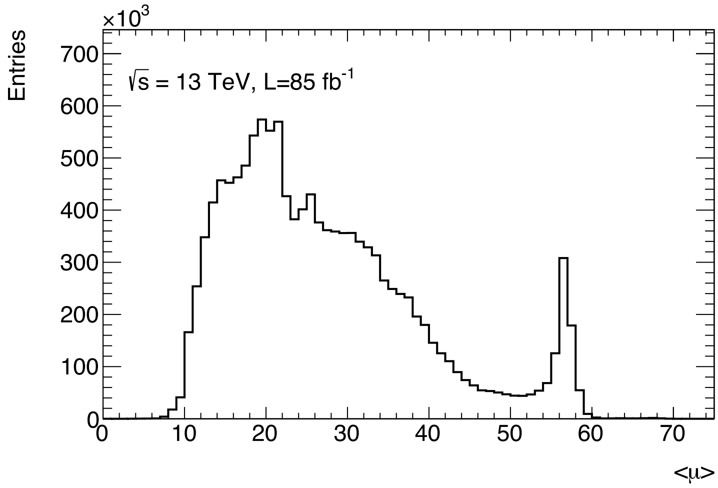

FIGURE B.1. Distribution of pile-up $<\mu>$ for events in the $B^\pm$ sample of selected events.

B.0.5 Systematic Uncertainties Due to the $B^\pm$ and B_s^0 Differences

A cross-check of the validity of the tagging procedure is to compare calibration curves, derived from simulation, between B_s and $B^\pm$. It should be noted that the use of the MC to derive the calibration is rather complex and prone to the effects of modelling the underlying events, treatment of oscillations and of other tunings to match the data. It should, however, be possible to make a check between the different processes such that the calibration curves agree within errors. Following the same strategy as done in the data, calibration curves are prepared for each sample and overlaid.

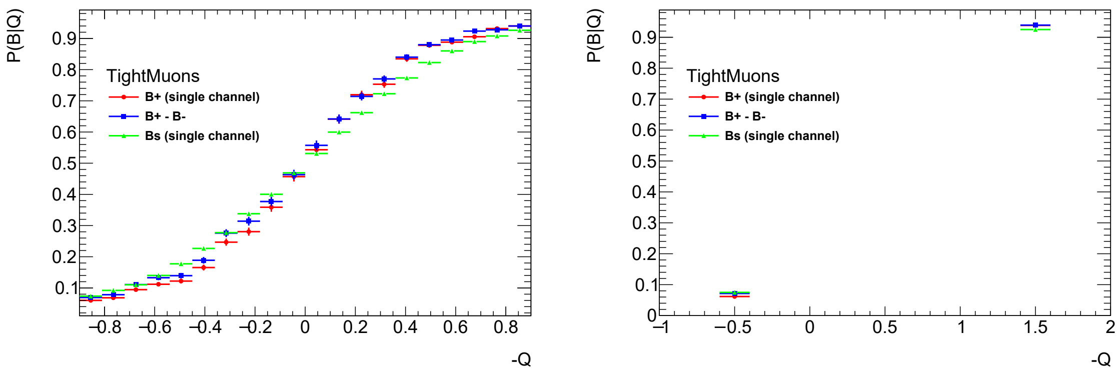

Figure B.2: The calibration distributions extracted from B_s^0 and $B^{\pm}$ MC samples.

Here the differences are more pronounced, and the impact of this is accounted for within the systematic variations. As the MC curves should not be directly applied to the data, the difference between samples is considered and shown in Figure B.2. The variation is within 10%, and a systematic effect based on this scaling is propagated into the main B_s fitting procedure. A scaling is applied, such that if the event has probability $p = 0.5 + \delta$, then the scaled probability propagated into the fit becomes $p' = 0.5 + \delta \times \lambda$, where $\lambda = 1.1$. Table B.5 shows the differences between nominal fit results and fit with scaled tag probability.

	Δ	Δ/σ
ϕ_s [rad]	0.0104	0.2160
$\|A_0(0)\|^2$	0.0000	0.0233
$\|A_S(0)\|^2$	0.0003	0.0641
$\|A_{\|\|}(0)\|^2$	0.0000	0.0036
$\Delta\Gamma_s$ [ps^{-1}]	0.0002	0.0298
Γ_s [ps^{-1}]	0.0000	0.0042
$\delta_{\|\|}$ [rad]	0.0030	0.0484
$\delta_\perp$ [rad]	0.0168	0.1073
$\delta_\perp - \delta_S$ [rad]	0.0003	0.0159

TABLE B.4. Systematic test due to effect of pile-up on tagging. Δ is the largest difference between the nominal fit results and the alternative fit from pile-up subsamples, Δ/σ is the difference divided by the nominal fit statistical uncertainties.

	Δ	Δ/σ
ϕ_s [rad]	0.00772	0.19
$\lvert A_0(0)\rvert^2$	0.00008	0.06
$\lvert A_S(0)\rvert^2$	0.00073	0.22
$\lvert A_{\parallel}(0)\rvert^2$	0.00007	0.04
$\Delta\Gamma_s$ [ps^{-1}]	0.00013	0.03
Γ_s [ps^{-1}]	0.00003	0.02
$\delta_{\parallel}$ [rad]	0.00683	0.09
$\delta_{\perp}$ [rad]	< 0.00001	< 0.01
$\delta_{\perp} - \delta_S$ [rad]	0.00118	0.03

TABLE B.5. Table of systematic shifts for the MC calibration Δ and their relative shift Δ/σ, where σ is statistical uncertainty of each parameter from the nominal fit.

APPENDIX C

TRIGGER LISTS

The analyses are using di-muon triggers, dominantly based on $J/\psi \to \mu^+\mu^-$ identification with p_T threshold of either 4 or 6 GeV. The trigger scheme was changed between 2015 and 2018 data taking as well as the naming of the triggers. In 2016 data taking two different streams were introduced. The main stream and BPhysics delayed stream. The main stream of 2016 - at the beginning of data taking - data contains a group of triggers with higher lifetime bias, which was corrected after run number 302737, this group of triggers is referred to as early, while the rest of the main stream of 2016 data is referred as late. Here follows the list of the most contributing triggers for each data period and stream separately.

C.1 $B_s^0 \to J/\psi\phi$ Trigger List

2015 Data:

HLT_2mu4_bJpsimumu_noL2

HLT_mu6_mu4_bBmumuxv2

HLT_mu18_2mu0noL1_JpsimumuFS

Data 2016 Main Stream Early runs:

HLT_mu6_mu4_bBmumuxv2

HLT_2mu6_bBmumuxv2

HLT_mu10_mu6_bBmumuxv2

HLT_mu20_2mu0noL1_JpsimumuFS

HLT_mu10_mu6_bJpsimumu

HLT_mu6_mu4_bJpsimumu

Data 2016 Main Stream Late runs:

HLT_2mu4_bJpsimumu_L1BPH_2M8_2MU4

HLT_2mu10_bBmumuxv2

HLT_2mu6_bBmumux_BsmumuPhi_L1BPH_2M9_2MU6_BPH_2DR15_2MU6

HLT_mu20_2mu0noL1_JpsimumuFS

HLT_2mu6_bBmumuxv2

HLT_mu6_mu4_bBmumuxv2

HLT_mu10_mu6_bBmumuxv2

HLT_3mu4_bDimu

HLT_mu20_nomucomb_mu6noL1_nscan03

HLT_mu6_mu4_bJpsimumu_L12MU4_B

HLT_mu4_mu4_idperf_bJpsimumu_noid

HLT_3mu6_msonly

HLT_2mu6_bDimu

HLT_mu6_mu4_bBmumux_BsmumuPhi_L1BPH_2M8_MU6MU4_BPH_0DR15_MU6MU4

HLT_mu20_2mu4_JpsimumuL2

HLT_mu6_mu4_bJpsimumu

HLT_2mu4_bBmumux_BsmumuPhi_L1BPH_2M8_2MU4

Data 2016 delayed stream:

HLT_mu6_mu4_bBmumuxv2_delayed

HLT_2mu6_bBmumuxv2_delayed

HLT_mu6_mu4_bBmumux_BsmumuPhi_delayed_L1BPH_2M8_MU6MU4_BPH_0DR15_MU6MU4

HLT_2mu4_bBmumux_BsmumuPhi_delayed_L1BPH_2M8_2MU4

HLT_mu6_mu4_bBmumux_BsmumuPhi_delayed

HLT_mu6_2mu4_bJpsi_delayed

HLT_mu6_nomucomb_2mu4_nomucomb_delayed_L1MU6_3MU4

HLT_mu6_mu4_bJpsimumu_delayed

Data 2017 Main and delayed stream:

HLT_mu6_mu4_bBmumux_BsmumuPhi_L1BPH_2M9_MU6MU4_BPH_0DR15_MU6MU4

HLT_mu11_mu6_bDimu

HLT_2mu6_bJpsimumu_L1BPH_2M9_2MU6_BPH_2DR15_2MU6

HLT_mu20_2mu2noL1_JpsimumuFS

HLT_3mu4_bDimu

HLT_2mu6_bBmumuxv2_L1LFV_MU6

HLT_mu11_2mu4noL1_bNocut_L1MU11_2MU6

HLT_mu22_mu8noL1

HLT_2mu6_bJpsimumu

HLT_mu20_2mu4_JpsimumuL2

HLT_2mu4_mu3_mu2noL1_bNocut_L13MU4

HLT_mu6_mu4_bBmumuxv2

HLT_2mu4_invm1_j20_xe40_pufit_2dphi10_L12MU4_J20_XE30_DPHI_J20s2XE30

HLT_3mu4

HLT_3mu6_msonly

HLT_2mu14

C.2 $B_d^0 \to J/\psi K^{*0}$ Trigger List

2015 Data:

HLT_2mu4_bJpsimumu_noL2

HLT_mu6_mu4_bBmumuxv2

HLT_mu18_2mu0noL1_JpsimumuFS

Data 2016 Early runs:

HLT_2mu6_bBmumuxv2

HLT_mu6_mu4_bBmumuxv2

HLT_mu10_mu6_bBmumuxv2

Data 2016 Late runs:

HLT_2mu6_bJpsimumu_delayed

HLT_2mu6_bBmumuxv2_delayed

HLT_mu6_mu4_bBmumuxv2_delayed

HLT_2mu4_bJpsimumu_L1BPH_2M8_2MU4

HLT_mu6_mu4_bJpsimumu_delayed

HLT_2mu6_bBmumuxv2

HLT_mu6_mu4_bJpsimumu

HLT_mu20_2mu4_JpsimumuL2

Data 2017:

HLT_2mu6_bJpsimumu_L1BPH_2M9_2MU6_BPH_2DR15_2MU6

HLT_2mu6_bBmumuxv2_L1LFV_MU6

HLT_mu11_mu6_bDimu

HLT_mu11_mu6_bBmumuxv2

HLT_mu20_2mu2noL1_JpsimumuFS

HLT_mu6_mu4_bBmumuxv2

HLT_2mu14

HLT_mu50

Data 2018:

HLT_2mu6_bJpsimumu_L1BPH_2M9_2MU6_BPH_2DR15_2MU6

HLT_2mu6_bBmumuxv2_L1LFV_MU6

HLT_mu11_mu6_bDimu

HLT_mu11_mu6_bBmumuxv2

HLT_mu20_2mu2noL1_JpsimumuFS

HLT_mu6_mu4_bBmumuxv2

HLT_2mu14

HLT_mu50

HLT_mu22_mu8noL1

HLT_mu20_2mu4_JpsimumuL2

Appendix D

Full Results of the $B_s^0 \to J/\psi\phi$ CP violation Measurement

D.1 Fit Status

FitStatus	1
HesseStatus	1
MinosStatus	0
fcn	12439501.1

D.2 Parameters Fit Results

Parameter	Starting Value	Fitted Value	Range	Step	Constraint
$\|A_0(0)\|^2$	0.5	0.5156 ± 0.0013	(0 → 1)	1e-06	
$\|A_{\|\|}(0)\|^2$	0.25	0.2195 ± 0.0021	(0 → 1)	1e-06	
$\|A_S(0)\|^2$	0.000315377	0.0378 ± 0.0035	(0 → 1)	1e-06	
Γ_s [ps^{-1}]	0.6686	0.6662 ± 0.0014	(0.4 → 0.9)	1e-06	
$\Delta\Gamma$ [ps^{-1}]	0.09	0.0668 ± 0.0046	(0.01 → 0.6)	1e-06	
ΔM [$\hbar$s^{-1}]	17.757	17.757	fixed	0	
ϕ_s	0	−0.093 ± 0.041	(-20 → 20)	1e-06	
$\delta_{\|\|}$ [rad]	3.3	3.309 ± 0.063	(3.1 → 10)	1e-06	
$\delta_{\perp}$ [rad]	2.95	3.07 ± 0.11	(-6 → 7.9)	1e-06	
$\delta_{\perp} - \delta_S$ [rad]	0	−0.233 ± 0.041	(-10 → 10)	1e-06	
m_{Bs} [GeV]	5.3	5.366679 ± 0.000037	(5 → 6)	1e-06	
SF m_{Bs}	1.25	1.2627 ± 0.0021	(0 → 10)	1e-06	
SF τ_{Bs}	1	1.0326 ± 0.0013	(0.8 → 1.2)	1e-06	
f_{sig}	0.16	0.15372 ± 0.00025	(0 → 1)	1e-06	
a	0.1	1.47 ± 0.12	(0 → 1000)	1e-06	
m_0 [MeV]	0.1	0.671 ± 0.022	(0 → 1000)	1e-06	
AsScale	0.51	0.51	fixed	0	
f_{prompt}	0.6	0.6347 ± 0.0018	(0 → 1)	1e-06	
f_{indirect}	0.16	0.2354 ± 0.0011	(0 → 1)	1e-06	
f_{tails}	0.11	0.0976 ± 0.0021	(0 → 0.5)	1e-06	
f_{tails2}	0.00465478	0.0057 ± 0.0015	(1e-06 → 0.01)	1e-06	
τ_{fast} [ps]	0.28	0.21934 ± 0.00080	(0.01 → 10)	1e-06	
τ_{slow} [ps]	1.6	1.6829 ± 0.0065	(0.01 → 10)	1e-06	
τ_{tails} [ps]	0.01	0.0882 ± 0.0029	(0.001 → 0.5)	1e-06	
τ_{tails2} [ps]	0.37009	0.257 ± 0.021	(0.01 → 1)	1e-06	
$f_{\mathrm{Bd}K^*}$	0.0431	0.0431	(0 → 1)	0	
frac$_{\Lambda}$	0.021	0.021	(0 → 1)	0	
τ_{BdBs} [ps]	1.5451	1.5451	(0.5 → 2)	0	
$\tau_{\mathrm{LambdabBs}}$ [ps]	1.4039	1.4039	(0.5 → 2)	0	
mean$^{g1}_{\mathrm{Bd}K*}$ [GeV]	5.38399	5.38399	(5 → 6)	0	
sigma$^{g1}_{\mathrm{Bd}K*}$ [GeV]	0.0412153	0.0412153	(0.03 → 0.4)	0	
frac$^{g1}_{\mathrm{Bd}K*}$	0.410763	0.410763	(0 → 0.54)	0	
mean$^{g2}_{\mathrm{Bd}K*}$ [GeV]	5.4448	5.4448	(5 → 6)	0	
sigma$^{g2}_{\mathrm{Bd}K*}$ [GeV]	0.0608577	0.0608577	(0.03 → 0.8)	0	
frac$^{g1+g2}_{\mathrm{Bd}K*}$	0.343479	0.343479	(0 → 0.45)	0	
mean$^{g3}_{\mathrm{Bd}K*}$ [GeV]	5.45882	5.45882	(5 → 6)	0	
sigma$^{g3}_{\mathrm{Bd}K*}$ [Gev]	0.145705	0.145705	(0.05 → 0.8)	0	
TagMethod$_{\mathrm{sig}} = 0$	0.768742	0.768742	(0 → 1)	0	

Parameter	Starting Value	Fitted Value	Range	Step	Constraint
$\mathrm{TagMethod}_{\mathrm{sig}} = 1$	0.039952	0.039952	(0 → 1)	0	
$\mathrm{TagMethod}_{\mathrm{sig}} = 2$	0.0290955	0.0290955	(0 → 1)	0	
$\mathrm{TagMethod}_{\mathrm{sig}} = 3$	0.14356	0.14356	(0 → 1)	0	
$\mathrm{TagMethod}_{\mathrm{bck}} = 4$	0	0	(0 → 1)	0	
$\mathrm{TagMethod}_{\mathrm{sig}} = 5$	0.0186506	0.0186506	(0 → 1)	0	
$\mathrm{TagMethod}_{\mathrm{bck}} = 0$	0.807652	0.807652	(0 → 1)	0	
$\mathrm{TagMethod}_{\mathrm{bck}} = 1$	0.0316128	0.0316128	(0 → 1)	0	
$\mathrm{TagMethod}_{\mathrm{bck}} = 2$	0.0263695	0.0263695	(0 → 1)	0	
$\mathrm{TagMethod}_{\mathrm{bck}} = 3$	0.119572	0.119572	(0 → 1)	0	
$\mathrm{TagMethod}_{\mathrm{bck}} = 4$	0	0	(0 → 1)	0	
$\mathrm{TagMethod}_{\mathrm{bck}} = 5$	0.0147932	0.0147932	(0 → 1)	0	
$\mathrm{TagMethod} = 1\ f_{\mathrm{sig}}(\mathrm{tag} = +1)$	0.069023	0.069023	(0 → 1)	0	
$\mathrm{TagMethod} = 1\ f_{\mathrm{sig}}(\mathrm{tag} = -1)$	0.07505	0.07505	(0 → 1)	0	
$\mathrm{TagMethod} = 2\ f_{\mathrm{sig}}(\mathrm{tag} = +1)$	0.108771	0.108771	(0 → 1)	0	
$\mathrm{TagMethod} = 2\ f_{\mathrm{sig}}(\mathrm{tag} = -1)$	0.116554	0.116554	(0 → 1)	0	
$\mathrm{TagMethod} = 3\ f_{\mathrm{sig}}(\mathrm{tag} = +1)$	0.045051	0.045051	(0 → 1)	0	
$\mathrm{TagMethod} = 3\ f_{\mathrm{sig}}(\mathrm{tag} = -1)$	0.045757	0.045757	(0 → 1)	0	
$\mathrm{TagMethod} = 5\ f_{\mathrm{sig}}(\mathrm{tag} = +1)$	0.198665	0.198665	(0 → 1)	0	
$\mathrm{TagMethod} = 5\ f_{\mathrm{sig}}(\mathrm{tag} = -1)$	0.185139	0.185139	(0 → 1)	0	
$\mathrm{TagMethod} = 1\ f_{\mathrm{bck}}(\mathrm{tag} = +1)$	0.0469222	0.0469222	(0 → 1)	0	
$\mathrm{TagMethod} = 1\ f_{\mathrm{bck}}(\mathrm{tag} = -1)$	0.049032	0.049032	(0 → 1)	0	
$\mathrm{TagMethod} = 2\ f_{\mathrm{bck}}(\mathrm{tag} = +1)$	0.0704716	0.0704716	(0 → 1)	0	
$\mathrm{TagMethod} = 2\ f_{\mathrm{bck}}(\mathrm{tag} = -1)$	0.075609	0.075609	(0 → 1)	0	
$\mathrm{TagMethod} = 3\ f_{\mathrm{bck}}(\mathrm{tag} = +1)$	0.0375943	0.0375943	(0 → 1)	0	
$\mathrm{TagMethod} = 3\ f_{\mathrm{bck}}(\mathrm{tag} = -1)$	0.038577	0.038577	(0 → 1)	0	
$\mathrm{TagMethod} = 5\ f_{\mathrm{bck}}(\mathrm{tag} = +1)$	0.167525	0.167525	(0 → 1)	0	
$\mathrm{TagMethod} = 5\ f_{\mathrm{bck}}(\mathrm{tag} = -1)$	0.173059	0.173059	(0 → 1)	0	
$\mathrm{tag1Sig}_{\mathrm{exp}}1$	-16.459	-16.459	(-200 → 0)	0	
$\mathrm{tag1Sig}_{\mathrm{exp}}2$	12.524	12.524	(0 → 200)	0	
$\mathrm{tag1Sig}_{P}1$	0	0	(-200 → 200)	0	
$\mathrm{tag1Sig}_{P}2$	0	0	(-200 → 200)	0	
$\mathrm{tag1Sig}_{P}3$	0	0	(-200 → 200)	0	
$\mathrm{tag1Sig}_{P}4$	0	0	(-200 → 200)	0	
$\mathrm{tag1Sig}_{f}Fraction1$	0.18005	0.18005	(0 → 1)	0	
$\mathrm{tag1Sig}_{f}Fraction2$	0.64017	0.64017	(0 → 1)	0	
$\mathrm{tag1Sig}_{\mathrm{min}}$	0.193521	0.193521	(0 → 1)	0	
$\mathrm{tag1Sig}_{\mathrm{max}}$	0.810954	0.810954	(0 → 1)	0	
$\mathrm{tag2Sig}_{\mathrm{Mu}}$	0.51036	0.51036	(0 → 1)	0	
$\mathrm{tag2Sig}_{\mathrm{Sigma}}$	0.25	0.25	(0 → 0.3)	0	
$\mathrm{tag2Sig}_{\mathrm{min}}$	0.295062	0.295062	(0 → 1)	0	
$\mathrm{tag2Sig}_{\mathrm{max}}$	0.717363	0.717363	(0 → 1)	0	
$\mathrm{tag3Sig}_{\mathrm{Mu}}$	0.5041	0.5041	(0 → 1)	0	
$\mathrm{tag3Sig}_{\mathrm{Sigma}}$	0.11449	0.11449	(0 → 1)	0	
$\mathrm{tag3Sig}_{\mathrm{min}}$	0.273089	0.273089	(0 → 1)	0	
$\mathrm{tag3Sig}_{\mathrm{max}}$	0.735249	0.735249	(0 → 1)	0	

Parameter	Starting Value	Fitted Value	Range	Step	Constraint
tag5Sig$_{\mathrm{exp}}$1	-99.999	-99.999	(-100 → 0)	0	
tag5Sig$_{\mathrm{exp}}$2	69.538	69.538	(0 → 100)	0	
tag5Sig$_P$1	-3.6416	-3.6416	(-200 → 200)	0	
tag5Sig$_P$2	3.62	3.62	(-200 → 200)	0	
tag5Sig$_f Fraction1$	0.1029	0.1029	(0 → 1)	0	
tag5Sig$_f Fraction2$	0.79233	0.79233	(0 → 1)	0	
tag5Sig$_{\mathrm{min}}$	0.246658	0.246658	(0 → 1)	0	
tag5Sig$_{\mathrm{max}}$	0.754703	0.754703	(0 → 1)	0	
tag1Bck$_{\mathrm{exp}}$1	-45.0091	-45.0091	(-1500 → 0)	0	
tag1Bck$_{\mathrm{exp}}$2	25.187	25.187	(0 → 1000)	0	
tag1Bck$_P$1	-1.1926	-1.1926	(-200 → 200)	0	
tag1Bck$_P$2	1.003	1.003	(-200 → 200)	0	
tag1Bck$_P$3	0	0	(-200 → 200)	0	
tag1Bck$_P$4	0	0	(-200 → 200)	0	
tag1Bck$_f Fraction1$	0.04154	0.04154	(0 → 1)	0	
tag1Bck$_f Fraction2$	0.8895	0.8895	(0 → 1)	0	
tag1Bck$_{\mathrm{min}}$	0.193521	0.193521	(0 → 1)	0	
tag1Bck$_{\mathrm{max}}$	0.810954	0.810954	(0 → 1)	0	
tag2Bck$_{\mathrm{Mu}}$	0.50074	0.50074	(0 → 1)	0	
tag2Bck$_{\mathrm{Sigma}}$	0.15496	0.15496	(0 → 0.25)	0	
tag2Bck$_{\mathrm{min}}$	0.295062	0.295062	(0 → 1)	0	
tag2Bck$_{\mathrm{max}}$	0.717363	0.717363	(0 → 1)	0	
tag3Bck$_P$1	-1178.9	-1178.9	(-2000 → 2000)	0	
tag3Bck$_P$2	5769.6	5769.6	(-6000 → 6000)	0	
tag3Bck$_P$3	-3351.1	-3351.1	(-4000 → 4000)	0	
tag3Bck$_P$4	-7259.9	-7259.9	(-8000 → 8000)	0	
tag3Bck$_P$5	-1574.9	-1574.9	(-2000 → 2000)	0	
tag3Bck$_P$6	8725.6	8725.6	(-9000 → 9000)	0	
tag3Bck$_P$7	11047	11047	(-12000 → 12000)	0	
tag3Bck$_P$8	-13128	-13128	(-20000 → 20000)	0	
tag3Bck$_{\mathrm{min}}$	0.273089	0.273089	(0 → 1)	0	
tag3Bck$_{\mathrm{max}}$	0.735249	0.735249	(0 → 1)	0	
tag5Bck$_{\mathrm{exp}}$1	-64.419	-64.419	(-100 → 0)	0	
tag5Bck$_{\mathrm{exp}}$2	57.05	57.05	(0 → 100)	0	
tag5Bck$_P$1	-3.4406	-3.4406	(-200 → 200)	0	
tag5Bck$_P$2	3.4444	3.4444	(-200 → 200)	0	
tag5Bck$_f Fraction1$	0.11292	0.11292	(0 → 1)	0	
tag5Bck$_f Fraction2$	0.78815	0.78815	(0 → 1)	0	
tag5Bck$_{\mathrm{min}}$	0.246658	0.246658	(0 → 1)	0	
tag5Bck$_{\mathrm{max}}$	0.754703	0.754703	(0 → 1)	0	
BmassLambdabDummyParam	1	1	(0 → 1)	0	

D.3 Correlation Tables

Correlations	$\lvert A_0(0)\rvert^2$	$\lvert A_{\vert\vert}(0)\rvert^2$	$\lvert A_S(0)\rvert^2$	Γ_s	$\Delta\Gamma$	ϕ_s	$\delta_{\vert\vert}$	$\delta_\perp$	$\delta_\perp - \delta_S$	m_{Bs}	SF m_{Bs}	SF τ_{Bs}	f_{sig}	a	m_0	f_{prompt}	f_{indirect}	f_{tails}	f_{tails2}	τ_{fast}	τ_{slow}	τ_{tails}	τ_{tails2}
$\lvert A_0(0)\rvert^2$	1.000	-0.345	0.283	-0.037	0.093	-0.006	-0.118	-0.052	0.061	0.000	-0.007	0.002	-0.015	0.003	0.003	-0.001	0.009	-0.002	0.001	-0.001	-0.005	0.001	0.001
$\lvert A_{\vert\vert}(0)\rvert^2$	-0.345	1.000	-0.207	-0.142	0.095	-0.000	0.561	0.174	-0.047	-0.000	0.006	-0.000	0.014	-0.004	-0.004	0.001	-0.002	0.001	-0.000	-0.001	-0.000	-0.000	-0.000
$\lvert A_S(0)\rvert^2$	0.283	-0.207	1.000	0.104	0.044	-0.014	-0.400	-0.173	0.204	-0.000	0.018	0.005	0.030	-0.010	-0.010	0.009	-0.010	-0.003	0.002	-0.002	-0.003	0.003	0.002
Γ_s	-0.037	-0.142	0.104	1.000	-0.565	0.019	-0.107	-0.033	0.020	-0.001	0.026	0.001	0.103	-0.032	-0.032	0.013	0.003	0.004	-0.000	0.006	0.129	0.000	0.000
$\Delta\Gamma$	0.093	0.095	0.044	-0.565	1.000	-0.104	0.039	0.002	0.012	-0.001	0.003	0.007	0.013	-0.004	-0.004	0.004	0.022	-0.004	0.002	-0.009	-0.040	0.003	0.002
ϕ_s	-0.006	-0.000	-0.014	0.019	-0.104	1.000	0.015	0.011	-0.009	0.002	0.000	-0.003	-0.001	0.000	0.000	-0.002	-0.004	0.002	-0.001	0.001	0.006	-0.001	-0.001
$\delta_{\vert\vert}$	-0.118	0.561	-0.400	-0.107	0.039	0.015	1.000	0.315	-0.067	-0.001	0.009	-0.001	0.025	-0.007	-0.007	0.002	-0.005	0.002	-0.001	-0.001	0.003	-0.001	-0.001
$\delta_\perp$	-0.052	0.174	-0.173	-0.033	0.002	0.011	0.315	1.000	0.028	-0.001	0.003	-0.001	0.006	-0.002	-0.001	-0.000	-0.001	0.001	-0.001	-0.000	0.002	-0.001	-0.001
$\delta_\perp - \delta_S$	0.061	-0.047	0.204	0.020	0.012	-0.009	-0.067	0.028	1.000	-0.001	0.003	0.001	0.007	-0.002	-0.002	0.002	-0.002	-0.000	0.000	-0.001	-0.001	0.001	0.000
m_{Bs}	0.000	-0.000	-0.000	-0.001	-0.001	0.002	-0.001	-0.001	-0.001	1.000	-0.027	0.000	-0.017	0.001	-0.003	-0.001	0.009	-0.001	0.000	0.002	-0.001	0.000	0.000
SF m_{Bs}	-0.007	0.006	0.018	0.026	0.003	0.000	0.009	0.003	0.003	-0.027	1.000	0.004	0.205	-0.048	-0.047	0.028	-0.096	0.006	0.001	-0.008	0.021	0.002	0.002
SF τ_{Bs}	0.002	-0.000	0.005	0.001	0.007	-0.003	-0.001	-0.001	0.001	0.000	0.004	1.000	0.007	-0.002	-0.002	0.767	0.148	-0.723	0.411	0.386	0.095	0.553	0.384
f_{sig}	-0.015	0.014	0.030	0.103	0.013	-0.001	0.025	0.006	0.007	-0.017	0.205	0.007	1.000	-0.096	-0.093	0.043	-0.097	0.011	0.000	-0.007	0.029	0.002	0.001
a	0.003	-0.004	-0.010	-0.032	-0.004	0.000	-0.007	-0.002	-0.002	0.001	-0.048	-0.002	-0.096	1.000	0.989	-0.012	0.021	-0.003	0.000	0.002	-0.007	-0.000	-0.000
m_0	0.003	-0.004	-0.010	-0.032	-0.004	0.000	-0.007	-0.001	-0.002	-0.003	-0.047	-0.002	-0.093	0.989	1.000	-0.011	0.020	-0.003	0.000	0.002	-0.006	-0.000	-0.000
f_{prompt}	-0.001	0.001	0.009	0.013	0.004	-0.002	0.002	-0.000	0.002	-0.001	0.028	0.767	0.043	-0.012	-0.011	1.000	0.127	-0.816	0.661	0.558	0.153	0.826	0.617
f_{indirect}	0.009	-0.002	-0.010	0.003	0.022	-0.004	-0.005	-0.001	-0.002	0.009	-0.096	0.148	-0.097	0.021	0.020	0.127	1.000	-0.123	0.076	-0.298	-0.557	0.100	0.071
f_{tails}	-0.002	0.001	-0.003	0.004	-0.004	0.002	0.002	0.001	-0.000	-0.001	0.006	-0.723	0.011	-0.003	-0.003	-0.816	-0.123	1.000	-0.323	-0.340	-0.084	-0.609	-0.270
f_{tails2}	0.001	-0.000	0.002	-0.000	0.002	-0.001	-0.001	-0.001	0.000	0.000	0.001	0.411	0.000	0.000	0.000	0.661	0.076	-0.323	1.000	0.254	0.065	0.923	0.972
τ_{fast}	-0.001	-0.001	-0.002	0.006	-0.009	0.001	-0.001	-0.000	-0.001	0.002	-0.008	0.386	-0.007	0.002	0.002	0.558	-0.298	-0.340	0.254	1.000	0.443	0.332	0.240
τ_{slow}	-0.005	-0.000	-0.003	0.129	-0.040	0.006	0.003	0.002	-0.001	-0.001	0.021	0.095	0.029	-0.007	-0.006	0.153	-0.557	-0.084	0.065	0.443	1.000	0.085	0.062
τ_{tails}	0.001	-0.000	0.003	0.000	0.003	-0.001	-0.001	-0.001	0.001	0.000	0.002	0.553	0.002	-0.000	-0.000	0.826	0.100	-0.609	0.923	0.332	0.085	1.000	0.870
τ_{tails2}	0.001	-0.000	0.002	0.000	0.002	-0.001	-0.001	-0.001	0.000	0.000	0.002	0.384	0.001	-0.000	-0.000	0.617	0.071	-0.270	0.972	0.240	0.062	0.870	1.000

Bibliography

[1] ATLAS Collaboration. Measurement of the CP-violating phase ϕ_s in $B_s^0 \to J/\psi\phi$ decays in ATLAS at 13 TeV. *Eur. Phys. J. C*, 81(4):342, 2021. doi:10.1140/epjc/s10052-021-09011-0.

[2] Adam Edward et al. Barton. Precision measurement of B meson lifetime in $B_d^0 \to J/\psi K^*$ decay (ATLAS member protected). Technical report, CERN, Geneva, 2022. URL https://cds.cern.ch/record/2845218.

[3] John Dalton. *A New System of Chemical Philosophy*. Executors of S. Russell, Manchester, England, 1808. URL https://digital.sciencehistory.org/works/ff365590j.

[4] J. J. Thomson. Cathode rays. *Phil. Mag. Ser. 5*, 44:293–316, 1897. doi:10.1080/14786449708621070.

[5] E. Rutherford. The scattering of alpha and beta particles by matter and the structure of the atom. *Phil. Mag. Ser. 6*, 21:669–688, 1911. doi:10.1080/14786440508637080.

[6] N. Bohr. On the Constitution of Atoms and Molecules. *Phil. Mag. Ser. 6*, 26:1–24, 1913. doi:10.1080/14786441308634955.

[7] W. a Heisenberg. Uber den anschaulichen Inhalt der quantentheoretischen Kinematik und Mechanik. *Z. Phys.*, 43:172–198, 1927. doi:10.1007/BF01397280.

[8] J. Chadwick. The Existence of a Neutron. *Proc. Roy. Soc. Lond. A*, 136(830):692–708, 1932. doi:10.1098/rspa.1932.0112.

[9] J. Clerk Maxwell. A dynamical theory of the electromagnetic field. *Phil. Trans. Roy. Soc. Lond.*, 155:459–512, 1865. doi:10.1098/rstl.1865.0008.

[10] H. Hertz. Ueber strahlen electrischer kraft. *Annalen der Physik*, 272(4): 769–783, 1889. doi:https://doi.org/10.1002/andp.18892720402. URL `https://onlinelibrary.wiley.com/doi/abs/10.1002/andp.18892720402`.

[11] Max Planck. On the Law of Distribution of Energy in the Normal Spectrum. *Annalen Phys.*, 4:553, 1901.

[12] A. Einstein. Über die vom Relativitätsprinzip geforderte Trägheit der Energie. *Annalen Phys.*, 23(7):371–384, 1907. doi:10.1002/andp.19073280713.

[13] Albert Einstein. A New Formal Interpretation of Maxwell's Field Equations of Electrodynamics. *Sitzungsber. Preuss. Akad. Wiss. Berlin (Math. Phys.)*, 1916: 184–188, 1916.

[14] Hideki Yukawa. On the Interaction of Elementary Particles I. *Proc. Phys. Math. Soc. Jap.*, 17:48–57, 1935. doi:10.1143/PTPS.1.1.

[15] S. H. Neddermeyer and C. D. Anderson. Note on the Nature of Cosmic Ray Particles. *Phys. Rev.*, 51:884–886, 1937. doi:10.1103/PhysRev.51.884.

[16] C. M. G. Lattes, H. Muirhead, G. P. S. Occhialini, and C. F. Powell. PROCESSES INVOLVING CHARGED MESONS. *Nature*, 159:694–697, 1947. doi:10.1038/159694a0.

[17] G. D. Rochester and C. C. Butler. Evidence for the Existence of New Unstable Elementary Particles. *Nature*, 160:855–857, 1947. doi:10.1038/160855a0.

[18] M. Gell-Mann. Isotopic Spin and New Unstable Particles. *Phys. Rev.*, 92:833–834, 1953. doi:10.1103/PhysRev.92.833.

[19] A. Pais. Relative Parity of Charged and Neutral K-Particles. *Phys. Rev.*, 112: 624–641, 1958. doi:10.1103/PhysRev.112.624.

[20] T. Nakano and K. Nishijima. Charge Independence for V-particles. *Prog. Theor. Phys.*, 10:581–582, 1953. doi:10.1143/PTP.10.581.

[21] Murray Gell-Mann. The Eightfold Way: A Theory of strong interaction symmetry. 3 1961. doi:10.2172/4008239.

[22] Murray Gell-Mann. A Schematic Model of Baryons and Mesons. *Phys. Lett.*, 8: 214–215, 1964. doi:10.1016/S0031-9163(64)92001-3.

[23] G. Zweig. An SU(3) model for strong interaction symmetry and its breaking. Version 1. 1 1964.

[24] Donald H. Perkins. *Introduction to High Energy Physics*. Cambridge University Press, 4 edition, 2000. doi:10.1017/CBO9780511809040.

[25] O. W. Greenberg. Spin and Unitary Spin Independence in a Paraquark Model of Baryons and Mesons. *Phys. Rev. Lett.*, 13:598–602, 1964. doi:10.1103/PhysRevLett.13.598.

[26] S. L. Glashow, J. Iliopoulos, and L. Maiani. Weak Interactions with Lepton-Hadron Symmetry. *Phys. Rev. D*, 2:1285–1292, 1970. doi:10.1103/PhysRevD.2.1285.

[27] J. D. Bjorken and S. L. Glashow. Elementary Particles and SU(4). *Phys. Lett.*, 11: 255–257, 1964. doi:10.1016/0031-9163(64)90433-0.

[28] J. E. Augustin et al. Discovery of a Narrow Resonance in e^+e^- Annihilation. *Phys. Rev. Lett.*, 33:1406–1408, 1974. doi:10.1103/PhysRevLett.33.1406.

[29] J. J. Aubert et al. Experimental Observation of a Heavy Particle J. *Phys. Rev. Lett.*, 33:1404–1406, 1974. doi:10.1103/PhysRevLett.33.1404.

[30] Martin L. Perl et al. Evidence for Anomalous Lepton Production in e+ - e- Annihilation. *Phys. Rev. Lett.*, 35:1489–1492, 1975. doi:10.1103/PhysRevLett.35.1489.

[31] S. W. Herb et al. Observation of a Dimuon Resonance at 9.5-GeV in 400-GeV Proton-Nucleus Collisions. *Phys. Rev. Lett.*, 39:252–255, 1977. doi:10.1103/PhysRevLett.39.252.

[32] F. Abe et al. Observation of top quark production in $\bar{p}p$ collisions. *Phys. Rev. Lett.*, 74:2626–2631, 1995. doi:10.1103/PhysRevLett.74.2626.

[33] E. Fermi. An attempt of a theory of beta radiation. 1. *Z. Phys.*, 88:161–177, 1934. doi:10.1007/BF01351864.

[34] S. L. Glashow. Partial Symmetries of Weak Interactions. *Nucl. Phys.*, 22:579–588, 1961. doi:10.1016/0029-5582(61)90469-2.

[35] Steven Weinberg. A Model of Leptons. *Phys. Rev. Lett.*, 19:1264–1266, 1967. doi:10.1103/PhysRevLett.19.1264.

[36] Abdus Salam. Weak and Electromagnetic Interactions. *Conf. Proc. C*, 680519: 367–377, 1968. doi:10.1142/9789812795915_0034.

[37] G. Arnison et al. Experimental Observation of Isolated Large Transverse Energy Electrons with Associated Missing Energy at $\sqrt{s} = 540$ GeV. *Phys. Lett. B*, 122: 103–116, 1983. doi:10.1016/0370-2693(83)91177-2.

[38] M. Banner et al. Observation of Single Isolated Electrons of High Transverse Momentum in Events with Missing Transverse Energy at the CERN anti-p p Collider. *Phys. Lett. B*, 122:476–485, 1983. doi:10.1016/0370-2693(83)91605-2.

[39] Peter W. Higgs. Broken Symmetries and the Masses of Gauge Bosons. *Phys. Rev. Lett.*, 13:508–509, 1964. doi:10.1103/PhysRevLett.13.508.

[40] F. Englert and R. Brout. Broken Symmetry and the Mass of Gauge Vector Mesons. *Phys. Rev. Lett.*, 13:321–323, 1964. doi:10.1103/PhysRevLett.13.321.

[41] Georges Aad et al. Observation of a new particle in the search for the Standard Model Higgs boson with the ATLAS detector at the LHC. *Phys. Lett. B*, 716:1–29, 2012. doi:10.1016/j.physletb.2012.08.020.

[42] Serguei Chatrchyan et al. Observation of a New Boson at a Mass of 125 GeV with the CMS Experiment at the LHC. *Phys. Lett. B*, 716:30–61, 2012. doi:10.1016/j.physletb.2012.08.021.

[43] Paul A. M. Dirac. The quantum theory of the electron. *Proc. Roy. Soc. Lond. A*, 117:610–624, 1928. doi:10.1098/rspa.1928.0023.

[44] Carl D. Anderson. Cosmic-Ray Positive and Negative Electrons. *Phys. Rev.*, 44: 406–416, 1933. doi:10.1103/PhysRev.44.406.

[45] O. Chamberlain, E. Segrè, and C. Wiegand. Experiments on Proton-Proton Scattering from 120 to 345 Mev. *Phys. Rev.*, 83(5):923, 1951. doi:10.1103/PhysRev.83.923.

[46] R. L. Workman et al. Review of Particle Physics. *PTEP*, 2022:083C01, 2022. doi:10.1093/ptep/ptac097.

[47] B. P. Abbott et al. Observation of Gravitational Waves from a Binary Black Hole Merger. *Phys. Rev. Lett.*, 116(6):061102, 2016. doi:10.1103/PhysRevLett.116.061102.

[48] W. Pauli. Dear radioactive ladies and gentlemen. *Phys. Today*, 31N9:27, 1978.

[49] C. L. Cowan, F. Reines, F. B. Harrison, H. W. Kruse, and A. D. McGuire. Detection of the free neutrino: A Confirmation. *Science*, 124:103–104, 1956. doi:10.1126/science.124.3212.103.

[50] C. F. Powell, G. P. S. Occhialini, D. L. Livesey, and L. V. Chilton. A New Photographic Emulsion for the Detection of Fast Charged Particles. *J. Sci. Instrum.*, 23: 102–106, 1946. doi:10.1088/0950-7671/23/5/304.

[51] D. H. Perkins. *Introduction to high energy physics*. 1982. ISBN 9780521621960.

[52] T. Morii, C. S. Lim, and S. N. Mukherjee. *The physics of the standard model and beyond*. 2004.

[53] Paul Langacker. *The Standard Model and Beyond*. Taylor & Francis, 2017. ISBN 978-1-4987-6322-6, 978-1-4987-6321-9, 978-0-367-57344-7, 978-1-315-17062-6. doi:10.1201/b22175.

[54] F. Halzen and Alan D. Martin. *QUARKS AND LEPTONS: AN INTRODUCTORY COURSE IN MODERN PARTICLE PHYSICS*. 1984. ISBN 978-0-471-88741-6.

[55] R. P. Feynman. Space - time approach to quantum electrodynamics. *Phys. Rev.*, 76: 769–789, 1949. doi:10.1103/PhysRev.76.769.

[56] R. P. Feynman. Mathematical formulation of the quantum theory of electromagnetic interaction. *Phys. Rev.*, 80:440–457, 1950. doi:10.1103/PhysRev.80.440.

[57] Julian S. Schwinger. On Quantum electrodynamics and the magnetic moment of the electron. *Phys. Rev.*, 73:416–417, 1948. doi:10.1103/PhysRev.73.416.

[58] S. Tomonaga. On a relativistically invariant formulation of the quantum theory of wave fields. *Prog. Theor. Phys.*, 1:27–42, 1946. doi:10.1143/PTP.1.27.

[59] Jeffrey Goldstone, Abdus Salam, and Steven Weinberg. Broken Symmetries. *Phys. Rev.*, 127:965–970, 1962. doi:10.1103/PhysRev.127.965.

[60] Chen-Ning Yang and Robert L. Mills. Conservation of Isotopic Spin and Isotopic Gauge Invariance. *Phys. Rev.*, 96:191–195, 1954. doi:10.1103/PhysRev.96.191.

[61] H. L. Anderson, E. Fermi, E. A. Long, and D. E. Nagle. Total Cross-sections of Positive Pions in Hydrogen. *Phys. Rev.*, 85:936, 1952.

[62] O. W. Greenberg. Spin and unitary-spin independence in a paraquark model of baryons and mesons. *Phys. Rev. Lett.*, 13:598–602, Nov 1964. URL https://link.aps.org/doi/10.1103/PhysRevLett.13.598.

[63] O. W. Greenberg. Spin and Unitary Spin Independence in a Paraquark Model of Baryons and Mesons. *Phys. Rev. Lett.*, 13:598–602, 1964.

[64] C.W. Misner, K.S. Thorne, and J.A. Wheeler. *Gravitation*. 1970. ISBN 9781400889099.

[65] Barry R. Holstein. Graviton Physics. *Am. J. Phys.*, 74:1002–1011, 2006.

[66] Ahmed Ali, Christian Hambrock, and M. Jamil Aslam. A Tetraquark interpretation of the BELLE data on the anomalous Upsilon(1S) pi+pi- and Upsilon(2S) pi+pi- production near the Upsilon(5S) resonance. *Phys. Rev. Lett.*, 104:162001, 2010.

[67] Roel Aaij et al. Observation of the resonant character of the $Z(4430)^{-}$ state. *Phys. Rev. Lett.*, 112(22):222002, 2014.

[68] Roel Aaij et al. Observation of $J/\psi p$ Resonances Consistent with Pentaquark States in $\Lambda_b^0 \to J/\psi K^- p$ Decays. *Phys. Rev. Lett.*, 115:072001, 2015.

[69] Murray Gell-Mann. A Schematic Model of Baryons and Mesons. *Phys. Lett.*, 8: 214–215, 1964.

[70] C. S. Wu, E. Ambler, R. W. Hayward, D. D. Hoppes, and R. P. Hudson. Experimental Test of Parity Conservation in Beta Decay. *Phys. Rev.*, 105:1413–1414, 1957.

[71] P. A. M. Dirac. A Theory of Electrons and Protons. *Proc. Roy. Soc. Lond.*, A126: 360, 1930.

[72] Bernard Aubert et al. Search for CPT and Lorentz violation in B0 - anti-B0 oscillations with dilepton events. *Phys. Rev. Lett.*, 100:131802, 2008.

[73] Nima Arkani-Hamed, Hsin-Chia Cheng, Markus Luty, and Jesse Thaler. Universal dynamics of spontaneous lorentz violation and a new spin-dependent inverse-square law force. *Journal of High Energy Physics*, 2005(07):029, 2005.

[74] D. Babusci et al. Test of CPT and Lorentz symmetry in entangled neutral kaons with the KLOE experiment. *Phys. Lett.*, B730:89–94, 2014.

[75] *The CKM matrix and the unitarity triangle. Workshop, CERN, Geneva, Switzerland, 13-16 Feb 2002: Proceedings*, 2003. doi:10.5170/CERN-2003-002-corr. URL `http://lss.fnal.gov/cgi-bin/find_paper.pl?conf-02-422`.

[76] Nicolas Maximilian Köhler. *Searches for the Supersymmetric Partner of the Top Quark, Dark Matter and Dark Energy at the ATLAS Experiment*. PhD thesis, Munich, Tech. U., 2018.

[77] Jogesh C. Pati and Abdus Salam. Lepton Number as the Fourth Color. *Phys. Rev. D*, 10:275–289, 1974. doi:10.1103/PhysRevD.10.275. [Erratum: Phys.Rev.D 11, 703–703 (1975)].

[78] Prem P. Singh. Discovery of the B_c meson. In *12th Les Rencontre de Physique de la Vallee d'Aoste: Results and Perspectives in Particle Physics*, 3 1998.

[79] A. Abulencia et al. Evidence for the exclusive decay $B_c^{\pm} \to J/\psi\pi^{\pm}$ and measurement of the mass of the B_c meson. *Phys. Rev. Lett.*, 96:082002, 2006. doi:10.1103/PhysRevLett.96.082002.

[80] J. Charles et al. Current status of the Standard Model CKM fit and constraints on $\Delta F = 2$ New Physics. *Phys. Rev. D*, 91(7):073007, 2015. doi:10.1103/PhysRevD.91.073007. Numbers updated using the results from the 2021 values in `http://ckmfitter.in2p3.fr/www/results/plots_spring21/num/ckmEval_results_spring21.html`.

[81] M. Bona et al. The Unitarity Triangle Fit in the Standard Model and Hadronic Parameters from Lattice QCD: A Reappraisal after the Measurements of Delta m(s) and BR(B —> tau nu(tau)). *JHEP*, 10:081, 2006. doi:10.1088/1126-6708/2006/10/081.

[82] Georges Aad et al. Measurement of the CP-violating phase ϕ_s and the B_s^0 meson decay width difference with $B_s^0 \to J/\psi\phi$ decays in ATLAS. *JHEP*, 08:147, 2016. doi:10.1007/JHEP08(2016)147.

[83] Y. Amhis et al. Averages of b-hadron, c-hadron, and τ-lepton properties as of summer 2016. *Eur. Phys. J. C*, 77(12):895, 2017. doi:10.1140/epjc/s10052-017-5058-4.

[84] Alexander Lenz and Gilberto Tetlalmatzi-Xolocotzi. Model-independent bounds on new physics effects in non-leptonic tree-level decays of B-mesons. *JHEP*, 07:177, 2020. doi:10.1007/JHEP07(2020)177.

[85] T. Aaltonen et al. Measurement of the Bottom-Strange Meson Mixing Phase in the Full CDF Data Set. *Phys. Rev. Lett.*, 109:171802, 2012. doi:10.1103/PhysRevLett.109.171802.

[86] Victor Mukhamedovich Abazov et al. Measurement of the CP-violating phase $\phi_s^{J/\psi\phi}$ using the flavor-tagged decay $B_s^0 \to J/\psi\phi$ in 8 fb^{-1} of $p\bar{p}$ collisions. *Phys. Rev. D*, 85:032006, 2012. doi:10.1103/PhysRevD.85.032006.

[87] Vardan Khachatryan et al. Measurement of the CP-violating weak phase ϕ_s and the decay width difference $\Delta\Gamma_s$ using the $\mathrm{B}_s^0 \to J/\psi\phi(1020)$ decay channel in pp collisions at $\sqrt{s} = 8$ TeV. *Phys. Lett. B*, 757:97–120, 2016. doi:10.1016/j.physletb.2016.03.046.

[88] Roel Aaij et al. Precision measurement of CP violation in $B_s^0 \to J/\psi K^+K^-$ decays. *Phys. Rev. Lett.*, 114(4):041801, 2015. doi:10.1103/PhysRevLett.114.041801.

[89] Roel Aaij et al. Resonances and CP violation in B_s^0 and $\overline{B}_s^0 \to J/\psi K^+K^-$ decays in the mass region above the $\phi(1020)$. *JHEP*, 08:037, 2017. doi:10.1007/JHEP08(2017)037.

[90] Roel Aaij et al. Measurement of the CP-violating phase ϕ_s in $\overline{B}_s^0 \to J/\psi\pi^+\pi^-$ decays. *Phys. Lett. B*, 736:186–195, 2014. doi:10.1016/j.physletb.2014.06.079.

[91] Roel Aaij et al. First study of the CP -violating phase and decay-width difference in $B_s^0 \to \psi(2S)\phi$ decays. *Phys. Lett. B*, 762:253–262, 2016. doi:10.1016/j.physletb.2016.09.028.

[92] Roel Aaij et al. Measurement of the CP-violating phase ϕ_s in $\bar{B}_s^0 \to D_s^+D_s^-$ decays. *Phys. Rev. Lett.*, 113(21):211801, 2014. doi:10.1103/PhysRevLett.113.211801.

[93] Georges Aad et al. Flavor tagged time-dependent angular analysis of the $B_s \to J/\psi\phi$ decay and extraction of $\Delta\Gamma$s and the weak phase ϕ_s in ATLAS. *Phys. Rev. D*, 90(5):052007, 2014. doi:10.1103/PhysRevD.90.052007.

[94] Y. Amhis et al. Averages of b-hadron, c-hadron, and τ-lepton properties as of 2021. 6 2022. doi:10.48550/ARXIV.2206.07501.

[95] M. Kirk, A. Lenz, and T. Rauh. Dimension-six matrix elements for meson mixing and lifetimes from sum rules. *JHEP*, 12:068, 2017. doi:10.1007/JHEP12(2017)068. [Erratum: JHEP 06, 162 (2020)].

[96] Damir Becirevic. Theoretical progress in describing the B meson lifetimes. *PoS*, HEP2001:098, 2001. doi:10.22323/1.007.0098.

[97] LHC Design Report Vol.1: The LHC Main Ring. 6 2004. doi:10.5170/CERN-2004-003-V-1.

[98] `https://lhc-commissioning.web.cern.ch/schedule/LHC-long-term.htm`. Accessed: 2022-09-19.

[99] ATLAS Collaboration. Public atlas luminosity results for run-2 of the lhc. `https://twiki.cern.ch/twiki/bin/view/AtlasPublic/LuminosityPublicResultsRun2`. Accessed: 2022-09-19.

[100] *CAS - CERN Accelerator School: Intermediate Accelerator Physics: Zeuthen, Germany 15 - 26 Sep 2003. CAS - CERN Accelerator School: Intermediate Course on Accelerator Physics*, Geneva, 2006. CERN, CERN. doi:10.5170/CERN-2006-002. URL `https://cds.cern.ch/record/603056`.

[101] LHC Machine. *JINST*, 3:S08001, 2008. doi:10.1088/1748-0221/3/08/S08001.

[102] M. Martini. An Introduction to transverse beam dynamics in accelerators. 3 1996.

[103] B. J. Holzer. Introduction to Transverse Beam Dynamics. In *CERN Accelerator School: Course on Superconductivity for Accelerators*, pages 27–45, 2013. doi:10.5170/CERN-2013-007.27.

[104] F Zimmermann. Parameter Space Beyond 1034. Technical report, 2010. URL `https://cds.cern.ch/record/1304238`.

[105] Ewa Lopienska. The CERN accelerator complex, layout in 2022. Complexe des accélérateurs du CERN en janvier 2022. 2022. URL `https://cds.cern.ch/record/2800984`. General Photo.

[106] Georges Aad et al. Improved luminosity determination in pp collisions at sqrt(s) = 7 TeV using the ATLAS detector at the LHC. *Eur. Phys. J. C*, 73(8):2518, 2013. doi:10.1140/epjc/s10052-013-2518-3.

[107] R. Bruce, C. Bracco, R. De Maria, M. Giovannozzi, A. Mereghetti, D. Mirarchi, S. Redaelli, E. Quaranta, and B. Salvachua. Reaching record-low β^* at the cern large hadron collider using a novel scheme of collimator settings and optics. *Nuclear Instruments and Methods in Physics Research Section A: Accelerators, Spectrometers, Detectors and Associated Equipment*, 848:19–30, 2017. ISSN 0168-9002. doi:https://doi.org/10.1016/j.nima.2016.12.039. URL https://www.sciencedirect.com/science/article/pii/S0168900216313092.

[108] Z. Citron et al. Report from Working Group 5: Future physics opportunities for high-density QCD at the LHC with heavy-ion and proton beams. *CERN Yellow Rep. Monogr.*, 7:1159–1410, 2019. doi:10.23731/CYRM-2019-007.1159.

[109] R Bailey and Paul Collier. Standard Filling Schemes for Various LHC Operation Modes. Technical report, CERN, Geneva, 2003. URL http://cds.cern.ch/record/691782.

[110] Rende Steerenberg et al. Operation and performance of the CERN Large Hadron Collider during proton Run 2. In *10th International Particle Accelerator Conference*, page MOPMP031, 2019. doi:10.18429/JACoW-IPAC2019-MOPMP031.

[111] Jorg Wenninger. LHC status and performance. *PoS*, CHARGED2018:001, 2019. doi:10.22323/1.339.0001.

[112] T. Pieloni, X. Buffat, W. Herr, R. Giachino, E. Metral, and G. Papotti. Colliding High Brightness Beams in the LHC. In *52nd ICFA Advanced Beam Dynamics Workshop on High-Intensity and High-Brightness Hadron Beams*, page MOP250, 2012.

[113] Stephane Fartoukh et al. LHC Configuration and Operational Scenario for Run 3.

[114] I. Zurbano Fernandez et al. High-Luminosity Large Hadron Collider (HL-LHC): Technical design report. 10/2020, 12 2020. doi:10.23731/CYRM-2020-0010.

[115] G. Aad et al. The ATLAS Experiment at the CERN Large Hadron Collider. *JINST*, 3:S08003, 2008. doi:10.1088/1748-0221/3/08/S08003.

[116] Ana Maria Rodriguez Vera and Joao Antunes Pequenao. ATLAS Detector Magnet System. General Photo, 2021. URL https://cds.cern.ch/record/2770604.

[117] Georges Aad et al. Measurements of sensor radiation damage in the ATLAS inner detector using leakage currents. *JINST*, 16:P08025, 2021. doi:10.1088/1748-0221/16/08/P08025.

[118] M. Capeans, G. Darbo, K. Einsweiler, M. Elsing, T. Flick, M. Garcia-Sciveres, C. Gemme, H. Pernegger, O. Rohne, and R. Vuillermet. ATLAS Insertable B-Layer Technical Design Report. 9 2010.

[119] M. Backhaus. The upgraded Pixel Detector of the ATLAS Experiment for Run 2 at the Large Hadron Collider. *Nucl. Instrum. Meth. A*, 831:65–70, 2016. doi:10.1016/j.nima.2016.05.018.

[120] Alessandro La Rosa. The ATLAS Insertable B-Layer: from construction to operation. *JINST*, 11(12):C12036, 2016. doi:10.1088/1748-0221/11/12/C12036.

[121] M. Aleksa, W. Cleland, Y. Enari, M. Fincke-Keeler, L. Hervas, F. Lanni, S. Majewski, C. Marino, and I. Wingerter-Seez. ATLAS Liquid Argon Calorimeter Phase-I Upgrade Technical Design Report. 9 2013.

[122] Vincenzo Izzo. ATLAS upgrades. *PoS*, LHCP2020:094, 2021. doi:10.22323/1.382.0094.

[123] Expected tracking and related performance with the updated ATLAS Inner Tracker layout at the High-Luminosity LHC. 2021.

[124] Takuya Nobe. Triggering in ATLAS in Run 2 and Run 3. *PoS*, LHCP2021:168, 2021. doi:10.22323/1.397.0168.

[125] Georges Aad et al. Operation of the ATLAS trigger system in Run 2. *JINST*, 15 (10):P10004, 2020. doi:10.1088/1748-0221/15/10/P10004.

[126] Morad Aaboud et al. Performance of the ATLAS Trigger System in 2015. *Eur. Phys. J. C*, 77(5):317, 2017. doi:10.1140/epjc/s10052-017-4852-3.

[127] P. Calafiura, W. Lavrijsen, C. Leggett, M. Marino, and D. Quarrie. The Athena control framework in production, new developments and lessons learned. In *14th International Conference on Computing in High-Energy and Nuclear Physics*, pages 456–458, 2005.

[128] Gaudi project documentation. `https://gaudi.web.cern.ch/gaudi/`. Accessed: 2022-12-01.

[129] Charles Leggett et al. AthenaMT: upgrading the ATLAS software framework for the many-core world with multi-threading. *J. Phys. Conf. Ser.*, 898(4):042009, 2017. doi:10.1088/1742-6596/898/4/042009.

[130] R. Brun and F. Rademakers. ROOT: An object oriented data analysis framework. *Nucl. Instrum. Meth. A*, 389:81–86, 1997. doi:10.1016/S0168-9002(97)00048-X. See also `root.cern.ch`.

[131] Wouter Verkerke and David P. Kirkby. The RooFit toolkit for data modeling. *eConf*, C0303241:MOLT007, 2003. See also `https://roofit.sourceforge.net/`.

[132] Lorenzo Moneta, Kevin Belasco, Kyle S. Cranmer, S. Kreiss, Alfio Lazzaro, Danilo Piparo, Gregory Schott, Wouter Verkerke, and Matthias Wolf. The RooStats Project. *PoS*, ACAT2010:057, 2010. doi:10.22323/1.093.0057.

[133] David Adams et al. Dual-use tools and systematics-aware analysis workflows in the ATLAS Run-2 analysis model. *J. Phys. Conf. Ser.*, 664(3):032007, 2015. doi:10.1088/1742-6596/664/3/032007.

[134] F. Akesson et al. ATLAS Inner Detector Event Data Model. 12 2007.

[135] Kyle Cranmer, Lukas Heinrich, Roger Jones, and David M. South. Analysis Preservation in ATLAS. *J. Phys. Conf. Ser.*, 664(3):032013, 2015. doi:10.1088/1742-6596/664/3/032013.

[136] James Catmore, Jack Cranshaw, Thomas Gillam, Eirik Gramstad, Paul Laycock, Nurcan Ozturk, and Graeme Andrew Stewart. A new petabyte-scale data derivation framework for ATLAS. *J. Phys. Conf. Ser.*, 664(7):072007, 2015. doi:10.1088/1742-6596/664/7/072007.

[137] Christian Bierlich et al. A comprehensive guide to the physics and usage of PYTHIA 8.3. 3 2022. doi:10.21468/SciPostPhysCodeb.8.

[138] Johannes Bellm et al. Herwig 7.2 release note. *Eur. Phys. J. C*, 80(5):452, 2020. doi:10.1140/epjc/s10052-020-8011-x.

[139] D. J. Lange. The EvtGen particle decay simulation package. *Nucl. Instrum. Meth. A*, 462:152–155, 2001. doi:10.1016/S0168-9002(01)00089-4.

[140] N. C. Benekos et al. B-physics performance with Initial and Complete Inner detector layouts in Data Challenge-1. 2004.

[141] S. Agostinelli et al. GEANT4–a simulation toolkit. *Nucl. Instrum. Meth. A*, 506: 250–303, 2003. doi:10.1016/S0168-9002(03)01368-8.

[142] Ian Bird. Computing for the Large Hadron Collider. *Ann. Rev. Nucl. Part. Sci.*, 61: 99–118, 2011. doi:10.1146/annurev-nucl-102010-130059.

[143] Worldwide lhc computing grid. `https://wlcg.web.cern.ch/`. Accessed: 2022-12-03.

[144] LHC computing Grid. Technical design report. 6 2005.

[145] Rene Brun, Federico Carminati, and Giuliana Galli Carminati, editors. *From the web to the grid and beyond: Computing paradigms driven by high-energy physics*. The frontiers collection. Springer, Berlin, Germany, 2012. ISBN 978-3-642-43881-3, 978-3-642-23157-5. doi:10.1007/978-3-642-23157-5.

[146] Noemi Calace. Track and Vertex reconstruction in ATLAS for LHC Run-3 and High-Luminosity phases. 2021. URL `https://cds.cern.ch/record/2777660`.

[147] Andreas Salzburger. Optimisation of the ATLAS Track Reconstruction Software for Run-2. *J. Phys. Conf. Ser.*, 664(7):072042, 2015. doi:10.1088/1742-6596/664/7/072042.

[148] M. Aaboud et al. Performance of the ATLAS Track Reconstruction Algorithms in Dense Environments in LHC Run 2. *Eur. Phys. J. C*, 77(10):673, 2017. doi:10.1140/epjc/s10052-017-5225-7.

[149] R. Fruhwirth. Application of Kalman filtering to track and vertex fitting. *Nucl. Instrum. Meth. A*, 262:444–450, 1987. doi:10.1016/0168-9002(87)90887-4.

[150] Georges Aad et al. Muon reconstruction performance of the ATLAS detector in proton-proton collision data at $\sqrt{s}$ =13 TeV. *Eur. Phys. J. C*, 76(5):292, 2016. doi:10.1140/epjc/s10052-016-4120-y.

[151] Development of ATLAS Primary Vertex Reconstruction for LHC Run 3. 2019.

[152] Vertex Reconstruction Performance of the ATLAS Detector at $\sqrt{s} = 13$ TeV. 2015.

[153] E. Norrbin and T. Sjostrand. Production and hadronization of heavy quarks. *Eur. Phys. J.*, C17:137–161, 2000.

[154] E. Norrbin and T. Sjostrand. Production and hadronization of heavy quarks. *Eur. Phys. J. C*, 17:137–161, 2000. doi:10.1007/s100520000460.

[155] Simon George. Atlas: triggers for b-physics. *Nuclear Instruments and Methods in Physics Research Section A: Accelerators, Spectrometers, Detectors and Associated Equipment*, 446(1):274–281, 2000. ISSN 0168-9002. doi:https://doi.org/10.1016/S0168-9002(00)00002-4. URL `https://www.sciencedirect.com/science/article/pii/S0168900200000024`.

[156] 2015 start-up trigger menu and initial performance assessment of the ATLAS trigger using Run-2 data. Technical report, CERN, Geneva, 2016. URL `https://cds.cern.ch/record/2136007`.

[157] Georges Aad et al. Measurement of b-quark fragmentation properties in jets using the decay $B^{\pm} \to J/\psi K^{\pm}$ in pp collisions at $\sqrt{s} = 13$ TeV with the ATLAS detector. *JHEP*, 12:131, 2021. doi:10.1007/JHEP12(2021)131.

[158] Matteo Cacciari, Gavin P. Salam, and Gregory Soyez. The anti-k_t jet clustering algorithm. *JHEP*, 04:063, 2008. doi:10.1088/1126-6708/2008/04/063.

[159] Georges Aad et al. Study of $\mathrm{B_c^+} \to \mathrm{J/\psi D_s^+}$ and $\mathrm{B_c^+} \to \mathrm{J/\psi D_s^{*+}}$ decays in pp collisions at $\sqrt{\mathrm{s}} = 13$ TeV with the ATLAS detector. *JHEP*, 08:087, 2022. doi:10.1007/JHEP08(2022)087.

[160] Morad Aaboud et al. Study of the rare decays of B_s^0 and B^0 mesons into muon pairs using data collected during 2015 and 2016 with the ATLAS detector. *JHEP*, 04:098, 2019. doi:10.1007/JHEP04(2019)098.

[161] Combination of the ATLAS, CMS and LHCb results on the $B^0_{(s)} \to \mu^+\mu^-$ decays. 2020.

[162] Georges Aad et al. ATLAS b-jet identification performance and efficiency measurement with $t\bar{t}$ events in pp collisions at $\sqrt{s} = 13$ TeV. *Eur. Phys. J. C*, 79(11):970, 2019. doi:10.1140/epjc/s10052-019-7450-8.

[163] R Aaij et al. Measurement of the polarization amplitudes in $B^0 \to J/\psi K^*(892)^0$ decays. *Phys. Rev. D*, 88:052002, 2013. doi:10.1103/PhysRevD.88.052002.

[164] B Storaci. Updated average f_s/f_d b-hadron production fraction ratio for 7 TeV pp collisions. 7 2013.

[165] R. Aaij et al. Study of the kinematic dependences of Λ_b^0 production in pp collisions and a measurement of the $\Lambda_b^0 \to \Lambda_c^+ \pi^-$ branching fraction. *JHEP*, 08:143, 2014. doi:10.1007/JHEP08(2014)143.

[166] R. Aaij et al. Study of the production of Λ_b^0 and $\overline{B}^0$ hadrons in pp collisions and first measurement of the $\Lambda_b^0 \to J/\psi pK^-$ branching fraction. *Chin. Phys. C*, 40(1): 011001, 2016. doi:10.1088/1674-1137/40/1/011001.

[167] Studies of radial distortions of the ATLAS Inner Detector. 3 2018.

[168] CMS Collaboration. Measurement of the cp-violating phase ϕ_{s} in the $\mathrm{b}_{\mathrm{s}}^0 \to \mathrm{j}/\psi\,\phi(1020) \to \mu^+\mu^-\mathrm{k}^+\mathrm{k}^-$ channel in proton-proton collisions at $\sqrt{s} = 13$ tev. *Phys. Lett. B*, 816:136188, 2020. doi:10.1016/j.physletb.2021.136188.

[169] LHCb Collaboration. Updated measurement of time-dependent CP-violating observables in $B_s^0 \to J/\psi K^+K^-$ decays. *Eur. Phys. J.*, C79(8):706, 2019. doi:10.1140/epjc/s10052-019-7159-8.

[170] LHCb Collaboration. First study of the CP -violating phase and decay-width difference in $B_s^0 \to \psi(2S)\phi$ decays. *Phys. Lett. B*, 762:253–262, 2016. doi:10.1016/j.physletb.2016.09.028.

[171] LHCb Collaboration. Measurement of the CP-violating phase ϕ_s in $\bar{B}_s^0 \to D_s^+D_s^-$ decays. *Phys. Rev. Lett.*, 113(LHCB-PAPER-2014-051. LHCB-PAPER-2014-051. CERN-PH-EP-2014-223):211801,, 9 2014. doi:10.1103/PhysRevLett.113.211801.

[172] LHCb Collaboration. Measurement of the CP-violating phase ϕ_s from $B_s^0 \to J/\psi\pi^+\pi^-$ decays in 13 TeV pp collisions. *Phys. Lett.*, B797:134789, 2019. doi:10.1016/j.physletb.2019.07.036.

[173] Robert Fleischer and Robert Knegjens. Effective Lifetimes of B_s Decays and their Constraints on the B_s^0-$\bar{B}_s^0$ Mixing Parameters. *Eur. Phys. J. C*, 71:1789, 2011. doi:10.1140/epjc/s10052-011-1789-9.

[174] N. L. Johnson. Systems of frequency curves generated by methods of translation. *Biometrika*, 36:149–176, 1949. doi:10.1093/biomet/36.1-2.149.

[175] Muriel Pivk. sPLOT: A Quick introduction. In *Statistical Problems in Particle Physics, Astrophysics and Cosmology (PHYSTAT 05): Proceedings, Oxford, UK, September 12-15, 2005*, pages 173–177, 2006.

[176] Measurement of the B0 and Bs0 lifetimes in the decay modes B0 $\to$ J/ψK∗0 and Bs0 $\to$ J/$\psi\varphi$ in ATLAS. 7 2011.

[177] LHCb Collaboration. Measurements of the B^+,B^0,B^0_s meson and Λ^0_b baryon lifetimes. *JHEP*, 04:114, 2014. doi:10.1007/JHEP04(2014)114.

[178] LHCb Collaboration. Effective lifetime measurements in the $B^0_s ı K^+K^-$,$B^0 ı K^+\pi^-$ and $B^0_s ı \pi^+K^-$ decays. *Phys. Lett. B*, 736:446–454, 2014. doi:10.1016/j.physletb.2014.07.051.

[179] Albert M Sirunyan et al. Measurement of b hadron lifetimes in pp collisions at $\sqrt{s}$ = 8 TeV. *Eur. Phys. J. C*, 78(6):457, 2018. doi:10.1140/epjc/s10052-018-5929-3. [Erratum: Eur.Phys.J.C 78, 561 (2018)].

[180] Shohei Nishida. Recent results from the belle ii experiment. Oct 2022. The Tenth Annual Conference on Large Hadron Collider Physics - LHCP2022 16-20 May 2022.

[181] Victor Mukhamedovich Abazov et al. Measurement of the B^0_s Lifetime in the Flavor-Specific Decay Channel $B^0_s \to D^-_s \mu^+ \nu X$. *Phys. Rev. Lett.*, 114(6):062001, 2015. doi:10.1103/PhysRevLett.114.062001.

[182] Alexander Lenz, Maria Laura Piscopo, and Aleksey V. Rusov. Disintegration of beauty: a precision study. 8 2022.

[183] G. Cowan. *Statistical data analysis*. 1998. ISBN 978-0-19-850156-5.

[184] Giovanni Punzi. Comments on likelihood fits with variable resolution. *eConf*, C030908:WELT002, 2003.

[185] Louis Lyons, Duncan Gibaut, and Peter Clifford. How to Combine Correlated Estimates of a Single Physical Quantity. *Nucl. Instrum. Meth. A*, 270:110, 1988. doi:10.1016/0168-9002(88)90018-6.

[186] A. Valassi. Combining correlated measurements of several different physical quantities. *Nucl. Instrum. Meth. A*, 500:391–405, 2003. doi:10.1016/S0168-9002(03)00329-2.

Glossary

ALICE (A Large Ion Collider Experiment) is the detector at the Large Hadron Collider devoted to study of heavy ion collisions. Quark-gluon plasma is believed to be created in the collisions of heavy ions. 66, 69

ATLAS (A Toroidal LHC ApparatuS) is one of the four particle detectors developed for the LHC at CERN. The ATLAS experiment aims to investigate a wide range of physics, including the search for the Higgs boson, extra dimensions, and particles that could make up dark matter. The experiment is described in detail in chapter 4. xxiv, 1, 2, 53, 55, 59, 60, 63, 66, 67, 69, 71–75, 77–81, 83–86, 88, 89, 91, 92, 95, 97, 98, 101, 103, 105–107, 109–114, 118, 129, 131, 145, 148, 153, 154, 163–167, 207–211

ATLAS Cathode Strip Chambers (CSC) are multi-wire proportional chambers using the cathode plates. As a part of ATLAS Muon Spectrometer, the chambers are responsible for the precise muon momentum measurement at large pseudorapidities of $2.0 < |\eta| < 2.7$. 83, 84, 208

ATLAS Electromagnetic Calorimeter (ECAL) is part of the ATLAS calorimetry system designed to measure the energies of photons and charged particles interacting via the electromagnetic interaction. The barrel part of ECAL covers the pseudorapidity region of $|\eta| < 1.475$. The two end-cap ECALs cover the region of $1.375 < |\eta| < 3.2$. 2, 74–76, 80–83, 92, 103, 207, 209, 211

ATLAS Hadronic Calorimeter (HCAL) is part of the ATLAS calorimetry system designed to measure the energies of photons and charged particles interacting via the strong interaction. It envelopes the Electromagnetic Calorimeter and is composed of Tile Calorimeter (barrel region) covering the region of $|\eta| < 1.7$ and the Hadronic End-cap Calorimeter (HEC) located in the region covering the range $1.5 < |\eta| < 3.2$. The forward regions with $3.1 < |\eta| < 4.9$ are occupied by forward calorimeters (FCAL). 2, 74, 80–82, 92, 211

ATLAS Inner Detector (ID) is the inner-most sub-detector system of the ATLAS detector. It is built of semiconductor pixel (Pixel Detector and Insertable B-Layer) and strip (Semiconductor Tracker) detectors to reconstruct the tracks and measure their momenta with high resolution. The last part of ID is Transition Radiation Tracker, partly helping improve the resolution and focusing on particle identification. 2, 74–79, 81, 83, 89, 93, 101–104, 109, 208, 209

ATLAS Insertable B-Layer (IBL) is the additional inner-most layer of the PIX detector system inserted before the Run2 started. Situated 5 cm from the beam pipe, the IBL provides the further resolution needed for the B mesons and $\tau^{\pm}$ tracks (they decay before reaching the other layers of PIX). 76, 78, 79, 208

ATLAS Monitored Drift Tubes (MDT) is the part of the ATLAS MS system at the region $|\eta| < 2.7$. The chambers consisting of three to eight layers of drift tubes are responsible for precise muon momentum measurement. 83–86, 104, 208

ATLAS Muon Spectrometer (MS) the ATLAS outer-most detector subsystem responsible for the muon momentum measurement and muon identification (Cathode Strip Chambers and Monitored Drift Tubes). Other modules (Resistive Plate Chambers and Thin Gap Chambers) are designed for triggering. 2, 74, 76, 83, 84, 91, 93, 102–104, 207, 208

ATLAS Pixel Detector (PIX) are the first three layers of the ATLAS Inner Detector, composed of the high granularity semiconductor pixel sensors, providing excellent resolution of the track and vertex reconstruction. In Long Shutdown 1, an additional layer of sensors (IBL) was inserted closest to the beam pipe. 76–80, 102–104, 208

ATLAS Resistive Plate Chambers (RPC) are mounted on both sides of the MDT and cover the pseudorapidity of $|\eta| < 1.05$. RPC system is included in the ATLAS MS system, capable of triggering thanks to its fast readout (a few tens of nanoseconds). 83, 85, 86, 88, 92, 208, 211

ATLAS SemiConductor Tracker (SCT) is the part of the ATLAS Inner Detector, surrounding the PIX. Four layers of silicon strip sensors are responsible for tracking with large resolution onwards from the beam pipe. 76, 78–80, 102–104, 208

ATLAS Thin Gap Chambers (TGC) are multi-wire proportional chambers in the ATLAS MS used for trigger system (similar to the RPC). 83, 85, 86, 92, 208, 211

ATLAS Transition Radiation Tracker (TRT) is the outer-most part of the current ATLAS Inner Detector. It comprises many layers of gaseous straw tubes. The passing particle transiting many tubes creates radiation, detected by the wire at the centre of each straw tube. On average, 36 hits per track are created in TRT, improving the momentum resolution. Moreover, it provides supplementary electron identification to the ECAL. 76, 78, 80, 81, 102, 208

ATLAS Trigger and Data Acquisition (TDAQ) describes the ATLAS system that collects and filters the signal from the detector sensors and modules. It consists of Level-1 Trigger and High Level Trigger. Section 5.1 provides ATLAS TDAQ full description. 2, 88, 89, 91, 92, 97, 109, 210, 211

CDF (Collider Detector at Fermilab) is one of the two large detector systems (the second is DØ) at the Tevatron Collider at Fermilab in Batavia, Illinois. It operated between 1983 and 2011. 10, 39, 53, 55, 153, 166, 209, 213

Charge-Parity invariance states that all interactions are invariant under the application of the charge and parity operators. This invariance is holding in strong and electromagnetic interaction, but weak interaction violates it. 1, 2, 28–30, 32–35, 39, 40, 44, 45, 48, 51, 53, 67, 72, 110, 115, 129, 146, 148, 150, 153, 165

CMS (Compact Muon Solenoid) is the second largest experiment at the LHC. It has similar physics goals as ATLAS but uses a different technological approach and detector design to accomplish them. 53, 55, 66, 67, 150–153, 166

DØ is one of the two large detector systems (the second is CDF) at the Tevatron Collider at Fermilab in Batavia, Illinois. It operated between 1983 and 2011. 53, 55, 153, 166, 209, 213

European Organization for Nuclear Research (European Organization for Nuclear Research, in French: Conseil Européen de la Recherche Nucléaire) is the world's largest particle physics laboratory near Geneva on the border between France and Switzerland. CERN's main function is to provide the particle accelerators (like LHC) and other infrastructure needed for high-energy physics research. 10, 53, 57, 63, 64, 66, 92, 207, 210, 211

Grand Unified Theories (GUT) predict the theory that unifies all the Standard Model fundamental interactions. They follow the symmetry with only one gauge coupling (and several force carriers). 35, 36

Heavy Quark Effective Theory (HQET) permits calculation of B-meson observables through perturbative expansion in powers of the reciprocal of the b-quark mass, m_b. 55, 56

HFLAV (Heavy Flavor Averaging Group, `https://hflav.web.cern.ch/`) is a group providing a combination of heavy flavour quantities. The combination is continuously updated with new results. 55

High Level Trigger (HLT) is a part of the ATLAS Trigger and Data Acquisition system. It is the software-based system taking events that pass the L1. HLT reconstruct the tracks and vertices in the region of interest selected by the L1 and apply an additional set of requirements. Some of the requirements can fully throw out the event. The remaining events are recorded with information about passing the rest of the HLT requirements. 2, 89, 91–96, 98, 109, 209, 211

High Luminosity Large Hadron Collider (HL-LHC) is the LHC operating with increased peak luminosity by a factor of 5 than the designed peak luminosity for Run1, Run2 and Run3. HL-LHC will start by Run4. 69, 70, 88, 89

Interaction Point (IP) is the place of the accelerator where two beams can collide. 62, 65–67, 71, 73, 86, 87, 103

Large Electron–Positron Collider (LEP) was built at CERN and collided electrons with positrons at energies that reached 209 GeV. It was a circular collider with a circumference of 27 kilometres built in a tunnel roughly 100 m underground. LEP was used from 1989 until 2000. Then, it was replaced by the LHC. 57, 58

Large Hadron Collider (LHC) is the world's largest and highest-energy particle collider. It was built by the European Organization for Nuclear Research (CERN) between 1998 and 2008. It lies in a tunnel 27 kilometres in circumference and as deep as 175 metres beneath France–Switzerland border near Geneva. The LHC is described in detail in chapter 3. 1, 2, 11, 53, 54, 57–71, 94, 97, 108, 116, 129, 145, 154, 165, 167, 207, 209–213

Lattice QCD is a non-perturbative approach to solving the Quantum chromodynamics theory of quarks and gluons. It is a lattice gauge theory formulated on a grid or lattice of points in space and time. 55, 56

Level-1 Trigger (L1) is hardware-based system looking for the high-p_{T} muons, electrons and jets. As a part of the ATLAS TDAQ, it uses only ECAL, Hadronic Calorimeter, RPC and TGC information due to their fast readout of the signal. The region of interest is only used to evaluate the event. Events passing the required conduction are used in the further trigger system, HLT. 2, 91–95, 98, 109, 209, 210

LHC Long Shutdown 1 (LS1) is a period of the LHC upgrade, starting in January 2012 and ending in March 2015. 58, 68, 78, 208

LHC Long Shutdown 2 (LS2) is a period of the LHC upgrade, starting in January 2019 and ending in March 2022. 58, 69, 88

LHC Run1 is a period of the LHC operation, starting in November 2009 and ending in December 2012. xxiv, 58, 63, 64, 67, 68, 113, 114, 129, 145, 148, 163, 166, 210

LHC Run2 is a period of the LHC operation, starting in March 2015 and ending in December 2018. 1, 58, 60, 63, 64, 67, 68, 87, 88, 92, 96, 114, 130, 162, 164, 208, 210

LHC Run3 is a period of the LHC operation, starting in July 2022. This run is expected to last until 2026. 58, 63, 64, 69, 70, 87, 89, 96, 210

LHCb (Large Hadron Collider beauty) experiment is one of eight particle physics detector experiments collecting data at the LHC at CERN. It specializes in investigating the slight differences between matter and antimatter by studying a type of particle called the beauty quark (b quark). 53, 55, 66, 67, 69, 95, 135, 150–153, 166

Linear accelerator 3 (Linac3) is part of the LHC accelerator complex. It is a linear accelerator providing the lead ions to the next accelerator: Low Energy Ion Ring. 64, 211

Linear accelerator 4 (Linac4) is part of the LHC accelerator complex. It is a linear accelerator that increases the energy of proton from the stripped hydrogen to 50 MeV. Linac4 also forms the protons into bunches. 63, 212

Low Energy Ion Ring (LEIR) is part of the LHC accelerator complex. It uses the lead ions from Linac3 and accelerates them from 4.2 MeV to 72 MeV. When the final energy is reached, the ions are sent to Proton Synchrotron. 64, 211, 212

Minimal Supersymmetric Standard Model (MSSM) is a minimal extension of the SM using the supersymmetry theories. 33–35

Proton Synchrotron (PS) is a part of the LHC injection chain, accelerating the proton or heavy ions. It uses protons from Proton Synchrotron Booster or heavy ions from LEIR. PS started its operation with the first acceleration of protons on 24 November 1959. 63, 64, 211, 212

Proton Synchrotron Booster (PSB) is designed to take protons from Linac4 and increase their energy to 1.4 GeV before entering the PS. 63, 212

Quantum chromodynamics (QCD) is a type of quantum field theory called a non-abelian gauge theory, with symmetry group SU(3), describing the interactions of quarks and gluons. Detailed information can be found in section 1.2.1.3. 19–21, 56, 107, 108, 110, 111, 211

Quantum electrodynamics (QED) is the relativistic quantum field theory of electrodynamics. Technically, QED is an abelian gauge theory with the symmetry group $U(1)$ and describes the interaction as a perturbation theory of the electromagnetic quantum vacuum. Detailed information can be found in section 1.2.1.1. 15–17, 19, 20, 26, 27

Standard Model (SM) of particle physics is a gauge quantum field theory with an internal group $\mathrm{SU(3)_C \otimes SU(2)_L \otimes U(1)_Y}$ formulated in the 1970s. Its theoretical implications are discussed in chapter 1. 1, 2, 12–14, 17–19, 21–23, 26, 28, 29, 32–35, 37, 39, 42, 46, 53, 54, 57, 66, 67, 71, 107, 110, 113, 114, 129, 151, 153, 166, 210, 212

Super Proton Synchrotron (SPS) is the last part of the LHC injection chain, accelerating the proton or heavy ions. It is 6.90 km in circumference and accelerates protons up to 450 GeV. 10, 63–65, 68

Supersymmetry (SUSY) is a theory that extends the SM. It predicts that each of the Standard Model particles has its superpartner using a generalization of the space-time symmetries of quantum field theory that causes lepton superpartners are bosons and vice versa. 33, 36, 71, 72

Tevatron was a circular particle accelerator in the United States, at the Fermilab in Illinois. With two large experiments CDF and DØ, it operated until 2011. It accelerated protons and antiprotons in a 6.28 km ring to energies of up to 1 TeV. The main achievement of the Tevatron was the discovery of the top quark in 1995. 53, 54, 209

Worldwide LHC Computing Grid (WLCG) is a system of connected worldwide clusters. It provides extensive computing resources and storage capacities for the LHC experiments. 92, 97, 98, 100